CHEMICAL PROBES FOR STUDYING CYCLOOXYGENASE-2 AND NITRIC OXIDE IN LIVING SYSTEMS

BY

CHRISTOPHER J. REINHARDT

DISSERTATION

Submitted in partial fulfillment of the requirements
for the degree of Doctor of Philosophy in Chemistry
in the Graduate College of the
University of Illinois at Urbana-Champaign, 2020

Urbana, Illinois

Doctoral Committee:

Assistant Professor Jefferson Chan, Chair
Professor John A. Gerlt
Professor Paul J. Hergenrother
Professor Wilfred A. van der Donk

ABSTRACT

Molecular imaging enables the direct detection of analytes and biomolecular species within their native biological environment. Although the field derives from diagnostic biomedical imaging, there has been a significant shift over the past couple decades towards using imaging to evaluate and discover biology. In general, molecular imaging relies on the development of chemical or biochemical tools that accumulate at the site of interest or under undergo a selective, observable change following target engagement. Activity-based sensing is a powerful expansion of molecular imaging because it measures chemical reactivity rather than concentration. Chapter 1 serves as an introduction to molecular imaging with a historical tone. It also defines and highlights key examples of binding-based and activity-based sensing probes to contextualize the following chapters. Chapter 2 discusses the design and validation of a fluorescent probe for detecting cyclooxygenase-2 activity with live cells, as well as the discovery of oxygen-dependent regulation that is not observed on the protein expression level. Chapter 3 summarizes our progress towards the development of photoacoustic probes for imaging nitric oxide within live animals. Topics include the preparation of a photoacoustic probe for imaging nitric oxide in a small animal model of inflammation, the optimization of the aza-BODIPY dye platform to detect cancer-derived nitric oxide, and progress towards a multimodal dye platform for photoacoustic and fluorescence imaging.

ACKNOWLEDGMENTS

I would like to begin by thanking my advisor, Prof. Jeff Chan, for his support and guidance over the past five years. I am truly grateful for the opportunity to work with you and to watch the lab evolve. Under your mentorship, I have learned the importance of being courageous when tackling important problems (even if it may not work); fostering a collaborative environment where coworkers grow together; and being an open, honest, and caring person in science. Moreover, I would like to thank you for providing me with significant intellectual freedom, as well as being perpetually excited and available to discuss science. These were critical for my development as a passionate, independent scientist and they will undoubtably benefit me in my career. I would also like to thank my thesis committee for their feedback and support throughout my Ph.D. studies and postdoctoral applications. I was fortunate to have an excellent committee who brought diverse viewpoints and will continue to serve as role models as I traverse through my career.

Next, I would like to thank the Chan lab (past and present) for their comradery and support. I cannot express how important you have all been through this intellectual and personal journey. The past five years have been some of the hardest, but most rewarding years, of my life and it would not have been the same without you. Thank you all for being such great friends and colleagues. I am grateful for the time we shared whether we were in lab or out and about grabbing coffee, breaking bread, or experiencing new beers. Thank you to the first class of students (Lukas Smaga, Hao Li, Chelsea Anorma, and Pamela Zhang) for establishing the lab and helping to getting us started when we joined, the second class (Hailey Knox, Thomas Bearrood, and Effie Zhou) for being the best cohort to learn and grow alongside, and all those

that followed who each brought new skills, perspectives, and fun (Nick Pino, Sarah Gardner, Melissa Lucero, Katie Brady, Amanda East, Gabby Ibarra, Michael Lee, Joe Forzano, Selena Hernandez, and Chelsea Swartchick). Also, thank you to the dedicated Chan lab undergraduates and postdoctoral researchers that I had the pleasure of working with over the course of the past five years. In particular, I would like to acknowledge my exceptional mentees (Michael Jorgensen, Gina Partipilo, Ruiwen "Irian" Xu, and Rodrigo Hernandez Tapia) and collaborators (Andres Arango and Zuo Hong "Gareth" Yu) for their help, dedication, and hard work. Additionally, I would like to thank Prof. Vern Schramm and the Schramm lab for welcoming me as a research intern and providing me with a unique perspective during my graduate studies.

Finally, I would like to thank everyone who has helped me to get to this point. I am grateful to all of my family and past mentors who prepared me for this experience. Unfortunately, I cannot list everyone that deserves acknowledgement, but I would like to highlight some significant contributors below. I am deeply indebted to my parents, brother, and grandparents for your support and encouragement. Together, you taught me the importance of education, morality, dedication, and passion in life. Next, I would like to thank my mentors at the University at Buffalo: Prof. John Richard, Dr. Tina Amyes, Dr. Xiang Zhai, Dr. Archie Reyes, Prof. Joseph Gardella, and Prof. Jessica Poulin. Your support and mentorship were instrumental for my development as a scientist, as I applied for graduate school, and you all helped me discover my passion for science. Finally, I would like to express my overwhelming gratitude to Lauren Carnevale. You are the best partner that I could have ever asked for. Your unfaltering drive towards excellence and deep desire to help others through research, outreach, and education is inspiring. Thank you for your tremendous support and for always making me strive to be the best that I can be.

To Lauren and my family

TABLE OF CONTENTS

CHAPTER 1: MOLECULAR IMAGING AND ACTIVITY-BASED SENSING: FROM BASIC BIOLOGY TO CLINICAL TRANSLATION[1]

1.1 Background and significance

Molecular imaging emerged from the genomic revolution and key advances in biomedical imaging. The rapid generation of genomic data and new strategies for *in vitro* validation identified a wealth of molecular markers for human disease. These targets provided an unprecedented opportunity for drug development and diagnostic approaches. Molecular imaging aims to utilize this molecular information to discover biology, facilitate early disease detection, and guide treatment regimen in living specimen.[1–4]

Molecular imaging contrast agents were initially non-targeted, but they quickly evolved to utilize targeting strategies for selective accumulation. More recently, contrast agents harness stimulus-selective binding or reactivity to directly measure target concentration or activity in complex, heterogenous systems. These activatable contrast agents substantially increased the accessibility and utility of molecular imaging. This chapter will discuss the evolution of molecular imaging with a focus on fluorescence and photoacoustic imaging, as well as the development of activity-based sensing (ABS) approaches for studying small-molecule and enzyme targets. This chapter aims to contextualize the subsequent chapters by introducing the field of molecular imaging with a focus on its application for studying biology within living systems (e.g., live cells and animals).

[1]Portions of this chapter are reprinted or adapted with permissions from the following publications: (1) Gardner, S. H.; Reinhardt, C. J.; Chan, J. Advances in Activity-Based Sensing Probes for Isoform-Selective Imaging of Enzymatic Activity. *Angew. Chem. Int. Ed.* **2020,** 10.1002/anie.202003687.[107] Copyright © 2020 John Wiley and Sons, Inc. (2) Reinhardt, C. J.; Chan, J. Development of Photoacoustic Probes for *in Vivo* Molecular Imaging. *Biochemistry* **2018**, *57* (2), 194–199.[108] Copyright © 2018 American Chemical Society.

1.2 Molecular imaging

1.2.1 Origins of molecular imaging

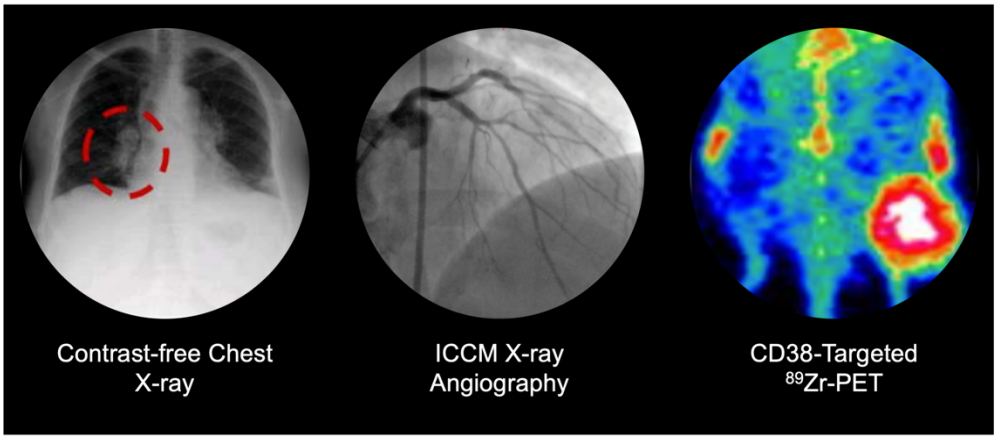

Figure 1.1: Molecular imaging derives from traditional biomedical imaging techniques (left) and early, non-targeted contrast agents (iodine-containing contrast agent, ICCM; middle). Molecular imaging provides information about the presence and concentration of analytes or biomolecules to complement anatomical data. Images are adapted with permission from ref. 5 (left, Copyright © IEEE 2017), ref. 6 (middle, Copyright © IEEE 2012), and ref. 7 (right, Copyright © American Chemical Society 2017).

Traditional biomedical imaging measures physical processes (e.g., absorption, scattering, relaxation rates) to define structural and/or physiological information. Originally this was based on the differential absorption of X-rays in tissue—the basis of X-ray tomography and computed tomography (CT). Unfortunately, most targets are indistinguishable using X-rays and require exogenous contrast agents for visualization. For example, iodine or barium can be administered for vascular and gastrointestinal imaging, respectively. The limited range of X-ray contrast agents prompted the widespread development and application of nuclear medicine. Rather than external energy sources, nuclear medicine uses radioactive compounds as the radiation source. This radiation can be in the form of γ-rays, for single-photon emission computerized tomography (SPECT), or the photons that are released after positron annihilation, for positron emission tomography (PET). Strategic tracer design provides a platform for selective accumulation at the

site of interest using either small molecule (e.g., ^{99}Tm-methylene diphosphonate, ^{19}F-fluorodeoxyglucose) or biomolecular (e.g., antibody) targeting approaches. These advances, along with those in computer science and molecular biology, prompted the shift towards technologies that access molecular information to complement the existing anatomical and physiological strategies. This field, coined "molecular imaging", directly links basic biological discovery with diagnostic applications[2,3,8] and has attracted widespread interest—both within industry and academia—as a tool for streamlining fundamental discoveries and drug development, as well as for their use as clinical diagnostics.[9]

1.2.2 Modalities suitable for molecular imaging

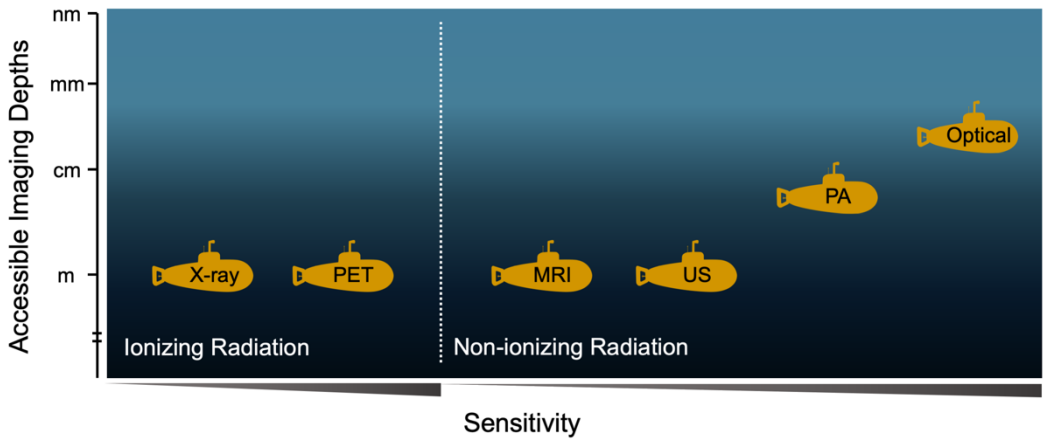

Figure 1.2: Summary of key ionizing and non-ionizing molecular imaging modalities. Depth of the yellow submarine represents general accessible imaging depths and order (from left to right) indicates relative sensitivity.

The goal of molecular imaging is to access biochemical or molecular information in unperturbed biological states (e.g., living cells, tissues, or animals). Key imaging modalities include SPECT, PET, ultrasound, optical (e.g., fluorescence, bioluminescence), and magnetic resonance imaging (MRI).[1–4,10] While ionizing methods have proven impactful, clinically relevant frequencies and doses have been correlated with an increased risk of cancer.[11] For this reason, recent efforts have focused on non-invasive and non-ionizing approaches, such as optical,[12,13] acoustic,[14] and MRI methods.[15–17] It is important to note that sensitivity, resolution, and depth

penetration are intrinsically linked. This poses an inherent challenge for any imaging modality where methods with the highest sensitivity and resolution are typically limited to the shallowest imaging depths and *vice versa*. For example, optical methods can provide subcellular resolution, but are constrained to imaging at millimeter depths.[4,10] Regardless, there has been an overwhelming focus on optical contrast agents because of their superior spatiotemporal resolution, sensitivity, cost, instrument accessibility (e.g., confocal and two-photon microscopy, *in vivo* fluorescence imaging systems), and wavelength tunability. This has led to a wealth of information regarding the development, modulation, and optimization of optical properties.[12,18]

1.3 Fluorescence activity-based sensing

1.3.1 Activity-based sensing: Small molecule targets

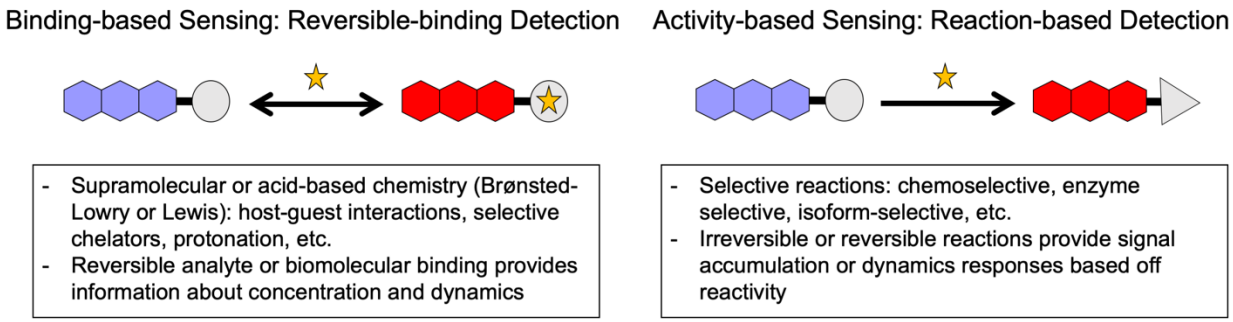

Figure 1.3: Schematic representation of a chromophore interacting with the target (star) for reversible, binding-based sensing or reaction-based activity-based sensing.

Early fluorescence imaging employed fluorescent dyes or proteins to label subcellular compartments or proteins in cellular monolayers. Later, stimulus-responsive probes were prepared to extend the range of targets that could be interrogated using fluorescence imaging.[19] Generally, these activatable contrast agents, or probes, undergo a stimulus-induced change that alters its photophysical properties. This change can either be in terms of absorption (e.g. extinction coefficient) or the propensity to undergo emissive relaxation (e.g., photo-induced electron transfer

or Förster energy transfer rates).[20] Seminal examples harnessed supramolecular concepts, such as selective chelators,[21] to modulate the probe's optical properties.[22] This strategy has been widely elaborated for the detection of biological metals since its inception.[23] Key examples discovered phospholipase C-dependent positive feedback between calcium and inositol 1,4,5-triphosphate,[24] identified the calcium-inducing factor,[25,26] visualized the zinc spark upon conception,[27] and illuminated labile copper's involvement in the locus coeruleus–norepinephrine system.[28]

Later, a wide range of reaction-based or ABS probes were established which harness chemoselective reactivity as a means of modifying or unmasking the optical handle.[13] Perhaps expectedly, reliable organic and organometallic chemistries serve as the basis for most ABS probes.[29] These compounds have also been categorized as chemodosimeters[18] or biodosimeters;[13] however, the differences are semantic and insignificant. We elect to use the ABS terminology because it highlights the technology's key feature: the ability to detect the analyte's or enzyme's activity rather than concentration. This feat significantly increased the breadth of detectable species, particularly towards enzyme targets[19,32] and reactive signaling molecules (e.g., nitric oxide, superoxide).[13,30,31] It is important to note that ABS probes are often the only approach for performing live-specimen, high resolution imaging of signaling molecules because of targets fleeting nature and the lack of approaches for tagging. Notable ABS probes have uncovered the role of endogenous formaldehyde in the one-carbon-metabolism system[33] and the implication of nitroxyl in TRPA1-based noci- and chemo-sensing.[34]

1.3.2 Activity-based sensing: Enzyme targets

Although reliable methods exist for quantifying transcription (e.g., Northern blotting, quantitative polymerase chain reaction) and translation (e.g., Western blotting, enzyme-linked immunosorbent assay), direct detection of enzymatic activity remains a significant challenge. ABS

is a powerful approach to facilitate post-translational monitoring because it provides a direct read-out of enzymatic activity with a biocompatible detection method.[35] Since it is ultimately the activity and not the concentration of an enzyme that dictates function, it is crucial to be able to directly monitor this within the target's native cellular environment.[36]

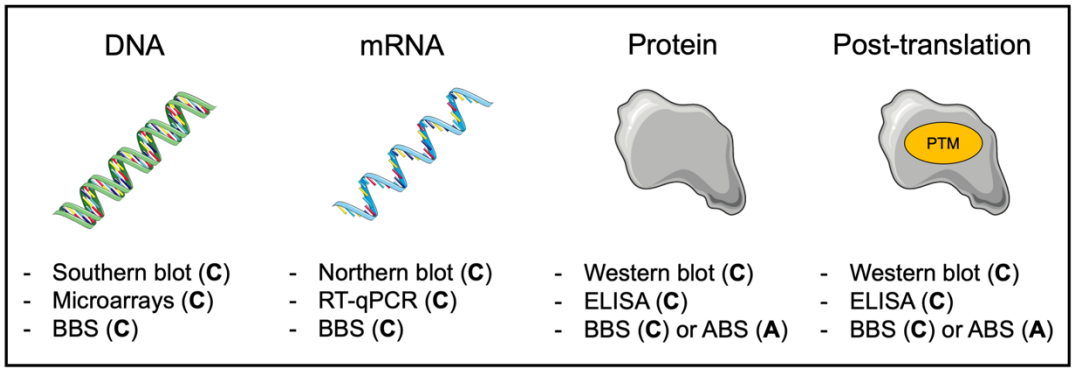

Figure 1.4: Common detection strategies for studying enzymes *ex vivo* (blotting, microarrays, RT-qPCR, ELISA) or in living systems (binding-based sensing, BBS; activity-based sensing, ABS) at the DNA, RNA, protein, or post-translational level. Concentration and activity measurement compatibility are indicated with a bolded C or A, respectively.

The origins of enzyme ABS date back to early biochemical analyses when substrates were prepared for measuring general enzymatic activities (e.g., esterase, phosphatase, galactosidase, lipase) *in vitro*.[37–40] More recently, the focus has shifted towards providing probes with cellular and live animal compatibilities.[41] Rather than chemoselective functionalization, enzyme ABS probes utilize enzyme recognition and catalysis to unmask the optical reporter. Therefore, ABS strategies can monitor regulation beyond the concentration level and can shed light on previously hidden regulatory mechanisms.[42] This regulation may operate through post-translational modifications, intracellular availability of cofactors or substrates, and/or feedback mechanisms.[43–45] For example, localized biosynthetic pathways (metabolons) can form through chemotaxis and alter local substrate availability. This enhances the pathway's flux beyond what would be observed *in vitro*.[46–48]

ABS probes facilitate exploratory biological experiments, as well as providing a method for drug discovery and diagnosis. For example, acyl-protein thioesterase probes uncovered cysteine depalmitoylation as a dynamic lipid signaling mechanism in the cytoplasm and mitochondria. The live-cell compatibility and spatiotemporal resolution were essential for identifying the location and source of the enzymatic activity in these experiments.[49–51] On the other hand, enzyme ABS probes can be applied for high throughput screening in biochemical or live specimen contexts. The latter has clear applications in traditional cell and high-content screening[52] with rapid validation in small animal models.[53,54] The same types of probes can then be been translated into clinical trials for cancer detection, with several examples as of 2017,[55] or serve as contrast agents for image-guided surgery.[56]

ABS development becomes more complicated when several functionally related, but non-identical, enzymes exist. These proteins (isoforms) typically display high sequence and structural similarities and operate on near-identical substrates. Isoforms often emerge via gene duplication or alternative splicing and enable differential regulation of the protein for increased phenotypic robustness.[57] The ability to distinguish between isoforms is critical for differentiating their function because of their distinct expression, activation, and/or substrate preferences. These conditions manifest themselves in physiological and pathological contributions that are simultaneously operative. Without isoform-selective ABS probes it would be difficult to decipher their relative contributions to a specific condition. Exemplary isoform-selective probes have suggested peripheral blood cell MAO-B activity as a biomarker for Parkinson's disease,[58] confirmed that the elevated expression of CE2 in the liver and intestine correspond with increased *in vivo* activity,[59] and demonstrated that cancer stem cell populations retain their elevated ALDHA1A activity for weeks after implantation.[60]

The major limitation of optical methods is their depth penetration. Typical experiments are constrained to millimeter imaging depths due to extensive light scattering in biological tissue and, for this reason, are most suitable for endoscopic imaging. In particular, it is the low-intensity, emitted light that restricts tomographic applications.[61] This can be addressed by increasing the wavelengths of the light to limit autofluorescence, absorption, and scattering because shorter wavelengths (ultraviolet-visible) are prone to absorption by endogenous chromophores and elicit non-trivial amounts of autofluorescence. At longer wavelengths (near-infrared) the scattering coefficient dominates and this parameter decreases as a function of wavelength.[62–64] Recent efforts have focused on accessing probes within the NIR I (600 – 950 nm) or NIR II (1000 – 1700 nm) windows, which can reach up to about a centimeter in depth.[64,65]

1.4 Photoacoustic activity-based sensing

1.4.1 Basics of photoacoustic imaging

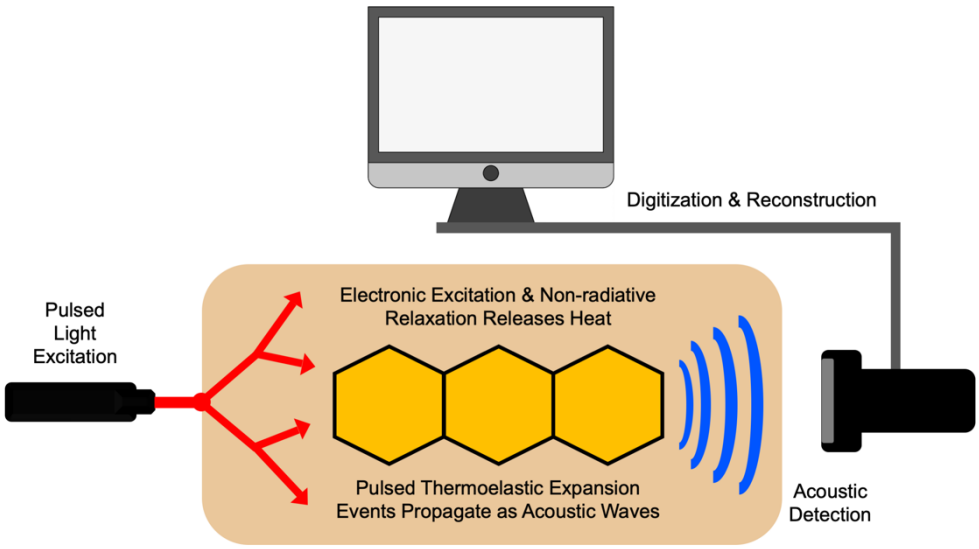

Figure 1.5: Schematic representation of photoacoustic imaging with tissue-penetrant pulsed excitation, non-radiative relaxation-induced heating-cooling cycles, ultrasound detection, and signal reconstruction to provide three-dimensional images in deep tissue.

Photoacoustic (PA) imaging offers a promising alternative to purely optical methods by combines non-ionizing, tissue-penetrant excitation light with acoustic detection. By detecting sound, rather than emitted light, PA imaging overcomes the limited imaging depths associated with fluorescence imaging. This enhancement stems from the decreased scattering of sound within biological tissue (circa 10^3-fold less relative to light) and therefore extends high-resolution imaging to centimeter depths.[66] Since its initial discovery over a century ago,[67] this technology has grown significantly through advances in instrumental design and data reconstruction methods. These improvements have facilitated an impressive range of biological studies, pre-clinical and clinical trials.[68–70]

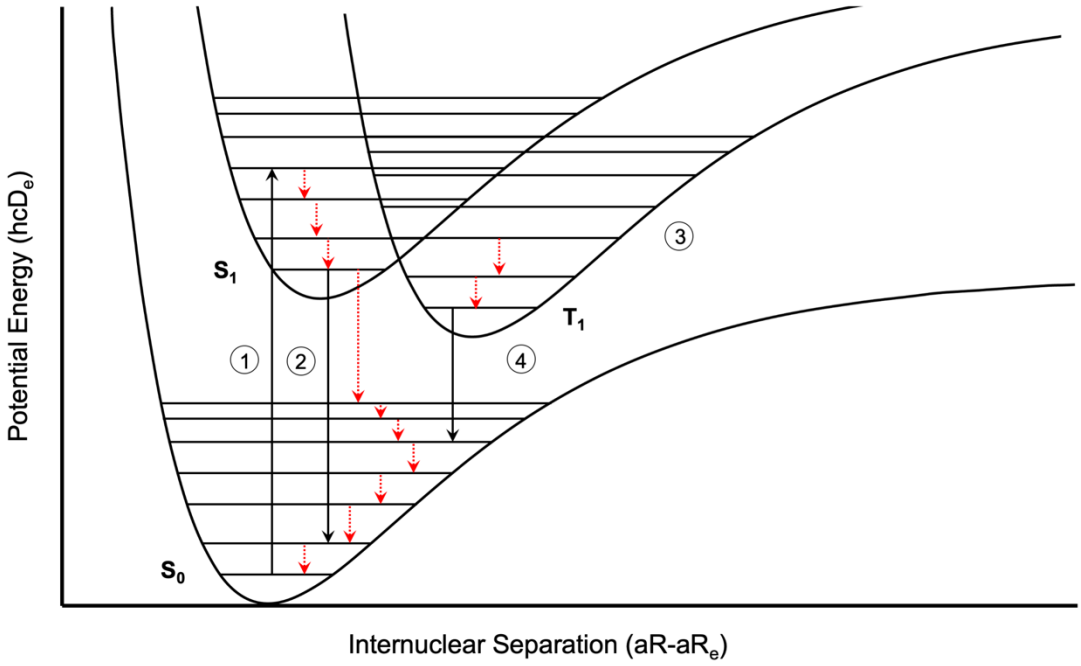

Figure 1.6: Stylized Jabłoński diagram for relaxation from an excited electronic and/or vibrational state. Vibrational energies are represented in their Morse potential. Absorption (1) or emission events (2, fluorescence; 4, phosphorescence) are indicated with black arrows, while non-radiative events are presented as red, dotted arrows. Intersystem crossing can occur due to spin-orbital coupling between S_1 and T_1. The non-radiative relaxation between a higher energy and lower energy singlet state (internal conversion) is omitted for clarity.

PA imaging relies on the PA effect to convert incident light into the detectable ultrasound signal. Mechanistically, this begins with the light excitation of an endogenous (e.g., hemoglobin,

deoxyhemoglobin, or melanin) or exogenous chromophore (e.g., organic dye or nanomaterial). Once excited, the chromophore can return to its ground state via radiative relaxation (e.g., fluorescence or phosphorescence) or non-radiative decay (Figure 6). In the case of non-radiative relaxation, the chromophore releases energy as heat (approximately 1 mK). This rapid increase in the local temperature produces a thermoelastic expansion event and a corresponding pressure change (approximately 800 Pa). By pulsing the excitation source, it is possible to generate fluctuating (megahertz) pressure waves, which propagate through the medium as acoustic waves. An array of ultrasound transducers convert the detected sound to electronic signals for reconstruction into three-dimensional images.[66,71] Selective excitation source, detector, and scanning selection allow the researcher to tune the achievable resolution, sensitivity, and imaging depths.[72] This empirically manifests with experimental resolutions that are about one two hundredth of the imaging depth.[66]

1.4.2 Origins of activatable photoacoustic probes

In principle, any material that absorbs light can produce a PA signal; however, coupling signal generation to a specific biological stimulus remained largely unexplored until recently. In 2010, the first activatable probe was reported for imaging matrix metallo-protease-2 (MMP-2) activity. The design employed an MMP-2-selective peptide linker to connect two chromophores. Attaching one fragment to a cell-penetrating peptide sequence facilitated targeted uptake of one fragment post-cleavage. Selective imaging of the targeted product was achieved by subtracting the signal at the two absorbance maxima.[73] Although this approach was initially evaluated in tissue-mimicking phantoms and fibrosarcoma cells, the approach has since been employed for pre-clinical *in vivo* imaging[74] and elaborated to image other tumor-associated enzymes (e.g., MMP-9 and MMP-13).[74,75] More broadly, this seminal work highlighted that factors beyond extinction

coefficient and fluorescent quantum yield affect the PA properties.[73] For example, excited-state absorption, relaxation kinetics, photobleaching, and triplet state contributions, are also key considerations in the context of PA probe development.[76–79] At the moment, these prove more difficult to predict, and a better connection between the property and chemical structure is required. Regardless, substantial progress has been made regarding the development of nanomaterial and small-molecule activatable PA probes.[71,80–84]

1.4.3 Photoacoustic activity-based sensing

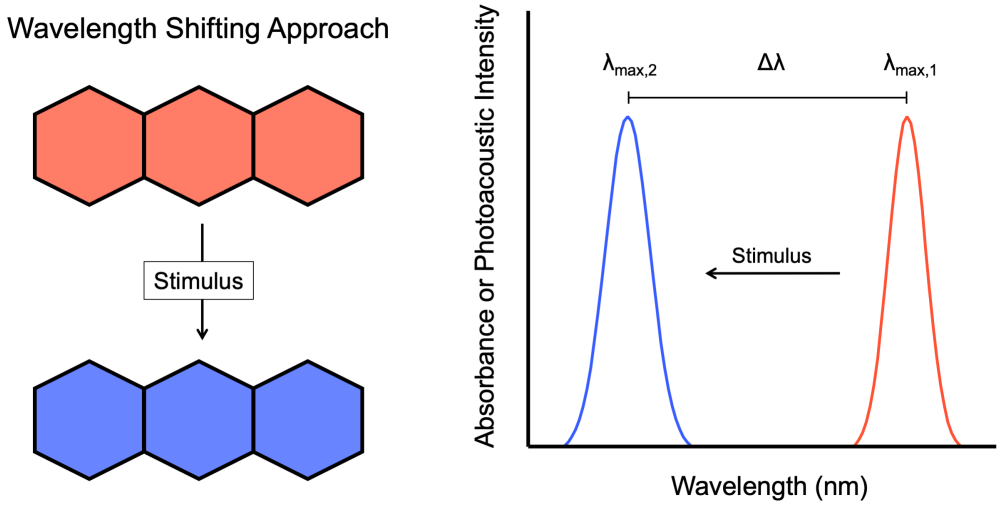

Figure 1.7: Wavelength shifting is a reliable approach for designing activatable PA probes. Reaction between the initial probe and the stimulus (analyte or biomolecule) results in either a reversible or irreversible change in the absorption and photoacoustic spectra. Selective imaging at of the initial probe ($\lambda_{max,1}$) and product ($\lambda_{max,2}$) facilitate ratiometric imaging. Note that bathochromic shift approaches are equally effective.

PA probe development functions largely as an extension of and complement for optical probes. For example, ideal PA probes also absorb within the NIR-I[71] or NIR-II windows[85] to limit scattering and absorption of the incident light[62–65] and have been prepared to image a panel of small-molecule analytes and enzyme targets.[71,80–84]

Wavelength shifting has emerged as a prominent and reliable approach for developing both binding-based and ABS probes for PA imaging[83] for three main reasons. First, it facilitates simultaneous detection of the non-activated and activated states. This approach is called

ratiometric imaging and it can be used to overcome imaging artifacts due to heterogeneous dye loading or distribution, variability in imaging depths, tissue-dependent signal attenuation, or inconsistent irradiation.[86] Second, this approach circumvents the uncertainties associated with the parameters that influence the PA signal beyond excitation coefficient and fluorescent quantum yield.[83] Third, wavelength shifting is compatible with most established NIR dye platforms (i.e., cyanine, semi-cyanine, aza-BODIPY, squarine, porphyrinoid) and common optical sensing mechanisms. For example, binding-based PA probes have imaged pH, metals, and glycans using existing, selective receptors.[87–94] Noteworthy examples enhanced PA brightness through nanoparticle-dye quenching to detect tumor acidity,[89] measured pentylenetetrazol-stimulated calcium influx in live zebrafish,[92] and imaged copper accumulation in murine Alzheimer's brains by forming a stable copper radical complex.[94]

The first small-molecule ABS PA probe was reported in 2015 and it enabled the detection of copper in tissue-mimicking phantoms. APC-2 was an aza-BODIPY-based probe featuring a 2-picolinic ester as a responsive-element for copper(II).[95] Following complexation, the divalent metal promotes rate-limiting attack by water or hydroxide[96] to uncage a phenolate with a corresponding 80 nm shift in the wavelength of maximal absorption. This facilitated selective imaging of APC-2 and the uncaged product below a centimeter of chicken breast tissue at 697 and 767 nm, respectively. Since this initial report, the field has focused on increasing the selectivity, sensitivity, and range of the detectable species with examples for a range of reactive oxygen,[97,98] nitrogen,[99] sulfur,[100,101] and metal species.[102] For example, chemoselective reactions with nanoparticle dopants converted a promiscuous boronic ester trigger into a selective peroxynitrite nanoprobe[99] and a liposome-based horseradish peroxidase-substrate system enabled efficient hydrogen peroxide imaging in cancer and inflammation.[97] Only modest expansion of enzyme

targets has been observed over the same time, where they have remained mostly within the protease and peptidase families.[103–106]

1.5 Summary and outlook

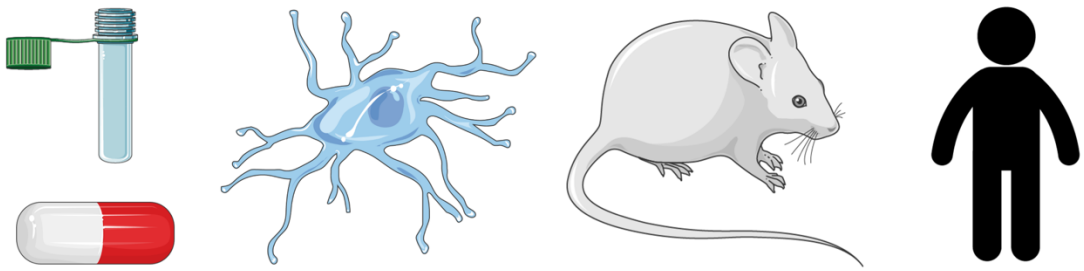

Figure 1.8: Molecular imaging provides unique opportunities for *in vitro* (e.g., high-throughput inhibitor screens, cell biology) and *in vivo* (e.g., animal model development, diagnostics) experimentation.

Molecular imaging emerged in the 1990's as a mechanism to harness genomic and biological data for personalized medicine and biological investigations. By directly measuring the molecular and biochemical contributors, it is possible to expand the obtainable information beyond tissue structures. This approach holds promise for earlier diagnostic tests to improve patient prognosis and enables direct interrogation within the target's native complexity. While ionizing technologies proved critical for diagnostic medical imaging, their hazards have driven significant efforts towards non-ionizing alternatives. In particular, optical imaging has been widely successful because of its high resolution (i.e. spatial, temporal, and spectral), sensitivity, affordability, and accessibility. ABS probes employ selective (bio)chemistries to detect the target's activity, rather than concentration, to discovery regulatory mechanisms that are only present in living systems. More recently, PA imaging has emerged as a complement for purely optical methods by extending imaging depths from the millimeter (e.g., cell monolayers, tissue slices) to centimeter range (e.g., organoids, whole-organ imaging, live specimen). Current limitations of these fields include the range of available probes, accessible imaging depths, translation into the clinic (e.g., diagnostics,

image-guided surgery, theranostics), and systematic validation of *in vitro* conclusions within live cells and animals. In the following chapters, we will discuss the development of an isoform-selective fluorescent probe for cyclooxyengase-2 activity (Chapter 2) and PA probes for detecting endogenous nitric oxide in live animal models (Chapter 3).

1.6 Software

Figures were prepared using Microsoft PowerPoint, GraphPad Prism (version 6.0 or 8.0), and/or Adobe Illustrator (version 22.0.2). Some images were adapted from Servier Medical ART (Les Laboratoires Servier, https://smart.servier.com/) with permission.

1.7 References

(1) Pysz, M. A.; Gambhir, S. S.; Willmann, J. K. Molecular Imaging: Current Status and Emerging Strategies. *Clin. Radiol.* **2010**, *65* (7), 500–516.

(2) Weissleder, R. Molecular Imaging: Exploring the next Frontier. *Radiology* **1999**, *212* (3), 609–614.

(3) Weissleder, R.; Mahmood, U. Molecular Imaging. *Radiology* **2001**, *219*, 316.

(4) James, M. L.; Gambhir, S. S. A Molecular Imaging Primer: Modalities, Imaging Agents, and Applications. *Physiol. Rev.* **2012**, *92* (2), 897–965.

(5) Wang, X.; Peng, Y.; Lu, L.; Lu, Z.; Bagheri, M.; Summers, R. M. ChestX-Ray8: Hospital-Scale Chest X-Ray Database and Benchmarks on Weakly-Supervised Classification and Localization of Common Thorax Diseases. In *2017 IEEE Conference on Computer Vision and Pattern Recognition (CVPR)*; 2017; Vol. 2017, pp 3462–3471.

(6) Cardenes, R.; Novikov, A.; Gunn, J.; Hose, R.; Frangi, A. F. 3D Reconstruction of Coronary Arteries from Rotational X-Ray Angiography. In *9th IEEE International Symposium on Biomedical Imaging (ISBI)*; IEEE, 2012; pp 618–621.

(7) Ehlerding, E. B.; England, C. G.; Jiang, D.; Graves, S. A.; Kang, L.; Lacognata, S.; Barnhart, T. E.; Cai, W. CD38 as a PET Imaging Target in Lung Cancer. *Mol. Pharm.* **2017**, *14* (7), 2400–2406.

(8) Bradley, W. G. History of Medical Imaging. *Proc. Am. Philos. Soc.* **2008**, *152* (3), 349–361.

(9) Marx, V. Molecular Imaging. *Chem. Eng. News* **2005**, *83* (30), 25–34.

(10) Weissleder, R.; Pittet, M. J. Imaging in the Era of Molecular Oncology. *Nature* **2008**, *452* (7187), 580–589.

(11) Miglioretti, D. L.; Lange, J.; Van Den Broek, J. J.; Lee, C. I.; Van Ravesteyn, N. T.; Ritley, D.; Kerlikowske,

K.; Fenton, J. J.; Melnikow, J.; De Koning, H. J.; et al. Radiation-Induced Breast Cancer Incidence and Mortality from Digital Mammography Screening a Modeling Study. *Ann. Intern. Med.* **2016**, *164* (4), 205–214.

(12) Chan, J.; Dodani, S. C.; Chang, C. J. Reaction-Based Small-Molecule Fluorescent Probes for Chemoselective Bioimaging. *Nat. Chem.* **2012**, *4* (12), 973–984.

(13) Bruemmer, K. J.; Crossley, S. W. M.; Chang, C. J. Activity-Based Sensing: A Synthetic Methods Approach for Selective Molecular Imaging and Beyond. *Angew. Chemie Int. Ed.* **2020**, 10.1002/anie.201909690.

(14) Walker, J. A.-T.; Wang, X.; Peter, K.; Kempe, K.; Corrie, S. R. Dynamic Solid-State Ultrasound Contrast Agent for Monitoring PH Fluctuations In Vivo. *ACS Sensors* **2020**, *5*, 1190–1197.

(15) Louie, A. Y.; Hüber, M. M.; Ahrens, E. T.; Rothbächer, U.; Moats, R.; Jacobs, R. E.; Fraser, S. E.; Meade, T. J. In Vivo Visualization of Gene Expression Using Magnetic Resonance Imaging. *Nat. Biotechnol.* **2000**, *18* (3), 321–325.

(16) Major, J. L.; Meade, T. J. Bioresponsive, Cell-Penetrating, and Multimeric MR Contrast Agents. *Acc. Chem. Res.* **2009**, *42* (7), 893–903.

(17) Wahsner, J.; Gale, E. M.; Rodríguez-Rodríguez, A.; Caravan, P. Chemistry of MRI Contrast Agents: Current Challenges and New Frontiers. *Chem. Rev.* **2019**, *119* (2), 957–1057.

(18) Yang, Y.; Zhao, Q.; Feng, W.; Li, F. Luminescent Chemodosimeters for Bioimaging. *Chem. Rev.* **2013**, *113* (1), 192–270.

(19) Giepmans, B. N. G.; Adams, S. R.; Ellisman, M. H.; Tsien, R. Y. The Fluorescent Toolbox for Assessing Protein Location and Function. *Science* **2006**, *312* (5771), 217–224.

(20) Kobayashi, H.; Ogawa, M.; Alford, R.; Choyke, P. L.; Urano, Y. New Strategies for Fluorescent Probe Design in Medical Diagnostic Imaging. *Chem Rev* **2010**, *110* (5), 2620–2640.

(21) Tsien, R. Y. New Calcium Indicators and Buffers with High Selectivity Against Magnesium and Protons: Design, Synthesis, and Properties of Prototype Structures. *Biochemistry* **1980**, *19* (11), 2396–2404.

(22) Grynkiewicz, G.; Poenie, M.; Tsien, R. Y. A New Generation of Ca2+ Indicators with Greatly Improved Fluorescence Properties. *J. Biol. Chem.* **1985**, *260* (6), 3440–3450.

(23) Carter, K. P.; Young, A. M.; Palmer, A. E. Fluorescent Sensors for Measuring Metal Ions in Living Systems. *Chem. Rev.* **2014**, *114* (8), 4564–4601.

(24) Harootunian, A. T.; Kao, J. P. Y.; Paranjape, S.; Tsien, R. Y. Generation of Calcium Oscillations in Fibroblasts by Positive Feedback Between Calcium and IP3. *Science* **1991**, *251* (4989), 75–78.

(25) Randriamampita, C.; Tsien, R. Y. Emptying of Intracellular Ca2+ Stores Releases a Novel Small Messenger That Stimulates Ca2+ Influx. *Nature* **1993**, *364* (6440), 809–814.

(26) Bolotina, V. M.; Csutora, P. CIF and Other Mysteries of the Store-Operated Ca2+-Entry Pathway. *Trends Biochem. Sci.* **2005**, *30* (7), 378–387.

(27) Que, E. L.; Bleher, R.; Duncan, F. E.; Kong, B. Y.; Gleber, S. C.; Vogt, S.; Chen, S.; Garwin, S. A.; Bayer, A. R.; Dravid, V. P.; et al. Quantitative Mapping of Zinc Fluxes in the Mammalian Egg Reveals the Origin of Fertilization-Induced Zinc Sparks. *Nat. Chem.* **2015**, *7* (2), 130–139.

(28) Xiao, T.; Ackerman, C. M.; Carroll, E. C.; Jia, S.; Hoagland, A.; Chan, J.; Thai, B.; Liu, C. S.; Isacoff, E. Y.;

Chang, C. J. Copper Regulates Rest-Activity Cycles through the Locus Coeruleus-Norepinephrine System. *Nat. Chem. Biol.* **2018**, *14* (7), 655–663.

(29) Bearrood, T. E.; Chan, J. Disproportionate Impact of Named Reactions on Chemical Biology. *Aldrichimica Acta* **2017**, *50* (2), 31–42.

(30) Chen, X.; Tian, X.; Shin, I.; Yoon, J. Fluorescent and Luminescent Probes for Detection of Reactive Oxygen and Nitrogen Species. *Chem. Soc. Rev.* **2011**, *40* (9), 4783–4804.

(31) Lin, V. S.; Chen, W.; Xian, M.; Chang, C. J. Chemical Probes for Molecular Imaging and Detection of Hydrogen Sulfide and Reactive Sulfur Species in Biological Systems. *Chem. Soc. Rev.* **2015**, *44* (44), 4596–4618.

(32) Chyan, W.; Raines, R. T. Enzyme-Activated Fluorogenic Probes for Live-Cell and in Vivo Imaging. *ACS Chem. Biol.* **2018**, *13* (7), 1810–1823.

(33) Burgos-Barragan, G.; Wit, N.; Meiser, J.; Dingler, F. A.; Pietzke, M.; Mulderrig, L.; Pontel, L. B.; Rosado, I. V.; Brewer, T. F.; Cordell, R. L.; et al. Mammals Divert Endogenous Genotoxic Formaldehyde into One-Carbon Metabolism. *Nature* **2017**, *548* (7669), 549–554.

(34) Eberhardt, M.; Dux, M.; Namer, B.; Miljkovic, J.; Cordasic, N.; Will, C.; Kichko, T. I.; De La Roche, J.; Fischer, M.; Suárez, S. A.; et al. H2S and NO Cooperatively Regulate Vascular Tone by Activating a Neuroendocrine HNO-TRPA1-CGRP Signalling Pathway. *Nat. Commun.* **2014**, *5*, 4381.

(35) Aron, A. T.; Reeves, A. G.; Chang, C. J. Activity-Based Sensing Fluorescent Probes for Iron in Biological Systems. *Curr. Opin. Chem. Biol.* **2018**, *43*, 113–118.

(36) Chan, J.; Dodani, S. C.; Chang, C. J. Reaction-Based Small-Molecule Fluorescent Probes for Chemoselective Bioimaging. *Nat. Chem.* **2012**, *4* (12), 973–984.

(37) Rotman, B.; Zderic, J. A.; Edelstein, M. Fluorogenic Substrates for B-D-Galactosidases and Phosphatases Derived from Fluorescein (3,6-Dihydroxyfluoran) and Its Monomethyl Ether. *Proc. Natl. Acad. Sci. USA* **1963**, *50* (1), 1–6.

(38) Rotman, B. Measurement of Activity of Single Molecules of Beta-D-Galactosidase. *Proc. Natl. Acad. Sci. USA* **1961**, *47*, 1981–1991.

(39) Morillas, M.; Goble, M. L.; Virden, R. The Kinetics of Acylation and Deacylation of Penicillin Acylase from Escherichia Coli ATCC 11105: Evidence for Lowered PK(a) Values of Groups near the Catalytic Centre. *Biochem. J.* **1999**, *338* (1), 235–239.

(40) Bier, M. . Lipases. In *Methods Enzymol., I*; 1955; pp 627–642.

(41) Chyan, W.; Raines, R. T. Enzyme-Activated Fluorogenic Probes for Live-Cell and in Vivo Imaging. *ACS Chem. Biol.* **2018**, *13* (7), 1810–1823.

(42) Baruch, A.; Jeffery, D. A.; Bogyo, M. Enzyme Activity - It's All about Image. *Trends Cell Biol.* **2004**, *14* (1), 29–35.

(43) Pawson, T.; Scott, J. D. Protein Phosphorylation in Signaling – 50 Years and Counting. *Trends Biochem. Sci.* **2005**, *30* (6), 283–286.

(44) Beltrao, P.; Bork, P.; Krogan, N. J.; Van Noort, V. Evolution and Functional Cross-Talk of Protein Post-Translational Modifications. *Mol. Syst. Biol.* **2013**, *9* (1), 1–13.

(45) Zotter, A.; Bäuerle, F.; Dey, D.; Kiss, V.; Schreiber, G. Quantifying Enzyme Activity in Living Cells. *J. Biol. Chem.* **2017**, *292* (38), 15838–15848.

(46) An, S.; Kumar, R.; Sheets, E. D.; Benkovic, S. J. Reversible Compartmentalization of de Novo Purine Biosynthetic Complexes in Living Cells. *Science* **2008**, *320* (5872), 103–106.

(47) Zhao, X.; Palacci, H.; Yadav, V.; Spiering, M. M.; Gilson, M. K.; Butler, P. J.; Hess, H.; Benkovic, S. J.; Sen, A. Substrate-Driven Chemotactic Assembly in an Enzyme Cascade. *Nat. Chem.* **2018**, *10* (3), 311–317.

(48) Pareek, V.; Tian, H.; Winograd, N.; Benkovic, S. J. Metabolomics and Mass Spectrometry Imaging Reveal Channeled de Novo Purine Synthesis in Cells. *Science* **2020**, *368* (6488), 283–290.

(49) Kathayat, R. S.; Elvira, P. D.; Dickinson, B. C. A Fluorescent Probe for Cysteine Depalmitoylation Reveals Dynamic APT Signaling. *Nat. Chem. Biol.* **2017**, *13* (2), 150–152.

(50) Kathayat, R. S.; Cao, Y.; Elvira, P. D.; Sandoz, P. A.; Zaballa, M. E.; Springer, M. Z.; Drake, L. E.; Macleod, K. F.; Van Der Goot, F. G.; Dickinson, B. C. Active and Dynamic Mitochondrial S-Depalmitoylation Revealed by Targeted Fluorescent Probes. *Nat. Commun.* **2018**, *9* (1).

(51) Cao, Y.; Qiu, T.; Kathayat, R. S.; Azizi, S. A.; Thorne, A. K.; Ahn, D.; Fukata, Y.; Fukata, M.; Rice, P. A.; Dickinson, B. C. ABHD10 Is an S-Depalmitoylase Affecting Redox Homeostasis through Peroxiredoxin-5. *Nat. Chem. Biol.* **2019**, *15* (12), 1232–1240.

(52) Zanella, F.; Lorens, J. B.; Link, W. High Content Screening: Seeing Is Believing. *Trends Biotechnol.* **2010**, *28* (5), 237–245.

(53) Rudin, M.; Weissleder, R. Molecular Imaging in Drug Discovery and Development. *Nat. Rev. Drug Discov.* **2003**, *2* (2), 123–131.

(54) Cai, W.; Rao, J.; Gambhir, S. S.; Chen, X. How Molecular Imaging Is Speeding up Antiangiogenic Drug Development. *Mol. Cancer Ther.* **2006**, *5* (11), 2624–2633.

(55) Zhang, R. R.; Schroeder, A. B.; Grudzinski, J. J.; Rosenthal, E. L.; Warram, J. M.; Pinchuk, A. N.; Eliceiri, K. W.; Kuo, J. S.; Weichert, J. P. Beyond the Margins: Real-Time Detection of Cancer Using Targeted Fluorophores. *Nat. Rev. Clin. Oncol.* **2017**, *14* (6), 347–364.

(56) Yim, J. J.; Tholen, M.; Klaassen, A.; Sorger, J.; Bogyo, M. Optimization of a Protease Activated Probe for Optical Surgical Navigation. *Mol. Pharm.* **2018**, *15* (3), 750–758.

(57) Tomaiuolo, M.; Bertram, R.; Houle, D. Enzyme Isoforms May Increase Phenotypic Robustness. *Evolution (N. Y).* **2008**, *62* (11), 2884–2893.

(58) Li, L.; Zhang, C. W.; Chen, G. Y. J.; Zhu, B.; Chai, C.; Xu, Q. H.; Tan, E. K.; Zhu, Q.; Lim, K. L.; Yao, S. Q. A Sensitive Two-Photon Probe to Selectively Detect Monoamine Oxidase B Activity in Parkinson's Disease Models. *Nat. Commun.* **2014**, *5*, 3276.

(59) Jin, Q.; Feng, L.; Wang, D. D.; Wu, J. J.; Hou, J.; Dai, Z. R.; Sun, S. G.; Wang, J. Y.; Ge, G. B.; Cui, J. N.; et al. A Highly Selective Near-Infrared Fluorescent Probe for Carboxylesterase 2 and Its Bioimaging Applications in Living Cells and Animals. *Biosens. Bioelectron.* **2016**, *83*, 193–199.

(60) Anorma, C.; Hedhli, J.; Bearrood, T. E.; Pino, N. W.; Gardner, S. H.; Inaba, H.; Zhang, P.; Li, Y.; Feng, D.; Dibrell, S. E.; et al. Surveillance of Cancer Stem Cell Plasticity Using an Isoform-Selective Fluorescent Probe for Aldehyde Dehydrogenase 1A1. *ACS Cent. Sci.* **2018**, *4* (8), 1045–1055.

(61) Sensarn, S.; Zavaleta, C. L.; Segal, E.; Rogalla, S.; Lee, W.; Gambhir, S. S.; Bogyo, M.; Contag, C. H. A

Clinical Wide-Field Fluorescence Endoscopic Device for Molecular Imaging Demonstrating Cathepsin Protease Activity in Colon Cancer. *Mol. Imaging Biol.* **2016**, *18* (6), 820–829.

(62) Patterson, M. S.; Wilson, B. C.; Wyman, D. R. The Propagation of Optical Radiation in Tissue I. Models of Radiation Transport and Their Application. *Lasers Med. Sci.* **1991**, *6* (2), 155–168.

(63) Matcher, S. J.; Cope, M.; Delpy, D. T. In Vivo Measurements of the Wavelength Dependence of Tissue-Scattering Coefficients between 760 and 900 Nm Measured with Time-Resolved Spectroscopy. *Appl. Opt.* **1997**, *36* (1), 386.

(64) Hong, G.; Antaris, A. L.; Dai, H. Near-Infrared Fluorophores for Biomedical Imaging. *Nat. Biomed. Eng.* **2017**, *1* (1), 0010.

(65) Cao, J.; Zhu, B.; Zheng, K.; He, S.; Meng, L.; Song, J.; Yang, H. Recent Progress in NIR-II Contrast Agent for Biological Imaging. *Front. Bioeng. Biotechnol.* **2020**, *7*, 487.

(66) Wang, L. V.; Hu, S. Photoacoustic Tomography: In Vivo Imaging from Organelles to Organs. *Science* **2012**, *335* (6075), 1458–1462.

(67) Bell, A. G. On the Production and Reproduction of Sound by Light. *J. Soc. Telegr. Eng.* **1880**, *9* (34), 404–426.

(68) Beard, P. Biomedical Photoacoustic Imaging. *Interface Focus* **2011**, *1* (4), 602–631.

(69) Zackrisson, S.; Van De Ven, S. M. W. Y. W. Y.; Gambhir, S. S. Light in and Sound out: Emerging Translational Strategies for Photoacoustic Imaging. *Cancer Res.* **2014**, *74* (4), 979–1004.

(70) Attia, A. B. E.; Balasundaram, G.; Moothanchery, M.; Dinish, U. S.; Bi, R.; Ntziachristos, V.; Olivo, M. A Review of Clinical Photoacoustic Imaging: Current and Future Trends. *Photoacoustics* **2019**, *16*, 100144.

(71) Weber, J.; Beard, P. C.; Bohndiek, S. E. Contrast Agents for Molecular Photoacoustic Imaging. *Nat. Methods* **2016**, *13* (8), 639–650.

(72) Brown, E.; Brunker, J.; Bohndiek, S. E. Photoacoustic Imaging as a Tool to Probe the Tumour Microenvironment. *Dis. Model. Mech.* **2019**, *12* (7), dmm039636.

(73) Levi, J.; Kothapalli, S. R.; Ma, T.; Hartman, K.; Khuri-yakub, B. T.; Sam, S. Design and Synthesis of an Activatable Photoacoustic Probe. *J. Am. Chem. Soc.* **2010**, No. 132, 11264–11269.

(74) Levi, J.; Kothapalli, S.-R.; Bohndiek, S.; Yoon, J.-K.; Dragulescu-Andrasi, A.; Nielsen, C.; Tisma, A.; Bodapati, S.; Gowrishankar, G.; Yan, X.; et al. Molecular Photoacoustic Imaging of Follicular Thyroid Carcinoma. *Clin. Cancer Res.* **2013**, *19* (6), 1494–1502.

(75) Yang, K.; Zhu, L.; Nie, L.; Sun, X.; Cheng, L.; Wu, C.; Niu, G.; Chen, X.; Liu, Z. Visualization of Protease Activity in Vivo Using an Activatable Photo-Acoustic Imaging Probe Based on CuS Nanoparticles. *Theranostics* **2014**, *4* (2), 134–141.

(76) Frenette, M.; Hatamimoslehabadi, M.; Bellinger-Buckley, S.; Laoui, S.; La, J.; Bag, S.; Mallidi, S.; Hasan, T.; Bouma, B.; Yelleswarapu, C.; et al. Shining Light on the Dark Side of Imaging: Excited State Absorption Enhancement of a Bis-Styryl Bodipy Photoacoustic Contrast Agent. *J. Am. Chem. Soc.* **2014**, *136* (45), 15853–15856.

(77) Buschmann, V.; Weston, K. D.; Sauer, M. Spectroscopic Study and Evaluation of Red-Absorbing Fluorescent Dyes. *Bioconjug. Chem.* **2003**, *14* (1), 195–204.

(78) Boguta, A.; Wróbel, D. Fluorescein and Phenolphthalein - Correlation of Fluorescence and Photoelectric Properties. *J. Fluoresc.* **2001**, *11* (2), 129–137.

(79) Ashkenazi, S. Photoacoustic Lifetime Imaging of Dissolved Oxygen Using Methylene Blue. *J. Biomed. Opt.* **2010**, *15* (4), 040501.

(80) Jiang, Y.; Pu, K. Advanced Photoacoustic Imaging Applications of Near-Infrared Absorbing Organic Nanoparticles. *Small* **2017**, *13* (30), 1–19.

(81) Rong, G.; Corrie, S. R.; Clark, H. A. In Vivo Biosensing: Progress and Perspectives. *ACS Sensors* **2017**, *2* (3), 327–338.

(82) Fu, Q.; Zhu, R.; Song, J.; Yang, H.; Chen, X. Photoacoustic Imaging: Contrast Agents and Their Biomedical Applications. *Adv. Mater.* **2018**, *31*, 1805875.

(83) Knox, H. J.; Chan, J. Acoustogenic Probes: A New Frontier in Photoacoustic Imaging. *Acc. Chem. Res.* **2018**, *51* (11), 2897–2905.

(84) Zeng, L.; Ma, G.; Lin, J.; Huang, P. Photoacoustic Probes for Molecular Detection: Recent Advances and Perspectives. *Small* **2018**, *14* (30), 1–18.

(85) Jiang, Y.; Upputuri, P. K.; Xie, C.; Lyu, Y.; Zhang, L.; Xiong, Q.; Pramanik, M.; Pu, K. Broadband Absorbing Semiconducting Polymer Nanoparticles for Photoacoustic Imaging in Second Near-Infrared Window. *Nano Lett.* **2017**, *17* (8), 4964–4969.

(86) Zhuang, Y.; Xu, Q.; Huang, F.; Gao, P.; Zhao, Z.; Lou, X.; Xia, F. Ratiometric Fluorescent Bioprobe for Highly Reproducible Detection of Telomerase in Bloody Urines of Bladder Cancer Patients. *ACS Sens.* **2016**, *1* (5), 572–578.

(87) Wu, X.; Lin, B.; Yu, M.; Yang, L.; Han, J.; Han, S. A Carbohydrate-Grafted Nanovesicle with Activatable Optical and Acoustic Contrasts for Dual Modality High Performance Tumor Imaging. *Chem. Sci.* **2015**, *6*, 2002–2009.

(88) Yu, M.; Wu, X.; Lin, B.; Han, J.; Yang, L.; Han, S. Lysosomal PH Decrease in Inflammatory Cells Used To Enable Activatable Imaging of Inflammation with a Sialic Acid Conjugated Profluorophore. *Anal. Chem.* **2015**, *87* (13), 6688–6695.

(89) Miao, Q.; Lyu, Y.; Ding, D.; Pu, K. Semiconducting Oligomer Nanoparticles as an Activatable Photoacoustic Probe with Amplified Brightness for in Vivo Imaging of PH. *Adv. Mater.* **2016**, *28* (19), 3662–3668.

(90) Ho, I.-T.; Sessler, J. L.; Gambhir, S. S.; Jokerst, J. V. Parts per Billion Detection of Uranium with a Porphyrinoid-Containing Nanoparticle and in Vivo Photoacoustic Imaging. *Analyst* **2015**, *140* (11), 3731–3737.

(91) Mishra, A.; Jiang, Y.; Roberts, S.; Ntziachristos, V.; Westmeyer, G. G. Near-Infrared Photoacoustic Imaging Probe Responsive to Calcium. *Anal. Chem.* **2016**, *88* (22), 10785–10789.

(92) Roberts, S.; Seeger, M.; Jiang, Y.; Mishra, A.; Sigmund, F.; Stelzl, A.; Lauri, A.; Symvoulidis, P.; Rolbieski, H.; Preller, M.; et al. Calcium Sensor for Photoacoustic Imaging. *J. Am. Chem. Soc.* **2018**, *140* (8), 2718–2721.

(93) Wang, J.; Chen, F.; Arconada-Alvarez, S. J.; Hartanto, J.; Yap, L. P.; Park, R.; Wang, F.; Vorobyova, I.; Dagliyan, G.; Conti, P. S.; et al. A Nanoscale Tool for Photoacoustic-Based Measurements of Clotting Time and Therapeutic Drug Monitoring of Heparin. *Nano Lett.* **2016**, *16* (10), 6265–6271.

(94) Wang, S.; Sheng, Z.; Yang, Z.; Hu, D.; Long, X.; Feng, G.; Liu, Y.; Yuan, Z.; Zhang, J.; Zheng, H.; et al. Activatable Small-Molecule Photoacoustic Probes That Cross the Blood–Brain Barrier for Visualization of Copper(II) in Mice with Alzheimer's Disease. *Angew. Chemie - Int. Ed.* **2019**, *58* (36), 12415–12419.

(95) Li, H.; Zhang, P.; Smaga, L. P.; Hoffman, R. A.; Chan, J. Photoacoustic Probes for Ratiometric Imaging of Copper(II). *J. Am. Chem. Soc.* **2015**, *137* (50), 15628–15631.

(96) Fife, T. H.; Przystas, T. J. Divalent Metal Ion Catalysis in the Hydrolysis of Esters of Picolinic Acid. Metal Ion Promoted Hydroxide Ion and Water Catalyzed Reactions. *J. Am. Chem. Soc.* **1985**, *107* (4), 1041–1047.

(97) Chen, Q.; Liang, C.; Sun, X.; Chen, J.; Yang, Z.; Zhao, H.; Feng, L.; Liu, Z. H2O2-Responsive Liposomal Nanoprobe for Photoacoustic Inflammation Imaging and Tumor Theranostics via in Vivo Chromogenic Assay. *Proc. Natl. Acad. Sci. U. S. A.* **2017**, 201701976.

(98) Weber, J.; Bollepalli, L.; Belenguer, A. M.; Antonio, M. Di; De Mitri, N.; Joseph, J.; Balasubramanian, S.; Hunter, C. A.; Bohndiek, S. E. An Activatable Cancer-Targeted Hydrogen Peroxide Probe for Photoacoustic and Fluorescence Imaging. *Cancer Res.* **2019**, *79* (20), 5407–5417.

(99) Zhang, J.; Zhen, X.; Upputuri, P. K.; Pramanik, M.; Chen, P.; Pu, K. Activatable Photoacoustic Nanoprobes for In Vivo Ratiometric Imaging of Peroxynitrite. *Adv. Mater.* **2017**, *29*, 1604764.

(100) Shi, B.; Gu, X.; Fei, Q.; Zhao, C. Photoacoustic Probes for Real-Time Tracking of Endogenous H2S in Living Mice. *Chem. Sci.* **2017**, *8*, 2150–2155.

(101) Li, X.; Tang, Y.; Li, J.; Hu, X.; Yin, C.; Yang, Z.; Wang, Q.; Wu, Z.; Lu, X.; Wang, W.; et al. A Small-Molecule Probe for Ratiometric Photoacoustic Imaging of Hydrogen Sulfide in Living Mice. *Chem. Commun.* **2019**, *55* (42), 5934–5937.

(102) Liu, Y.; Wang, S.; Ma, Y.; Lin, J.; Wang, H. Y.; Gu, Y.; Chen, X.; Huang, P. Ratiometric Photoacoustic Molecular Imaging for Methylmercury Detection in Living Subjects. *Adv. Mater.* **2017**, *29* (17), 1606129.

(103) Dragulescu-Andrasi, A.; Kothapalli, S. R.; Tikhomirov, G. A.; Rao, J.; Gambhir, S. S. Activatable Oligomerizable Imaging Agents for Photoacoustic Imaging of Furin-like Activity in Living Subjects. *J. Am. Chem. Soc.* **2013**, *135* (30), 11015–11022.

(104) Laufer, J.; Delpy, D.; Elwell, C.; Laufer, J.; Elwell, C.; Delpy, D.; Johnson, J. L.; Wijk, K. Van; Caron, J. N. Multispectral Photoacoustic Imaging of Tumours in Mice Injected with an Enzyme- Activatable Photoacoustic Probe. *J. Opt.* **2017**, 014002.

(105) Yin, L.; Sun, H.; Zhang, H.; He, L.; Qiu, L.; Lin, J.; Xia, H.; Zhang, Y.; Ji, S.; Shi, H.; et al. Quantitatively Visualizing Tumor-Related Protease Activity in Vivo Using a Ratiometric Photoacoustic Probe. *J. Am. Chem. Soc.* **2019**, *141* (7), 3265–3273.

(106) Zhang, D.; Qi, G. Bin; Zhao, Y. X.; Qiao, S. L.; Yang, C.; Wang, H. In Situ Formation of Nanofibers from Purpurin18-Peptide Conjugates and the Assembly Induced Retention Effect in Tumor Sites. *Adv. Mater.* **2015**, *27* (40), 6125–6130.

(107) Gardner, S. H.; Reinhardt, C. J.; Chan, J. Advances in Activity-Based Sensing Probes for Isoform-Selective Imaging of Enzymatic Activity. *Angew. Chem. Int. Ed.* **2020**, 10.1002/anie.202003687.

(108) Reinhardt, C. J.; Chan, J. Development of Photoacoustic Probes for in Vivo Molecular Imaging. *Biochemistry* **2018**, *57* (2), 194–199.

CHAPTER 2: A FLUORESCENT PROBE FOR MONITORING CYCLOOXYGENASE-2 ACTIVITY IN LIVE CELLS[2]

2.1 Background and significance

One powerful application of molecular imaging is to discover novel regulatory mechanisms that are operative only in living systems. Cyclooxygenase-2 (COX-2) is an important pharmacological target and potential biomarker for acute and chronic inflammatory conditions. To date, nearly all biocompatible detection methods rely on binding-based sensing for detection. As a result, only the presence, but not the functionality of the protein can be assessed. To overcome this limitation, we sought to develop a fluorogenic substrate that could undergo COX-2-mediated activation in a manner similar to the natural substrate. Ultimately, this could investigate regulation that exists beyond the protein expression level, facilitate the deconvolution of isoform contributions, and possibly be applied for inhibitor screening, lead development, and diagnostics.

2.1.1 Cyclooxygenase and the prostaglandins

Cyclooxygenase (COX, E.C. 1.14.99.1) is the biosynthetic enzyme that initiates the synthesis of prostaglandins from the linear lipid precursor, arachidonic acid (AA).[1–3] After production, the prostaglandins function as important lipid-based mediators that regulate physiological processes, such as gastric epithelial protection, hemostasis, and sodium metabolism.[4,5] At higher concentrations the prostaglandins act as potent pro-inflammatory compounds through the production of cytokines.[6,7] These prostaglandins can be further elaborated by a variety of tissue-specific isomerases and synthases to afford the entire gambit of prostanoids

[2]Portions of this chapter are reprinted or adapted with permissions from the following publication: Yadav, A. K.; Reinhardt, C. J.; Arango, A. S.; Huff, H. C.; Dong, L.; Malkowski, M. G.; Das, A.; Tajkhorshid, E.; Chan, J. An Activity-Based Sensing Approach for the Detection of Cyclooxygenase-2 in Live Cells. *Angew. Chemie Int. Ed.* **2020**, *59*, 3307–3314.[142] Copyright © 2020 John Wiley and Sons, Inc.

(AA-derived prostaglandins).[5] The prostanoids exert their unique biological activities by binding and activating G-coupled protein receptors or nuclear hormone receptors.[8]

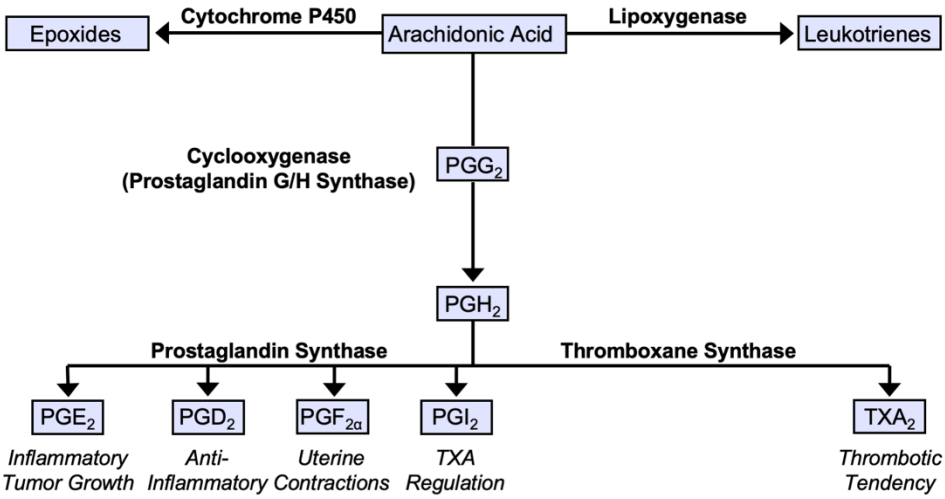

Figure 2.1: Arachidonic acid is the precursor for the lipoxygenase-, cyclooxygenase-, and cytochrome P450 monooxygenase-derived eicosanoids. Cyclooxygenase, or prostaglandin G/H synthase, catalyzes the oxidation of arachidonic acid to PGG_2, followed by reduction to PGH_2. A range of prostaglandin synthases or thromboxane synthase elaborates this intermediate to yield a range of prostanoids with distinct biological activities.

2.1.2 Cyclooxygenase enzymology and pharmacology

Two isoforms of human COX have been identified (COX-1 and COX-2), which display a high level of structural homology (~60% sequence identity).[9] Both are glycosylated, heme-containing homodimers that are embedded on the luminal surface of the endoplasmic reticulum, the inner nuclear envelope, or cytosolic face of the cell membrane through contacts with the membrane-binding domain. Of the four oligosaccharides, three are present on both isoforms and participate in protein folding. The fourth oligosaccharide is unique to COX-2 and facilitates proteasomal degradation or trafficking. COX-2's localization can be altered by stimuli, are catalytically active, and facilitate interactions with other related enzymes. For example, the calcium-dependent recruitment of cytosolic phospholipase A2α to the nuclear envelope releases AA for eicosanoid biosynthesis by COX-2 and the partial colocalization of COX-2 and

thromboxane synthase may promote thromboxane synthesis at the endoplasmic reticulum, but not the nuclear envelope.[10–14]

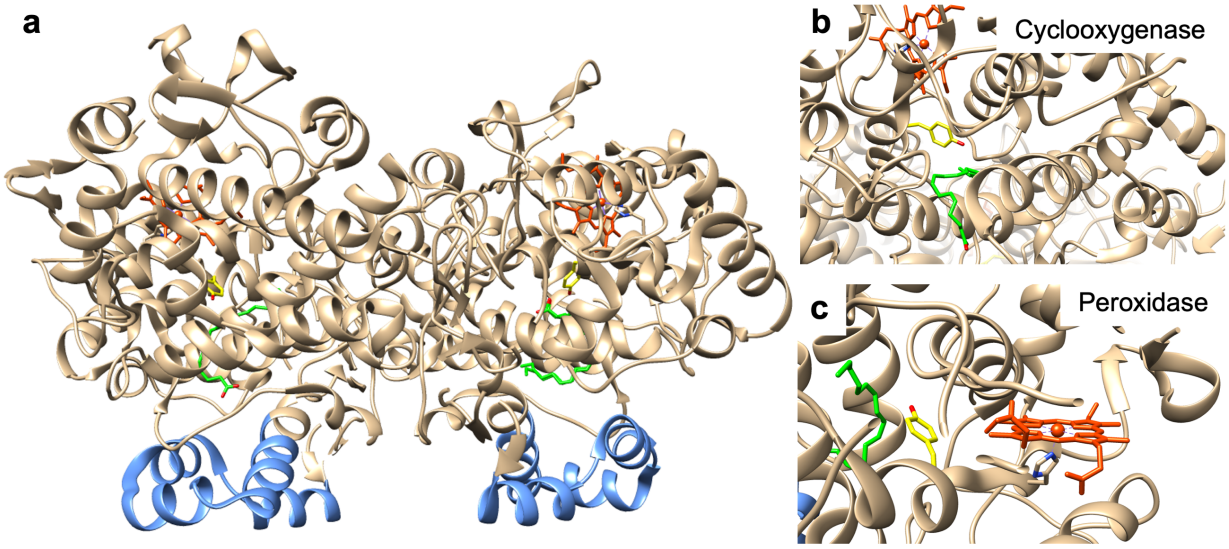

Figure 2.2: (a) Structure of murine COX-2 bound to arachidonic acid (green, PDB: 3HS5) with the heme (red orange) and active site Tyr385 (yellow) shown to indicate the location of the peroxidase and cyclooxygenase active sites, respectively. Membrane binding domain (blue) and globular portions of the protein (tan) are highlighted for orientation. (b) Zoomed in image of the cyclooxygenase active site highlights the proximity of Tyr385 for the initial oxidation by the peroxidase activity, as well as the proper orientation for CH abstraction at carbon-13 of the substrate. Note the competent orientation was only observed in only the left subunit. (c) Zoomed in image of the peroxidase active site cleft the ligating His388.

Both isoforms catalyze the committed step for production of prostaglandin H2 (PGH_2) through the alkyl-peroxide intermediate prostaglandin G2 (PGG_2). The protein's structure is mostly globular and contains distinct cyclooxygenase and peroxidase active sites. The cyclooxygenase active site is proximal to the membrane interface to facilitate substrate binding and the peroxidase active site is solvent exposed. Mechanistically, the catalysis begins with the peroxidase activity, where oxidation of the active site tyrosine (in the cyclooxygenase active site) is coupled to the reduction of hydrogen peroxide, an organic peroxide, or peroxynitrite. Next, the active tyrosyl radical (Tyr385) performs a rate-limiting H-atom abstraction from the pro-*S* hydrogen of carbon-13 and templates the peroxidation and cyclization with molecular oxygen to yield PGG_2 with minor side products.[1,15–19] This intermediate is then likely channeled to the distal

active site under physiologically relevant conditions[20,21] for reduction to PGH_2.[1,15–19] While the protein is a homodimer, it displays half-of-sites reactivity and can be modulated through allosteric binding, presumably within the non-active active site.[22,23]

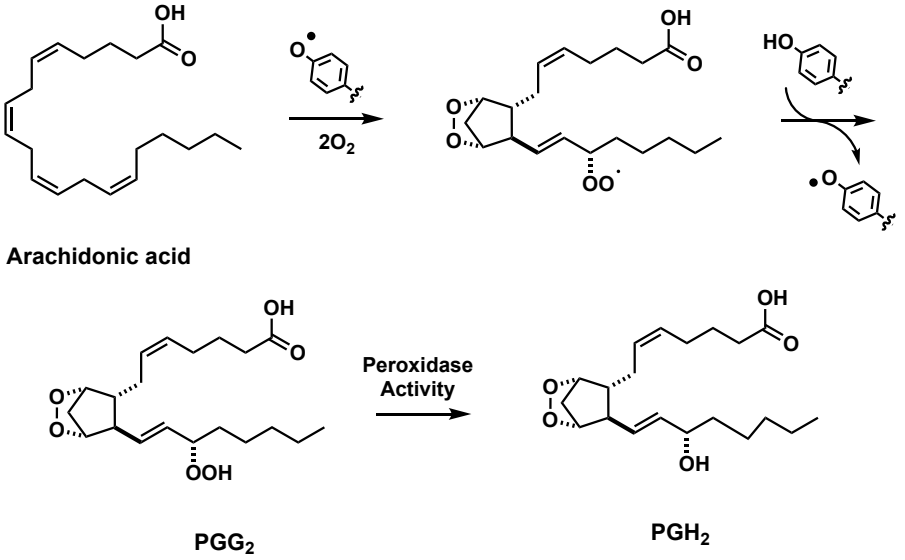

Scheme 2.1: Cyclooxygenase's catalytic mechanism for synthesizing PGG_2 and PGH_2 from arachidonic acid. An active-site tyrosyl radical performs a hydrogen atom abstraction from the substrate to generate a carbon-centered radical intermediate. The cyclooxygenase active site then templates an efficient peroxidation with molecular oxygen before the translocating the intermediate, PGG_2, to the peroxidase active site for reduction to PGH_2.

The major difference between the two isoforms is their expression profile: COX-1 is constitutively expressed in most cell types, whereas COX-2 expression can be either constitutive or induced for rapid prostaglandin production depending on the tissue type.[2,4,24–27] COX overexpression represents a prominent phenotype in inflammation,[28,29] neurodegenerative disorders,[30] and cancer.[25,31,32] For example, high expression levels and cross-talk with inducible nitric oxide synthase in cancer can correlate with poor clinical outcomes through increased angiogenesis, proliferation, and cell migration.[33–38]

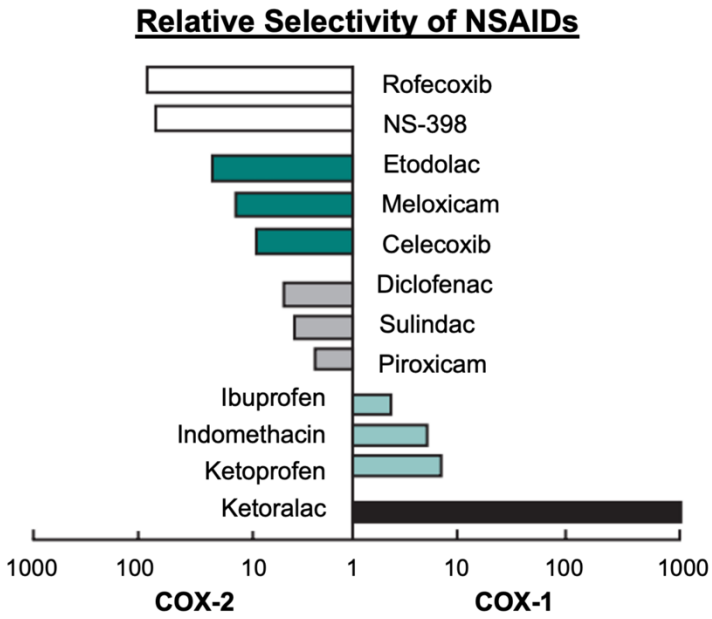

Figure 2.3: COX inhibitors display imperfect selectivity at COX-1 and COX-2. Reprinted (adapted) with permission from ref. 39. Copyright © 2001 Harcourt Publishers Ltd.

COX inhibition has been successful for treating acute and chronic inflammation. Aspirin was serendipitously discovered as a covalent inhibitor with slight preference for a COX-1. Since this discovery, a range of inhibitors were reported with ranging isoform selectivity.[39] Collectively, these drugs are referred to as non-steroidal anti-inflammatory drugs (NSAIDs). After identifying COX-1-dependent gastrointestinal toxicity[40] there was a push for achieving COX-2 selectivity.[8,39] Moreover, epidemiological analyses and preclinical studies verified that COX-2 selective inhibitors, such as celecoxib, could inhibit carcinogenesis and tumor growth, poising them for both cancer prevention and treatment.[8,31,41] Interestingly, the pro-metastatic contributions of the isoforms appear to be context-dependent.[36,42,43] Regardless, unexpected dysregulation of COX-1-derived thromboxane A2 concentrations by COX-2-derived prostaglandin I2 increased the risk of heart attack and stroke in patients. This limits the application of NSAIDs for cancer prevention and treatment.[5,44] Nevertheless, widespread NSAID use and the role of COX-2 in inflammatory

disease continues to drive the development of chemical tools for detecting the protein for basic biological studies and diagnostic applications.

2.1.3 Cyclooxygenase detection strategies

Early studies evaluated COX activity by directly or indirectly quantifying the substrates, intermediates, or product as a measure of *in vitro* enzyme activity (e.g., HPLC, radiochemical assays, oxygen electrodes, chromogenic reductants, horseradish peroxidase coupled assays).[20,45,46] Only a limited number of strategies have been introduced for detecting COX-2 in living cells or animals. For example, selective inhibitors of COX-2 have been radiolabeled[47–53] or appended to dyes[54,55] for PET/SPECT or fluorescence imaging, respectively. These imaging agents report on relative COX-2 expression profiles; however, they remain in a constant 'on' state, regardless of whether they are bound to COX-2. More recently, activatable fluorescent inhibitors have been reported that afford an turn-on response, where protein binding sequesters the inhibitor away from the fluorophore, disrupts the inhibitor-mediated fluorescence quenching, and renders the protein-small-molecule adduct fluorescent.[56,57] Despite these notable improvements, these technologies only report on whether COX-2 is present, but not whether the enzyme is catalytically active. It is important to highlight that a variety of factors beyond concentration can influence COX-2 activity, such as substrate concentration, allosteric regulators, and post-translational modifications.[18,22,23,58,59] To address these limitations, we developed CoxFluor, the first isoform-selective, activity-based fluorescent probe for COX-2.

2.2 Design and development of CoxFluor

CoxFluor consists of 3,7-dihydroxyphenoxazine (reduced form of resorufin) linked to AA through a cleavable amide bond. We proposed this design with the hypothesis that the lipid tail

could serve as a substrate for COX-2 in a manner similar to the AA (Scheme 2.1). After binding within the cyclooxygenase active site, the probe could undergo hydrogen atom abstraction by the enzyme's Tyr385, followed by peroxidation and cyclization to afford the CoxFluor-PGG_2 intermediate. Subsequent translocation to the peroxidase active site and oxidation by Compound I or II could yield an unstable oxygen-centered resorufin radical followed by dismutation and amide hydrolysis to release the fluorescent product and either PGG_2 or PGH_2 (after reduction, Scheme 2.2).[1,60–62] When proposing this structure, we hypothesized that we could utilize the bulky dye to prevent COX-1 binding and catalysis. This was based on previous reports that indicate COX-1 is unable to accommodate large groups at the carboxylate[2] and that this moiety provides critical interactions with Arg120 for binding.[63–65] On the other hand, COX-2's larger substrate pocket and expanded substrate scope, including amides, suggested that CoxFluor should be competent for catalysis.[66]

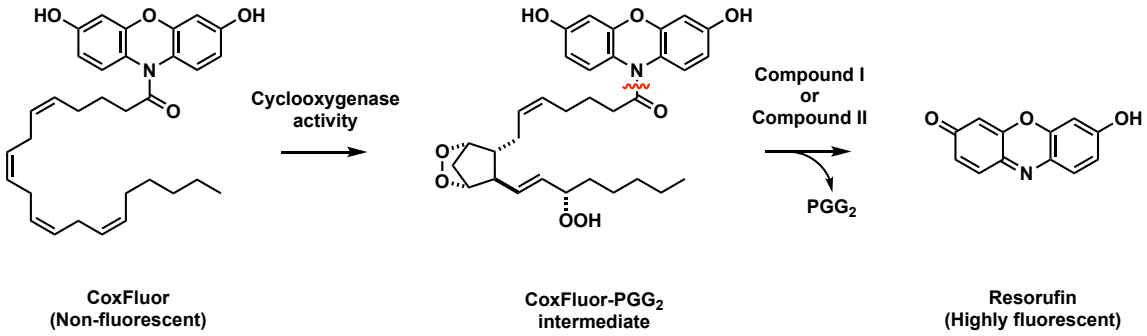

Scheme 2.2: Proposed mechanism of enzyme-catalyzed resorufin production by COX via a CoxFluor-PGG_2 intermediate via either compound I (π cationic porphyrin radical) or compound II (oxyferryl). The reaction between two CoxFluor-PGG_2 intermediate radicals, dismutation, and hydrolysis are omitted for simplicity.

The synthesis of CoxFluor began with the zinc-mediated reduction of resazurin, followed by acetylation with acetic anhydride to afford compound **2.1** in 63% yield over two steps.[67] This intermediate was then coupled to arachidonoyl chloride in the presence of potassium iodide to afford compound 2.2 in 49% yield. Finally, treatment of compound **2.2** with sodium methoxide

(generated *in situ*) facilitated acetyl deprotection and provided CoxFluor in 68% yield (overall 21% yield over 4 steps, Scheme 2.3).

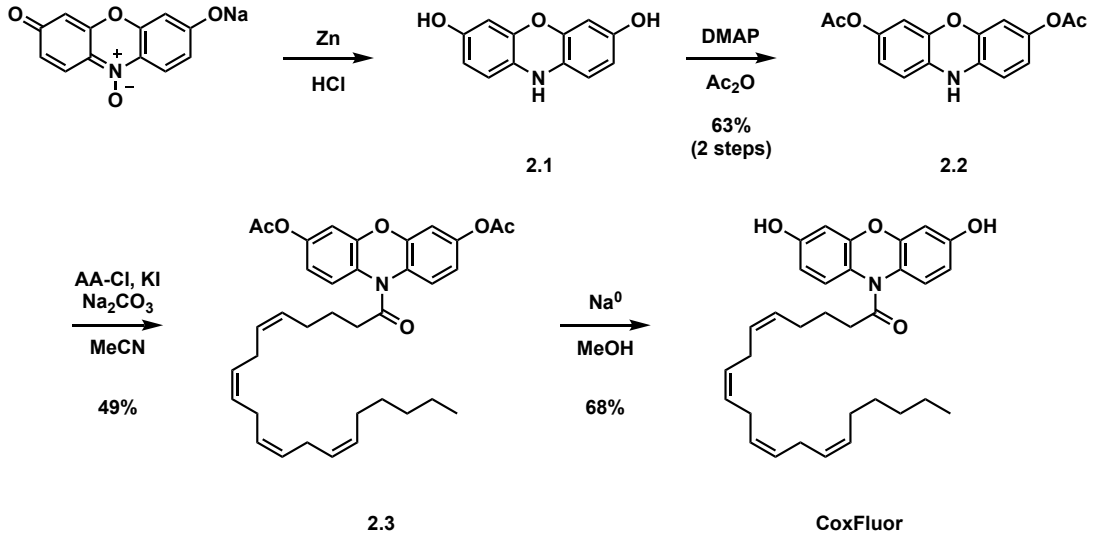

Scheme 2.3: Synthesis of CoxFluor from resazurin in three steps with an overall 21% yield.

We first evaluated CoxFluor's response to recombinant human COX-2. Treatment of CoxFluor (Φ = 0.29 , ε = 820 $M^{-1}cm^{-1}$ at 572 nm) with COX-2 resulted in the production of resorufin (Φ = 0.55, ε = 73,000 $M^{-1}cm^{-1}$ at 573 nm)[68] and PGH_2 (confirmed by LC-HRMS, Figure A.1) with a 41-fold fluorescent turn-on response (Figure 2.4a). To confirm that activation was a consequence of enzyme-catalyzed oxidation rather than unbiased peroxidase activity, we prepared a control compound, Ctrl-CoxFluor, in which the AA lipid was replaced with the saturated lipid tail (arachidic acid, Scheme 2.4).

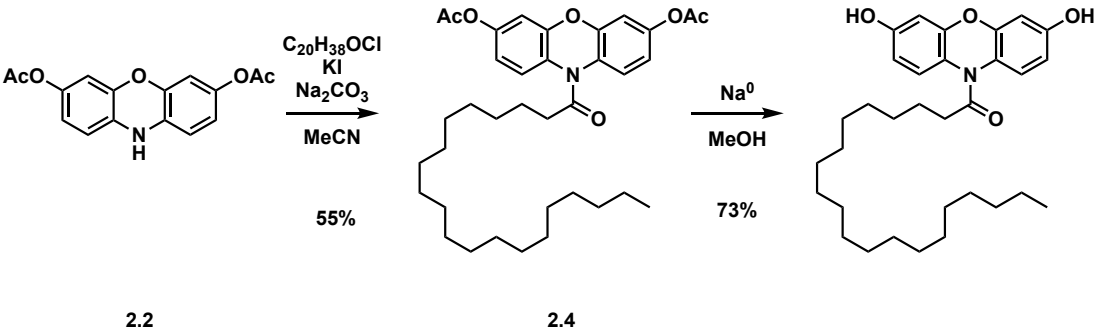

Scheme 2.4: Synthesis of Ctrl-CoxFluor from compound 2.2 in two steps. Overall 25% yield from resazurin.

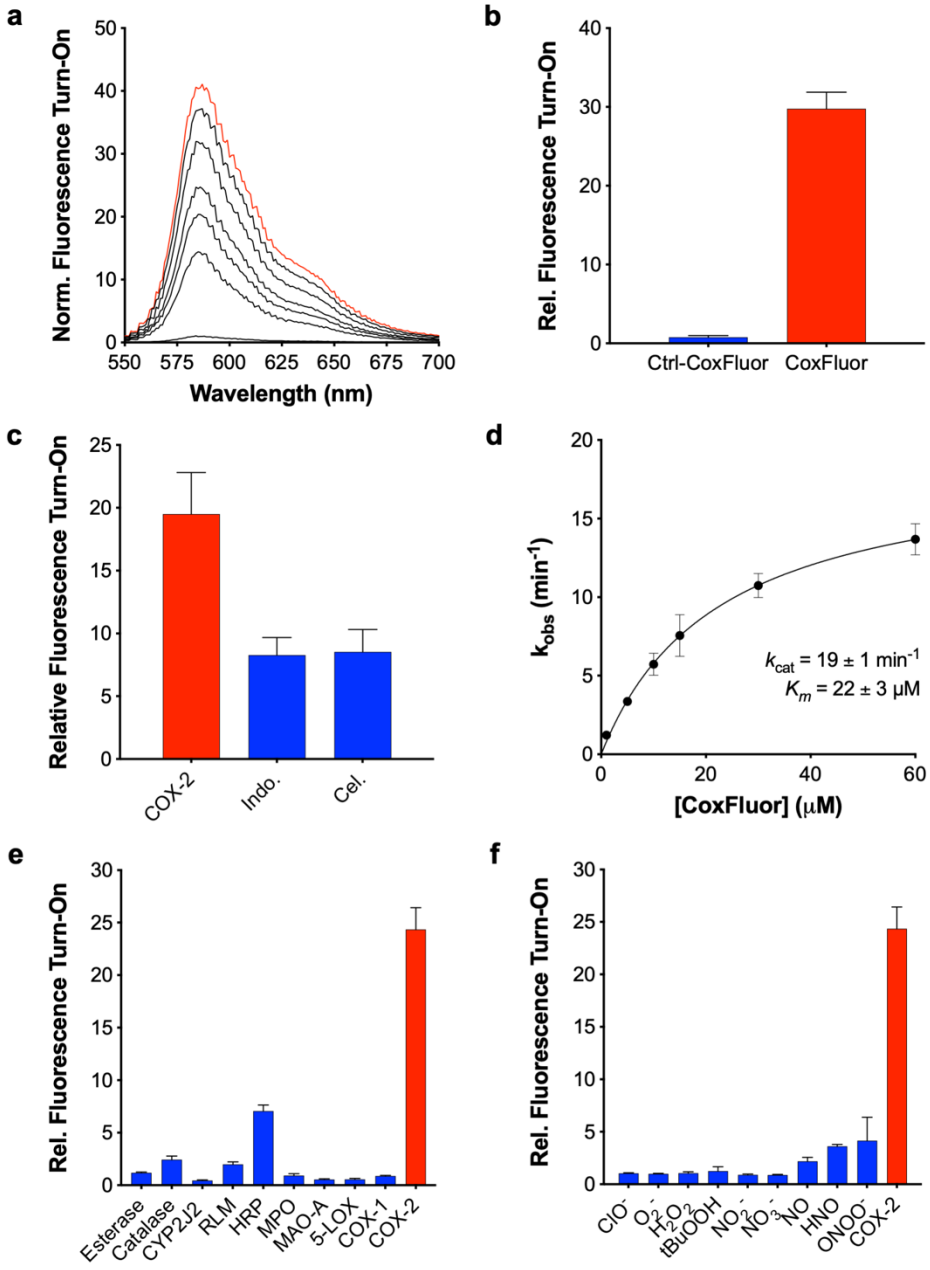

Figure 2.4: (a) Relative fluorescence for CoxFluor (10 μM) incubated with COX-2 (250 nM) and hemin (1 μM) over the course of 4 h. (b) Relative fluorescent intensity of CoxFluor and Ctrl-CoxFluor after incubation with COX-2 (250 nM) and hemin (1 μM) for 4 h. (c) Michaelis-Menten kinetics for COX-2-catalyzed (50 nM) release of resorufin in the presence of hemin (200 nM). (d) Inhibition of COX-2 (250 nM) and hemin (1 μM) by indomethacin (Indo., 10 μM) and celecoxib (Cel., 10 μM). (e) Relative fluorescence for CoxFluor incubated COX-2 (0.101 U), a panel of enzymes (10-fold excess) or (f) panel of reactive oxygen/nitrogen species (500 μM, 50 equiv). All experiments were conducted at room temperature in 100 mM Tris HCl buffer (pH 8.0) except MPO, and 5-LOX (additional information in the section 2.6.9). All data is reported as the mean ± standard deviation (n = 3) for parts b, d, e and f or the error from fitting for part c. Parts a/c and b/d-f were performed according to the fluorimeter and plate reader assays, respectively.

Ctrl-CoxFluor proved to be unreactive under the same reaction conditions (Figure 2.4b), strongly suggesting that the signal enhancement observed for CoxFluor was due to enzymatic activity. Under steady state conditions, CoxFluor underwent oxidation to resorufin by COX-2 with a k_{cat} of 19 min^{-1} and K_m of 22 μM (Figure 2.4c). The K_m value is similar to those obtained for arachidonoyl ethanolamide (K_m = 24 μM) and is within an order of magnitude of AA (K_m = 6 μM). The measured rate for turn-over is also within 100-fold of the natural substrate.[66] Importantly, CoxFluor's fluorescence response was inhibited by both indomethacin and celecoxib (Figure 2.4d).

Isoform selectivity was evaluated by incubating CoxFluor with COX-1 that was isolated from bovine vesicles. Only a minimal change in fluorescence was observed over the course of 4 h (1.3-fold fluorescence enhancement, 5% of the COX-2 response, Figure A.2). Off-target activation was also assessed across a panel of enzymes that possess closely related activities (lipoxygenase, peroxidase, catalase), could potentially cleave the amide (esterase), or are capable of metabolizing AA analogs (cytochrome P450s).[69] Even in the presence of 10-fold excess enzyme, CoxFluor displayed good selectivity against all of the tested enzymes (Figure 2.4e). Likewise, no undesirable activation was observed when CoxFluor was incubated with various biologically relevant reactive oxygen species, reactive nitrogen species, or other cellular oxidants/reductants (Figure 2.4f and A.3). Moreover, no bleaching was observed when resorufin was treated with the same panel of reactive oxygen and nitrogen species (Figure A.3). Incubation of CoxFluor with COX-2 in the presence of glutathione (GSH, 1 mM) maintained significant COX-2-specific fluorescence enhancement confirming the potential for use for live-cell imaging (Figure A.4). This is in contrast to Amplex® Red-based assays, which display cross-reactivity with GSH in the presence of peroxidases[70] or direct quenching of the radical intermediate.[62] Together, these data suggest that

CoxFluor can be utilized to identify and/or evaluate COX-2 inhibitors, overcoming key drawbacks in existing methodologies that require radiolabeled compounds, purification of intermediates/products, or coupled-enzyme systems.[71,72] This also provides further support for the formation of a CoxFluor-PGG_2 intermediate because both inhibitors bind within the cyclooxygenase active site of the protein.[73,74]

2.3 Mechanistic insights into CoxFluor's activation by cyclooxygenase-2

To further investigate the mechanism of CoxFluor activation by COX-2, we employed molecular dynamics (MD) and ensemble docking. Previous structures of COX-1 (PDB 5U6X)[75] and COX-2 (PDB 5KIR)[76] were selected, ligands were removed and the holoenzyme was simulated in explicit water over a period of 200 ns. Importantly, no global differences were observed for the peptide backbone across a panel of COX-1 and COX-2 structures, even in the presence of ligands and substrate (*www.rcsb.org*, all root-mean-standard-deviation < 2.5 Å, Table A.1–A.2 and Figure A.5).[77] Next, CoxFluor was docked into each pose along the simulation trajectory to probe the most probable binding modes (based on the predicted binding score),[78] where clear differences in the number and area available for binding were observed both overall and within the cyclooxygenase active site of COX-2 as compared to COX-1 (Figure 2.5a–c and A.6). This finding is consistent with the difference in solvent accessible surfaces harbored within each cyclooxygenase active site.[2] CoxFluor also docks in a similar location to the reported indomethacin fluorescent inhibitors (Figure A.7),[55,79] further supporting the proposed cyclooxygenase-dependent release of resorufin (Scheme 2.2).

To begin to interrogate the sequence of events, CoxFluor and the CoxFluor-PGG_2 intermediate were docked within COX-2. Consistent with the proposed mechanism, CoxFluor

binds significantly at the cyclooxygenase active site (66/597 poses at -7 kcal/mol cutoff). On the other hand, the CoxFluor-PGG_2 intermediate displayed increased binding at the peroxidase active site for oxidation by either Compound I or Compound II (356/368 poses at -7 kcal/mol cutoff).

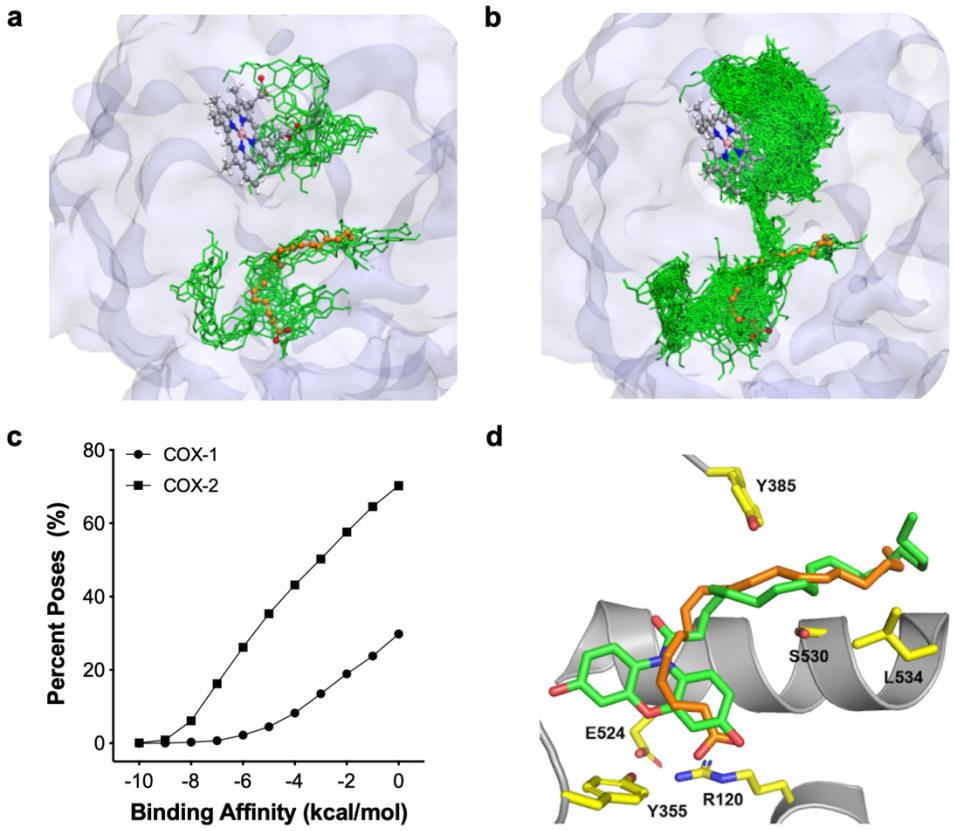

Figure 2.5: Molecular dynamics and ensemble docking studies of (a) COX-1 and (b) COX-2 with CoxFluor (green). Initial protein structures were prepared from PDB 5U6X and 5KIR and crystal bound AA (orange) is superimposed for comparison from PDB 1DIY and 3HS5, respectively. Structures display an overlay of all CoxFluor docked poses with scoring less than or equal to -7 kcal/mol. The heme from the simulation is represented as a ball and stick model to distinguish the cyclooxygenase and peroxidase active sites. (c) Percent of CoxFluor poses within the docking score binding affinities. (d) Competent binding of CoxFluor within the cyclooxygenase active site. Tyr385 (yellow) is oriented for hydrogen atom extraction from either CoxFluor (green) or AA (orange, PDB 3HS5).

This increased selectivity for the CoxFluor-PGG_2 intermediate at the peroxidase active site is consistent over all spontaneous interactions (Figure A.8). It is important to note that these results are consistent with the peroxidase-based oxidation[80] of CoxFluor in a similar manner to Amplex® Red[62] and 2,2′-azinobis(3-ethylbenzothiazolinesulfonic acid by horseradish peroxidase.[61,81] Finally, to confirm that CoxFluor can adopt the requisite conformation for oxidation by the active

site Tyr385, CoxFluor was docked within the cyclooxygenase active site and compared to crystal bound AA (PDB 3HS5).[82] Structural comparisons indicate that CoxFluor can bind within the cyclooxygenase active site with proper orientation for oxidation (Figure 2.5d). Similar poses are also observed within the larger box that contains both the cyclooxygenase and peroxidase active sites. Together, these results suggest that CoxFluor binds within the substrate binding pocket or adjacent solvent-exposed sites to undergo oxidation and formation of the CoxFluor-PGG_2 intermediate. After dissociation from the active site, the intermediate displays increased binding to the peroxidase active site for oxidation by Compound I or Compound II and subsequent release of resorufin.

2.4 Cellular detection of cyclooxygenase-2 activity with CoxFluor

Prior to performing cellular experiments, we evaluated CoxFluor's stability and biocompatibility. Negligible fluorescence response was observed after 8 h of incubation at room temperature or 37 °C (Figure A.9) and typical staining conditions yielded minimal toxicity in HEK 293T and RAW 264.7 macrophage cells (Figure A.10). Next, we generated a transiently transfected HEK 293T cell line over-expressing human COX-2. GSH depletion was performed with *N*-ethylmaleimide (NEM)[83] prior to staining because GSH can generate[70] or quench radical intermediates of other peroxidase-based probes complicating the interpretation of the results.[62,84] Moreover, past work has demonstrated that COX-2 inhibitors (e.g., celecoxib analogs and indomethacin) can alter GSH levels,[85–88] which is consistent with our initial experimental observations (Figure A.11). After incubation with CoxFluor for 3 h we observed a 1.2-fold fluorescence increase for transfected cells compared to the control, and no fluorescence enhancement was observed upon treatment with indomethacin (Figure A.12).

Next, we applied CoxFluor for the detection and imaging of endogenous COX-2 activity within RAW 264.7 macrophage cells. As a key player in inflammatory and immune responses, macrophages undergo phenotypic changes to pro-inflammatory or anti-inflammatory states upon stimulation.[89] Because COX-2 activity is the rate-limiting step in prostaglandin biosynthesis (pro-inflammatory mediators), COX-2 expression and subsequent prostaglandin production can be measured in well-established lipopolysaccharide (LPS)-induced inflammation models as a biomarker for inflammation.[3,90–95] To date, these studies typically rely on mRNA quantification, western blot analysis, or downstream product quantification (e.g., ELISA assays) rather than direct quantification of COX-2 activity. This is due to the lack of isoform selectivity in current cyclooxygenase assays.

First, we measured the effect of LPS stimulation time on COX-2's specific activity in RAW 264.7 macrophage lysates. Variations due to GSH fluctuations were again minimized using NEM, which we and others have shown does not affect COX activity (Figure A.13).[96] Only a modest 2.4-fold increase in COX-2 activity was observed within the first 4 h of activation. Over the next several hours, the activity increased in a linear fashion to a maximum of 17.6-fold at 19 h (Figure A.14). These results are similar to previous reports of prostaglandin biosynthesis within both murine[94] and human[93] macrophage cells under LPS-stimulated conditions. The activity differences were then confirmed within live cells using both confocal microscopy (Figure 2.6) and flow cytometry (Figure A.15). Rather than using NEM, we pre-treated with buthionine sulfoximine (BSO), a γ-glutamylcysteine synthase inhibitor because it is a less cytotoxic alternative.[97,98] Under these conditions we observed a 1.2-fold fluorescent enhancement for LPS-stimulated cells relative to the control using confocal microscopy and a 1.6-fold increase in median fluorescence for cells activated for 19 h as compared to 4 h with flow cytometry (Figure 2.6 and A.15). Moreover,

monitoring the ratio of fluorescence from CoxFluor stained cells to CoxFluor stained cells treated with indomethacin clearly identified COX-2 activity across activation states (M0 versus M1, Figure A.15). Of note, we confirmed that CoxFluor could detect activity changes without GSH depletion, in which a 1.2-fold increase in activity was observed after 19 h LPS-activation relative to 4 h LPS-stimulated cells using flow cytometry (Figure A.16).

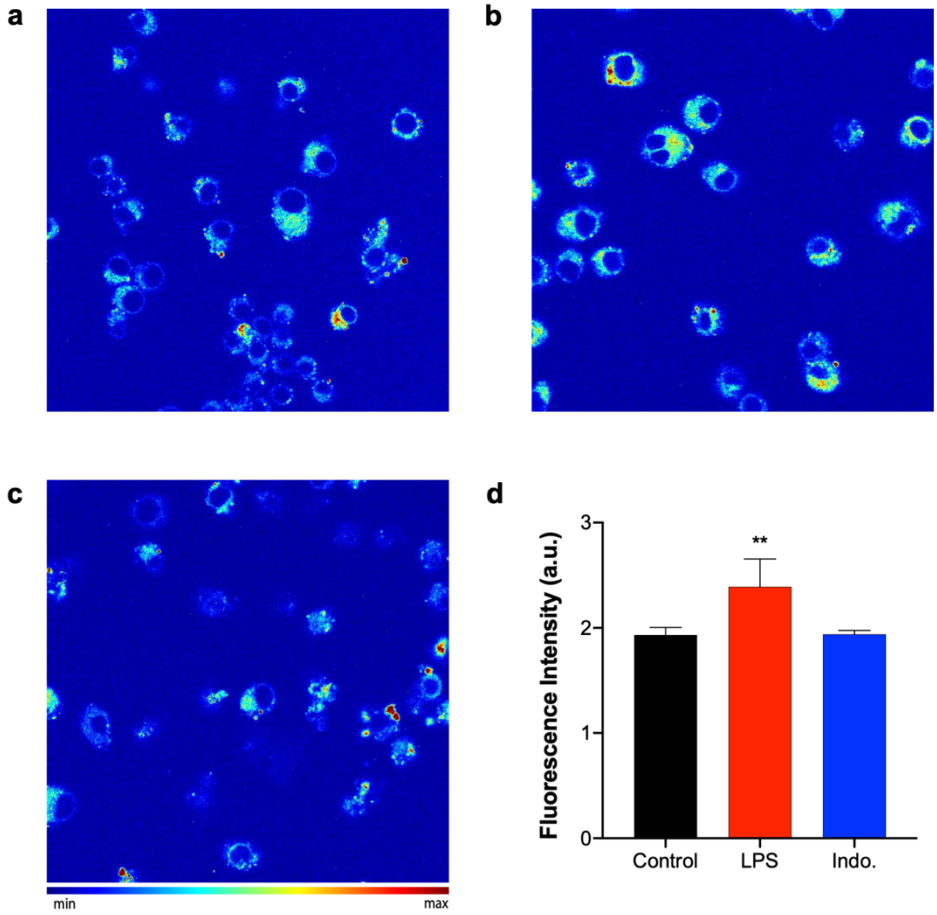

Figure 2.6: Confocal imaging of COX-2 activity in (a) control, (b) LPS-stimulated (1 μg/mL), and (c) indomethacin-treated (Indo., 10 μM), LPS stimulated RAW 264.7 cells after 4 h incubation with CoxFluor (10 μM) at 37 ºC following treatment with BSO (began 19 h prior to staining, 200 μM). Scale bar (white) represents 10 μm. (d) Quantified data. Values are reported as the mean ± standard deviation (n = 3). Statistical analysis was performed using one-way ANOVA ($\alpha = 0.05$). **, $p < 0.01$.

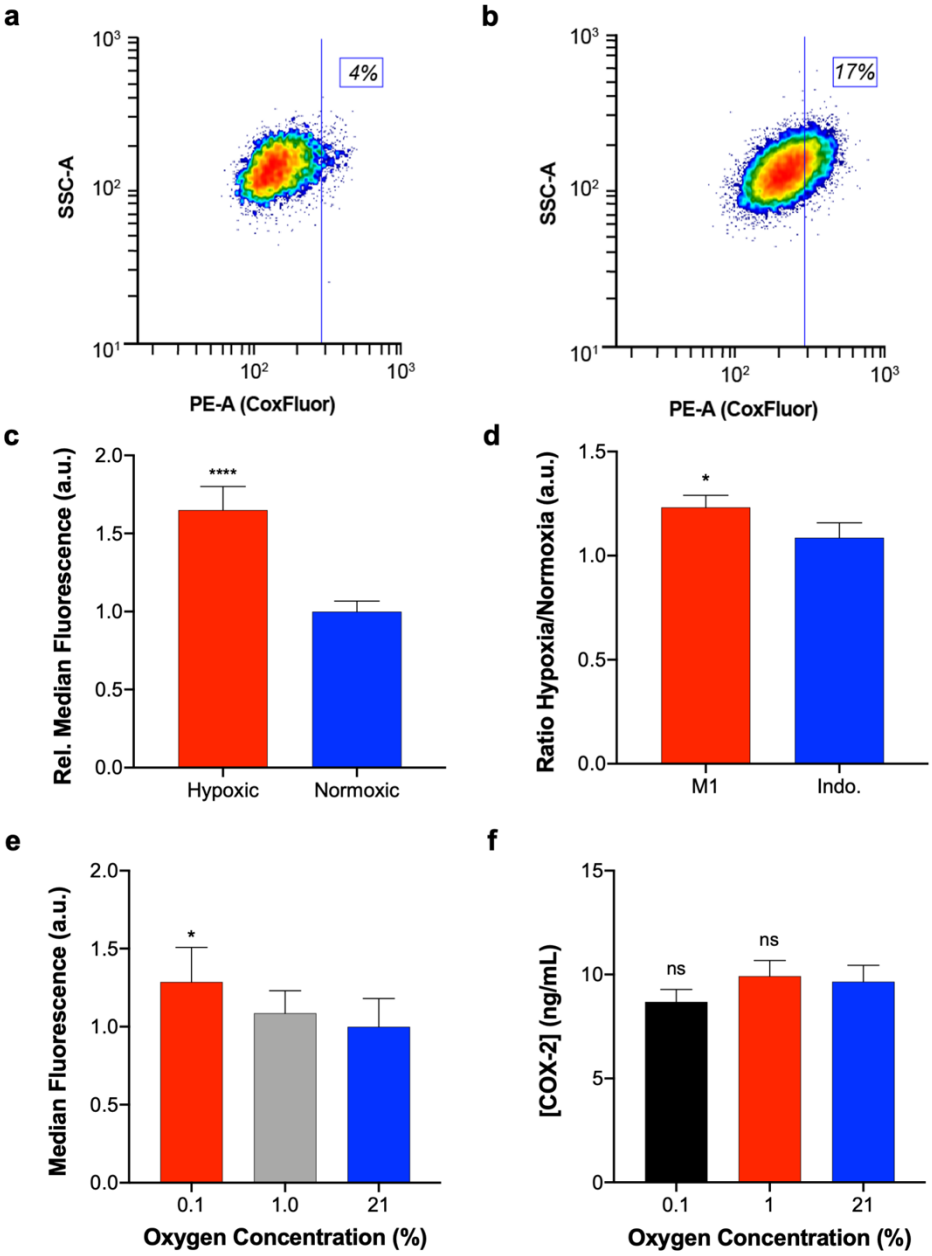

Figure 2.7: Contour plots of flow cytometry data from live LPS-activated RAW 264.7 macrophage cells stained with CoxFluor (10 µM) under (a) normoxic and (b) hypoxic conditions. (c) Quantified median fluorescence for hypoxic and normoxic cells. (d) Effect of indomethacin (20 µM) treatment on the ratio of hypoxic to normoxic median fluorescence. (e) Median fluorescence of RAW 264.7 macrophage cells stained under 0.1% (red), 1.0% (grey), or 21% (blue) oxygen concentrations. (f) ELISA quantification of COX-2 protein expression levels in 25 µg/mL protein lysates. Values are reported as the mean ± propagated standard deviation (n = 6 for flow cytometry data; n = 3 indomethacin inhibition and ELISA data). All staining was performed following treatment with BSO (began 2 h prior to staining, 200 µM) and oxygen dependent flow cytometry data was replicated on two separate days. Statistical analysis was performed with two-tail Student's t test for c, one-tail Student's t test for d, or one-way ANOVA for e (α = 0.05). *, $p < 0.05$, ****, $p < 0.0001$.

Finally, we were interested in asking whether COX-2 activity can be regulated beyond the protein level within the native cellular environment. We hypothesized that oxygen concentrations may influence COX-2 activity because oxygen acts as a substrate but can also bind the heme prosthetic groups in the ferric state, yielding an off-cycle resting state.[99]

The effect of oxygen on COX-2 activity was evaluated in RAW 264.7 macrophage cells after a 19 h activation with LPS. The cells were then stained under normoxic (approximately 21%) or hypoxic conditions (prepared using AneroPack® for < 0.1% oxygen in a sealed container) and the fluorescent response was monitored with flow cytometry. Interestingly, higher activity was observed under hypoxic conditions, as indicated by a substantial shift in the population's median fluorescence (Figure 2.7a–c). This increase in median fluorescence was COX-2-dependent, where indomethacin treatment resulted in a 12% decrease in the ratio of median fluorescence for hypoxic to normoxic M1 macrophages (Figure 2.7d). To confirm the result and evaluate the dose-dependency of oxygen, we repeated the experiment with staining under an atmosphere containing 1 or 0.1% oxygen. Here we observe an oxygen-dependent decrease in COX-2 activity as a function of oxygen (Figure 2.7d–e). This enhanced enzymatic activity was observed without a change in COX-2's protein expression, as measured by ELISA (Figure 2.7f), highlighting the uniqueness of CoxFluor from all previously reported, biocompatible detection strategies.

These results provide strong evidence that the local cellular environment plays a critical role in regulating the activity of COX-2. This emphasizes the importance of measuring enzymatic activity in addition to measuring transcription and translation levels. To the best of our knowledge, this represents the first example in which an ABS approach has revealed activity differences that result from regulation beyond the protein expression levels.

2.5 Summary and outlook

CoxFluor represents the first isoform-selective probe for measuring COX-2 activity in living systems. Strategic utilization of the bulky resorufin precursor and AA tail provided CoxFluor with the requisite selectively for interrogating COX-2 biology in complex mixtures (e.g., in the presence of COX-1), where current inhibitors display imperfect selectivity.[40] This isoform selectivity enables researchers to directly study COX-2 within its native environment and to account for factors beyond transcription and translation that influence enzymatic activity.[100] Along these lines, we report that COX-2 activity can be regulated by oxygen availability within live cells. Taken together, these results suggest that CoxFluor will be a powerful tool for evaluating new therapeutics and for studying COX-2 in live cells.

There a range of applications to investigate moving forward. First, we discovered that high concentrations of CoxFluor induce cytotoxic effects in a COX-2-dependent manner. Specifically, there are cell-type differences in toxicity as measured by the MTT assay after 48 h incubation with CoxFluor: HEK 293T IC_{50} = 24.10 μM (19.90 – 29.67 μM, 95% confidence interval); 4T1 IC_{50} = 14.89 μM (13.67 – 16.24 μM, 95% confidence interval); and MDA-MB231 IC_{50} = 3.235 μM (2.995 – 3.496 μM, 95% confidence interval). The increased potency in breast cancer cells agrees well with the increased expression relative to non-cancerous cell lines.[56,57,101] This is also consistent with previous reports regarding anandamide, the ethanolamine ester of AA, where AA-conjugate metabolism induced toxicity through the production of the downstream prostaglandins or their conjugates.[102,103] The development of selective COX-2 substrates, rather than inhibitors, could serve as a new approach for targeting cancer via COX-2.

Second, it would be interesting to use CoxFluor to screen for COX-2 activity across a panel of cells lines. Normalization of the enzyme activity to protein expression levels could serve to

identify other systems where COX-2 is regulated at or beyond the translational level (e.g., between cancer types or stem cells versus differentiated cells). Along the same lines, one could validate the widespread *in vitro* data regarding allosteric regulation of COX-2 lipids within live cells.[23]

Finally, it is imperative to optimize CoxFluor for non-invasive imaging within living systems. To accomplish this goal, it is necessary to shift the optical properties into the NIR range, as well as overcome the GSH quenching. A reasonable approach for shifting the absorbance would be to increase the electron density within dye. Similar methods have been reported on the xanthene dye platform (e.g., replacement of the endocyclic oxygen or extending the conjugation).[104–107] While neither GSH nor agents for depleting cellular GSH (e.g., NEM or BSO) appear to directly inhibit COX-2 activity, GSH does regulate the resulting product distribution (i.e., increasing the production of 12-hydroxyheptadecatrienoic acid, malondialdehyde, and prostaglandin F2α).[84,108,109] It is important to note that *in vitro* conditions used for monitoring the product distribution do not account for the oxidizing environment within the endoplasmic reticulum[110] and that product distributions are an intrinsic problem with COX activity, in which product distributions are observed even in the absence of GSH.[108] Together, these properties complicate experimental design, favoring protocols where the same cell population is directly compared, as well as limit direct application in live animal models. One approach would be to tune the redox properties of the resorufin dye precursor to outcompete reduction by GSH.

All in all, CoxFluor opens the door for studying activity-based regulation in live cells, proposes the application of COX-2-activatable substrates for targeting cancer, and sets the stage for imaging COX-2 activity in live animals.

2.6 Experimental methods

2.6.1 Materials

Materials were purchased from commercial vendors and used without further purification. All deuterated solvents were purchased from Cambridge Isotope Laboratories. Isoamyl nitrite was purchased from Acros Organic. Disodium ethylenediaminetetraacetate dihydrate (EDTA) was purchased from Alfa Aesar. 13(S)-HpODE, recombinant human 5-lipoxygenase, and methylamine hexamethylene methylamine NONOate (MAHMA-NONOate) was purchased from Cayman Chemicals. Sodium diethyldithiocarbamate trihydrate (DETC) was purchased from Chem-Impex Incorporated. Corning® Supersomes™ Human Monoamine Oxidase A was purchased from Corning Inc. Acetone, ammonium chloride, Mitsubishi™ AnaeroPack™-Anaero Anaerobic gas generator, bovine serum albumin (lyophilized), dichloromethane, dimethyl sulfoxide, glacial acetic acid, oxalyl chloride (Acros), phosphate saline buffer (Corning), sodium bicarbonate, sodium carbonate, sodium chloride, sodium hydroxide, sodium perchlorate (monohydrate), and Triton X-100 were purchased from Thermo Fisher Scientific. Anhydrous methanol, conc. hydrochloric acid, and hydrogen peroxide (30 % v/v) were purchased from Macron Fine Chemicals. Zinc dust was purchased from Mallinckrodt Incorporated. Acetic anhydride, adenosine triphosphate, anhydrous acetonitrile, anhydrous dichloromethane, anhydrous dimethylformamide, arachidic acid, arachidonic acid, β-nicotinamide adenine dinucleotide 2′-phosphate reduced tetrasodium salt hydrate (NADPH), calcium chloride, catalase from bovine liver (lyophilized), celite 545, copper(II) chloride, esterase from porcine liver (lyophilized), formaldehyde (37 % w/w in water), glutathione (reduced), glyoxal (40 % w/w in water), hemin from bovine, hexanes, horseradish peroxidase (type 1), L-ascorbic acid, L-cysteine, L-dehydroascorbic acid, lipopolysaccharides from Escherichia coli O111:B4 (purified by phenol extraction), manganese(II)

chloride, myeloperoxidase from human leukocytes, *p*-nitrophenylacetate, potassium superoxide, propidium iodide, rat liver microsomes (pooled, male), resazurin, sodium acetate, sodium hydrosulfide (hydrate), sodium metal, tris base, and trypan blue powder were purchased from Millipore-Sigma Aldrich. Porcine hematin was purchased from MP Biomedical LLC. 4-dimethylaminopyridine, potassium iodide, and sodium sulfate (anhydrous) were purchased from Oakwood Chemicals. *N*-ethylmaleimide was purchased from Pierce Chemical Company. Celecoxib, indomethacin, phenol, and resorufin were purchased from Tokyo Chemical Industry. L-buthionine-(S,R)-sulfoximine was purchased from Toronto Research Chemicals.

2.6.2 Instruments and software

^{1}H and ^{13}C NMR spectra were acquired on a Varian 500 or Carver B500 spectrometer. The following abbreviations were used to describe coupling constants: singlet (s), doublet (d), triplet (t), or multiplet (m). Spectra were visualized and analyzed using MestReNova (version 10.0) and referenced to trace non-deuterated solvent. High-resolution mass spectra were acquired on a Waters Q-TOF Ultima ESI mass spectrometer or a Waters Synapt G2-Si ESI/LC-MS spectrometer. Ultraviolet-visible spectroscopy was performed on a Cary 60 or NanoDrop 2000 spectrometer. Fluorescence spectra were acquired on a QuantaMaster-400 scanning spectrofluorometer or SpectraMax M2 plate reader. Ultraviolet-visible spectroscopy and fluorimetry were performed with a micro fluorescence quartz cuvette (Science Outlet), sub-mircroquartz fluorimeter cell (Starna Cells, Inc.), or 96-well plates (clear or black with flat bottom, Corning). Refractive indices were measured using an RHB-32ATC Brix Refractometer. A Strathkelvin oxygen electrode was used for measuring cyclooxygenase activity. Cells were visualized on an EVOS FL epifluorescence microscope and cellular imaging was performed using a Zeiss LSM 700 confocal microscope. A Countess® II FL Automated Cell Counter was used for cell viability assays. Flow

cytometry was performed on a BD LSR Fortessa Flow Cytometry Analyzer. Confocal images and flow data were analyzed using ImageJ (NIH)[111] and FCS Express 6.04, respectively. Data were analyzed using Microsoft Excel and GraphPad Prism (version 6.0 or 8.0) and some figures were prepared in Adobe Illustrator (version 22.0.2). Crystallographic figures were prepared using UCSF Chimera or VMD.[112,113]

2.6.3 Synthetic procedures

Thin-layer chromatography (TLC) was performed on glass-backed TLC plates precoated with silica gel containing an UV254 fluorescent indicator (Macherey-Nagel). TLC's were visualized with a 254/365 nm UV hand-held lamp (UVP). Flash silica gel chromatography was performed using 0.04 – 0.063 mm 60 M silica (Macherey-Nagel). All glassware used under anhydrous reaction conditions were flame-dried under vacuum and cooled immediately before use.

10H-phenoxazine-3,7-diyl diacetate (2.2): The compound was prepared according to the previous report by Kodera and coworkers.[67] Briefly, a mixture of resazurin (200. mg, 0.796 mmol, 1 equiv) and zinc dust (240. mg, 3.67 mmol, 4.6 equiv) in glacial acetic acid (6 mL) was stirred at room temperature for 2 h under N_2 atmosphere (in the dark). The reaction was concentrated under inert atmosphere to afford **2.1**, which was immediately dissolved in acetone (4 mL) and treated with DMAP (68.4 mg, 0.560 mmol, 0.7 equiv) and then acetic anhydride (0.16 mL, 1.69 mmol, 2.1 equiv) was added dropwise and stirred under N_2 atmosphere in the dark for 3 h. After completion, the reaction was concentrated and then purified via silica gel chromatography (20% EtOAc/Hexanes) to afford the product as a yellow solid (150. mg, 0.501 mmol, 63% yield). ^{1}H NMR (500 MHz, $CDCl_3$) δ 6.45 (dd, J = 8.4, 2.2 Hz, 2H), 6.39 (d, J = 2.0 Hz, 2H), 6.26 (d, J = 8.4 Hz, 2H), 5.32 (s, 1H), 2.25 (s, 6H). 13C NMR (125 MHz, $CDCl_3$) δ 169.76, 144.59, 142.94,

129.24, 116.25, 113.12, 109.88, 21.02. HRMS $[M+H]^+$ calc'd mass for $C_{16}H_{14}NO_5$ = 300.0872, found = 300.0879.

10-((5Z,8Z,11Z,14Z)-icosa-5,8,11,14-tetraenoyl)-10H-phenoxazine-3,7-diyl diacetate (2.3): A solution of **2.2** (61.2 mg, 0.204 mmol, 1.1 equiv) in anhydrous acetonitrile (1.2 mL) was treated sequentially with Na_2CO_3 (23.6 mg, 0.223 mmol, 1.2 equiv) and then arachidonoyl chloride[114] (60.0 mg, 0.186 mmol, 1 equiv) in anhydrous acetonitrile (1 mL) at 0 ºC. The reaction was allowed to warm to room temperature before potassium iodide (83.3 mg, 0.502 mmol, 2.7 equiv) was added and the mixture was allowed to continue for 5 h under N_2 atmosphere in the dark. Once complete, the reaction was filtered, washed with EtOAc (3×), concentrated and purified by silica gel chromatography (90% CH_2Cl_2/Hexanes) to obtain the product as an orange solid (53.3 mg, 0.091 mmol, 49% yield). ^{1}H NMR (500 MHz, $CDCl_3$) δ 7.44 (d, *J* = 8.7 Hz, 2H), 6.95 – 6.85 (m, 4H), 5.45 – 5.25 (m, 8H), 2.84 – 2.73 (m, 6H), 2.59 (t, *J* = 7.4 Hz, 2H), 2.30 (s, 6H), 2.07 (dq, *J* = 21.7, 7.3 Hz, 4H), 1.75 (q, *J* = 7.4 Hz, 2H), 1.39 – 1.26 (m, 6H), 0.88 (t, *J* = 6.8 Hz, 3H). ^{13}C NMR (125 MHz, $CDCl_3$) δ 171.84, 168.98, 151.18, 148.79, 130.42, 128.93, 128.85, 128.49, 128.12, 128.09, 127.82, 127.49, 126.74, 125.42, 116.62, 110.80, 33.39, 31.46, 29.27, 27.16, 26.42, 25.58, 25.57, 25.53, 24.90, 22.52, 21.02, 14.03. HRMS $[M+H]^+$ calc'd mass for $C_{36}H_{44}NO_6$ = 586.3169, found = 586.3180.

CoxFluor: A solution of **2.3** (50. mg, 0.085 mmol, 1 equiv) in anhydrous MeOH (3 mL) was treated with Na (2 mg, 0.087 mmol, 1 equiv) at 0 ºC and the reaction was allowed to continue at the same temperature for 0.5 h. When complete, the reaction was treated with aq. satd. $NaHCO_3$ and extracted with EtOAc (3×). The organic layer was dried over anhydrous sodium sulfate and purified by silica gel chromatography (1% MeOH/CH_2Cl_2) to afford the product as an off-white solid (29.2 mg, 58.2 μmol, 68% yield). ^{1}H NMR (500 MHz, CD_3OD) δ 7.88 (s, 2H), 7.28 (d, *J* =

8.8 Hz, 2H), 6.59 – 6.55 (m, 4H), 5.39 – 5.24 (m, 8H), 2.80 (q, *J* = 5.4 Hz, 4H), 2.74 (t, *J* = 6.7 Hz, 2H), 2.60 (t, *J* = 7.3 Hz, 2H), 2.04 (dt, *J* = 11.7, 5.8 Hz, 4H), 1.66 (q, *J* = 7.3 Hz, 2H), 1.38 – 1.29 (m, 6H), 0.88 (t, *J* = 7.0 Hz, 3H). ^{13}C NMR (125 MHz, $CDCl_3$) δ 173.29, 154.95, 151.90, 130.52, 128.96, 128.84, 128.55, 128.15, 127.87, 127.52, 125.64, 121.95, 110.44, 104.29, 33.36, 31.49, 29.69, 29.30, 27.20, 26.51, 25.62, 25.59, 25.55, 25.02, 22.56, 14.07. HRMS $[M+H]^+$ calc'd mass for $C_{32}H_{40}NO_4$ = 502.2957, found = 502.2943.

Arachidoyl Chloride: The material was prepared in an identical manner to arachidonoyl chloride and according to a previously reported protocol.[114] Briefly, arachidic acid (50 mg, 0.160 mmol, 1.0 equiv) was dissolved in anhydrous CH_2Cl_2 (1 mL) and anhydrous DMF (30 μL) and placed under N_2 atmosphere. The solution was cooled to -5 °C in an ammonium chloride ice bath before oxalyl chloride (28 μL, 0.326 mmol, 2.0 equiv) in anhydrous CH_2Cl_2 (200 μL) was added. The reaction was maintained at the same temperature for 4 h and then allowed to sit at -20 °C overnight. The reaction was complete according to crude NMR and then it was concentrated. The residue was purified by dissolving in anhydrous hexanes, filtering, and re-concentrating the filtrate. The material was used without further purification.

10-icosanoyl-10H-phenoxazine-3,7-diyl diacetate (2.4): 2.2 (49.7 mg, 0.166 mmol, 1.1 equiv) in anhydrous acetonitrile (3 mL) was cooled to 0 °C and treated with Na_2CO_3 (19.2 mg, 0.181 mmol, 1.2 eq). A solution of arachidoyl chloride (50. mg, 0.151 mmol, 1 equiv) in anhydrous acetonitrile (3 mL) was added dropwise and allowed to warm to room temperature. Next, potassium iodide (124 mg, 0.747 mmol, 4.9 eq) was added and the mixture was allowed to stir at room temperature for 5 h under N_2 atmosphere in the dark. Once complete, the reaction was filtered, washed with EtOAc (3×), concentrated and purified by silica gel chromatography (90% CH_2Cl_2/Hexanes) to obtain the product as a white solid (50.0 mg, 84.2 μmol, 55% yield). ^{1}H NMR

(500 MHz, $CDCl_3$) δ 7.45 (d, *J* = 8.6 Hz, 2H), 6.94 – 6.85 (m, 4H), 2.57 (t, *J* = 7.5 Hz, 2H), 2.30 (s, 6H), 1.64 (q, *J* = 7.3 Hz, 2H), 1.24 (m, 32H), 0.88 (t, *J* = 6.8 Hz, 3H). ^{13}C NMR (125 MHz, $CDCl_3$) δ 172.20, 169.05, 151.24, 148.78, 126.87, 125.45, 116.65, 110.81, 34.06, 31.91, 29.69, 29.66, 29.63, 29.57, 29.42, 29.38, 29.35, 29.15, 25.30, 22.68, 21.06, 14.12. HRMS $[M + H]^+$ calculated mass for $C_{36}H_{52}NO_6$ = 594.3795, found = 594.3806.

Ctrl-CoxFluor: To a suspension of **2.4** (40. mg, 0.067 mmol, 1eq) in dry MeOH (3 mL) at 0 ºC was added Na (2 mg, 0.087 mmol, 1.3 equiv) and the reaction was stirred for 0.5 h. After completion, the reaction was treated with aq. satd. $NaHCO_3$ and extracted with EtOAc (3×). The organic layer was concentrated and purified by silica gel chromatography (1% MeOH/CH_2Cl_2) to afford the product as a white solid (25 mg, 49 μmol, 73% yield). ^{1}H NMR (500 MHz, $CDCl_3$) δ 7.17 (d, *J* = 7.5 Hz, 2H), 6.58 – 6.43 (m, 4H), 2.47 (t, *J* = 7.5 Hz, 2H), 1.53 (q, *J* = 7.2, 6.7 Hz, 2H), 1.17 (d, *J* = 13.3 Hz, 32H), 0.81 (t, *J* = 6.9 Hz, 3H). ^{13}C NMR (125 MHz, $(CD_3)_2CO$) δ 172.85, 157.04, 152.83, 126.86, 122.80, 110.85, 104.21, 34.34, 32.65, 30.40, 30.37, 30.22, 30.09, 29.84, 25.96, 23.34, 14.36. HRMS $[M+H]^+$ calc'd mass for $C_{32}H_{48}NO_4$ = 510.3583, found = 510.3583.

2.6.4 Photophysical characterization

Extinction coefficients and fluorescence quantum yields were acquired (*n* = 3) and reported as the average with a relative standard deviation less than 15%. Extinction coefficients were acquired by titrating compound in 100 mM Tris-HCl (pH 8.0) within the linear range. Fluorescence quantum yields were obtained using the modified method for relative fluorescence quantum yield.[115] Dye was titrated into the solution and the absorbance and emission were monitored (excitation at 540 nm). The absorbance was maintained below 0.1 to limit secondary absorbance events. Total emission spectra were integrated, and the relative quantum yield was calculated

relative to Rhodamine B (ϕ = 0.70, ethanol).[116] The refractive index of 100 mM Tris-HCl (pH 8.0) was measured to be 1.33514.

2.6.5 Protein expression and purification

Human COX-2-His_6 was expressed[82,117] and purified according to previously reported protocols.[118] The purification of COX-1 was carried out based on previous protocols with minor modifications.[119,120] Bovine seminal vesicles (~25 g) were obtained from a butcher (Arends Farms Meats and Butcher Shop, Ivesdale, IL) and were mechanically homogenized using a Bio-homogenizer 2-speed (Model no. M133/1281-0) in 50 mL buffer A (50 mM Tris-HCl, 5 mM EDTA, 5 mM DETC, 1 mM phenol, pH 8.0). Note that all centrifugation was performed at 4 °C on a Sorvall RC 6+ centrifuge with a Fiberlite F21 8x50 y rotor for less than 10,000 rpm and Sorvall WX Ultra 80 with a SureSpin 630 rotor equipped with a swinging bucket for more than 10,000 rpm. Once homogenized, cellular debris was removed via centrifugation at 9,500 rpm for 15 minutes. The supernatant was collected and centrifuged at 30,000 rpm for 1 h to obtain the microsomal pellet containing COX-1. This pellet was resuspended in 50 mL buffer B (50 mM Tris-HCl, 1 mM EDTA, 0.1 mM $NaClO_4$, 0.1 mM DETC, 0.5 mM phenol, pH 8.0), using a homogenizer, before centrifugation at 30,000 rpm for 1 h. The corresponding pellet was resuspended in 50 mL buffer C (50 mM Tris-HCl, 1 mM EDTA, 1 mM phenol, pH 8.0), 10% Triton X-100 was added dropwise with stirring until a final concentration of 1% (v/v) was obtained, and the resulting solution was allowed to stir for 1 h at 4 °C. A final centrifugation at 30,000 rpm was performed for 1 h before the supernatant was loaded onto a DEAE-Sepharose column (GoldBio) that was previously equilibrated with buffer C. The column was washed with 40 mL buffer C and then COX-1 was eluted using a stepwise NaCl gradient prepared from different ratios of buffer C to buffer D (50 mM Tris-HCl, 1 mM EDTA, 1 mM phenol, 400 mM NaCl, pH

8.0). Specifically, the column was washed with sequential 40 mL portions at each concentration (90% buffer C – 0% buffer C in 10% steps). A Bradford assay (Thermo Scientific) was used to determine which fractions contained eluted protein; these fractions were concentrated and frozen after the addition of glycerol (10% v/v final). Porcine hematin (1 mM) was titrated into concentrated protein until λ_{407} stabilized at a maximum. Human CYP2J2 cDNA was obtained from OriGene (Catalog No. SC321730) and N-terminally modified.[121] This truncated M2D34G-CYP2J2 was expressed and purified via Ni-NTA chromatography (GoldBio) as previously published.[121–123] Full length *R. norvegicus* cytochrome P450 reductase (CPR) was expressed and purified via ADP-agarose chromatography (GoldBio) following previously published protocols.[124] Protein concentration for COX-1 and COX-2 (MW = 140 kDa). were determined using the bicinchoninic acid assay (BCA Assay, Thermo Fisher Scientific) relative to a bovine serum albumin standard according to the manufacturer's protocol. The molecular weights for all proteins were calculated using the ExPASy tool.[125] CYP2J2 (MW = 57 kDa, ε = 110 $mM^{-1}cm^{-1}$ at λ = 417 nm) and CPR (MW = 77 kDa, ε = 21.4 $mM^{-1}cm^{-1}$ at λ = 454 nm) were quantified spectroscopically using their Soret absorbance.

2.6.6 Fluorimeter fluorescence assay

The fluorescence assays were performed in microquartz cuvettes or submicroquartz cuvettes with a maximum volume of 600 µL. Reactions were monitored at room temperature using 540 nm excitation and emission was collected from 550 – 700 nm with a slit width of 1.25 mm. Total volumes of the reaction mixtures were maintained at 570 µL. To 100 mM Tris-HCl buffer (480 µL, pH 8.0) was added hemin (30 µL, 19 µM in 4% DMSO in 100 mM Tris-HCl, pH 8.0), COX-2 (30 µL, 4.75 µM 100 mM Tris-HCl, pH 8.0) and the reaction was initiated with CoxFluor (30 µL, 190 µM 10% DMSO in 100 mM Tris-HCl, pH 8.0). Final reaction concentrations were 1

μM hemin, 250 nM COX-2 and 10 μM CoxFluor in 100 mM Tris-HCl with 1.26% DMSO (v/v). Experiments in the presence of reduced GSH were conducted according to the same procedure, but GSH (30 μL, 19 mM in 100 mM Tris-HCl, pH 8.0) was added before the addition of CoxFluor for a final concentration of 1 mM. Assays performed in submicroquartz cuvettes were performed maintaining the same ratios, but with a final volume of 142.5 μL.

2.6.7 Plate reader fluorescence assay

The fluorescence assays were performed at room temperature using 540 nm excitation and 590 nm emission. Total volume of the reaction mixture was maintained at 190 μL. To 100 mM Tris-HCl buffer (160 μL, pH 8.0) was added hemin (10 μL, 3.8 μM in 4% DMSO in 100 mM Tris-HCl, pH 8.0), COX-2 (10 μL, 950 nM in 100 mM Tris-HCl buffer, pH 8.0) and the reaction was initiated with CoxFluor (10 μL, 190 μM in 10% DMSO in 100 mM Tris-HCl, pH 8.0). Final reaction concentrations were 200 nM hemin, 50 nM COX-2 and 10 μM CoxFluor in 100 mM Tris-HCl with 1.26% DMSO (v/v). Inhibition assays were performed according to the same procedure, but COX-2 was preincubated with hemin and inhibitor for 0.5 h at 0 °C before initiation with CoxFluor. Relative fluorescence enhancement is calculated by comparing to a buffer control with 10 μM CoxFluor.

2.6.8 Enzyme selectivity

Enzyme activity was defined as the amount substrate (μmol) consumed during one minute by one milligram of enzyme in 100 mM Tris-HCl at pH 8.0 under saturating conditions. Enzyme concentrations were measured using the BCA assay (Thermo Fisher Scientific) according to the published protocol with bovine serum albumin for the standard curve. COX-1 and COX-2 cyclooxygenase activities were measured using Strathkelvin oxygen electrode with arachidonic acid (200 μM). The oxygen electrode was calibrated using 1% sodium sulfite for 0% oxygen and

atmosphere equilibrated 100 mM Tris-HCl at pH 8.0 for 100% oxygen. The reaction was monitored at 37 ºC in a glass chamber with a total reaction volume of 1 mL. Hemin (5 μM), phenol (1 mM), and COX (2 μg) were added to atmosphere equilibrated buffer and then the reaction was initiated with AA (200 μM). Porcine esterase activity was measured spectroscopically at 405 nm using *p*-nitrophenyl acetate (1.5 mM) as the substrate. Bovine catalase activity was measured using a discontinuous Amplex® Red-horseradish peroxidase assay to quantify the amount of hydrogen peroxide (initially 31.25 μM) remaining after 0.5 h incubation with excitation at 540 nm and emission at 590 nm. CYP2J2 activity was measured spectroscopically at 340 nm using cytochrome P reductase (3-fold excess), NADPH (1 mM), and arachidonic acid (70 μM) as the substrate. Rat liver microsome selectivity was performed at concentrations ranging from 12.5 μg/mL to 200 μg/mL and the largest turn-on was reported. Horseradish peroxidase activity was measured using hydrogen peroxide (31.25 μM) and Amplex® Red (50 μM) as the substrates with excitation at 540 nm and emission at 590 nm. Myeloperoxidase selectivity was measured using the manufacturer's conditions (50 mM sodium acetate, pH 6.0, 100 mM NaCl) because the lysosomal enzyme is inactive at pH 8.0. Selectivity was assessed using 10-fold excess protein (350 μg/mL) and the solution was brought to a pH of 8.0 after 4 h with 0.5 M aq. NaOH prior to measurement. Monoamine oxidase A selectivity was assessed using human supersomes with 10-fold excess protein (350 μg/mL) under the standard COX conditions. 5-lipoxygenase selectivity was performed using the manufacturer's protocol and reported activity. Specifically, the active recombinant human protein in the insect cell lysate was diluted for a final activity of 1.01 U in 50 mM Tris-HCl buffer (pH 7.5) containing 2 mM $CaCl_2$, 1 mM ATP, and 4.6 μM 13(S)-HpODE. Prior to measuring the fluorescence, the solution was titrated with 0.5 M aq. NaOH for a pH 8.0. When measured, all enzyme activities were confirmed to be under saturating conditions and within

the first 20% of the reaction. The selectivity of CoxFluor (10 μM) was monitored after incubation with either 0.101 U COX-2 or 1.01 U of the other enzymes, unless noted otherwise above, in 100 mM Tris-HCl buffer at pH 8.0 using the plate reader with excitation at 540 nm and emission at 590 nm. Total reaction volume was maintained at 95 μL with a final DMSO concentration of 1.26% (v/v). Relative fluorescence enhancement is calculated by comparing to a buffer control containing 10 μM CoxFluor.

2.6.9 Analyte selectivity

Response of CoxFluor (10 μM) to a variety of reactive oxygen, nitrogen, carbonyl, metals and sulfur species (1, 3, 5, or 50 equiv) were monitored using the plate reader assay. Total volume of the reaction mixture was maintained at 190 μL in 100 mM Tris-HCl buffer (pH 8.0) with a final DMSO concentration of 1.26% (v/v). Assays for CoxFluor or resorufin were initiated by the addition of the analytes and the reactions were incubated at room temperature for up to 4 h. Measurements were recorded at a range of time points, and the relative turn-on was determined relative to a buffer control containing 10 μM CoxFluor or resorufin. Superoxide anion was added as a solution of potassium superoxide in DMSO. Nitroxyl was generated *in situ* from a solution of Angeli's salt in degassed 10 mM potassium hydroxide solution. Angeli's salt was prepared according to previously reported literature.[126] NO was generated *in situ* from a solution of MAHMA-NONOate in degassed 10 mM potassium hydroxide. Peroxynitrite was prepared according to previously reported literature.[127] All metals were prepared from their chloride salt. Formaldehyde solutions were prepared by depolymerizing saturated aqueous solutions at 100 ºC before use. Dehydroascorbic acid was prepared by dissolving the solid at 65 ºC in water before cooling to room temperature for use. All other analytes were prepared by dilution or dissolution from commercially available sources.

2.6.10 Structure preparation for molecular dynamics simulations and ensemble molecular docking

The preferential binding of CoxFluor to COX-2 over COX-1 was probed using ensemble docking and molecular dynamics techniques. The structure of sheep COX-1 (PDB 5U6X)[75] and human COX-2 (PDB 5KIR)[76] were obtained from X-ray diffraction data. Before simulations, all non-heme cofactors were removed; the heme bound cobalt in COX-2 was replaced with an iron; cysteine bridges and the iron histidine were patched and preserved using PSFGEN; and the coordinates and topology for missing hydrogens were predicted using PSFGEN. To validate the selected structures, we calculated root mean squared deviation (RMSD) for 5U6X and 5KIR versus a myriad of resolved structures using SuperPose (Tables S1-2).[128] Additional information can be found in Appendix B.

2.6.11 Equilibrium molecular dynamics simulations of COX-1 and COX-2

Parameters and protocols for simulations were followed according to literature precedence with minor modifications.[129,130] Molecular dynamics simulations were performed using NAMD 2.12[131] with the CHARMM36m force field.[132] Constant temperature and pressure were maintained using Langevin dynamics and Langevin piston Nosé−Hoover methods[133,134] at 310 K and 1 atmosphere, respectively. The particle mesh Ewald (PME) method was used to calculate long-range electrostatic forces[135,136] using a 1 Å grid spacing. The van der Waals interactions were evaluated with a cutoff of 12 Å, with a force-based switching scheme after 10 Å. A 2 fs integration time step was applied with the SETTLE algorithm.[137] VMD 1.9.3 was used for visualization and analysis.[113] Both COX-1 and COX-2 were first equilibrated for 10 ns with the entire protein restrained (1.0 kcal/mol/Å^2) to allow for solvation of the protein, followed by progressively decreasing harmonic restraints over the course of 10 ns on protein Cα atoms (2.5 ns at 1.0

kcal/mol/Å^2, 2.5 ns at 0.75 kcal/mol/Å^2, 2.5 ns at 0.50 kcal/mol/Å^2, 2.5 ns at 0.25 kcal/mol/Å^2). This was followed by 200 ns production simulation without restraints. RMSD was calculated using MDAnalysis[138,139] for the simulation trajectories against AA bound crystal structures of COX-1 (PDB 1DIY)[140] and COX-2 (PDB 3HS5)[82] to confirm no major deviations. Additional information can be found in Appendix B.

2.6.12 Ensemble molecular docking

Ensemble docking of CoxFluor to COX-1 and COX-2 was performed using AutoDock Vina.[78] The previously discussed simulations were used to sample the dynamics of COX-1 and COX-2 for docking. Because both COX-1 and COX-2 are homodimers in the crystallographic state it was possible to double the sampling time by overlaying the monomers throughout the docking process for a total of 400 ns sampling time (200 ns sampling time for docking to each monomer). For each snapshot, a 26 × 26 × 26 Å^3 cube containing both the cyclooxygenase and peroxidase active sites was used to fully sample the suspected binding sites. Each snapshot was docked with an exhaustiveness of 10, yielding a maximum of 4000 docked poses. These poses where then characterized based on location and binding affinities. To determine the location of the binding, poses were grouped based off of their proximity to the iron, within the heme, where greater than 8 Å was defined as cyclooxygenase binding (confirmed that this cutoff was consistent with structural understanding of the protein). The same protocol for docking was implemented for the CoxFluor-PGG$_2$ intermediate. Docking within the cyclooxygenase site was performed within a 22 × 22 × 22 Å^3 cube using the same protocol where the box only included the cyclooxygenase active site. Using the VMD plugin Multiseq,[141] a STAMP structural alignment was done on 5U6X and 1DIY, as well as on 5KIR and 3HS5 to identify relevant AA positions in COX-1 and COX-2

respectively, followed by visualization in PYMOL (Version 1.7.0.0; Schrodinger, LLC). Additional information can be found in Appendix B.

2.6.13 CoxFluor, Ctrl-CoxFluor & resorufin stability assays

Stability assays were performed for a 10 μM solution of each compound in a series of buffers/solvents (100 mM Tris-HCl at pH 8.0, DMEM with 10% FBS, DMEM without serum and DMSO). Stability was assessed at room temperature or at 37 °C and in the presence or absence of ambient light. Fluorescence was measured using the plate reader with excitation at 540 nm and emission from 560 – 700 nm and the relative turn-on was determined by the change of fluorescence intensity at 590 nm.

2.6.14 Cell culture

HEK 293T and RAW 264.7 macrophage cells were acquired from ATCC and Prof. Elvira de Mejia (Food Science and Human Nutrition, UIUC), respectively. Cells were cultured in phenol-red free Dulbecco's modified eagle medium (DMEM, Corning) supplemented with 10% fetal bovine serum (FBS, Sigma Aldrich), and 1% penicillin/streptomycin (Corning). Incubation with 0.25% trypsin containing EDTA and phenol red (Gibco™, Fisher Scientific) or manual scrapping is used for passaging for HEK 293T and RAW 264.7 macrophage cells, respectively. Cells were incubated at 37 °C with 5% CO_2. Experiments were performed in 4-well chambered cover glasses (Lab-Tek, Thermo Scientific), 96-well plates (Nunc, Thermo Scientific), or 6-well plates (BioLite, Thermo Scientific).

2.6.15 Trypan blue exclusion cytotoxicity assay

6-well plates were seeded with 300,000 cells per well (2 mL of 150,000 cells/mL) and incubated at 37 °C with 5% CO_2 for 48 to 72 h (~60–80% confluent). Media was removed and replaced with either 5, 10, or 25 μM CoxFluor in fresh serum-free DMEM media (1.25% DMSO

v/v final concentration). After 6 h the media was removed, and cells were trypsinized with 200 µL 0.25% trypsin-EDTA for less than 5 minutes at 37 °C. The trypsin was quenched with the addition of 1.8 mL DMEM media containing 10% FBS and the cells were mixed thoroughly before diluting 1:1 with trypan blue (0.4% in PBS w/v). Percent viability was measured using a Countess® II FL Automated Cell Counter (Thermo Fisher Scientific), where the parameters were optimized to identify live and dead cells. Viability was calculated by the relative to the vehicle control.

2.6.16 MTT cytotoxicity assay

96-well plates were seeded with 20,000 cells per well (200 µL of 100,000 cells/mL, RAW 264.7 macrophage) or 25,000 cells per well (200 µL of 125,000 cells/mL, HEK 293T cells) and incubated at 37 °C with 5% CO_2 for 72 h (~90% confluent). Media was removed and fresh serum-free DMEM media containing 0, 5, 10, or 25 µM CoxFluor (1.25% DMSO final v/v) was added. The media was removed at various time points (3 or 6 h) and replaced with 200 µL 20:1 mixture of FBS-free DMEM and (3- (4,5-dimethylthiazol-2-yl)-2,5-diphenyl-tetrazolium bromide (MTT, 5 mg/mL stock in PBS). The cells were incubated for 4 h under the same conditions and then the medium was removed and replaced with DMSO (200 µL/well). The absorbance of each well was recorded after a 1:5 dilution in DMSO at 555 nm on a microplate reader. Viability was calculated by the absorbance relative to the vehicle control.

2.6.17 HEK 293T transfection with human COX-2

The plasmid containing human COX-2 (pcDNA3.1-hPTGS2-2flag) was purchased from Addgene (Catalog# 102498, deposited by Prof. Jun Yu, The Chinese University of Hong Kong).[32] The plasmid was isolated from a single colony that was grown to turbidity overnight at 37 °C in Luria broth (LB) media with 100 µg/mL ampicillin (5 mL) using the GeneJET plasmid Miniprep (Thermo Scientific) according to the manufacturer's protocol (the plasmid was eluted with Milli-

Q water rather than the elution buffer). Plasmid concentration was determined using the absorbance at 260 nm on a NanoDrop 2000 spectrometer. Prior to plating onto 4-well chambered cover glasses, the surface exposed substrate was coated with R&D Systems™ Cultrex Poly-L-Lysine (Fisher Scientific) according to the manufacturer's protocol (allowed to dry > 3 h). Plates were seeded with 175,000 cells per well (500 µL of 350,000 cells/mL in DMEM media supplemented with 10% FBS) and allowed the cells to incubate for 40 h at 37 °C with 5% CO_2 (60–70% confluent). Transfections was performed using Lipofectamine 3000 (Thermo Fisher Scientific) according to the manufacturer's protocol. Briefly, 180 µL of transfection master mix was prepared by a 1:1 dilution of lipofectamine 3000 reagent (5.4 µL in 90 µL Opti-MEM™ Reduced Serum Media) and DNA complexed to P3000 reagent (1,800 ng plasmid with 3.6 µL P3000 in Opti-MEM™ Reduced Serum Media) and the master mix was allowed to incubate at room temperature for 5 to 10 minutes. Media was removed from each well and replaced with 500 µL Opti-MEM™ Reduced Serum Media followed by the addition of 20 µL transfection master mix. After 48 h incubation at 37 °C with 5% CO_2 (~90–100% confluent) the cells were subjected to experimental conditions for imaging.

2.6.18 Confocal fluorescence live-cell imaging of human COX-2 transfected HEK 293T cells

Transfections were performed using the Lipofectamine 3000 reagent according to the aforementioned protocol. Control wells were treated the same as the transfected wells without the addition of the transfection master mix. The media was removed from each well and replaced with serum-free DMEM media containing 10 µM CoxFluor or 10 µM CoxFluor with 10 µM indomethacin (1% DMSO final concentration). Cells were incubated at 37 °C with 5% CO_2 before imaging with excitation at 555 nm and emission collected from 565–700 nm. Each well was imaged using a Zeiss LSM 700 confocal microscope (n = 3 technical replicates; n = 4 biological

replicates). For GSH knockdown experiments, the initial media change was performed with 1 mM NEM (0.1 % DMSO final concentration) in serum-free DMEM media and the cells were allowed to incubate for 30 minutes before proceeding to the staining with CoxFluor. Images were quantified over the entire imaging window, without any processing, using ImageJ (v. 1.51, NIH). All publication images were processed using identical parameters and false colored (LUT: jet.lut) in ImageJ.[111]

2.6.19 RAW 264.7 macrophage activity assays

6-well plates were seeded with 250,000 cells per well (2.0 mL of 125,000 cells/mL) and the cells were allowed to incubate at 37 °C with 5 % CO_2 for 72 h (~70–80% confluent). The media was removed and replaced with serum-free DMEM (1.98 mL). Lipopolysaccharide was added in PBS (20 µL 100 µg/mL for final concentration of 1 µg/mL) at 2, 4, 6, 8, 10, 19, and 24 h (n = 3 biological replicates) prior to lysis. Control wells were prepared by adding PBS without LPS at the 24 h time point. The media was removed, and the cells were lysed by adding CelLytic M (200 µL, Millipore-Sigma) and mixing for 15 minutes at room temperature. The solution was mixed well via pipette followed by vortex for 10 seconds. Cellular debris was removed by centrifugation using a Fisher Scientific accuSpin Micro 17R centrifuge at 6,000 rpm for 10 minutes (4 °C). The samples were stored at 4 °C and activity was measured immediately. Activity was measured according to a modified fluorimeter assay with excitation at 540 nm, emission at 590 nm, and slit width of 0.8 mm. Specifically, to a solution of 888 µL 100 mM Tris-HCl buffer (pH 8.0) and 100 µL lysate was added 10 µL 100 mM *N*-ethylmaleimide (1 mM final concentration) and the solution was allowed to incubate at room temperature for 1 minute. The reaction was initiated with 2 µL 2 mM CoxFluor (4 µM final concentration, 1.2% DMSO final) and the kinetics were monitored over 2 minutes. Rates were measured within the linear region (usually the first 30 seconds after initiating

the reaction). A calibration curve was constructed with resorufin in buffer containing 1 mM *N*-ethylmaleimide, 10% CelLytic M, and a final DMSO concentration of 1.2%. Total protein concentration was measured using the BCA assay (Thermo Fisher Scientific) to calculate COX-2's specific activity.

2.6.20 Confocal fluorescence live-cell imaging of lipopolysaccharide-activated RAW 264.7 macrophages

The surface exposed substrate of 4-well chambered cover glasses was coated with R&D Systems™ Cultrex Poly-L-Lysine (Fisher Scientific) using the manufacturer's protocol. Plates were seeded with 180,000 cells per well (500 µL of 360,000 cells/mL in DMEM media supplemented with 10% FBS) and were allowed to incubate for 38 h at 37 °C with 5% CO_2 (70–80% confluent). The media was removed and replaced with serum-free DMEM media containing 0.2 mM BSO and either PBS or 1 µg/mL lipopolysaccharide in PBS (500 µL final volume). The cells were incubated under these conditions for 17 h at 37 °C with 5% CO_2. Next, the media was replaced with the same conditions with or without indomethacin (10 µM) for 2 h at 37 °C with 5% CO_2 (500 µL final volume containing 0.2% DMSO final concentration). Finally, the cells were stained under identical conditions supplemented with 10 µM CoxFluor (500 µL final volume containing 1.5% DMSO final concentration). After incubation at 37 °C with 5 % CO_2 for 4 h, each well was imaged using a Zeiss LSM 700 confocal microscope (n = 3 technical replicates; n = 4 biological replicates). Images were quantified over the entire imaging window, without any processing, using ImageJ (v. 1.51, NIH). All publication images were processed using identical parameters and false colored (LUT: jet.lut) in ImageJ.[111]

2.6.21 Flow cytometry of lipopolysaccharide-induced COX-2 expression in RAW 264.7 macrophages

RAW 264.7 macrophage cells (300,000 cells, 2 mL of 150,000 cells/mL) were seeded into 6-well plates and incubated for 48 to 72 h under standard conditions for a final confluency of ~60–80%. The media was removed and replaced with serum-free DMEM (1.98 mL) followed by LPS (1 μg/mL final concentration, 20 μL of 100 μg/mL in PBS) at 4 or 19 h before collection. Cellular GSH was depleted 2 h prior to collection via treatment with BSO (0.2 mM final concentration, 40 μL 10 mM solution in 1:1 DMSO: serum-free DMEM, 1% DMSO final concentration). Cells were collected by treatment with 0.5 mL 0.25% trypsin-EDTA for less than 5 minutes at 37 ºC and then the trypsin was inactivated with 1.0 mL DMEM media containing 10% FBS. The solution was partitioned for two samples, which were subsequently collected via centrifugation at 6,000 rpm at 4 ºC in 1.6 mL Eppendorf tubes. The media was removed, and cells were resuspended in 0.2 mM BSO either with or without 10 μM CoxFluor (1 mL, 1.5% DMSO final concentration in serum-free DMEM) for 90 minutes at 37 ºC with agitation. When performing inhibition studies, the aforementioned staining solutions were prepared with 20 μM indomethacin without affecting the final concentration of DMSO. After staining, cells were pelleted using the aforementioned procedure and were resuspended in PBS. Samples were stored on ice prior to analysis on a BD LSR Fortessa Flow Cytometry Analyzer with 561 nm excitation and 582/15 emission bandpass filter. Dead cells were excluded from the analysis by staining samples (~300 μL) with propidium iodide (1 μL of 1 mg/mL in deionized water) for 5 to 10 minutes at room temperature before analysis with 561 nm excitation and 595 nm longpass dichromic mirror and 610/20 emission bandpass filter. Data was gated for cells according to side and forward scatter areas, live cells using

the forward scatter area versus PE-Texas Red area, and for single cell events using the forward scatter width versus side scatter area. Replicate numbers correspond to biological replicates.

2.6.22 Flow cytometry measurement of COX-2 activity in RAW 264.7 macrophages under AneroPack® hypoxic conditions

RAW 264.7 macrophage cells (300,000 cells, 2 mL of 150,000 cells/mL) were seeded into 6-well plates and incubated for 48 to 72 h under standard conditions for a final confluency of ~60–80%. The media was removed and replaced with serum-free DMEM (1.98 mL) followed by LPS (1 μg/mL final concentration, 20 μL of 100 μg/mL in PBS) 19 h before collection. Cellular GSH was depleted 2 h prior to collection via treatment with BSO (0.2 mM final concentration, 40 μL 10 mM solution in 1:1 DMSO: serum-free DMEM, 1% DMSO final concentration). Cells were collected by treatment with 0.5 mL 0.25% trypsin-EDTA for less than 5 minutes at 37 ºC and then the trypsin was inactivated with 1.0 mL DMEM media containing 10% FBS. The solution was partitioned for two samples, which were subsequently collected via centrifugation at 6,000 rpm at 4 ºC in 1.6 mL Eppendorf tubes. The media was removed, and cells were resuspended in 0.2 mM BSO with 10 μM CoxFluor (1.0 mL 1.5% DMSO final concentration in degassed serum-free DMEM) and incubated for 90 minutes at 37 ºC in a sealed container either with or without an AneroPack® (Mitsubishi Gas Company). When performing inhibition studies, the aforementioned staining solutions were prepared with 20 μM indomethacin without affecting the final concentration of DMSO. After staining, cells were pelleted in 1.6 mL Eppendorf tubes using the aforementioned procedure and were resuspended in degassed PBS. Samples were stored on ice prior to analysis on a BD LSR Fortessa Flow Cytometry Analyzer with 561 nm excitation and 582/15 emission bandpass filter. Dead cells were excluded from the analysis by staining samples (~300 μL) with propidium iodide (1 μL of 1 mg/mL in deionized water) for 5 to 10 minutes at

room temperature before analysis with 561 nm excitation and 595 nm longpass dichromic mirror and 610/20 emission bandpass filter. Data was gated for live cells the forward scatter higher versus PE-Texas Red area, and for single cell events using the forward scatter width versus side scatter area. Replicate numbers correspond to biological replicates.

2.6.23 Flow cytometry measurement of COX-2 activity in RAW 264.7 macrophages under variable oxygen concentrations

RAW 264.7 macrophage cells (500,000 cells, 2 mL of 250,000 cells/mL) were seeded into 6-well plates and incubated for 48 h under standard conditions for a final confluency of ~80%. The media was removed and replaced with serum-free DMEM (1.98 mL) followed by LPS (1 μg/mL final concentration, 20 μL of 100 μg/mL in PBS) 19 h before collection. Cellular GSH was depleted 2 h prior to collection via treatment with BSO (0.2 mM final concentration, 40 μL 10 mM solution in 1:1 DMSO: serum-free DMEM, 1% DMSO final concentration). Cells were collected by treatment with 0.5 mL 0.25% trypsin-EDTA for less than 5 minutes at 37 ºC and then the trypsin was inactivated with 1.0 mL DMEM media containing 10% FBS. Three wells were pooled (1.5 mL × 3) for a final volume of 4.5 mL cell suspension before partitioning into three tubes (one tube per oxygen concentration) for centrifugation at 6,000 rpm at 4 ºC in 1.6 mL Eppendorf tubes. The media was removed, and cells were resuspended in 0.2 mM BSO with 10 μM CoxFluor (1.5 mL, 1.5% DMSO final concentration in pre-equilibrated serum-free DMEM; media was equilibrated for ~24 h at the desired oxygen concentration followed by ~2 h re-equilibration following the addition of BSO; CoxFluor was added immediately before use to prevent any photo-oxidation). The resulting cell suspension was incubated for 90 minutes at 37 ºC under ~21, 1.0, or 0.1% oxygen with 5% CO_2 in an ultra-low cell attachment six well plate (Corning® Costar®) to facilitate rapid oxygen exchange. After staining, cells were pelleted using the aforementioned procedure and were

resuspended in PBS. Samples were stored on ice prior to analysis on a BD LSR Fortessa Flow Cytometry Analyzer with 561 nm excitation and 582/15 emission bandpass filter. Dead cells were excluded from the analysis by staining samples (~300 µL) with propidium iodide (1 µL of 1 mg/mL in deionized water) for 5 to 10 minutes at room temperature before analysis with 561 nm excitation and 595 nm longpass dichromic mirror and 610/20 emission bandpass filter. Data was gated for live cells the forward scatter higher versus PE-Texas Red area, and for single cell events using the forward scatter width versus side scatter area. Replicate numbers correspond to biological replicates.

2.6.24 Enzyme-linked immunosorbent assay (ELISA) for mouse COX-2

Protein concentration was measured directly from the same samples as the Flow Cytometry Measurement of COX-2 Activity in RAW 264.7 Macrophages under Variable Oxygen Conditions. The ELISA was performed using the SimpleStep ELISA Mouse COX2 ELISA Kit (ab210574, Abcam) according to the manufacturer's protocol. Briefly, cells were washed with cold PBS (1.0 mL × 2) and then lysed in cold 1X Cell Extraction Buffer PTR for 20 minutes at 0 ºC. The debris was removed via centrifugation at 18,000 × g for 20 minutes at 4 ºC and the supernatants were collected and stored at -80 ºC prior to use. Protein concentration was measured using the BCA Assay (Thermo Fisher Scientific) according to the manufacturer's protocol and the lysate was diluted with 1X Cell Extraction Buffer PTR for a final concentration of 25 µg/mL total protein. Cell lysate (50 µL) and then Antibody Cocktail (50 µL) were added to each well in duplicate and the sealed plate was incubated with vigorous shaking (400 rpm) for 1 h at 22 ºC. After binding, each well was washed thoroughly with 1X Wash Buffer PT (350 µL × 3). TMB Substrate (100 µL) was added to each well and allowed to incubate in the dark with vigorous stirring for 10 minutes at 22 ºC before quenching with Stop Solution (100 µL). The optical density was measured

at 450 nm and the protein concentration was interpolated according to a standard curved (prepared in duplicate). Protein concentrations are reported for the COX-2 concentration in a 25 μg/mL total protein stock.

2.7 References

(1) Rouzer, C. A.; Marnett, L. J. Cyclooxygenases: Structural and Functional Insights. *J. Lipid Res.* **2009**, *50* (Suppl), S29–S34.

(2) Blobaum, A. L.; Marnett, L. J. Structural and Functional Basis of Cyclooxygenase Inhibition. *J. Med. Chem.* **2007**, *50* (7), 1425–1441.

(3) DeWitt, D. L. Prostaglandin Endoperoxide Synthase: Regulation of Enzyme Expression. *Biochim. Biophys. Acta* **1991**, *1083* (2), 121–134.

(4) Kargman, S.; Charleson, S.; Cartwright, M.; Frank, J.; Riendeau, D.; Mancini, J.; Evans, J.; O'Neill, G. Characterization of Prostaglandin G/H Synthase 1 and 2 in Rat, Dog, Monkey, and Human Gastrointestinal Tracts. *Gastroenterology* **1996**, *111* (2), 445–454.

(5) Smyth, E. M.; Grosser, T.; Wang, M.; Yu, Y.; FitzGerald, G. A. Prostanoids in Health and Disease. *J. Lipid Res.* **2009**, *50* (Suppl), S423–S428.

(6) St-Jacques, B.; Ma, W. Role of Prostaglandin E2 in the Synthesis of the Pro-Inflammatory Cytokine Interleukin-6 in Primary Sensory Neurons: An in Vivo and in Vitro Study. *J. Neurochem.* **2011**, *118*, 841–854.

(7) Liebert, M. A.; Williams, J. O. Y. A.; Pontzer, C. H.; Shacter, E. Expression by Prostaglandin E 2 : The Role of P38 Mitogen-Activated Protein Kinase. *J. Interf. Cytokine Res.* **2000**, *298*, 291–298.

(8) Marnett, L. J.; DuBois, R. N. COX-2: A Target for Colon Cancer Prevention. *Annu. Rev. Pharmacol. Toxicol.* **2002**, *42* (1), 55–80.

(9) Appleby, S. B.; Ristimaki, A.; Neilson, K.; Narko, K.; Hla, T. Structure of the Human Cyclo-Oxygenase-2 Gene. *Biochem. J.* **1994**, *302* (3), 723–727.

(10) Rollins., T. E.; Smith, W. L. Subcellular Localization of Prostaglandin-Forming Cyclooxygenase in Swiss Mouse 3T3 Fibroblasts by Electron Microscopic Immunocytochemistry. *J. Biol. Chem.* **1980**, *255* (10), 4872–4875.

(11) Spencer, A. G.; Woods, J. W.; Arakawa, T.; Singer, I. I.; Smith, W. L. Subcellular Localization of Prostaglandin Endoperoxide H Synthases-1 and -2 by Immunoelectron Microscopy. *J. Biol. Chem.* **1998**, *273* (16), 9886–9893.

(12) Liou, J. Y.; Deng, W. G.; Gilroy, D. W.; Shyue, S. K.; Wu, K. K. Colocalization and Interaction of Cyclooxygenase-2 with Caveolin-1 in Human Fibroblasts. *J. Biol. Chem.* **2001**, *276* (37), 34975–34982.

(13) Murakami, M.; Das, S.; Kim, Y. J.; Cho, W.; Kudo, I. Perinuclear Localization of Cytosolic Phospholipase A2α Is Important but Not Obligatory for Coupling with Cyclooxygenases. *FEBS Lett.* **2003**, *546* (2–3), 251–256.

(14) Yamashita, M.; Tsuji, S.; Nishiyama, A.; Myrvik, Q. N.; Henriksen, R. A.; Shibata, Y. Differential Subcellular Localization of COX-2 in Macrophages Phagocytosing Heat-Killed Mycobacterium Bovis BCG. *Am. J. Physiol. - Cell Physiol.* **2007**, *293* (1), 184–190.

(15) Marnett, L. J.; Rowlinson, S. W.; Goodwin, D. C.; Kalgutkar, A. S.; Lanzo, C. A. Arachidonic Acid Oxygenation by COX-1 and COX-2. Mechanisms of Catalysis and Inhibition. *J. Biol. Chem.* **1999**, *274* (33), 22903–22906.

(16) Smith, W. L.; Dewitt, D. L.; Garavito, R. M. Cyclooxygenases: Structural, Cellular, and Molecular Biology. *Annu. Rev. Biochem.* **2000**, *69*, 145–182.

(17) Mbonye, U. R.; Yuan, C.; Harris, C. E.; Sidhu, R. S.; Song, I.; Arakawa, T.; Smith, W. L. Two Distinct Pathways for Cyclooxygenase-2 Protein Degradation. *J. Biol. Chem.* **2008**, *283* (13), 8611–8623.

(18) Smith, W. L.; Urade, Y.; Jakobsson, P.-J. Enzymes of the Cyclooxygenase Pathways of Prostanoid Biosynthesis. *Chem. Rev.* **2011**, *111* (10), 5821–5865.

(19) Wu, G.; Lü, J. M.; Van Der Donk, W. A.; Kulmacz, R. J.; Tsai, A. L. Cyclooxygenase Reaction Mechanism of Prostaglandin H Synthase from Deuterium Kinetic Isotope Effects. *J. Inorg. Biochem.* **2011**, *105* (3), 382–390.

(20) Eling, T. E.; Glasgow, W. C.; Curtis, J. F.; Hubbard, W. C.; Handler, J. A. Studies on the Reduction of Endogenously Generated Prostaglandin G2 by Prostaglandin H Synthase. *J. Biol. Chem.* **1991**, *266* (19), 12348–12355.

(21) Furse, K. E.; Pratt, D. A.; Porter, N. A.; Lybrand, T. P. Molecular Dynamics Simulations of Arachidonic Acid Complexes with COX-1 and COX-2: Insights into Equilibrium Behavior. *Biochemistry* **2006**, *45* (10), 3189–3205.

(22) Yuan, C.; Rieke, C. J.; Rimon, G.; Wingerd, B. A.; Smith, W. L. Partnering between Monomers of Cyclooxygenase-2 Homodimers. *Proc. Natl. Acad. Sci.* **2006**, *103* (16), 6142–6147.

(23) Dong, L.; Zou, H.; Yuan, C.; Hong, Y. H.; Kuklev, D. V.; Smith, W. L. Different Fatty Acids Compete with Arachidonic Acid for Binding to the Allosteric or Catalytic Subunits of Cyclooxygenases to Regulate Prostanoid Synthesis. *J. Biol. Chem.* **2016**, *291* (8), 4069–4078.

(24) Dubois, R. N.; Abramson, S. B.; Crofford, L.; Gupta, R. A.; Simon, L. S.; A. Van De Putte, L. B.; Lipsky, P. E. Cyclooxygenase in Biology and Disease. *FASEB J.* **1998**, *12* (12), 1063–1073.

(25) Williams, C. S.; Mann, M.; DuBois, R. N. The Role of Cyclooxygenases in Inflammation, Cancer, and Development. *Oncogene* **1999**, *18* (55), 7908–7916.

(26) Fagerberg, L.; Hallström, B. M.; Oksvold, P.; Kampf, C.; Djureinovic, D.; Odeberg, J.; Habuka, M.; Tahmasebpoor, S.; Danielsson, A.; Edlund, K.; et al. Analysis of the Human Tissue-Specific Expression by Genome-Wide Integration of Transcriptomics and Antibody-Based Proteomics. *Mol. Cell. Proteomics* **2014**, *13* (2), 397–406.

(27) Kirkby, N. S.; Chan, M. V.; Zaiss, A. K.; Garcia-Vaz, E.; Jiao, J.; Berglund, L. M.; Verdu, E. F.; Ahmetaj-Shala, B.; Wallace, J. L.; Herschman, H. R.; et al. Systematic Study of Constitutive Cyclooxygenase-2 Expression: Role of NF-KB and NFAT Transcriptional Pathways. *Proc. Natl. Acad. Sci.* **2015**, *113* (2), 434–439.

(28) Kapoor, S.; Burke, A.; Mardini, I. A.; McAdam, B. F.; FitzGerald, G. A.; Habib, A.; Lawson, J. A. Effect of Regulated Expression of Human Cyclooxygenase Isoforms on Eicosanoid and Isoeicosanoid Production in Inflammation. *J. Clin. Invest.* **2000**, *105* (10), 1473–1482.

(29) Samad, T. A.; Moore, K. A.; Sapirstein, A.; Billet, S.; Allchorne, A.; Poole, S.; Bonventre, J. V.; Woolf, C. J. Interleukin-1 β-Mediated Induction of Cox-2 in the CNS Contributes to Inflammatory Pain Hypersensitivity. *Nature* **2001**, *410* (6827), 471–475.

(30) Teismann, P.; Tieu, K.; Choi, D.-K.; Wu, D.-C.; Naini, A.; Hunot, S.; Vila, M.; Jackson-Lewis, V.; Przedborski, S. Cyclooxygenase-2 Is Instrumental in Parkinson's Disease Neurodegeneration. *Proc. Natl. Acad. Sci.* **2003**, *100* (9), 5473–5478.

(31) Reddy, B. S.; Hirose, Y.; Lubet, R.; Steele, V.; Kelloff, G.; Paulson, S.; Seibert, K.; Rao, C. V. Chemoprevention of Colon Cancer by Specific Cyclooxygenase-2 Inhibitor, Celecoxib, Administered during Different Stages of Carcinogenesis. *Cancer Res.* **2000**, *60* (2), 293–297.

(32) Chen, H.; Cai, W.; Chu, E. S. H.; Tang, J.; Wong, C. C.; Wong, S. H.; Sun, W.; Liang, Q.; Fang, J.; Sun, Z.; et al. Hepatic Cyclooxygenase-2 Overexpression Induced Spontaneous Hepatocellular Carcinoma Formation in Mice. *Oncogene* **2017**, *36* (31), 4415–4426.

(33) Kargman, S. L.; O'Neill, G. P.; Vickers, P. J.; Evans, J. F.; Mancini, J. A.; Jothy, S. Expression of Prostaglandin G/H Synthase-1 and -2 Protein in Human Colon Cancer. *Cancer Res.* **1995**, *55*, 2556–2559.

(34) Basudhar, D.; Glynn, S. A.; Greer, M.; Somasundaram, V.; No, J. H.; Scheiblin, D. A.; Garrido, P.; Heinz, W. F.; Ryan, A. E.; Weiss, J. M.; et al. Coexpression of NOS2 and COX2 Accelerates Tumor Growth and Reduces Survival in Estrogen Receptor-Negative Breast Cancer. *Proc. Natl. Acad. Sci.* **2017**, *114* (49), 201709119.

(35) Mazhar, D.; Ang, R.; Waxman, J. COX Inhibitors and Breast Cancer. *Br. J. Cancer* **2006**, *94* (3), 346–350.

(36) Xu, L.; Stevens, J.; Hilton, M. B.; Seaman, S.; Conrads, T. P.; Veenstra, T. D.; Logsdon, D.; Morris, H.; Swing, D. A.; Patel, N. L.; et al. COX-2 Inhibition Potentiates Antiangiogenic Cancer Therapy and Prevents Metastasis in Preclinical Models. *Sci. Transl. Med.* **2014**, *6* (242), 242ra84.

(37) Howe, L. R.; Chang, S. H.; Tolle, K. C.; Dillon, R.; Young, L. J. T.; Cardiff, R. D.; Newman, R. A.; Yang, P.; Thaler, H. T.; Muller, W. J.; et al. HER2/Neu-Induced Mammary Tumorigenesis and Angiogenesis Are Reduced in Cyclooxygenase-2 Knockout Mice. *Cancer Res.* **2005**, *65* (21), 10113–10119.

(38) Xu, F.; Li, M.; Zhang, C.; Cui, J.; Liu, J.; Li, J.; Jiang, H. Clinicopathological and Prognostic Significance of COX-2 Immunohistochemical Expression in Breast Cancer: A Metaanalysis. *Oncotarget* **2017**, *8* (4), 6003–6012.

(39) Hawkey, C. J. COX-1 and COX-2 Inhibitors. *Best Pract. Res. Clin. Gastroenterol.* **2001**, *15* (5), 801–820.

(40) Warner, T. D.; Giuliano, F.; Vojnovic, I.; Bukasa, A.; Mitchell, J. A.; Vane, J. R. Nonsteroid Drug Selectivities for Cyclo-Oxygenase-1 Rather than Cyclo-Oxygenase-2 Are Associated with Human Gastrointestinal Toxicity: A Full in Vitro Analysis. *Proc. Natl. Acad. Sci.* **1999**, *96* (13), 7563–7568.

(41) Kawamori, T.; Rao, V.; Seibert, K.; Reddy, B. S. Chemopreventive Activity of Celecoxib, a Specific Cyclooxygenase-2 Inhibitor, against Colon Carcinogenesis. *Cancer Res.* **1998**, *58*, 409–412.

(42) Lucotti, S.; Cerutti, C.; Soyer, M.; Gil-Bernabé, A. M.; Gomes, A. L.; Allen, P. D.; Smart, S.; Markelc, B.; Watson, K.; Armstrong, P. C.; et al. Aspirin Blocks Formation of Metastatic Intravascular Niches by Inhibiting Platelet-Derived COX-1/Thromboxane A2. *J. Clin. Invest.* **2019**, *129* (5), 1845–1862.

(43) Zelenay, S.; Van Der Veen, A. G.; Böttcher, J. P.; Snelgrove, K. J.; Rogers, N.; Acton, S. E.; Chakravarty, P.;

Girotti, M. R.; Marais, R.; Quezada, S. A.; et al. Cyclooxygenase-Dependent Tumor Growth through Evasion of Immunity. *Cell* **2015**, *162* (6), 1257–1270.

(44) Lenzer, J. FDA Advisers Warn: COX 2 Inhibitors Increase Risk of Heart Attack and Stroke. *BMJ* **2005**, *330*, 440.

(45) Noreen, Y.; Ringbom, T.; Perera, P.; Danielson, H.; Bohlin, L. Development of a Radiochemical Cyclooxygenase-1 and -2 in Vitro Assay for Identification of Natural Products as Inhibitors of Prostaglandin Biosynthesis. *J. Nat. Prod.* **1998**, *61* (1), 2–7.

(46) Guenzle, J.; Garrelfs, N. W. C.; Goeldner, J. M.; Weyerbrock, A. Cyclooxygenase (COX) Inhibition by Acetyl Salicylic Acid (ASA) Enhances Antitumor Effects of Nitric Oxide in Glioblastoma In Vitro. *Mol. Neurobiol.* **2019**, *56* (9), 6046–6055.

(47) Mccarthy, T. J.; Sheriff, A. U.; Graneto, M. J.; Talley, J. J.; Welch, M. J. Radiosynthesis, In Vitro Validation, and In Vivo Evaluation of COX-1 and COX-2Inhibitors. *J. Nucl. Med.* **2002**, *43*, 117–124.

(48) de Vries, E. F. J.; van Waarde, A.; Buursma, A. R.; Vaalburg, W. Synthesis and in Vivo Evaluation of 18F-Desbromo-DuP-697 as a PET Tracer for Cyclooxygenase-2 Expression. *J. Nucl. Med.* **2003**, *44* (10), 1700–1706.

(49) Prabhakaran, J.; Underwood, M. D.; Parsey, R. V.; Arango, V.; Majo, V. J.; Simpson, N. R.; Van Heertum, R.; Mann, J. J.; Kumar, J. S. D. Synthesis and in Vivo Evaluation of [18F]-4-[5-(4-Methylphenyl)-3-(Trifluoromethyl)-1H-Pyrazol-1-Yl]Benzenesulfonamide as a PET Imaging Probe for COX-2 Expression. *Bioorganic Med. Chem.* **2007**, *15* (4), 1802–1807.

(50) Schuller, H. M.; Kabalka, G.; Smith, G.; Mereddy, A.; Akula, M.; Cekanova, M. Detection of Overexpressed COX-2 in Precancerous Lesions of Hamster Pancreas and Lungs by Molecular Imaging: Implications for Early Diagnosis and Prevention. *ChemMedChem* **2006**, *1* (6), 603–610.

(51) Wuest, F.; Kniess, T.; Bergmann, R.; Pietzsch, J. Synthesis and Evaluation in Vitro and in Vivo of a 11C-Labeled Cyclooxygenase-2 (COX-2) Inhibitor. *Bioorganic Med. Chem.* **2008**, *16* (16), 7662–7670.

(52) de Vries, E. F. J.; Doorduin, J.; Dierckx, R. A.; van Waarde, A. Evaluation of [11C]Rofecoxib as PET Tracer for Cyclooxygenase 2 Overexpression in Rat Models of Inflammation. *Nucl. Med. Biol.* **2008**, *35* (1), 35–42.

(53) Dileep Kumar, J. S.; Bai, B.; Zanderigo, F.; DeLorenzo, C.; Prabhakaran, J.; Parsey, R.; Mann, J. J. In Vivo Brain Imaging, Biodistribution, and Radiation Dosimetry Estimation of [11C]Celecoxib, a COX-2 PET Ligand, in Nonhuman Primates. *Molecules* **2018**, *23* (8), 1929.

(54) Uddin, M. J.; Crews, B. C.; Blobaum, A. L.; Kingsley, P. J.; Gorden, D. L.; McIntyre, J. O.; Matrisian, L. M.; Subbaramaiah, K.; Dannenberg, A. J.; Piston, D. W.; et al. Selective Visualization of Cyclooxygenase-2 in Inflammation and Cancer by Targeted Fluorescent Imaging Agents. *Cancer Res.* **2010**, *70* (9), 3618–3627.

(55) Uddin, M. J.; Crews, B. C.; Ghebreselasie, K.; Marnett, L. J. Design, Synthesis, and Structure-Activity Relationship Studies of Fluorescent Inhibitors of Cycloxygenase-2 as Targeted Optical Imaging Agents. *Bioconjug. Chem.* **2013**, *24* (4), 712–723.

(56) Zhang, H.; Fan, J.; Wang, J.; Dou, B.; Zhou, F.; Cao, J.; Qu, J.; Cao, Z.; Zhao, W.; Peng, X. Fluorescence Discrimination of Cancer from Inflammation by Molecular Response to COX-2 Enzymes. *J. Am. Chem. Soc.* **2013**, *135* (46), 17469–17475.

(57) Zhang, H.; Fan, J.; Wang, J.; Zhang, S.; Dou, B.; Peng, X. An Off-on COX-2-Specific Fluorescent Probe: Targeting the Golgi Apparatus of Cancer Cells. *J. Am. Chem. Soc.* **2013**, *135* (31), 11663–11669.

(58) Yuan, C.; Sidhu, R. S.; Kuklev, D. V.; Kado, Y.; Wada, M.; Song, I.; Smith, W. L. Cyclooxygenase Allosterism, Fatty Acid-Mediated Cross-Talk between Monomerso f Cyclooxygenase Homodimers. *J. Biol. Chem.* **2009**, *284* (15), 10046–10055.

(59) Dong, L.; Yuan, C.; Orlando, B. J.; Malkowski, M. G.; Smith, W. L. Fatty Acid Binding to the Allosteric Subunit of Cyclooxygenase-2 Relieves a Tonic Inhibition of the Catalytic Subunit. *J. Biol. Chem.* **2016**, *291* (49), 25641–25655.

(60) Kulmacz, R. J.; van der Donk, W. A.; Tsai, A. L. Comparison of the Properties of Prostaglandin H Synthase-1 and -2. *Prog. Lipid Res.* **2003**, *42* (5), 377–404.

(61) Gorris, H. H.; Walt, D. R. Mechanistic Aspects of Horseradish Peroxidase Elucidated through Single-Molecule Studies. *J. Am. Chem. Soc.* **2009**, *131* (17), 6277–6282.

(62) Debski, D.; Smulik, R.; Zielonka, J.; Michałowski, B.; Jakubowska, M.; Debowska, K.; Adamus, J.; Marcinek, A.; Kalyanaraman, B.; Sikora, A. Mechanism of Oxidative Conversion of Amplex® Red to Resorufin: Pulse Radiolysis and Enzymatic Studies. *Free Radic. Biol. Med.* **2016**, *95*, 323–332.

(63) Picot, D.; Loll, P. J.; Garavito, R. M. The X-Ray Crystal Structure of the Membrane Protein Prostaglandin H2 Synthase-1. *Nature* **1994**, *367* (6460), 243–249.

(64) Rieke, C. J.; Mulichak, A. M.; Garavito, R. M.; Smith, W. L. The Role of Arginine 120 of Human Prostaglandin Endoperoxide H Synthase- 2 in the Interaction with Fatty Acid Substrates and Inhibitors. *J. Biol. Chem.* **1999**, *274* (24), 17109–17114.

(65) Bhattacharyya, D. K.; Lecomte, M.; Rieke, C. J.; Garavito, R. M.; Smith, W. L. Involvement of Arginine 120, Glutamate 524, and Tyrosine 355 in the Binding of Arachidonate and 2-Phenylpropionic Acid Inhibitors to the Cyclooxygenase Active Site of Ovine Prostaglandin Endoperoxide H Synthase-1. *J. Biol. Chem.* **1996**, *271* (4), 2179–2184.

(66) Yu, M.; Ives, D.; Ramesha, C. S. Synthesis of Prostaglandin E2 Ethanolamide from Anandamide by Cyclooxygenase-2. *Biochemistry* **1997**, *272* (34), 21181–21186.

(67) Hitomi, Y.; Takeyasu, T.; Funabiki, T.; Kodera, M. Detection of Enzymatically Generated Hydrogen Peroxide by Metal-Based Fluorescent Probe. *Anal. Chem.* **2011**, *83* (24), 9213–9216.

(68) Klotz, A. V.; Stegeman, J. J.; Walsh, C. An Alternative 7-Ethoxyresorufin o-Deethylase Activity Assay: A Continuous Visible Spectrophotometric Method for Measurement of Cytochrome P-450 Monooxygenase Activity. *Anal. Biochem.* **1984**, *140* (1), 138–145.

(69) McDougle, D. R.; Watson, J. E.; Abdeen, A. A.; Adili, R.; Caputo, M. P.; Krapf, J. E.; Johnson, R. W.; Kilian, K. A.; Holinstat, M.; Das, A. Anti-Inflammatory ω-3 Endocannabinoid Epoxides. *Proc. Natl. Acad. Sci.* **2017**, *114* (30), E6034–E6043.

(70) Votyakova, T. V.; Reynolds, I. J. Detection of Hydrogen Peroxide with Amplex Red: Interference by NADH and Reduced Glutathione Auto-Oxidation. *Arch. Biochem. Biophys.* **2004**, *431* (1), 138–144.

(71) Ayoub, S. S.; Flower, R. J.; Seed, M. P. *Cyclooxygenases. Methods in Molecular Biology (Methods and Protocols)*; 2010; Vol. 644.

(72) Jiang, J.; Borisenko, G. G.; Osipov, A.; Martin, I.; Chen, R.; Shvedova, A. A.; Sorokin, A.; Tyurina, Y. Y.; Potapovich, A.; Tyurin, V. A.; et al. Arachidonic Acid-Induced Carbon-Centered Radicals and Phospholipid Peroxidation in Cyclo-Oxygenase-2-Transfected PC12 Cells. *J. Neurochem.* **2004**, *90* (5), 1036–1049.

(73) Mancini, J. A.; Riendeau, D.; Falgueyret, J.-P. P.; Vickers, P. J.; O'Neill, G. P.; Falgueyret, J.-P. P.; Vickers,

P. J.; O'Neill, G. P. Arginine 120 of Prostaglandin G/H Synthase-1 Is Required for the Inhibition by Nonsteroidal Anti-Inflammatory Drugs Containing a Carboxylic Acid Moiety. *J. Biol. Chem.* **1995**, *270* (49), 29372–29377.

(74) Hood, W. F.; Gierse, J. K.; Isakson, P. C.; Kiefer, J. R.; Kurumbail, R. G.; Seibert, K.; Monahan, J. B. Characterization of Celecoxib and Valdecoxib Binding to Cyclooxygenase. *Mol. Pharmacol.* **2003**, *63* (4), 870–877.

(75) Cingolani, G.; Panella, A.; Perrone, M. G.; Vitale, P.; Di Mauro, G.; Fortuna, C. G.; Armen, R. S.; Ferorelli, S.; Smith, W. L.; Scilimati, A. Structural Basis for Selective Inhibition of Cyclooxygenase-1 (COX-1) by Diarylisoxazoles Mofezolac and 3-(5-Chlorofuran-2-Yl)-5-Methyl-4-Phenylisoxazole (P6). *Eur. J. Med. Chem.* **2017**, *138*, 661–668.

(76) Orlando, B. J.; Malkowski, M. G. Crystal Structure of Rofecoxib Bound to Human Cyclooxygenase-2. *Acta Crystallogr. Sect. F Struct. Biol. Commun.* **2016**, *72* (10), 772–776.

(77) Berman, H. M.; Westbrook, J.; Feng, Z.; Gilliland, G.; Bhat, T. N.; Weissig, H.; Shindyalov, I. N.; Bourne, P. E. The Protein Data Bank. *Nucleic Acids Res.* **2000**, *28* (1), 235–242.

(78) Trott, O.; Olson, A. J. AutoDock Vina: Improving the Speed and Accuracy of Docking with a New Scoring Function, Efficient Optimization, and Multithreading. *J. Comput. Chem.* **2010**, *31* (2), 455–461.

(79) Xu, S.; Uddin, M. J. J.; Banerjee, S.; Marnett, L. J. L. J.; Jashim Uddin, M.; Banerjee, S.; Duggan, K.; Musee, J.; Kiefer, J. R.; Ghebreselasie, K.; et al. Conjugated Indomethacin Fluorescent Inhibitors Utilize Membrane Binding Domain of Cyclooxygenase-2 to Accommodate Tethered Moiety. *J. Biol. Chem.* **2019**, *294* (22), 8690–8689.

(80) Chance, B. The Kinetics and Stoichiometry of the Transition from the Primary to the Secondary Peroxidase Peroxide Complexes. *Arch. Biochem. Biophys.* **1952**, *41* (2), 416–424.

(81) Rodriguez-Lopez, J. N.; Gilabert, M. A.; Tudela, J.; Thorneley, R. N. F.; Garcia-Canovas, F. Reactivity of Horseradish Peroxidase Compound II toward Substrates: Kinetic Evidence for a Two-Step Mechanism. *Biochemistry* **2000**, *39* (43), 13201–13209.

(82) Vecchio, A. J.; Simmons, D. M.; Malkowski, M. G. Structural Basis of Fatty Acid Substrate Binding to Cyclooxygenase-2. *J. Biol. Chem.* **2010**, *285* (29), 22152–22163.

(83) Yuan, L.; Lin, W.; Zhao, S.; Gao, W.; Chen, B.; He, L.; Zhu, S. A Unique Approach to Development of Near-Infrared Fluorescent Sensors for in Vivo Imaging. *J. Am. Chem. Soc.* **2012**, *134* (32), 13510–13523.

(84) Tsikas, D.; Suchy, M. T.; Niemann, J.; Tossios, P.; Schneider, Y.; Rothmann, S.; Gutzki, F. M.; Frölich, J. C.; Stichtenoth, D. O. Glutathione Promotes Prostaglandin H Synthase (Cyclooxygenase)-Dependent Formation of Malondialdehyde and 15(S)-8-Iso-Prostaglandin F2α. *FEBS Lett.* **2012**, *586* (20), 3723–3730.

(85) Ryan, E. P.; Bushnell, T. P.; Friedman, A. E.; Rahman, I.; Phipps, R. P. Cyclooxygenase-2 Independent Effects of Cyclooxygenase-2 Inhibitors on Oxidative Stress and Intracellular Glutathione Content in Normal and Malignant Human B-Cells. *Cancer Immunol. Immunother.* **2008**, *57* (3), 347–358.

(86) Dengiz, G. O.; Odabasoglu, F.; Halici, Z.; Suleyman, H.; Cadirci, E.; Bayir, Y. Gastroprotective and Antioxidant Effects of Opipramol on Indomethacin-Induced Ulcers in Rats. *Arch. Pharm. Res* **2007**, *30* (11), 1426–1434.

(87) Pastoris, O.; Verri, M.; Boschi, F.; Kastsiuchenka, O.; Balestra, B.; Pace, F.; Tonini, M.; Natale, G. Effects of Esomeprazole on Glutathione Levels and Mitochondrial Oxidative Phosphorylation in the Gastric Mucosa of Rats Treated with Indomethacin. *Naunyn. Schmiedebergs. Arch. Pharmacol.* **2008**, *378* (4), 421–429.

(88) Abdel-Raheem, I. T. Gastroprotective Effect of Rutin against Indomethacin-Induced Ulcers in Rats. *Basic Clin. Pharmacol. Toxicol.* **2010**, *107* (3), 742–750.

(89) Martinez, F. O.; Gordon, S. The M1 and M2 Paradigm of Macrophage Activation: Time for Reassessment. *F1000Prime Rep.* **2014**, *6* (March), 13.

(90) Bienkowskis, M. J.; Petro, M. A.; Robinson, J. Inhibition of Thromboxane A Synthesis in U937 Cells by Glucocorticoids. *Biochemistry* **1989**, *264* (11), 6536–6544.

(91) Giroux, M.; Descoteaux, A. Cyclooxygenase-2 Expression in Macrophages: Modulation by Protein Kinase C-. *J. Immunol.* **2000**, *165* (7), 3985–3991.

(92) Eliopoulos, A. G.; Dumitru, C. D.; Wang, C. C.; Cho, J.; Tsichlis, P. N. Induction of COX-2 by LPS in Macrophages Is Regulated by Tpl2-Dependent CREB Activation Signals. *EMBO J.* **2002**, *21* (18), 4831–4840.

(93) Grkovich, A.; Johnson, C. A.; Buczynski, M. W.; Dennis, E. A. Lipopolysaccharide-Induced Cyclooxygenase-2 Expression in Human U937 Macrophages Is Phosphatidic Acid Phosphohydrolase-1-Dependent. *J. Biol. Chem.* **2006**, *281* (44), 32978–32987.

(94) Rouzer, C. A.; Jacobs, A. T.; Nirodi, C. S.; Kingsley, P. J.; Morrow, J. D.; Marnett, L. J. RAW264.7 Cells Lack Prostaglandin-Dependent Autoregulation of Tumor Necrosis Factor-α Secretion. *J. Lipid Res.* **2005**, *46* (5), 1027–1037.

(95) Font-Nieves, M.; Sans-Fons, M. G.; Gorina, R.; Bonfill-Teixidor, E.; Salas-Peŕdomo, A.; Mańquez-Kisinousky, L.; Santalucia, T.; Planas, A. M. Induction of COX-2 Enzyme and down-Regulation of COX-1 Expression by Lipopolysaccharide (LPS) Control Prostaglandin E 2 Production in Astrocytes. *J. Biol. Chem.* **2012**, *287* (9), 6454–6468.

(96) Smith, C. J.; Marnett, L. J. Effects of Cysteine-to-Serine Mutations on Structural and Functional Properties of Prostaglandin Endoperoxide Synthase. *Arch. Biochem. Biophys.* **1996**, *335* (2), 342–350.

(97) Buchmuller-Rouiller, Y.; Corradin, S. B.; Smith, J.; Schneider, P.; Ransijn, A.; Jongeneel, C. V.; Mauël, J. Role of Glutathione in Macrophage Activation: Effect of Cellular Glutathione Depletion on Nitrite Production and Leishmanicidal Activity. *Cell. Immunol.* **1995**, *164* (1), 73–80.

(98) Butzer, U.; Weidenbach, H.; Gansauge, S.; Gansauge, F.; Beger, H. G.; Nussler, A. K. Increased Oxidative Stress in the RAW 264.7 Macrophage Cell Line Is Partially Mediated via the S-Nitrosothiol-Induced Inhibition of Glutathione Reductase. *FEBS Lett.* **1999**, *445* (2–3), 274–278.

(99) Trushkin, N. A.; Filimonov, I. S.; Vrzheshch, P. V. Inhibition of Cyclooxygenase Activity of Prostaglandin-H-Synthase by Excess Substrate (Molecular Oxygen). *Biochem.* **2010**, *75* (11), 1368–1373.

(100) Mitchell, J. A.; Akarasereenont, P.; Thiemermann, C.; Flower, R. J.; Vane, J. R. Selectivity of Nonsteroidal Antiinflammatory Drugs as Inhibitors of Constitutive and Inducible Cyclooxygenase (Cytokines/Arachidonic Add/Prostanoids/Inflammation/Mitogen/Aspirin-like Drugs). *Proc. Natl. Acad. Sci. USA* **1993**, *90*, 11693–11697.

(101) Liu, X. H.; Rose, D. P. Differential Expression and Regulation of Cyclooxygenase-1 and -2 in Two Human Breast Cancer Cell Lines. *Cancer Res.* **1996**, *56* (22), 5125–5127.

(102) Patsos, H. A.; Hicks, D. J.; Dobson, R. R. H.; Greenhough, A.; Woodman, N.; Lane, J. D.; Williams, A. C.; Paraskeva, C. The Endogenous Cannabinoid, Anandamide, Induces Cell Death in Colorectal Carcinoma Cells: A Possible Role for Cyclooxygenase 2. *Gut* **2005**, *54* (12), 1741–1750.

(103) Kuc, C.; Jenkins, A.; van Dross, R. T. Arachidonoyl Ethanolamide (AEA)-Induced Apoptosis Is Mediated by J-Series Prostaglandins and Is Enhanced by Fatty Acid Amide Hydrolase (FAAH) Blockade. *Mol. Carcinog.* **2012**, *51* (2), 139–149.

(104) Grimm, J. B.; Muthusamy, A. K.; Liang, Y.; Brown, T. A.; Lemon, W. C.; Patel, R.; Lu, R.; Macklin, J. J.; Keller, P. J.; Ji, N.; et al. A General Method to Fine-Tune Fluorophores for Live-Cell and in Vivo Imaging. *Nat. Methods* **2017**, *14* (10), 987–994.

(105) Zhou, X.; Lai, R.; Beck, J. R.; Li, H.; Stains, C. I. Nebraska Red: A Phosphinate-Based near-Infrared Fluorophore Scaffold for Chemical Biology Applications. *Chem. Commun.* **2016**, *52* (83), 12290–12293.

(106) Grzybowski, M.; Taki, M.; Senda, K.; Sato, Y.; Ariyoshi, T.; Okada, Y.; Kawakami, R.; Imamura, T.; Yamaguchi, S. A Highly Photostable Near-Infrared Labeling Agent Based on a Phospha-Rhodamine for Long-Term and Deep Imaging. *Angew. Chemie - Int. Ed.* **2018**, *57* (32), 10137–10141.

(107) Niu, G.; Liu, W.; Zhou, B.; Xiao, H.; Zhang, H.; Wu, J.; Ge, J.; Wang, P. Deep-Red and Near-Infrared Xanthene Dyes for Rapid Live Cell Imaging. *J. Org. Chem.* **2016**, *81* (17), 7393–7399.

(108) Capdevila, J. H.; Morrow, J. D.; DuBois, R. N.; Capdevila, J. H.; Belosludtsev, Y. Y.; Falck, J. R.; Beauchamp, D. R. The Catalytic Outcomes of the Constitutive and the Mitogen Inducible Isoforms of Prostaglandin H2 Synthase Are Markedly Affected by Glutathione and Glutathione Peroxidase(S). *Biochemistry* **1995**, *34* (10), 3325–3337.

(109) Margalit, A.; Hauser, S. D.; Isakson, P. C. Regulation of in Vivo Prostaglandin Biosynthesis by Glutathione. *Am. J. Physiol. Integr. Comp. Physiol.* **1998**, *274* (2), R294.

(110) Birk, J.; Meyer, M.; Aller, I.; Hansen, H. G.; Odermatt, A.; Dick, T. P.; Meyer, A. J.; Appenzeller-Herzog, C. Endoplasmic Reticulum: Reduced and Oxidized Glutathione Revisited. *J. Cell Sci.* **2013**, *126* (7), 1604–1617.

(111) Schneider, C. A.; Rasband, W. S.; Eliceiri, K. W. NIH Image to ImageJ: 25 Years of Image Analysis. *Nat. Methods* **2012**, *9* (7), 671–675.

(112) Pettersen, E. F.; Goddard, T. D.; Huang, C. C.; Couch, G. S.; Greenblatt, D. M.; Meng, E. C.; Ferrin, T. E. UCSF Chimera - A Visualization System for Exploratory Research and Analysis. *J. Comput. Chem.* **2004**, *25* (13), 1605–1612.

(113) Humphrey Dalke Schulten, W. A. K. Visual Molecular Dyanmics. *J. Mol. Graph.* **1996**, *14* (1), 33–38.

(114) Sagnella, S. M.; Conn, C. E.; Krodkiewska, I.; Mulet, X.; Drummond, C. J. Anandamide and Analogous Endocannabinoids: A Lipid Self-Assembly Study. *Soft Matter* **2011**, *7* (11), 5319–5328.

(115) Würth, C.; Grabolle, M.; Pauli, J.; Spieles, M.; Resch-Genger, U. Relative and Absolute Determination of Fluorescence Quantum Yields of Transparent Samples. *Nat. Protoc.* **2013**, *8* (8), 1535–1550.

(116) Arbeloa, F. L.; Ojeda, P. R.; Arbeloa, I. L. Flourescence Self-Quenching of the Molecular Forms of Rhodamine B in Aqueous and Ethanolic Solutions. *J. Lumin.* **1989**, *44* (1–2), 105–112.

(117) Orlando, B. J.; McDougle, D. R.; Lucido, M. J.; Eng, E. T.; Graham, L. A.; Schneider, C.; Stokes, D. L.; Das, A.; Malkowski, M. G. Cyclooxygenase-2 Catalysis and Inhibition in Lipid Bilayer Nanodiscs. *Arch. Biochem. Biophys.* **2014**, *546*, 33–40.

(118) Orlando, B. J.; Borbat, P. P.; Georgieva, E. R.; Freed, J. H.; Malkowski, M. G. Pulsed Dipolar Spectroscopy Reveals That Tyrosyl Radicals Are Generated in Both Monomers of the Cyclooxygenase-2 Dimer. *Biochemistry* **2015**, *54* (50), 7309–7312.

(119) Kulmacz, R. J.; Lands, W. E. M. Quantitative Simularities in the Several Actions of Cyanide on Prostaglandin H Synthase. *Prostaglandins* **1985**, *29* (2), 175–190.

(120) Miyamoto, T.; Oging, N.; Yamamoto, S.; Hayaishi, O. Purification of Prostaglandin Enderperoxide Synthetase from Bovine Vesicular Gland Microsomes. *J. Biol. Chem.* **1976**, *251* (9), 2629–2636.

(121) McDougle, D. R.; Palaria, A.; Magnetta, E.; Meling, D. D.; Das, A. Functional Studies of N-Terminally Modified CYP2J2 Epoxygenase in Model Lipid Bilayers. *Protein Sci.* **2013**, *22* (7), 964–979.

(122) Huff, H. C.; Maroutsos, D.; Das, A. Lipid Composition and Macromolecular Crowding Effects on CYP2J2-Mediated Drug Metabolism in Nanodiscs. *Protein Sci.* **2019**, *28*, 928–940.

(123) Zelasko, S.; Palaria, A.; Das, A. Optimizations to Achieve High-Level Expression of Cytochrome P450 Proteins Using Escherichia Coli Expression Systems. *Protein Expr. Purif.* **2013**, *92* (1), 77–87.

(124) Shen, A. L.; Porter, T. D.; Wilson, T. E.; Kasper, C. B. Structural Analysis of the FMN Binding Domain of NADPH-Cytochrome P-450 Oxidoreductase by Site-Directed Mutagenesis. *J. Biol. Chem.* **1989**, *264* (13), 7584–7589.

(125) Gasteiger, E.; Gattiker, A.; Hoogland, C.; Ivanyi, I.; Appel, R. D.; Bairoch, A. ExPASy: The Proteomics Server for in-Depth Protein Knowledge and Analysis. *Nucleic Acids Res.* **2003**, *31* (13), 3784–3788.

(126) Hughes, M. N.; Cammack, R. [30] Synthesis, Chemistry, and Applications of Nitroxyl Ion Releasers Sodium Trioxodinitrate or Angeli's Salt and Piloty's Acid. *Methods Enzymol.* **1999**, *301* (1), 279–287.

(127) Uppu, R. M. Synthesis of Peroxynitrite Using Isoamyl Nitrite and Hydrogen Peroxide in a Homogeneous Solvent System. *Anal. Biochem.* **2006**, *354* (2), 165–168.

(128) Maiti, R.; Van Domselaar, G. H.; Zhang, H.; Wishart, D. S. SuperPose: A Simple Server for Sophisticated Structural Superposition. *Nucleic Acids Res.* **2004**, *32* (Web Server issue), W590–W594.

(129) Carnevale, L. N.; Arango, A. S.; Arnold, W. R.; Tajkhorshid, E.; Das, A. Endocannabinoid Virodhamine Is an Endogenous Inhibitor of Human Cardiovascular CYP2J2 Epoxygenase. *Biochemistry* **2018**, *57* (46), 6489–6499.

(130) Starr, M. L.; Sparks, R. P.; Arango, A. S.; Hurst, L. R.; Zhao, Z.; Lihan, M.; Jenkins, J. L.; Tajkhorshid, E.; Fratti, R. A. Phosphatidic Acid Induces Conformational Changes in Sec18 Protomers That Prevent SNARE Priming. *J. Biol. Chem.* **2019**, *294* (9), 3100–3116.

(131) Phillips, J. C.; Braun, R.; Wang, W.; Gumbart, J.; Tajkhorshid, E.; Villa, E.; Chipot, C.; Skeel, R. D.; Kalé, L.; Schulten, K. Scalable Molecular Dynamics with NAMD. *J. Comput. Chem.* **2005**, *26* (16), 1781–1802.

(132) Huang, J.; Rauscher, S.; Nawrocki, G.; Ran, T.; Feig, M.; De Groot, B. L.; Grubmüller, H.; MacKerell, A. D. CHARMM36m: An Improved Force Field for Folded and Intrinsically Disordered Proteins. *Nat. Methods* **2017**, *14* (1), 71–73.

(133) Feller, S. E.; Zhang, Y.; Pastor, R. W.; Brooks, B. R. Constant Pressure Molecular Dynamics Simulation: The Langevin Piston Method. *J. Chem. Phys.* **1995**, *103* (11), 4613–4621.

(134) Martyna, G. J.; Tobias, D. J.; Klein, M. L. Constant Pressure Molecular Dynamics Algorithms. *J. Chem. Phys.* **1994**, *101* (5), 4177–4189.

(135) Darden, T.; York, D.; Pedersen, L. Particle Mesh Ewald: An N·log(N) Method for Ewald Sums in Large Systems. *J. Chem. Phys.* **1993**, *98* (12), 10089–10092.

(136) Essmann, U.; Perera, L.; Berkowitz, M. L.; Darden, T.; Lee, H.; Pedersen, L. G. A Smooth Particle Mesh Ewald Method. *J. Chem. Phys.* **1995**, *103* (19), 8577–8593.

(137) Miyamoto, S.; Kollman, P. A. Settle: An Analytical Version of the SHAKE and RATTLE Algorithm for Rigid Water Models. *J. Comput. Chem.* **1992**, *13* (8), 952–962.

(138) Michaud-Agrawal, N.; Denning, E. J.; Woolf, T. B.; Beckstein, O. MDAnalysis: A Toolkit for Analysis of Molecular Dynamic Simulations. *J. Comput. Chem.* **2011**, *32* (10), 2319–2327.

(139) Gowers, R. J.; Linke, M.; Barnoud, J.; Reddy, T. J. E.; Melo, M. N.; Seyler, S. L.; Domański, J.; Dotson, D. L.; Buchoux, S.; Kenney, Ian, M.; et al. MDAnalysis: A Python Package for the Rapid Analysis of Molecular Dynamics Simulations. *Proc. 15th Python Sci. Conf.* **2016**, 98–105.

(140) Malkowski, M. G.; Ginell, S. L.; Smith, W. L.; Garavito, R. M. The Productive Conformation of Arachidonic Acid Bound to Prostaglandin Synthase. *Science* **2000**, *289* (5486), 1933–1937.

(141) Roberts, E.; Eargle, J.; Wright, D.; Luthey-Schulten, Z. MultiSeq: Unifying Sequence and Structure Data for Evolutionary Analysis. *BMC Bioinformatics* **2006**, *7*, 382.

(142) Yadav, A. K.; Reinhardt, C. J.; Arango, A. S.; Huff, H. C.; Dong, L.; Malkowski, M. G.; Das, A.; Tajkhorshid, E.; Chan, J. An Activity-Based Sensing Approach for the Detection of Cyclooxygenase-2 in Live Cells. *Angew. Chemie Int. Ed.* **2020**, *59*, 3307–3314.

CHAPTER 3: DEVELOPMENT OF PHOTOACOUSTIC PROBES FOR DETECTING ENDOGENOUS NITRIC OXIDE IN INFLAMMATION AND CANCER[3]

3.1 Background and significance

Small-molecule biomarkers are intriguing targets for biology evaluation and diagnostic applications. Nitric oxide (NO) was the founding member of the gasotransmitters (gaseous signaling molecules) and it is implicated as a key player in most biological and pathological processes. An expansive collection of optical probes has been reported to detect NO. While these purely optical approaches facilitated many biological discoveries, they have also illuminated inconsistencies between cell- and animal-based studies. These conflicting conclusions are most likely due to complex regulatory mechanisms that are only present within the intact system. We proposed that photoacoustic (PA) probes could limit these inconsistencies by non-invasively detecting NO within live animal models. This work could serve as a template for the rational development of activatable PA probes, a platform to optimize NIR dyes for PA imaging, and to begin to interrogate NO's biology in the context of cancer (e.g., source, dynamics, localization, etc.).

3.1.1 Nitric oxide biology

Reactive oxygen, nitrogen, and sulfur species represent a major class of biological signaling molecules.[1–3] NO, carbon monoxide, and hydrogen sulfide are a subset of this class that are collectively referred to as the gasotransmitters due to their gaseous nature.[4] NO was the first

[3]Portions of this chapter are reprinted or adapted with permissions from the following publications: (1) Reinhardt, C. J.; Zhou, E. Y.; Jorgensen, M. D.; Partipilo, G.; Chan, J. A Ratiometric Acoustogenic Probe for In Vivo Imaging of Endogenous Nitric Oxide. *J. Am. Chem. Soc.* **2018**, *140*, 1011–1018.[142] Copyright © 2018 American Chemical Society. (2) Reinhardt, C. J.; Xu, R.; Chan, J. Nitric Oxide Imaging in Cancer Enabled by Steric Relaxation of a Photoacoustic Probe Platform. *Chem. Sci.* **2020**, *11*, 1587–1592.[143] Copyright © 2020 Royal Society of Chemistry.

gasotransmitters identified and it was characterized for its role in the regulation of vascular tone in the 1980s.[5–8] Since then, NO has been implicated in a wide range of pharmacologically important processes, such as inflammation,[9] neuronal signaling,[10–12] and cancer.[13–15] Moreover, its signaling proceeds through distinct mechanisms.[16] A general and underappreciated conclusion from these works is that there are intrinsic connections between the concentration, cellular environment, and resulting biological effects of NO.[1] For example, high concentrations of NO are antitumoral, while low concentrations promote angiogenesis and tumor growth.[13,14,17–22] Along these lines, nitric oxide synthase (NOS) can serve as an early biomarker for a range of cancer types (e.g., breast, prostate, lung, colorectal), but its correlation with clinical stages depends on the cancer type.[23–27] Additionally, NO biology is intrinsically linked to the local oxygen availability, where biosynthesis is regulated by molecular oxygen (see section 3.1.2) and NO is chemically elaborated to other reactive nitrogen species via reactive oxygen species (including molecular oxygen).[19,28–30]

NO can either directly or indirectly exert the aforementioned biological effects. NO can directly bind to soluble guanylyl cyclase—at a distal heme—and promote a conformational change with a concomitant increase in the catalytic activity. The cyclic GMP then exerts a range of biological affects through protein kinases, phosphodiesterases, and ion channels. Alternatively, NO can ligate the heme of cytochrome P450s or cytochrome c oxidase, thereby inhibiting the protein's activity and increasing the availability of molecular oxygen within the cell.[29] More recently, dinitrosyl iron complexes (DNICs) were identified as the most abundant NO sink within the cell. The complexation stabilizes the free-radical and tunes the reactivity. DNICs can form with different biological thiols (e.g., cysteine, glutathione)[18,31,32] and display antioxidative and nitrosothiol-generating activities.[33,34] On the other hand, NO can indirectly nitrate electron-rich

aromatic amino acids (e.g., tyrosine and tryptophan), nitrosate or nitrosylate proteinaceous thiols (a potential intermediate prior to disulfide formation), or function in lipid oxidation.[29,35] Together, these signaling pathways are choreographed by the concentration, reactivity, and interconversion of NO with proteinaceous and non-proteinaceous targets.

3.1.2 Nitric oxide biosynthesis

NO is biosynthesized by NOS through the oxidation of L-arginine to L-citrulline under normoxic conditions (Scheme 3.1). The NOS family includes an inducible, calcium-independent isoform (iNOS), which is primarily linked to the immune response, and constitutively expressed, calcium-dependent isoforms (nNOS and eNOS), which are linked to homeostatic maintenance.[36] The subcellular localizations are cell-type and isoform specific. Dysregulation of the proteins localization can result in pathological effects given NO's short half-life. The enzyme's localization and activity are well-regulated through co- or post-translational modifications (e.g., acylation, phosphorylation) or protein-protein interactions. These modifications enable targeting to the cytosol, plasma membrane, cytoskeleton, Golgi, mitochondria, peroxisome, nucleus, caveolae and potentially the endo- and sarcoplasmic reticulum.[37,38]

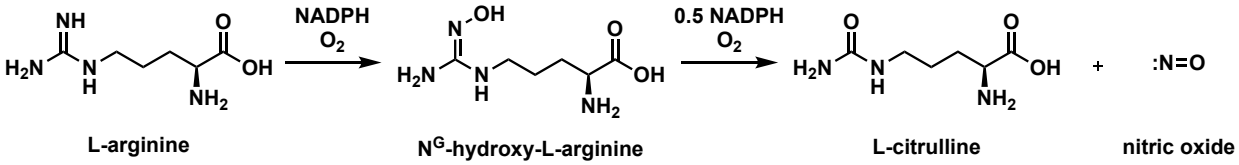

Scheme 3.1: Nitric oxide is biosynthesized by nitric oxide synthase in a two-step reaction from L-arginine.

Paradoxically, NO is one of the smallest natural products, but it requires a notably large (approximately 300 kDa homodimer) and complex enzyme with three substrates (molecular oxygen, L-arginine, NADPH) and at least five cofactors/prosthetic groups (FAD, FMN, calmodulin, tetrahydrobiopterin, and heme) for its biosynthesis. NOS monomers are composed of a fused cytochrome reductase and cytochrome P450 domain.[36,39] All three isoforms coordinate the

complicated five-electron oxidation of L-arginine with heme reduction coupled through choregraphed two-electron and one-electron reduction events. Electrons are shunted through the reductase domain from NADPH through the flavodomain (FAD and FMN) and into the heme, which is promoted through a calmodulin-mediated conformational change in calcium dependent isoforms (Figure 3.1).

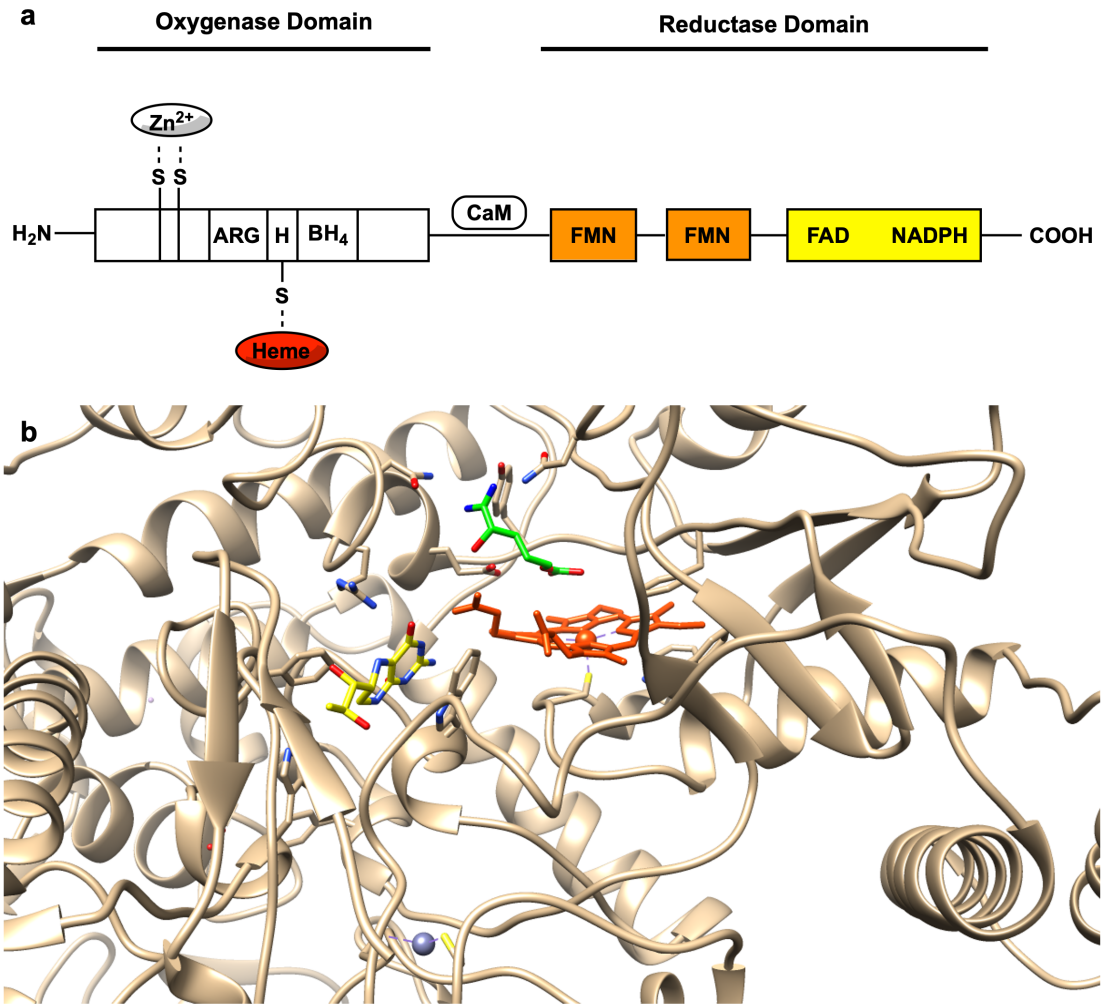

Figure 3.1: (a) Schematic of NOS's structural domains from the N to C terminus, including the L-arginine (Arg), heme (H), tetrahydrobiopterin (BH_4), and calmodulin binding sites (CaM) in the oxygenase domain and flavin mononucleotide (FMN), flavin adenine dinucleotide, and nicotinamide adenine dinucleotide phosphate binding sites in the reductase domain. S correspond to cysteine residues that are involved with zinc (grey) binding or ligation of the heme. (b) Structure of eNOS (PDB: 2NSE) bound to L-arginine (green) at the heme (red orange), in proximity to the tetrahydrobiopterin cofactor.

The initial catalytic cycle yields the *N*-hydroxylated product (N^G-hydroxy-L-arginine, L-

NHA), presumably through direct oxidation with anionic Compound 0. The subsequent oxidation of L-NHA to L-citrulline is initiated by the ferric superoxide radical abstracting the N-H hydrogen atom followed by nucleophilic attack of the peroxide at the carbon. Decomposition of the resulting tetrahedral intermediate affords the NO and L-citrulline (Scheme 3.1).[40–42] The tetrahydrobiopterin cofactor appears to be involved, but not required, for dimer formation, and essential for catalysis. Specifically, the it is believed to perform both the reduction of the ferrous dioxygen intermediate and the oxidation of the ferrous nitroxyl intermediate to afford the product.[43,44] NO can also be enzymatically by nitrite reductases (e.g., deoxyhemoglobin, deoxymyoglobin, mitochondrial reductases) under hypoxic conditions.[45–47] These enzymes are likely the source of the "non-enzymatically" nitric oxide observed in the ischemic heart that causes NO-mediated tissue damage.[48]

3.1.3 Nitric oxide detection strategies

Due to its various roles in physiological and pathological processes, the identification, detection, and quantification of NO continues to be an active area of research. *In vitro* and *ex vivo* analyses are limited in their ability to recapitulate the native system. For this reason, it is essential to develop new methods for the performing non-invasive, *in vivo* detection of NO with high spatiotemporal resolution. The current arsenal of NO donors[49] and *ex vivo* analyses have provided most of the previously described information; however, many outstanding questions remain.

Current methods for detecting NO are inadequate for *in vivo* applications. For example, the colorimetric Griess assay is useful for analyzing NO in cell lysates; however, this is performed indirectly via detection of nitrite and nitrate and requires acidic conditions that are not biocompatable.[50] NO's globin-based reactivity can be hijacked to evade the requirement of cell lysis; however, the poor permeability of hemoglobin limits its application to measuring NO after

it has diffused from live cells.[51] In contrast, techniques such as electron paramagnetic resonance (EPR) spectroscopy[52] and magnetic resonance imaging (MRI)[53] have been employed for NO detection at relevant imaging depths; however, these approaches are limited by low resolution and sensitivity, respectively.[54] Indeed, this approach facilitated the discovery of NO that was not derived from NOS.[48] Electrochemical analyses (e.g., amperometry) display some of the highest sensitivity (pM) and are arguably the most quantitative methods; however, this does not translate well for imaging with tissue because it requires invasive procedures and can only detect NO in direct contact with the probe.[55–57]

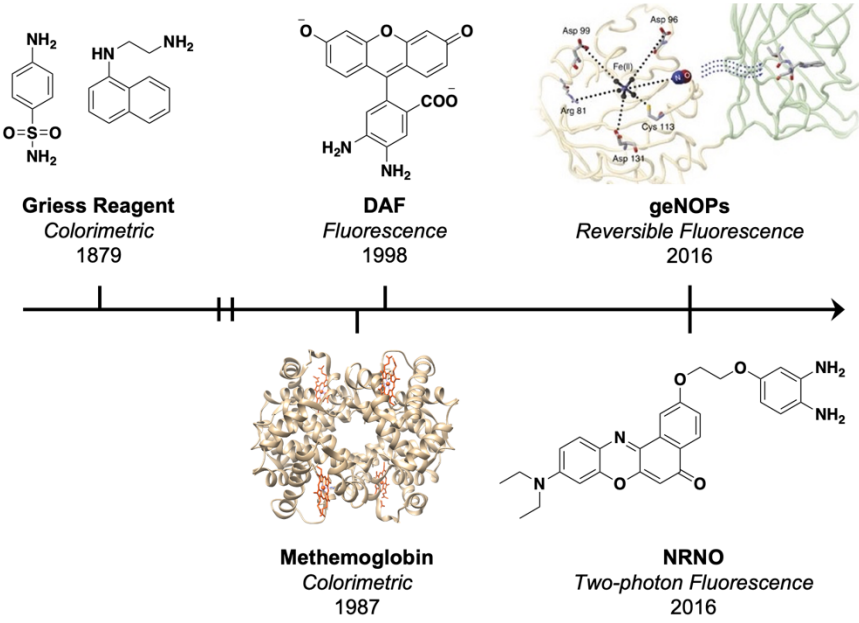

Figure 3.2: Timeline highlighting key examples of optical NO probes. As the field evolved, the tools moved away from cell lysates (Griess assay)[58] into the extracellular space (methemyoglobin, PDB = 1JYZ),[59] and eventually into live cells, tissue slices, and animals (DAF, NRNO, and geNOPs).[60–62] The structure of geNOPs is adapted with permission from ref. 62. Copyright © 2016 Springer Nature.

Optical methods, such as luminescence[63] and fluorescence imaging,[64] are non-invasive and provide high-resolution and high-contrast at shallow imaging depths.[54] As a result, a diverse palette of reaction-based fluorescent probes has been developed, primarily for cellular studies (Figure 3.2). In principle, many of the red-shifted and multiphoton congeners can be employed for *in vivo*

imaging, but these studies require invasive surgical procedures,[65] are confined to peripheral limbs,[66] and/or suffer from limited resolution[66,67] due to the scattering of emitted light. Several other fluorescent NO probes have been applied to living animals; however, these examples necessitate specimen sacrifice for *ex vivo* analysis of the tissue slices.[61,68–71] Photoacoustic (PA) imaging is a non-invasive imaging modality with the potential to overcome these challenges by coupling the precision of optical imaging with the deep tissue capabilities of ultrasound imaging (see Chapter 1 for additional information).

3.2 Design and development of APNO-5

It is essential to satisfy six general design criteria to optimize *in vivo* performance of small-molecular activatable PA probes. First, a probe must exhibit maximal absorption in the NIR-I or NIR-II[72] window to ensure incident light penetrates deep within tissue without significant attenuation. Second, it should possess a large extinction coefficient (greater than $10^4\ M^{-1}\ cm^{-1}$) and low quantum yield since absorptivity and non-emissive relaxation are proportional to PA signal intensity. Third, it must react with the target in a rapid and highly selective manner. Rapidity and selectivity must be considered in terms of the target and detection strategy (i.e., catalytic, stoichiometric, or super-stoichiometric). NO is present at low abundance (nM–μM steady-state concentration range) and has a short biological lifetime (seconds to minutes depending on concentration and oxygenation).[73] Fourth, a probe should be optimized for ratiometric imaging, which is necessary to account for imaging artifacts (see section 1.4. for additional information).[74] Fifth, the probe must display favorable pharmacokinetic and pharmacodynamic properties, such as rapid uptake by the region of interest. Finally, the probe should be biocompatible and produce minimal effects on the native biological system.[75]

To this end, we rationally developed and synthesized a panel of Acoustogenic Probe(s) for Nitric Oxide (APNO). We began by incorporating the *o*-phenylenediamine (OPD) functionality[60] onto the aza-BODIPY dye platform to afford APNO-1 (Figure 3.3). This scaffold and trigger were selected over the various alternatives because of the platform's well-documented photo- and chem-ostability and the overwhelming number of OPD examples.[63] We rationalized that strategic positioning of the trigger facilitate an NO-mediated perturbation of the push-pull system and a concomitant hypsochromic (blue) shift in the wavelength of maximum absorbance (λ_{max}). Empirically, a shift greater than 50 nm is desirable for ratiometric imaging such that each form can be selectively irradiated to produce a corresponding PA signal.

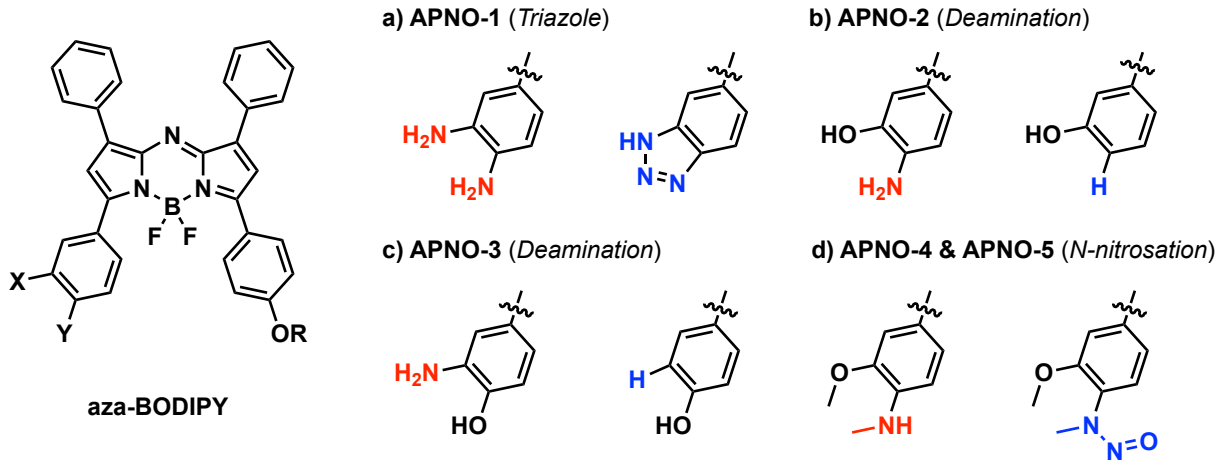

Figure 3.3: Structures, triggers, and sensing mechanisms for the panel of APNO (red) and tAPNO (blue). R = Me (APNO-1, APNO-2, APNO-3, and APNO-4) or tetraalkylammonium polyethylene chain (APNO-5).

Treatment of APNO-1 with NO resulted in a 55 nm blue-shift from 731 nm to 676 nm (Figure C.1). When APNO-1 and turned-over APNO-1 (tAPNO-1) were excited at 740 nm and 680 nm, respectively, a ratiometric turn-on PA response of 7.4-fold was observed (Figure C.2). Experimental excitation wavelengths differ from the reported λ_{max} values due to a combination of instrumental range (680–950 nm) and experimentally larger PA ratio. Although the observed ratiometric response would be sufficient to detect most analyte targets, we deemed it essential to

improve this property further due to the low biological abundance of NO. Additionally, the preparation of APNO-1 was hampered by decomposition of key synthetic intermediates which resulted in low overall yields.

Next, we turned our attention towards developing probes that rely on NO-mediated deamination.[76,77] Specifically, APNO-2 features an electron-rich *o*-aminophenol moiety that undergoes NO-mediated diazonium formation and subsequent homolytic bond cleavage to afford tAPNO-2 (Figure 3.3). It was rationalized that the removal of the strongly electron-donating aniline would have a larger effect on the wavelength than triazole formation. Treatment of APNO-2 with NO resulted in a 59 nm blue-shift from 735 nm to 676 nm (Figure C.1) and 13.1-fold ratiometric turn-on response when irradiated at 750 nm and 680 nm (Figure C.2). While this improvement in the dynamic range may have been sufficient, it was limited by the requirement of super-stoichiometric quantities of N_2O_3 and slow reaction kinetics. Specifically, the reaction proceeds via an *N*-nitroso intermediate (which was detected via fluorescence) followed by slow reaction with an additional equivalent of N_2O_3, diazonium formation, and decomposition to yield the product.[76] These properties significantly reduce the sensitivity of APNO-2 and complicate the PA imaging results. Of note, we also prepared APNO-3, a constitutional isomer; however, it suffered from pH dependence near neutral pH (Figure C.3).

In light of the rapid *N*-nitroso formation, we reasoned that mono-alkylation of the reactive aniline could enhance the reactivity, as well as block the necessary rearrangements for diazonium formation and deamination. This led to the development of APNO-4 which features an *N*-methylaniline nucleophile trigger (Figure 3.3). The hydroxyl group was replaced with a methoxy substituent for synthetic ease and to prevent possible pH dependence. While there are examples of photoinduced electron transfer (PET)-based fluorogenic probes relying on NO-responsive

secondary anilines in the literature;[70,71,78] APNO-4 represents the first probe (for any imaging modality) that employs *N*-nitrosation for modulation of a push-pull system and ratiometric imaging, to the best of our knowledge. We observed rapid formation of the anticipated *N*-nitrosated product (tAPNO-4) and a significant 86 nm blue-shift of the λ_{max} from 764 nm to 678 nm upon treatment with NO (Figure C.1); however, tAPNO-4 was poorly soluble in aqueous solutions. This resulted in inconsistent results due to aggregation and precipitation. To overcome this limitation, we developed APNO-5, a positively charged analog featuring a PEGylated tetraalkylammonium group to improve solubility, prevent dye aggregation, and facilitate uptake *in vivo*.

Table 3.1: Photophysical characterization of APNO and tAPNO in ethanolic 20 mM potassium phosphate buffer (pH 7.4, 50% v/v). [a] Measured relative to dimethoxy aza-BODIPY ($\Phi = 0.32$, $CHCl_3$). [b] Not determined: tAPNO-3 displays pH dependence under these conditions. [c] Not determined: tAPNO-4 precipitated out of solution. Data is reported as the average of experimental replicates ($n = 3$) with less than 15% error.

APNO	λ_{max} (nm)	ε ($M^{-1}cm^{-1}$)	Φ	tAPNO	λ_{max} (nm)	ε ($M^{-1}cm^{-1}$)	Φ
1	731	3.30×10^4	0.0065	1	676	3.71×10^4	0.14
2	735	7.40×10^4	0.0006	2	676	6.93×10^4	0.12
3	679	2.20×10^4	0.0708	3	678	2.28×10^4	0.09
4	764	3.70×10^4	0.0003	4	678	n.d.	n.d.
5	764	3.20×10^4	0.0003	5	673	3.30×10^4	0.23

Each APNO was synthesized by coupling two 4-nitro-1,3-diphenylbutan-1-one analogs under Paal-Knorr cyclization conditions, followed by boron chelation to afford the aza-BODIPY dye platform.[79] Synthetic procedures for each compound, including authentic tAPNO-5, can be found in Appendix C.

As anticipated, APNO-5 reacted rapidly with NO to afford the *N*-nitrosated product (tAPNO-5) with a significant 91 nm blue-shift of the λ_{max} from 764 nm to 673 nm. This was the largest wavelength shift observed in the APNO series (Figure 3.4). The extinction coefficient of APNO-5 was sufficiently large (3.2×10^4 M^{-1} cm^{-1}) to ensure the generation of strong PA signals *in vivo* (Table 3.1). Selective irradiation of APNO-5 and tAPNO-5 at 770 nm and 680 nm,

respectively, resulted in an 18.6-fold ratiometric PA turn-on response in tissue-mimicking phantoms (Figure 3.4). Additionally, the improved aqueous solubility due to appendage of the tetraalkylammonium PEG group enhanced its properties for ratiometric PA imaging.

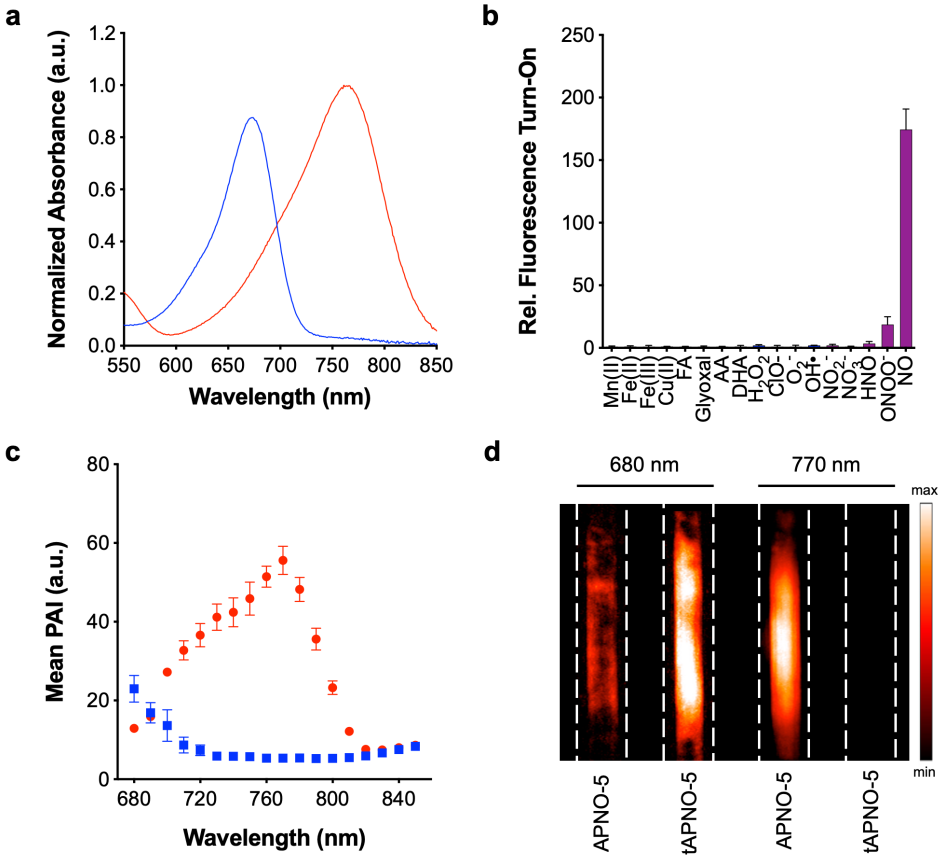

Figure 3.4: (a) Normalized absorbance spectra of 2 μM APNO-5 (red) and tAPNO-5 (blue). (b) APNO-5 (2 μM) fluorescence enhancement following 1 h treatment with excess (100 equiv) reactive metal (red), carbonyl (green), oxygen (blue), or nitrogen (purple) species (c) PA spectra of 10 μM APNO-5 (red) and tAPNO-5 (blue). (d) PA images of 10 μM APNO-5 and tAPNO-5 at 680 and 770 nm. All spectra and assays were performed in ethanolic 20 mM potassium phosphate buffer (pH 7.4, 50% v/v). Data presented as mean ± standard deviation (n = 3) for (b-c).

Insoluble aza-BODIPY dyes are known to form *J*-aggregates and nanoparticles, where the λ_{max} is red-shifted relative to the non-aggregated form.[80] Because our strategy relies on selective excitation using specific wavelengths, it is essential to minimize the formation of wavelength-shifted aggregates. To verify this, we monitored the degree of aggregation as a function of surfactant concentration at a fixed dye concentration. At 2 μM, aggregation was attenuated at concentrations as low as 0.1% surfactant for APNO-5, whereas APNO-4 required ≥ 10% (Figure

C.4). Moreover, the tetraalkylammonium PEG appendage increased the water solubility of APNO-5 and tAPNO-5, as indicated by clogP values of 3.8 and 3.8, relative to 7.6 and 7.3 for APNO-4 and tAPNO-4 (Table C.2). Since the calculation methods are unable to account for charge, APNO-5 and tAPNO-5's predicted values should serve as over-approximations of the true values.[81] This structural feature was also required for APNO-5 to permeate deep into tissue after subcutaneous administration into live mice. Other congeners pooled at the injection site and showed minimal response owing to poor tissue uptake (data not shown).

Next, we determined that the fluorescence quantum yields of APNO-5 and tAPNO-5 were sufficiently low (Table 3.1). This is ideal for PA imaging since the quantum yield is inversely proportional to the intensity of the PA signal. Nevertheless, we conducted selectivity assays using fluorimetry due its sensitivity and dynamic range. Treatment of APNO-5 with excess NO (100 equiv) resulted in a significant 174.4-fold fluorescence enhancement, whereas other reactive nitrogen species (RNS) (e.g., nitroxyl and peroxynitrite) did not elicit an appreciable response (Figure 3.4b). This is important because NO can rapidly convert into other RNS under biological conditions (besides N_2O_3, the hypothesized nitrosating species).[70] Importantly, most reported NO triggers react with N_2O_3 rather than directly with NO. While this decreases sensitivity, it is suggested to prevent perturbation of NO signal transduction.[60] When APNO-5 was treated with a panel of oxidants, no oxidation of the aza-BODIPY core nor the *N*-methylaniline trigger was observed. Finally, the reactivity of APNO-5 was assessed against a series of key biological carbonyl species including formaldehyde (FA), ascorbic acid (AA), dehydroascorbic acid (DHA), and glyoxal to test for side-reactivity and false turn-on via Schiff base formation (Figure 3.4b). Even with large stoichiometric excesses of each carbonyl no cross-reactivity was observed. Note that similar selectivity was observed for the other members of the series (Figure C.5).

We then determined the chemo- and photo-stability of APNO-5 in the interest of supporting *in vivo* imaging over extended periods (hours to days). First, the absorption spectra of a solution of APNO-5 was monitored over the course of five days. During this time, no significant decomposition of the probe was observed. Next, we subjected a solution of APNO-5 to continuous irradiation with an OPO laser at 770 nm for 60 min. Under these conditions, minimal photobleaching was observed (Figure C.6). Interestingly, it was discovered that tAPNO-5 undergoes photo-induced denitrosylation when continuously irradiated; however, only moderate signal loss is observed (< 30%) under standard imaging conditions (confirmed by UV-Vis; Figure D.1). Moreover, since APNO-5 is released as the product during prolonged irradiation, it is reasonable to predict minimal decrease in sensitivity. This would later serve as the blueprint for the development of an NIR light induced NO donor with an integrated PA monitoring, in which the nucleophilicity of the methylaniline was limited to prevent NO back-capture (additional information regarding light-induced denitrosylation and methods for performing EPR NO trapping studies can be found in Appendix D).[82]

After confirming the requisite selectivity, solubility, and stability, the probe's biocompatibility and subcellular localization were assessed. First, RAW 264.7 macrophages were incubated with APNO-5 (1 and 5 μM) for 3, 6, and 24 h. Biocompatibility was assessed in terms of membrane integrity (trypan blue assay) and cell metabolism (MTT assay). Both assays indicated that APNO-5 was minimally cytotoxic at a concentration of 5 μM, with greater than 79% viability observed after 24 hours (Figure C.7). Next the localization was determined via colocalization studies with organelle-specific dyes (LysoTracker Green™, MitoTracker® Green, and ER-Tracker® Green) within RAW 264.7 macrophages. Based on the overlap between APNO-5 and each of the trackers, it was clear that APNO-5 broadly localizes throughout the cell (except the

nucleus) with slight preference for the lysosome and mitochondria (Figure C.8).

3.3 Detection of nitric oxide in a murine subcutaneous inflammation model

As mentioned previously, the non-invasive detection of NO *in vivo* remains a significant challenge despite the general availability of NO-specific fluorescent probes. To evaluate the utility of APNO-5 for the detection of NO in live animals, we turned our attention to an LPS-induced murine inflammation model. This system was selected because mice show similar inflammatory responses to LPS as humans, making it a useful model for inflammation.[83]

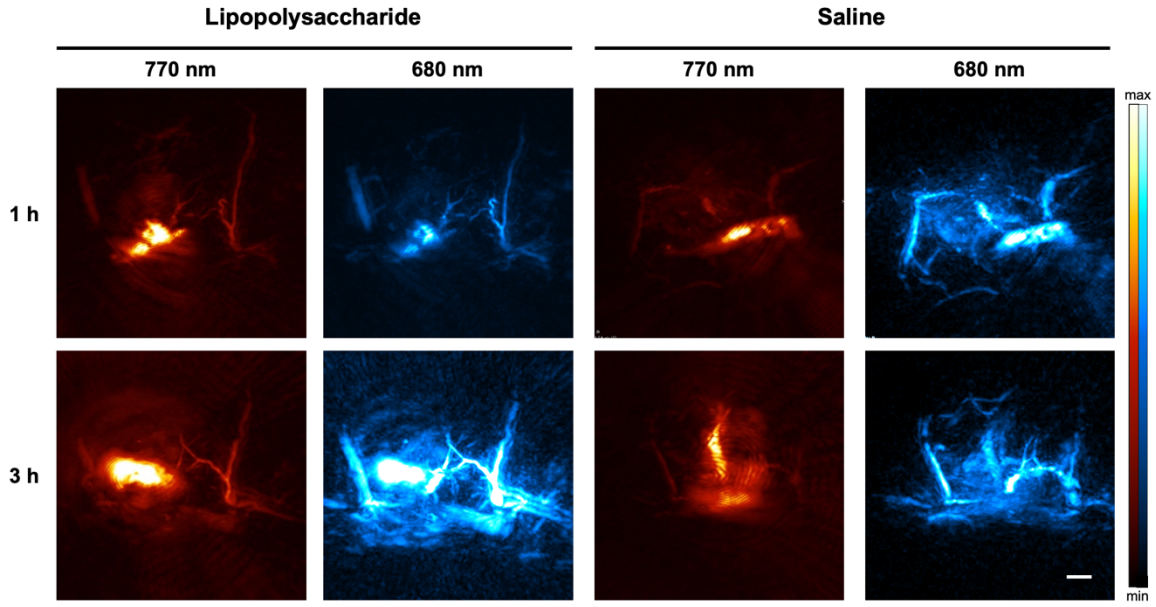

Figure 3.5: Representative PA images of APNO-5 responding to endogenous NO within a murine LPS-induced inflammation model. Images of APNO-5 (68 μg/kg) in a mouse flank following subcutaneous LPS or saline treatment. APNO-5 and tAPNO-5 were selectively imaged at 770 (red) and 680 (blue) nm, respectively. Scale bar represents 2 mm.

Mice were treated with either LPS or a saline vehicle control via subcutaneous injection into their flank. Following background scans, the dye was administered in the same location as the treatment. APNO-5 and tAPNO-5 were irradiated at 770 nm and 680 nm, respectively, and the change in ratiometric signal was monitored over time. Following administration, we observed significant pooling of the probe at the injection site. The initial broad absorbance band of APNO-

5 in the injection solution resulted in a ratio of ~1.07 at 1 h. Diffusion of the PA signal shortly thereafter (2 h) indicated uptake into the surrounding tissue. At this time, we observed conversion of APNO-5 to afford tAPNO-5 in LPS-treated animals as determined by an increase in the ratiometric PA signal to ~1.2, which remained constant for the remainder of the experiment. In contrast, the PA ratio for the saline-treated mice was ~0.9 and did not change throughout the experiment (Figure 3.5). The initial decrease in PA ratio for the control animal can be attributed to sharpening of APNO-5's absorbance profile following uptake and solubilization within the tissue. This was confirmed by monitoring the absorbance profile in the absence and presence of rat liver microsomes, a source of membrane lipids and proteins for association, and the PA spectrum of APNO-5 in a mouse as a function of time (Figure C.9). Taken together, this represents a 1.89-fold signal enhancement at 680 nm and 1.31-fold ratiometric response and after 5 h (Figure 3.6).

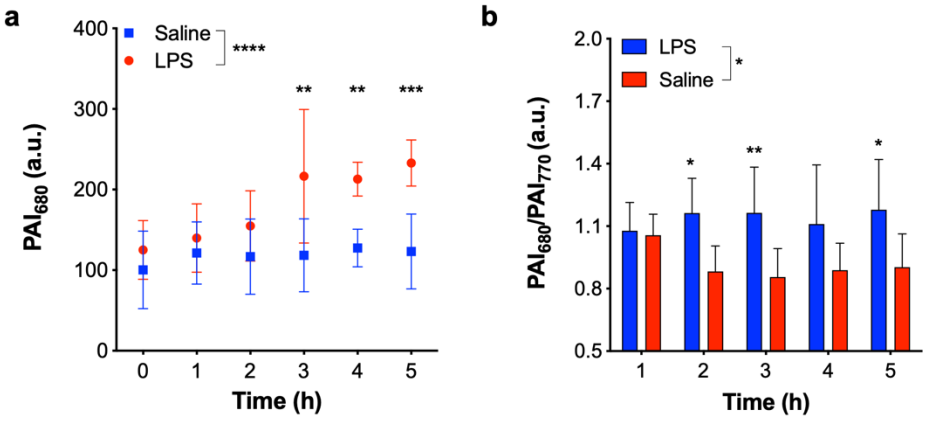

Figure 3.6: (a) Single wavelength (PAI_{680}) and (b) ratiometric imaging (PAI_{680}/PAI_{770}) of endogenously produced NO within an LPS-induced murine inflammation model over 5 hours. Data presented as mean ± standard deviation (n = 8). Statistical analysis between LPS and saline treated mice was performed using two-way ANOVA ($\alpha = 0.05$). LPS and saline ratiometric signals were compared at each time point using Sidak's multiple comparison test ($\alpha = 0.05$). *, $p < 0.05$; **, $p < 0.01$; ***, $p < 0.001$; ****, $p < 0.0001$.

To confirm that the signal was a result of APNO-5 nitrosation and not LPS-induced changes in endogenous chromophores (e.g., oxyhemoglobin, deoxyhemoglobin), PA spectra were acquired following LPS or saline treatment both in the presence and absence of dye. As expected, LPS

induces a small increase in ratiometric signal in the absence of dye; however, it does not account for the total signal enhancement (Figure C.10). This data, together with our *in vitro* results, provides compelling evidence that APNO-5 is capable of detecting endogenously generated NO *in vivo*.

3.4 Reflection on APNO-5's performance and areas for improvement

PA imaging is an emerging imaging technology that has the potential to perform non-invasive molecular imaging in deep tissue. In this work, we rationally developed a series of NO-responsive probes for PA imaging. Since we installed most common aerobic NO triggers on a single dye platform, it was possible to systematically compare OPD-, deamination-, and *N*-nitrosation-based sensing mechanisms (all products confirmed via LC-MS, Figure C.11–C.14). It is clear that the OPD-based trigger is a reasonable approach if triazole formation can be coupled to a robust readout. This is in contrast to some reports implicating cross-reactivity with ascorbic acid and dehydroascorbic acid.[84] This suggests that the side reaction is probe dependent, as we did not observe any response to these two carbonyl species, nor with glyoxal. While our work demonstrates that NO-mediated deamination can be expanded, it is limited by the requirement of super-stoichiometric amounts of NO and may proceed through meta-stable intermediates that would complicate interpretation. We found the *N*-nitrosation trigger to be the best of the three triggers examined. When the *N*-alkyl amine is sufficiently nucleophilic, the reaction with NO is rapid and gives rise to a single product with predictable chemostablity.[49] We also performed mechanistic studies regarding the sensing mechanism on the TokyoGreen[85] dye platform (see Appendix C for synthetic information), in which our results confirm that both deamination and *N*-nitrosation sensing mechanisms are oxygen-dependent and do not proceed with cysteine or

glutathione DNICs (Figure C.15). After exposing the probe-DNIC solutions to air, we only observed fluorescence enhancement in cysteine DNIC conditions. This suggests that these DNICs may be less stable, releasing NO over the course of the experiment, and that NO biology may have significant crosstalk with iron metabolism and redox signaling. Prior to this work, it was unclear whether the DNICs could serve as NO source.

It is important to note that while APNO-5 was able to detect NO concentrations relevant to the immune response (high nM–μM steady-state concentration, millimolar range over the course of the experiment), it was ineffective for NO detection in cancer (10^3-fold lower concentrations). For this reason, it is essential to enhance the sensitivity of the probe platform for imaging within deeper tissue and at lower NO concentrations.[21] Two areas for improvement were to decrease the propensity to undergo photo-denitrosylation and access more efficient irradiation of the *N*-nitrosated product.

It is important to note that only a handful of approaches have been successfully employed for increasing the sensitivity and ratiometric properties of small-molecule PA probes. Specifically, increasing the electron density within the aza-BODIPY[86] and conformational restriction of the pendant phenyl rings[87] have led to improved designs for ratiometric, activatable PA probes compared to non-ratiometric[88] or poorly ratiometric probes.[89] While successful in the selected example, increasing electron density may not be trivial, depending on the application. On the other hand, conformational restriction yields reliable red-shifts (approximately 30 nm per fusion) but increases the molecular weight (26 Da per fusion) and cLogP of the dye platform (increase from the parent aza-BODIPY cLogP = 7.8 to conformationally restricted aza-BODIPY cLogP = 8.2–8.6). Together, these properties decrease the probability of passive uptake into the cell and increase propensity for aggregate formation and peak broadening.

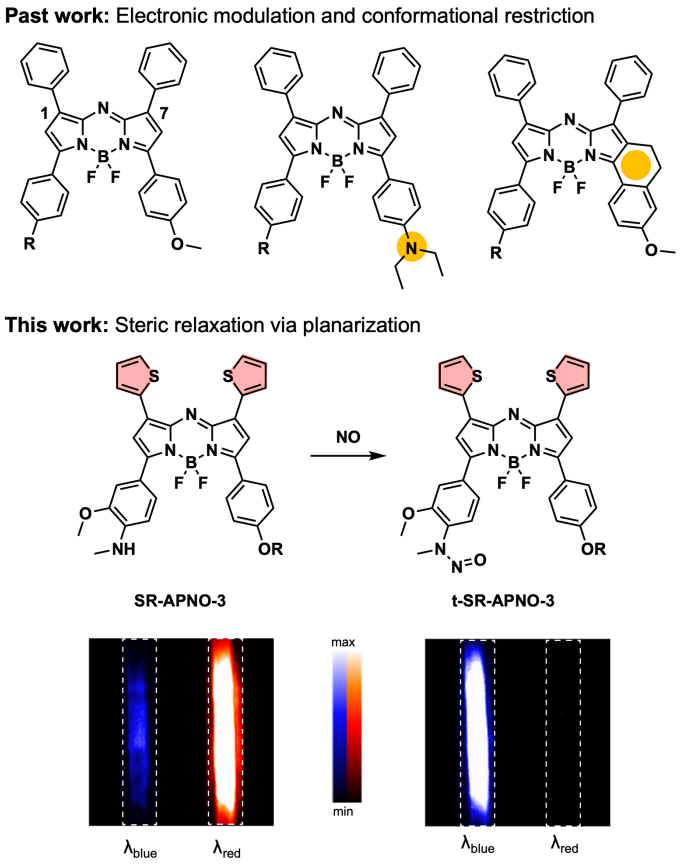

Figure 3.7: Examples of previous and current approaches for the optimization of aza-BODIPY PA probes. Yellow circles denote past locations of optimization, while red pentagons indicate the location for steric relaxation. SR-APNO-3, the lead compound, undergoes oxidative *N*-nitrosation and a wavelength shift for ratiometric PA imaging. Representative images of SR-APNO-3 and t-SR-APNO-3 (10 μM) at λ_{blue} (690 nm) and λ_{red} (790 nm) in a tissue-mimicking phantom. R = CH_2-$C_2H_3N_3$-PEG_3-$N(CH_3)_4I$.

We decided to investigate the photophysical effects of planarizing the pendant aromatic rings on the aza-BODIPY core by relaxing steric clash. We generally refer to this approach as "steric relaxation for planarization" with the corresponding PA platform being named SR-aza-BODIPY for sterically relaxed aza-BODIPY (Figure 3.7). Specifically, we proposed to replace the phenyls with thiophenes because the average diameter is ~75% the size. Similar thiophene-modified aza-BODIPYs have been previously prepared and analyzed using X-ray crystallography and UV-Vis spectroscopy.[90–93] These studies confirmed a substantial planarization of the dye backbone and red shifting. However, their applicability to activity-based sensors and PA imaging remain unexplored. Moreover, we hypothesized that incorporation of sulfur atoms would induce

the heavy-atom effect, causing a reduction in fluorescence quantum yield and increase in PA signal. Herein, we report the optimization of APNO-5 via the systematic replacement of the 1- and 7- position phenyl rings with thiophenes and the application of the optimized compound for imaging cancer-derived NO in live animal models.

3.5 Computational investigations into the feasibility of "steric relaxation for planarization"

To investigate the feasibility of this approach, we utilized density functional theory (DFT) and time-dependent DFT (TD-DFT) to study the effect of thiophene substitution on the dihedral angle and predicted absorption of the dyes (calculated in implicit methanol solvent). The method was validated by comparing the dihedral angle between the planes of the aromatic rings and the aza-BODIPY core to previous experimental data in which the computational and experimental data were in good agreement (~28° and ~18°, respectively, Figure C.16a–d).[90,91]

a

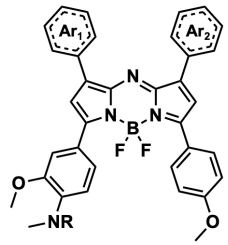

R = H or NO; Ar = Ph or Thio

b

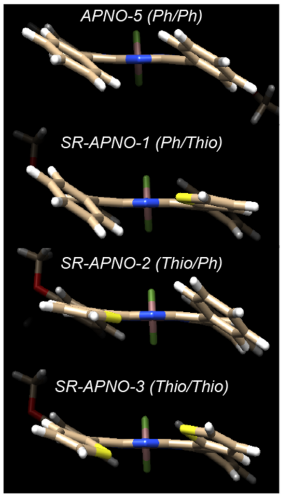

c

Name	Dihedral	$\Delta\lambda_{max,predicted}$
APNO-5	29	n.a.
SR-APNO-1	21	10/8
SR-APNO-2	21	4/11
SR-APNO-3	19	16/10

Figure 3.8: Computational investigation of the effect of thiophene replacement on the structural and absorptive properties of the SR-APNO series. Locations of the thiophenes and phenyls are indicated in parentheses (left indicates the same side of the molecule as the *o*-methoxy-methylaniline trigger, right indicates the anisole-containing side of the molecule). The solubilizing PEG chain was truncated to a methyl for computational analyses.

Replacement of the phenyls with thiophenes resulted in a decreased dihedral angle with a corresponding ~25 nm red shift per thiophene. Importantly, we observed an inverse linear

relationship between the calculated dihedral angle and experimental absorption maximum, suggesting the dihedral angle is predictive (R^2 = 0.60, Figure C.16e).

With the validated computational workflow, the probes and *N*-nitrosated products were built *in silico* with the polyethylene solubilizing group truncated to a methyl for computational analyses. The geometries were optimized, and the wavelength of maximal absorbance was calculated for each compound. In all cases, we observed a near complete decrease (8°, 80% of the disubstituted analog's effect) in dihedral angle after replacing a single phenyl and a 14 nm red shift per thiophene (Figure 3.8). Additionally, inverse correlations were observed between the dihedral angle and wavelength of maximal absorbance for both the initial probe (R^2 = 0.64) and the *N*-nitrosated product (R^2 = 0.59). These trends were consistent with the results from gas phase optimized geometries with the universal force field (R^2 = 0.60, 0.90) and B3LYP hybrid functional (R^2 = 0.69, 0.90), suggesting that these should be sufficient for predicting the effect of steric interactions on the aza-BODIPY's wavelength (Figure C.16e).

3.6 Development and characterization of SR-APNO

Encouraged by the computational results, we prepared both singly substituted constitutional isomers, SR-APNO-1 and SR-APNO-2, and the disubstituted analogue, SR-APNO-3, using similar chemistry to APNO-5 (see Appendix C for detailed synthetic information).

Table 3.2: Photophysical properties of APNO-5 and the SR-APNO series. λ_{max} and ε are reported in methanol and Φ is reported in ethanolic 20 mM potassium phosphate buffer (pH 7.4, 50% v/v). Data is reported as the average of experimental replicates (*n* = 3) with less than 15% error.

SR-APNO	λ_{max} (nm)	ε ($M^{-1}cm^{-1}$)	Φ	t-SR-APNO	λ_{max} (nm)	ε ($M^{-1}cm^{-1}$)	Φ
1	775	3.38×10^4	0.004	1	685	2.25×10^4	0.26
2	770	3.18×10^4	0.015	2	688	1.56×10^4	0.17
3	790	7.24×10^4	0.002	3	704	5.31×10^4	0.10

Photophysical characterization indicated that all probes and *N*-nitrosated products displayed maximal absorbance at greater than 680 nm, maintained high extinction coefficients and low quantum yields, and exhibited pH-independent absorbance and fluorescence properties (Table 3.2, Figure 3.9, C.17, and C.18). The NO-mediated nitrosation was confirmed using high resolution mass spectrometry, in which clean conversion was observed by liquid chromatography mass spectrometry for each compound (Figure C.19–C.21). As anticipated, each probe underwent rapid oxidation to afford the blue-shifted product. Incorporation of two sulfurs into the chromophore resulted in a decrease in *N*-nitrosated product's fluorescence quantum yield, presumably due to the heavy atom effect, and the planarization resulted in an increase in molar absorptivity due to more efficient orbital overlap. Striking similarities between the two constitutional isomers confirmed that the planarization is not dependent on the location relative to the trigger (consistent with our computational predictions, Table 3.2 and Figure C.17–C.18). This is in contrast to the conformational restriction approach in which the location of restriction effects both the photophysical and PA properties.[87] The SR-APNO series, along with previous reports,[90–93] indicate that planarization via steric relaxation is similarly efficient for red-shifting the absorbance (15 versus 0–30 nm following one modification; 30–67 nm versus 0–52 nm following two modifications).[87,94,95]

To evaluate the effect on the PA properties, the maximal ratiometric responses were measured for each compound following *N*-nitrosation (Figure 3.9 and C.17). Interestingly, neither SR-APNO-1 nor SR-APNO-2 resulted in any increase in sensitivity. On the other hand, SR-APNO-3 was 4.4-fold more sensitive than the parent molecule with a 44-fold maximal ratiometric PA turn-on response. It is important to note that the increased sensitivity arises from more efficient detection of the *N*-nitrosated product rather than changes in the initial probe (Figure 3.9b).

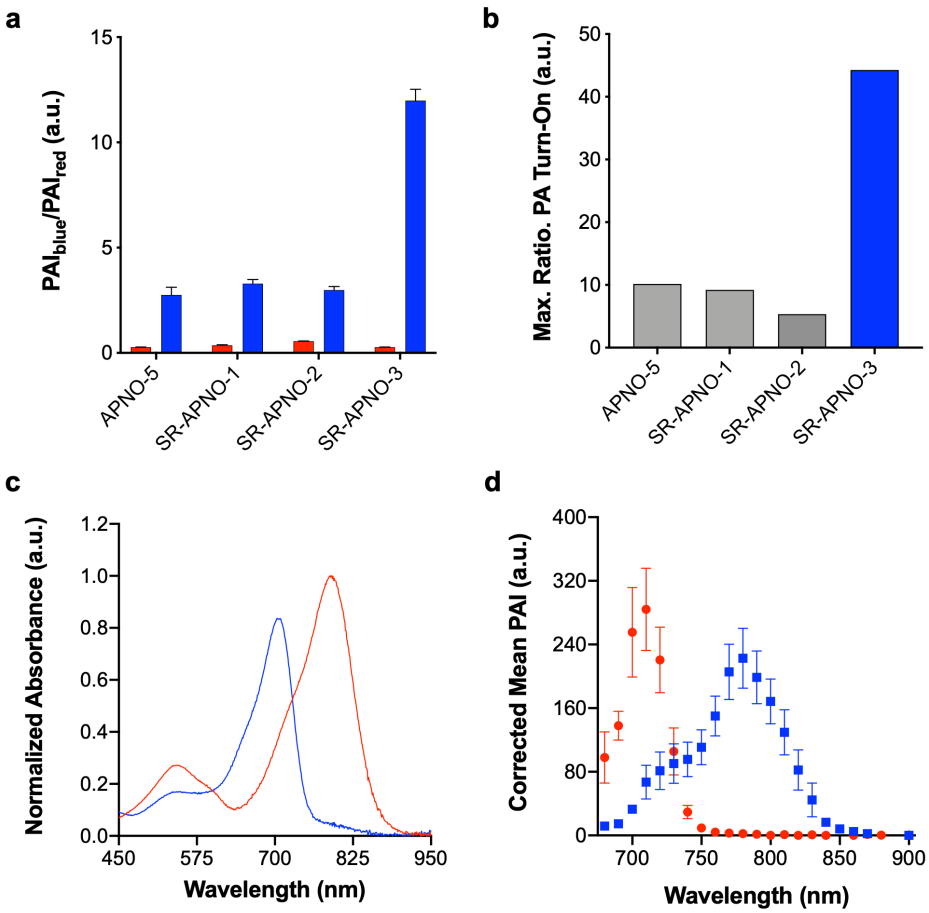

Figure 3.9: (a) Quantified PA ratios ($\lambda_{blue}/\lambda_{red}$) for each probe (red) and the corresponding *N*-nitrosated products (blue). (b) Theoretical maximal ratiometric PA responses for APNO-5, SR-APNO-1, SR-APNO-2, and SR-APNO-3 before and after nitrosation (25 µM dye, 500 equiv NO derived from MAHMA-NONOate). (c) UV-Vis (2 µM) and (d) PA spectra (10 µM) of SR-APNO-3 (red) and t-SR-APNO-3 (blue). All experiments were performed at room temperature in ethanolic 20 mM potassium phosphate buffer (pH 7.4, 50% v/v, final DMSO concentration is < 1.25% v/v). Data is reported as the mean ± standard deviation (n = 3). $\lambda_{blue}/\lambda_{red}$ (nm): APNO-5, 680/770; SR-APNO-1, 680/780; SR-APNO-2, 680/780; SR-APNO-3, 690/790.

With the ideal probe in hand, SR-APNO-3's applicability for NO imaging was evaluated. First, SR-APNO-3 and t-SR-APNO-3 were compared using UV-Vis spectroscopy and PA tomography, where maximal PA ratiometric responses were observed at 690 and 790 nm (Figure 3.9c–d). Changing the percent ethanol content of the buffer resulted in different ratiometric responses to NO; however, *N*-nitrosated product was observed at all tested concentrations (0–80% ethanol, Figure C.22a–b). The spectral changes were consistent with the formation of *J*-aggregates under aqueous conditions, which has been observed previously with the aza-BODIPY dye platform

and APNO-5.[80] Comparison between reactions performed in the presence and absence of ethanol suggest that the differences in ratiometric response occur due to differences in reaction depending on aggregation state and lower sensitivity due to beak broadening (Figure C.22c–d). Next, the selectivity of SR-APNO-3 was confirmed against a panel of reactive metals, carbonyl, oxygen, sulfur, and nitrogen species. The panel of potential cross-reactive biomolecules was selected due to the possibility of binding to the thiophenes or oxidation of the trigger, which could lead to false positives. Importantly, no changes were observed via fluorescence or UV-Vis (Figure C.23). Finally, the photostability of SR-APNO-3 and the corresponding *N*-nitrosated product were measured using an OPO laser for irradiation. All of the SR-aza-BODIPYs were photostable (greater than intensity 90% remaining after 60 s) and the *N*-nitrosated products showed reasonable stability towards denitrosylation (greater than 50% over 30 s, typical imaging is ~10 s per wavelength, Figure C.24). t-SR-APNO-3 proved to be the most photostable product. This finding is consistent with the proposed denitrosylation mechanism which includes photoinduced electron transfer from the chromophore into the N-NO bond, followed by NO release.[96,97] More broadly, this suggests that tuning intersystem crossing rates can be used to optimize both *N*-nitrosation-based NO probes and photo-activatable NO donors.[82]

The biocompatibility of SR-APNO-3 was assessed in RAW 264.7 macrophages and 4T1 murine breast carcinoma cells, where good viability was observed (Figure C.25). The cellular performance was then investigated in 4T1 cells to confirm uptake and sufficient reactivity for intracellular detection. Cells were stained with SR-APNO-3, washed to remove excess probe, and then incubated with DEA-NONOate. The cells were collected, and the cell pellet was imaged using PA tomography. Quantification revealed a dose-dependent ratiometric response (Figure C.26).

3.7 Detection of nitric oxide in a murine intramuscular inflammation model

Next, SR-APNO-3 was applied for imaging LPS-induced inflammation in BALB/c mice. To more accurately simulate the deeper tissue involved in cancer imaging, inflammation was induced through intramuscular administration of LPS rather than the subcutaneous model reported in our initial report. Under these conditions, APNO-5 was no longer able to detect NO. On the other hand, a statistically significant increase was observed using SR-APNO-3 after 3 h (Figure 3.10 and C.27). These results are consistent with the *in vitro* characterization, where SR-APNO-3 was shown to be more sensitive than APNO-5. Mice were then co-administered SR-APNO-3 and L- N^G-monomethyl-arginine (L-NMMA), a pan-selective nitric oxide synthase inhibitor,[98] to confirm that the signal enhancement was a result of NO. Under these conditions, we observed a 12% reduction in the ratiometric response (Figure 3.10b and C.27). This suggests that SR-APNO-3 could serve as a tool for evaluating anti-inflammatory small molecules within live mouse models.

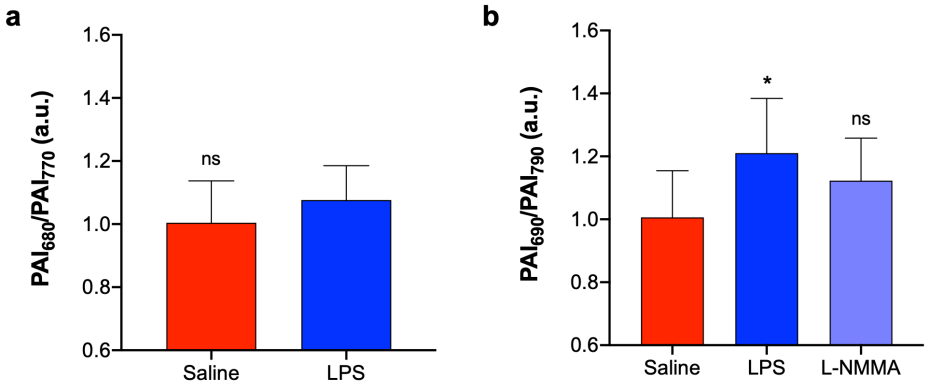

Figure 3.10: (a) APNO-5 (50 µM, 25 µL) and (b) SR-APNO-3 (50 µM, 25 µL) PA imaging of NO in an intramuscular LPS-induced inflammation model. Statistical analysis was performed using (a) an unpaired t test ($\alpha = 0.05$) or (b) Dunnet's multiple comparisons ($\alpha = 0.05$). *, $p < 0.05$. Data is reported as the mean ± standard deviation (APNO-5, $n = 5$; SR-APNO-3: saline, $n = 7$; LPS, $n = 8$; L-NMMA, $n = 4$).

3.8 Detection of nitric oxide in a heterotopic breast cancer model

As previously mentioned, NO plays a key role in cancer biology, where high concentrations are initially biosynthesized by macrophages to elicit anti-tumoral effects. After this brief window

of inflammation, emerging evidence suggests that the tumor microenvironment decreases macrophage motility, thereby trapping the macrophages within the tumor. These immune cells, often referred to as tumor-associated macrophages, produce lower levels of NO which promote tumor progression, angiogenesis and premetastatic potential.[99]

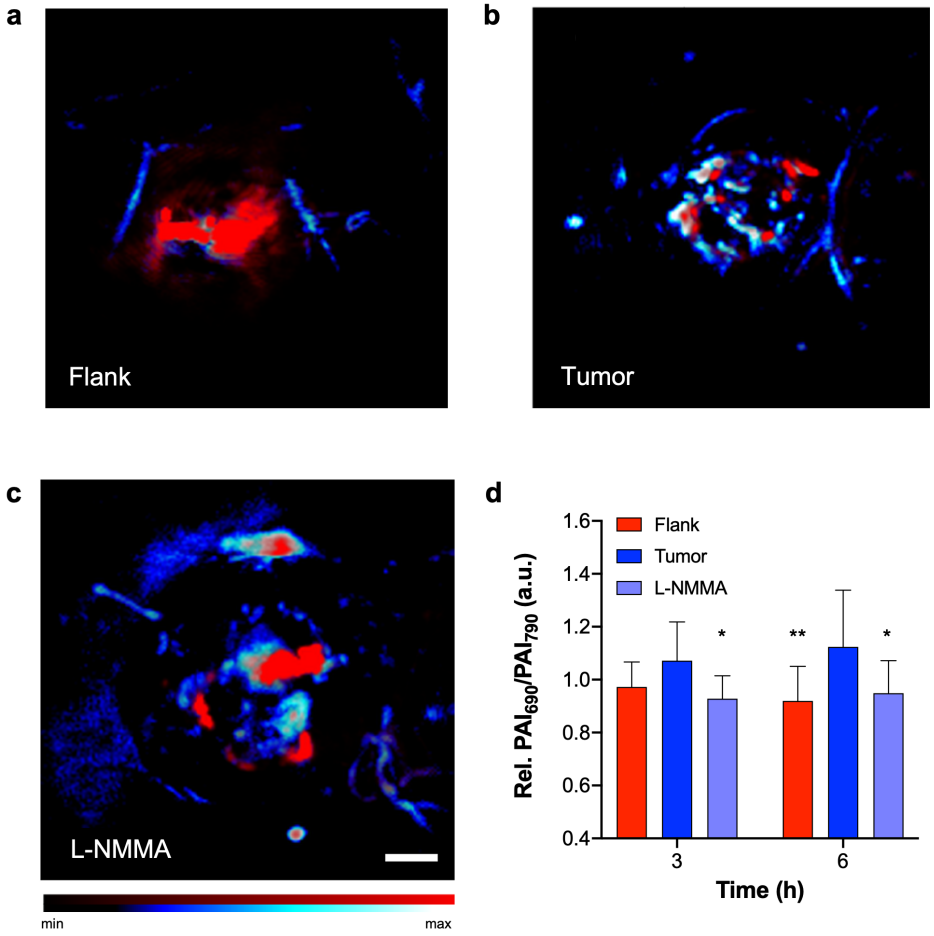

Figure 3.11: SR-APNO-3 PA imaging of cancer-derived NO. (a-c) Representative image overlays corresponding to the *N*-nitrosated product (690 nm, blue) and SR-APNO-3 (790 nm, red) after 6 h subcutaneous or intratumoral administration (25 µL, 50 µM, 15% DMF in saline v/v). (d) Quantified relative ratiometric PA at 3 and 6 h. Statistical analysis was performed using 2-way ANOVA ($\alpha = 0.05$) between the flank, tumor, and L-NMMA inhibited tumor. Relative ratiometric signals were compared to the tumor at each time point using Sidak's multiple comparison test ($\alpha = 0.05$). *, $p < 0.05$; **, $p < 0.01$. Data is reported as the mean ± standard deviation (flank, $n = 11$; tumor, $n = 18$; L-NMMA, $n = 9$). Scale bar represents 2.0 mm.

After local administration of SR-APNO-3 we observed a clear difference in the ratiometric PA response between the flank and tumor indicating that the probe was *N*-nitrosated. After 6 h, a 1.22-fold increase in the relative ratiometric PA response was observed between the flank and

tumor. To confirm these results, we deemed it necessary to inhibit NO biosynthesis within the tumor, where co-administration of L-NMMA and SR-APNO-3 resulted in an 81% decrease in the relative ratiometric PA response (Figure 3.11 and C.28). This represents the first example of where the PA imaging of cancer-derived NO has been validated using a NOS inhibitor. To confirm that the signal change was not due to changes in any endogenous absorbers (e.g., hemoglobin or deoxyhemoglobin), we performed an intratumoral injection of L-NMMA without SR-APNO-3. Under these conditions, we observed no change in the relative ratiometric PA response (Figure C.29). Together, these imaging studies demonstrate that SR-APNO-3 can be applied to facilitate deep tissue imaging of cancer NO, where concentrations are approximately three orders of magnitude less than those found in acute inflammation.

3.9 Reflection on SR-APNO-3's performance and areas for improvement

This represented the first systematic optimization of the aza-BODIPY dye platform that interrogates the effect of relieving steric interactions for dye planarization and PA signal optimization. A computational model was validated for predicting the effect of steric relaxation on the dihedral angle, which was confirmed experimentally. Replacement of a phenyl with a thiophene resulted in a circa 15 nm shift in the absorbance maxima, regardless of where the replacement was in comparison to the trigger. This contrasts with the conformational restriction approach, in which the location was essential for obtaining desirable PA properties. Replacing both aromatic rings with thiophenes had an additive effect and yielded the optimal compound, SR-APNO-3, which was 4.4-fold more sensitive than the parent molecule, APNO-5. SR-APNO-3's increased sensitivity allowed for higher ratiometric responses in an intramuscular inflammation model and the first successful detection of cancer-derived NO with a small-molecule PA contrast

agent. This small molecule approach for PA probe optimization is in contrast to recent nanoparticle-based examples which focus on for enhancing the sensitivity of NO-responsive PA by co-administering inert or analyte-selective probes for internal calibration or added sensitivity.[100,101]

Although SR-APNO-3 extended the accessible concentrations of detectable NO to nanomolar steady-state concentrations, this work also highlighted two necessary areas for improvement. The first problem is the unpredictable biodistribution of aza-BODIPY dyes, in which the properties depend significantly on the installed trigger. For example, Hyp-1 and photoNOD-1 can be administered systemically, but rHyp-1, photoNOD-2, APNO-5, and SR-APNO-3 require local administration.[82,86,88,102] This is of particular importance because the majority of the aforementioned dyes differ by a single functional group (e.g., methoxy versus diethyl aniline). The second problem is the lack of sensitivity that has been achieved in small animal models. Even with significant improvements obtained *in vitro* (greater than three-fold increase in the maximal ratiometric PA response), the live animal performance of the small molecule activatable PA probes remain low (approximately 1.2-fold).[87] This facilitated the detection of catalytic and super-stoichiometric stimuli; however, the limited dynamic range limits (semi)-quantitation and increases the required sample sizes for statistical analysis. We proposed that selecting a dye platform with superior pharmacokinetics and fluorescence capabilities could overcome these shortcomings. This prompted our investigation into the cyanine dye platform.

3.10 Development of a multimodal nitric oxide probe for fluorescence and photoacoustic imaging

Our initial investigations had elected to use the aza-BODIPY due to its superior photo- and

chemo-stability; however, we have discovered that probes built on this scaffold have unpredictable pharmacokinetics. Of the current dye families that possess desirable PA properties, (semi)-cyanines, aza-BODIPYs, squarines, and porphyrinoids,[75] the cyanine platform stands out because of their widespread success in optical imaging,[103,104] favorable biodistribution profiles,[105,106] and successful translation into the clinic (e.g., indocyanine green).

Cyanine dyes are classically defined as two nitrogen containing heterocycles that are linked (conjugated) through an odd number of carbons and where one of the nitrogen is positively charged.[107] Several targeted and activatable cyanine PA probes have emerged over the past ten years for imaging metals, reactive oxygen species, and enzyme targets.[108–112] The major limitation of this dye platform is its poor stability. The best-known decomposition occurs due to their propensity to undergo rapid photobleaching via type II photosensitization. Upon photoexcitation, the cyanines are poised for intersystem crossing to the lowest triplet state. Molecular oxygen then serves as excellent quencher (10^9 L mol^{-1} s^{-1}) via triplet-triplet energy transfer and this generates the ground state dye, as well as singlet oxygen. The proximity of this electrophilic oxygen promotes oxidation at the most nucleophilic site of the cyanine (typically the enamine), dioxetane formation, and cleavage to yield two carbonyl fragments.[113,114] Alternatively, electron rich cyanines are prone to oxidation by reactive oxygen species[115] or photobleaching through type I photosensitization mechanisms, where photo-induced electron transfer to molecular oxygen yields the superoxide radical for oxidation at the most electrophilic site.[116]

We began by attempting to translate our work on the aza-BODIPY platform as a framework for the cyanine probe. We had previous screened the most common NO sensing mechanisms when preparing the APNO series and determined that the *N*-nitrosation was optimal, both in terms of kinetics and the wavelength shift (which is correlated to the maximum ratiometric PA response).

The first example of an NO cyanine probe based was published in 2005 and employed an "off-on" fluorescence response following triazole formation.[68] Since then, an *N*-nitrosation-based optical sensor was reported on the Cy7 dye, in which *N*-nitrosation occurs at a *meso* methylamine to elicit a wavelength shift. This probe facilitated the detection of endogenous NO in live mice with NIR I fluorescence imaging; however, the optical properties are not compatible with the excitation range of lasers in commercially available tomographers (minimal absorbance at and above 680 nm).[117] We hypothesized that we could address this, and potential mitigate cross-reactivity with reactive oxygen species or cytochrome P450-dervied cytotoxic products, by trapping the *N*-nitroso on a less nucleophilic and sterically accessible aniline. To test this hypothesis, we design and synthesized the cyanine-based NO probe, CyAPNO, in three steps from 4-nitrophenol. First, 4-nitrophenol was alkylated with propargyl bromide and then reduced with stannous chloride to afford the aniline. The test compound, CyAPNO, was then obtained in 16% yield by alkylating the intermediate with the *meso*-chlorinated dye, Cyanine-Cl (Scheme 3.2).

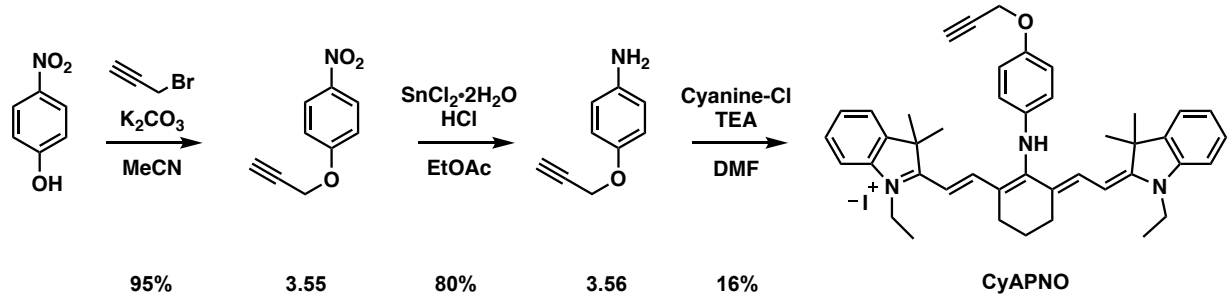

Scheme 3.2: Generalized synthesis for the CyAPNO in three steps from 4-nitrophenol with a 12% overall yield.

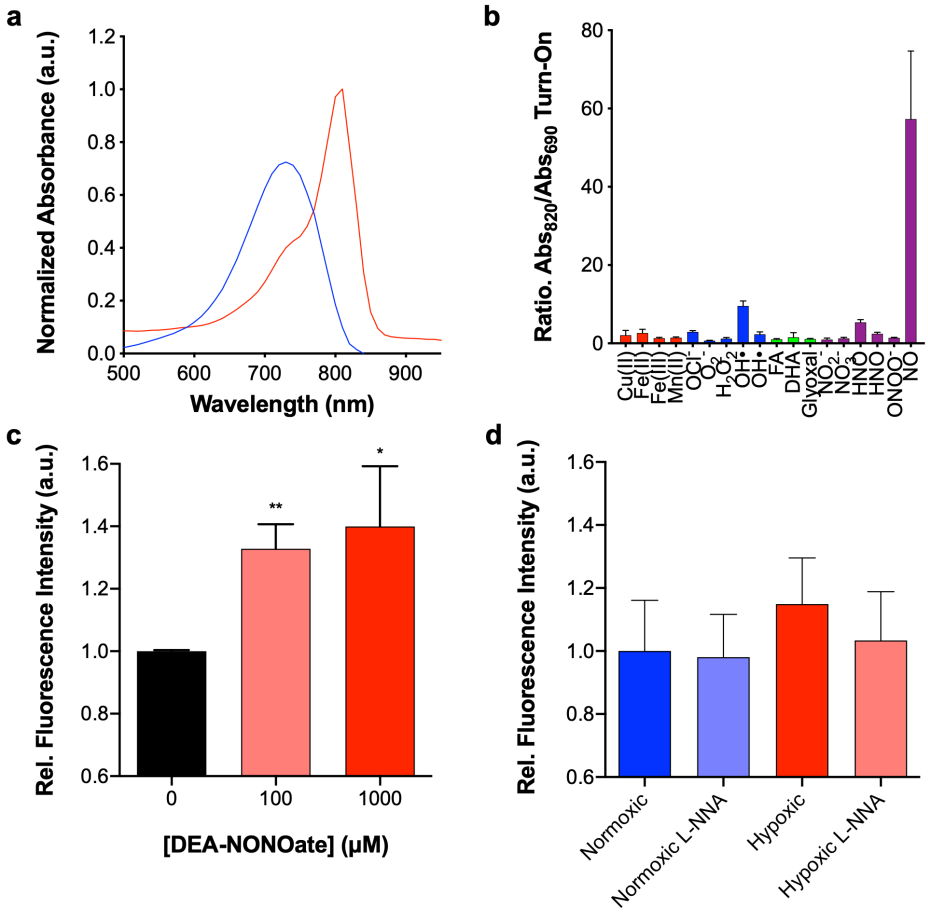

Figure 3.12: (a) Normalized absorbance spectra of CyAPNO (blue) and tCyAPNO (red). (b) CyAPNO (5 μM) fluorescence enhancement following 1 h treatment with excess (100 equiv) reactive metal (red), carbonyl (green), oxygen (blue), or nitrogen (purple) species with the exception of hydroxyl radical and peroxynitrite (10 equiv). (c) Relative fluorescence observed following exogenous NO administration or (d) endogenous hypoxic NO stimulation in 4T1 breast cancer cells. All spectra and assays were performed in 50 mM HEPES buffer (pH = 7.4) containing 0.1% CrEL (v/v). Relative fluorescence intensity was compared using an unpaired t test ($\alpha = 0.05$). *, $p < 0.05$; **, $p < 0.01$. Data presented as mean ± standard deviation ($n = 3$) for (b-c).

Initial studies were performed using absorbance (as a proxy for PA) and fluorescence spectroscopy. Treatment of CyAPNO with NO resulted in a substantial 77 nm shift of the λ_{max}. Ideal wavelengths were experimentally identified from the absorbance and fluorescence spectra. Under these conditions, we observed a 57-fold and 7.5-fold maximal ratiometric absorbance and fluorescence response. These responses were selective for NO and non-responsive across a range of reactive metal, oxygen, nitrogen, and metal species, confirming that the secondary aniline trigger maintains its functionality on the bulky cyanine dye platform (Figure 3.12).

As expected, both CyAPNO and tCyAPNO display some pH dependence (pK_a = 8.5); however, only modest changes are observed below pH = 8.0 (Figure 3.30). Moreover, CyAPNO's reactivity was sufficient to detect exogenous (from DEA-NONOate) and endogenous hypoxia-promoted NO in 4T1 breast cancer cells (Figure 3.12c).[15] More broadly, this strongly suggests that oxygen-dependent NO sensing mechanism do not hinder the ability to detect NO under typical hypoxic conditions. Inhibitor or siRNA studies targeting iNOS would strengthen this conclusion, but we proceeded to confirm whether CyAPNO was compatible with systemic (retro-orbital) injection because of its limited photostability (50% signal lost after approximately 3 h in buffer, Figure C.31).

CyAPNO was evaluated in a similar model to the SR-APNO-3 cancer imaging studies; however, the imaging was performed earlier to interrogate uptake shortly after the tumor vasculature is considered sufficient (approximate tumor volume of 100 mm^3 rather than 300 mm^3). This extends the period of time where one could study relative NO concentrations as a function of tumor progression. The CyAPNO concentration was selected to maximize the dose with reasonable organic cosolvent and the excitation and emission filter tests were selected based on maximal ratiometric responses following subcutaneous injection of authentic CyAPNO and tCyAPNO samples into the flank (50 μL of 50 μM solution in saline, 2.5% DMSO v/v). After administration (t = 0 h) we observed a sharp decrease in the fluorescent ratio of tCyAPNO to CyAPNO, both in the tumor and flank. This is consistent with systemic distribution with gradual uptake in the tumor (t = 0.5–5 h). Between 5 and 108 h, we observed the accumulation of tCyAPNO only in the tumor with a maximum 1.9-fold ratiometric response relative to the flank (t = 36 h). The probe cleared after ~204 h (Figure 3.13). Encouraged by these findings, we sought to improve on the dye platform's photostability with the hopes of increasing the dynamic range.

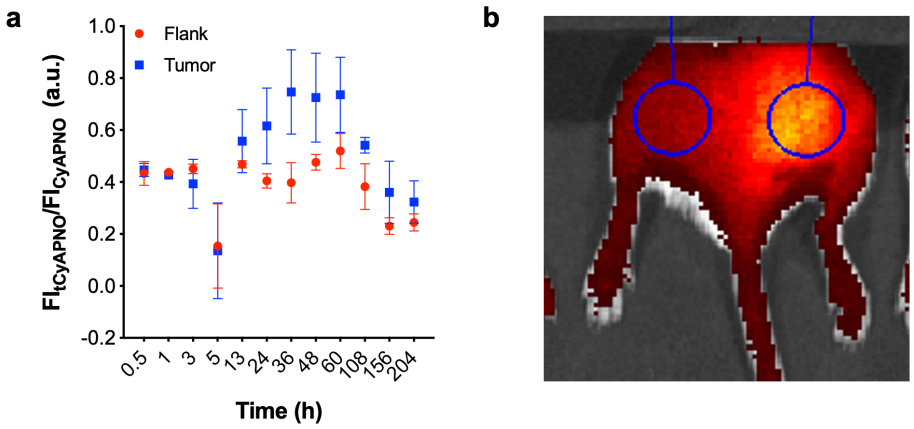

Figure 3.13: (a) Ratiometric fluorescence imaging of NO in a heterotopic 4T1 breast cancer model following systemic administration of CyAPNO (100 µL, 100 µM, retro-orbital) (b) Representative image of fluorescence corresponding to tCyAPNO in the flank (left) and tumor (right).Fluorescence intensity corresponding to CyAPNO is similar in the flank at tumor. Data presented as mean ± standard deviation (n = 3).

3.11 Progress towards a photostable dye for multimodal fluorescence and photoacoustic imaging following systemic administration

Several solutions have emerged to address this poor photostability with a central theme: decrease nucleophilicity to prevent photodecomposition via type II photosensitization. Generally, an inductive approach is employed, in which electron withdrawing functional groups are introduced in conjugation[114,116,118] with or at the reaction center.[113,119] Electron withdrawing group introduction would also likely decrease the *N*-nitrosated product from releasing NO through photo-electron transfer-based homolysis, further enhancing its sensitivity.[82,97,120] We were particularly intrigued by functionalization at the reaction site because polyfluorination of the cyanine decreased the extinction coefficient, increased the fluorescence quantum yield, and altered aggregation behaviors. These would be detrimental for PA probe development and are not readily explained We proposed that fluorination at the site of the reaction, rather than cyano-substitution,[113,119] would serve as the smallest perturbation and should therefore limit any photophysical changes.

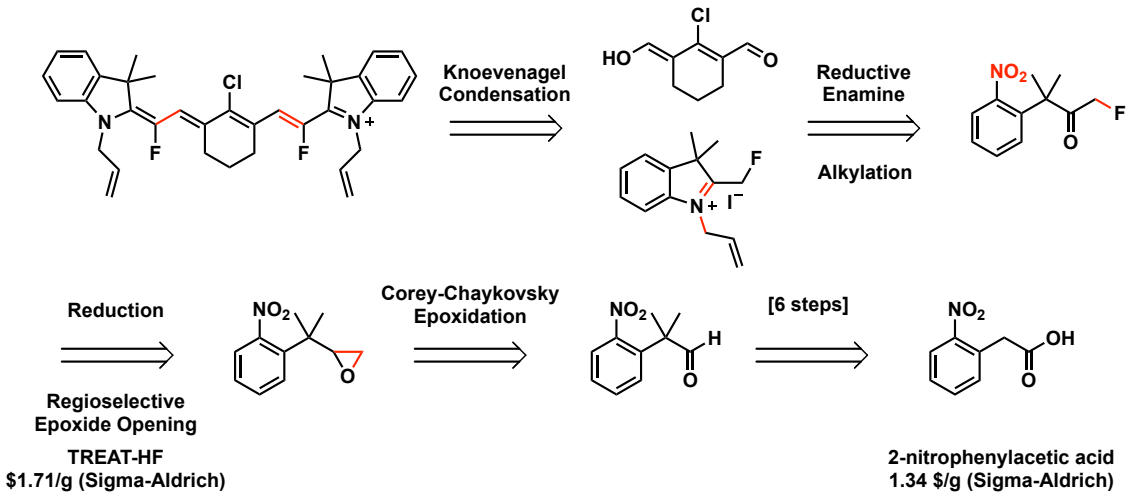

Scheme 3.3: Retrosynthetic analysis for the synthesis of F_2-Cyanine-Cl using nucleophilic fluoride sources.

The fluorinated cyanine scaffold was approached in a similar fashion to the non-fluorinated parent compound, in which 1-alkyl-2,3,3-trimethyl-3H-indol-1-ium is subjected to a Knoevenagel condensation reaction with the Vilsmeier-Haack product, (*E*)-2-chloro-3-(hydroxymethylene)cyclohex-1-ene-1-carbaldehyde. Preliminary efforts to directly fluorinate the 1-alkyl-2,3,3-trimethyl-3H-indol-1-ium or indole with radical or electrophilic fluorine sources proved unsuccessful. Thus, we proposed a novel retrosynthesis approach to the indoline through oxidative condensation between a fluorohydrin and aniline or reductive cyclization between an α-fluoroketone. We elected to proceed through the fluorohydrin as this is readily available via regioselective fluoride opening of an epoxide with nucleophilic fluoride and nucleophilic sources (e.g., mineral fluoride salts, ammonium fluoride salts) tend to be significantly cheaper than electrophilic (e.g., *N*-fluoropyridinium triflate, Selectfluor, NSFI) fluorination reagents. The epoxide could then be prepared directly from the aldehyde through Johnson-Corey-Chaykovsky epoxidation. The requisite aldehyde could be accessed in six steps from commercially available 2-nitrophenylacetic acid (Scheme 3.3).

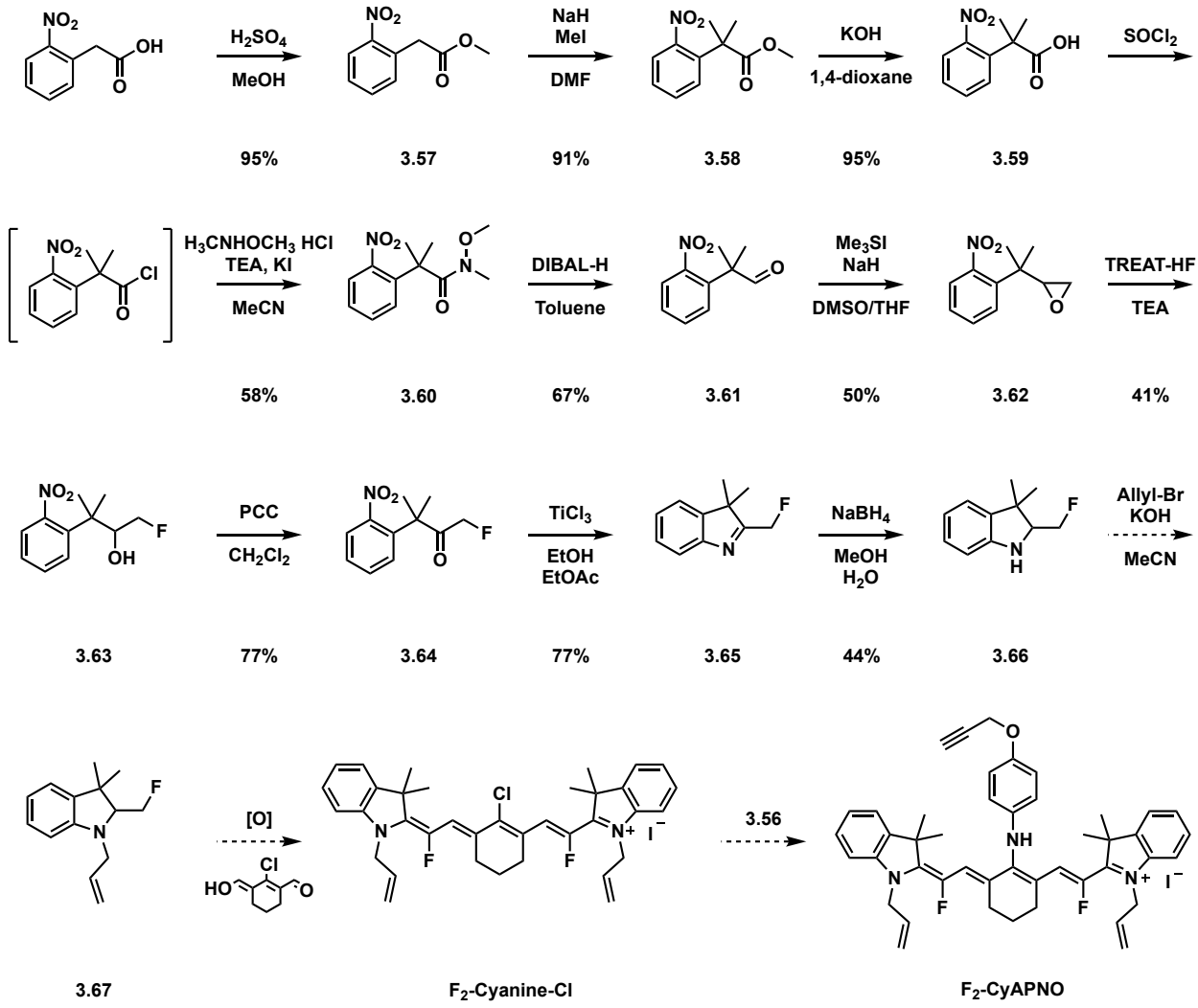

Scheme 3.4: Progress towards the synthesis of F_2-CyAPNO in 14 steps from 2-nitrophenylacetic acid.

The sequence began with Fisher esterification of 2-nitrophenylacetic acid in acidic methanol to afford the methyl ester, **3.57**, in 95% yield. The ester was then exhaustively methylated with methyl iodide and sodium hydride to afford compound **3.58** in a 91% yield. It is possible to directly treat 2-nitrophenylacetic acid with excess methyl iodide and sodium hydride; however, these conditions are less cost effective. Efforts to selectivity reduce the ester proved unsuccessful (AlH_3, limiting amounts of DIBAL-H, $NaBH_4$-$CeCl_3$, etc.) and resulted in significant reduction of the aryl nitro or poor yield. This is likely due to the steric hinderance proximal to the ester. Ester hydrolysis was performed at 130 °C with 10 M aq. potassium hydroxide in minimal 1,4 dioxane. The

carboxylic acid **3.59** could be ready isolated by precipitation in water. Next, the carboxylic acid was activated as an acyl iodide (*in situ* from the acid chloride) prior to Wienreb amide formation with *N*,*O*-dimethylhydroxylamine. Note that reduction to the alcohol, followed by oxidation to the aldehyde with pyridinium chlorochromate has been reported previously;[121] however, our reaction sequence scaled more efficiently (decagram scale in single pass). Direct epoxidation of the aldehyde was achieved under Johnson-Corey-Chaykovsky conditions with trimethylsulfonium iodide and sodium hydride in THF, providing the required terminal epoxide, **3.62**, in modest 50% yield. The major decomposition pathway was identified as producing, 1-(1-methoxyprop-1-en-2-yl)-2-nitrobenzene, presumably resulting from deprotonation at the methyl, epoxide opening, and subsequent methylation. Attempts to decrease this side reaction were unsuccessful due to the poor reactivity of the sterically hindered aldehyde.

Regioselective epoxide opening was performed with TREAT-HF in TEA (for a 1:1 ratio of TEA to HF). These conditions had previously been reported for favoring S_N2 fluorination at the terminal carbon.[122,123] The isolated fluorohydrin underwent smooth oxidation by PCC to afford the α-fluoroketone **3.64** in 84% yield. A variety of reductants were screened for the selective reduction of the nitro in the presence of the ketone; however, defluorination (iron, zinc) or *N*-oxide formation (palladium on carbon with hydrogen gas, stannous chloride monohydrate) prohibited access to the desired product. Titanium trichloride could reduce the *N*-oxide intermediate and, somewhat surprisingly, did not result in dehalogenation.[124] Moreover, titanium trichloride afforded efficient access to indoline **3.65** directly from nitroaryl **3.64** in 77% yield. Alkylation of the indoline with ethyl halides or pseudo-halides (X = Br, I, or triflate) resulted in either decomposition, dehalogenation, or no reaction depending on the temperature. To overcome this, we reduced the imine with sodium borohydride to increase the product's stability. While similar reactivity was

observed across the panel of electrophiles, we identified that treatment with allyl bromide, in the presence of potassium hydroxide, afford the product at room temperature for the non-fluorinated analog (67% yield). We are optimistic that these conditions can be translated to yield the tertiary amine, **3.67**, in reasonable yields. Current efforts are focused on the allylation and screening oxidants that can facilitate *in situ* oxidation of **3.67** to the desired indolium followed by direct Knoevenagel condensation to afford the fluorinated platform. This would circumvent the isolation of the unstable and reactive intermediate. With the desired F_2-Cyanine-Cl dye in hand, we would assess its photophysical properties, stability profile, and PA compatibility. The final NO probe could be synthesized in a similar manner as CyAPNO to yield the final product F_2-CyAPNO.

3.12 Summary and outlook

There has been significant progress over the past decade regarding the design and application of activatable PA probes (see section 1.4.3).[75,102,125–129] NO's complex regulation and diverse biological activities make it a prime target for molecular imaging. This is particularly true in the context of cancer, in which oxygen distribution, reactive oxygen species, and NOS crosstalk with other pro-inflammatory mediators serve to generate distinct phenotypes. Our initial goal was to development a PA probe that could detect NO at inflammatory concentrations (nM–μM steady-state concentration) in live animals. This was achieved by modifying the aza-BODIPY dye platform with most common NO triggers. The *N*-nitrosation sensing mechanism was identified as optimal because it yielded the largest maximal ratiometric PA response. This lead compound, APNO-5, was applied for the detection of NO in an LPS murine inflammation model and further established target-induced wavelength shifting as a reliable method for PA probe development. Unfortunately, APNO-5's sensitivity was not sufficient for detecting NO at lower concentrations

because of the poor spectral overlap between the *N*-nitrosated product and the excitation source on commercially available PA tomographers.

We tackled this hurdle by devising a new approach, termed "steric relaxation for planarization", to enhance the aza-BODIPY dye platform PA performance. A computational model was prepared for *ad hock* evaluation of the approach and this was experimentally validated. The disubstituted probe, SR-APNO-3, proved to be the best and displayed a 4.4-fold and 1.1-fold increases in ratiometric PA response (relative to APNO-5) within tissue-mimicking phantoms and an intramuscular LPS murine inflammation model, respectively. SR-APNO-3 enabled the first validated detection of NO in a murine 4T1 breast cancer model. While the 1.2-fold ratiometric PA response was sufficient for detection and validation with an inhibitor, it is insufficient for semi-quantitative comparisons and not compatible with systemic administration. As it stands, SR-APNO-3 has applications as a potential molecular imaging-based extension for inflammation animal models. This would serve to expand the current methods to provide information about the mechanism, where NO is often a direct or indirect target of anti-inflammatory compounds.[130]

From our work on the aza-BODIPY dye platform, it appears that the ratiometric responses are constrained to 2-fold ratiometric responses using commercially available PA tomographers. Moreover, the parameters dictating biodistribution and systemic compatibility remain unclear. This prompted investigations towards a cyanine-based multimodal fluorescence and PA dye platform because of their wide success in optical imaging and reasonable biodistributions in living specimen. Rather than rival methods, we proposed their complementary to access increased dynamic range, superior deep tissue resolution and three-dimensional information with a single activatable contrast agent. Preliminary studies employing a *N*-nitrosation-based cyanine probe, CyAPNO, provided promising results regarding probe localization following retro-orbital

injection and the ability to detect cancer-derived NO. However, poor photostability remains a challenge, particularly when performing multiple excitations with different imaging modalities. We devised a generalizable NIR I fluorinated cyanine platform to combat this instability and we are within two to three steps from the F_2-Cyanine-Cl dye platform with an additional step to access the multimodal NO probe, F_2-CyAPNPO. Current efforts are focused on completing the synthesis.

Future efforts should focus on completing the synthesis of F_2-Cyanine-Cl and comparing the photophysical properties between the fluorinated and non-fluorinated platforms. A benchmark of success would be a 10% decrease in the photobleaching rate–as this is comparable to previous optimization strategies–while maintaining the large extinction coefficient (approximately 10^6 M^{-1} cm^{-1}) and low–moderate quantum yields.[113,114,116,118,119] Additionally, *N*-nitrosated F_2-CyAPNO's stability against denitrosylation should be similar to SR-APNO-3. Ideally, this would enhance the ratiometric fluorescence signal for semi-quantitation of relative NO concentrations, while still achieving useful, three-dimensional data regarding the location within the tumor microenvironment. Together, these optimized properties should increase the signal-to-noise observed using JW41, a recent hydrogen peroxide cyanine probe for fluorescence and PA imaging, in which 40% conversion of the probe to the uncapped product corresponded to a 1.5-fold and 2-fold ratiometric fluorescent and PA responses. Note that these ratios are from the isosbestic point to a wavelength corresponding to background, rather than those selected to maximize the signal difference between probe and product, and should serve as an underestimate the JW41's sensitivity.[112]

There are many of future directions to consider for this project after a suitable probe is acquired, particularly in the realm of cancer biology. For example, examining the concentration and distribution of NO as a function of tumor progression. This could shed light on the timing and

regulatory mechanisms that drive the transition between anti-tumor and pro-tumor activity, as well as the source (i.e., iNOS, eNOS, nNOS, or nitrite reductases) and distribution throughout the tumor. Parallel amperometric and histochemical analyses could complement the imaging data to confirm the dynamics and spatial information. Investigations regarding the clinical relevance are also warranted. Chiefly those that compare and validate if activatable probes are superior to their non-targeted and targeted counterparts. In summary, the development of NO-selective probes facilitated the non-invasive imaging of NO within live mice, established new approaches for dye optimization, and set the stage for new biological discoveries and clinical applications.

3.13 Experimental Methods

Experimental protocols and information are included below in the following order and combined whenever possible: general materials, instrument, and software information; *in vitro* characterization; cell-based studies; and then *in vivo* experiments.

3.13.1 Materials

Materials were purchased from commercial vendors and used without further purification. 3-(4,5-Dimethylthiazol-2-yl)-2,5-diphenyltetrazolium bromide (MTT), dichloromethane, DIBAL-H in heptane, isoamyl nitrite, propargyl bromide (80% w/w in toluene), and triethylamine were purchased from Acros Organic. Hydrogen was purchased from Airgas. 1,3-Dimethylbarbituric acid, 4'-hydroxyacetophenone, 4'methoxyacetophenone, and ninhydrin were purchased from AK Scientific. Allyl bromide, nitromethane, sodium hypochlorite (14.5% available chlorine in water), and tetraethyleneglycol were purchased from Alfa Aesar. Ammonium acetate and sodium nitrate were purchased from Amersco. All deuterated solvents were purchased from Cambridge Isotope Laboratories. Diethylamine NONOate (DEA-NONOate), methylamine hexamethylene

methylamine NONOate (MAHMA-NONOate) and sodium α-oxyhyponitrite (Angeli's salt) were purchased from Cayman Chemicals. Tris(3-hydroxypropyltriazolylmethyl)amine was purchased from Click Chemistry Tools. 4'-Hydroxy-3'-nitroacetophenone was purchased from Combi-Blocks. Anhydrous ethanol (Decon Lab), ammonium chloride, chloroform, copper sulfate pentahydrate, Cremophor EL (Fluka), diethyl ether, ethyl acetate, glacial acetic acid, *n*-butanol, phosphate saline buffer (Corning), *o*-phosphoric acid, potassium phosphate dibasic, potassium phosphate monobasic, sodium bicarbonate, sodium chloride, and toluene were purchased from Fisher Scientific. Agarose LE (Molecular Biology Grade) was purchased from Gold Biotechnology. ER-Tracker™ Green, LysoTracker® Green DND-26, MitoTracker® Green FM were purchased from Life Technologies. Acetonitrile, anhydrous methanol, concentrated hydrochloric acid, hydrogen peroxide (30% v/v) and sodium hydroxide were purchased from Macron Fine Chemicals. Ammonium acetate, 2-aminophenol, 4'-fluoro-3'-nitroacetophenone, 4-dimethylaminopyridine, 4-methoxyacetophenone, aluminum trichloride, 4-bromo-3-methylaniline, carbonyldiimidazole, di-tert-butyl dicarbonate, diisopropylethylamine, ethylene dichloride, methanesulfonyl chloride, methyl iodide, *N*,*O*-dimethylhydroxylamine, potassium carbonate, potassium hydroxide, potassium iodide, pyridinium chlorochromate, sodium ascorbate, sodium azide, sodium sulfate (anhydrous), tetrakis(triphenylphosphine)palladium(0), thiophene-2-carbaldehyde, tin(II) chloride dihydrate, trimethylsulfonium iodide, and triphenylphosphine were purchased from Oakwood Chemicals. 1,4-Dioxane, acetyl chloride, ammonia (7 M in methanol), ammonium iron sulfate (Mohr's salt), anhydrous acetonitrile, anhydrous dichloromethane, anhydrous dimethylformamide, anhydrous dimethysulfoxide, anhydrous tetrahydrofuran, benzaldehyde, boric acid, boron trifluoride dietherate, *n*-BuLi in hexanes (2.5 M), t-BuLi in pentanes (1.7 M) celite 545, copper(II) chloride, dimethylamine (40% w/w in water),

dipropylamine, formaldehyde (37% w/w in water), glyoxal (40% w/w in water), HEPES, hexanes, indocynanine green, iron(II) sulfate heptahydrate, iron(III) chloride (anhydrous), iron powder, L-ascorbic acid, L-dehydroascorbic acid, lipopolysaccharides from Escherichia coli O111:B4 (purified by phenol extraction), L-N^G-monomethyl-arginine acetate salt (L-NMMA), manganese(II) chloride, nitric oxide, palladium on carbon (10% w/w), potassium permanganate, potassium superoxide, propargyl bromide (80% w/w in toluene), rat liver microsomes (pooled, male), sodium borohydride, sodium hydride (60% dispersion in mineral oil), sodium ascorbate, sodium nitrite, thionyl chloride, titanium(III) chloride, tosyl chloride, TREAT-HF, trifluoroacetic acid, and trypan blue powder were purchased from Sigma Aldrich. Fluorinated ethylene propylene (FEP) tubing (wall thickness 0.01", inner diameters 0.08" and 0.12") was purchased from McMaster-Carr.

3.13.2 Instruments and software

^{1}H, ^{13}C, ^{11}B, and ^{19}F NMRs were acquired on Varian 400, Varian 500, or Carver B500 spectrometers. The following abbreviations were used to describe coupling constants: singlet (s), doublet (d), triplet (t), quartet (q), quintet (quint), multiplet (m), and broad singlet (bs). Spectra were visualized and analyzed using MestReNova (version 10.0). High-resolution mass spectra were acquired with a Waters Q-TOF Ultima ESI mass spectrometer and a Waters Synapt G2-Si ESI/LC-MS mass spectrometer equipped with a PDA detector (200–500 nm). Ultraviolet-visible (UV-Vis) measurements or spectra were recorded on a Cary 60 spectrometer or SpectraMax M2 plate reader (Molecular Devices). Fluorescence spectra were acquired on a QuantaMaster-400 scanning spectrofluorometer with micro fluorescence quartz cuvettes (Science Outlet) or a Denovix QFX fluorometer for performing measurements under anoxic conditions. Refractive indices were measured using an RHB-32ATC Brix Refractometer. Cellular imaging was

performed on either an EVOS FL epifluorescence microscope or a Zeiss LSM 700 Confocal Microscope and analyzed using NIH ImageJ[131] (version 1.6 or 1.8) or Zen software. Photoacoustic imaging was performed using the Endra Nexus 128 or Endra Nexus 128+ photoacoustic tomography system (Ann Arbor, MI, USA), and the data were analyzed using either OsiriX (version 8.0) or Horos (version 3.0) imaging software. Final PA images were prepared in OsiriX (version 8.0), Horos (version 3.0) or NIH ImageJ[131] (version 1.6 or 1.8). Note that the instrument was modified to the Endra Nexus 128+ specifications after publishing the work on APNO. Additional data analysis was performed using Microsoft Excel or GraphPad Prism (version 6.0 or 8.0). Mettler Toledo SevenCompact pH meter was used for pH measurements. Some final figures were prepared in Adobe Illustrator (version 22.02.02). Crystallographic figures were prepared using UCSF Chimera.[132]

3.13.3 General synthetic methods

All materials were purchased from commercial vendors and used without further purification. Specific information regarding the material's sources can be found in the Supporting Information. Thin-layer chromatography (TLC) was performed on glass-backed TLC plates precoated with silica gel containing an UV254 fluorescent indicator (Macherey-Nagel). TLC's were visualized with a 254/365 nm UV hand-held amp (UVP). Flash silica gel chromatography was performed using 0.04 – 0.063 mm 60 M silica (Macherey-Nagel). Non-commercially available anhydrous solvents were dried over 4 Å molecular sieves activated via heating under a vacuum at 300 °C. All glassware used under anhydrous reaction conditions were flame-dried under vacuum and cooled immediately before use. When required, solutions were degassed by bubbling nitrogen through the solution for a minimum of 20 minutes. Saturated solutions of NO were generated by bubbling gaseous NO from the reaction between iron sulfate heptahydrate and sodium nitrite at 100 °C

through the desired, degassed solvent (27 g iron sulfate heptahydrate and 12.5 g of sodium nitrite for ~2.5 L of NO).[133] Detailed synthetic procedures can be found in Appendix C and are provided in the following order for ease of access: APNO-1, APNO-2, APNO-3, APNO-4, APNO-5, TG-2 (deamination-based TokyoGreen probe), TG-3 (*N*-nitrosation-based TokyoGreen probe), SR-APNO-1, SR-APNO-2, SR-APNO-3, CyAPNO, and F_2-CyAPNO.

3.13.4 Photophysical characterization

Extinction coefficients and fluorescence quantum yields were acquired in experimental triplicates. *N*-nitrosated products were generated by reacting APNO with NO (500 equiv from MAHMA-NONOate solution in ethanolic 20 mM potassium phosphate buffer, pH 7.4, 50% v/v) or SR-APNO with NO (150 equiv from MAHMA-NONOate solution in ethanolic 20 mM potassium phosphate buffer, pH 7.4, 50% v/v or 60 equiv in methanol, generated from ~15 mM saturated methanolic solution) for greater than 1 h at room temperature, where complete conversion was confirmed via UV-Vis spectroscopy. Extinction coefficients were acquired by titrating or diluting compound into chloroform, methanol or ethanolic 20 mM potassium phosphate buffer (pH = 7.4, 50% v/v) within the linear range (typically absorbance values 0.05 – 1.50, final DMSO concentration < 1%). Fluorescence quantum yields were obtained using a modified method for relative fluorescence quantum yield.[134] Samples were prepared in ethanolic 20 mM potassium phosphate buffer (pH 7.4, 50% v/v, final DMSO concentration < 1%) and sequentially diluted (n > 4) while monitoring both absorbance and fluorescence. Absorbance was kept low (< 0.1) to prevent secondary absorbance events. Relative quantum yields were calculated relative to dimethoxy aza-BODIPY (ϕ = 0.36, chloroform)[94] with refractive indexes of 1.445 and 1.3573 for chloroform and ethanolic 20 mM potassium phosphate buffer (pH 7.4, 50% v/v), respectively. All SR-APNO samples were excited at 640 nm and the emission was monitored from 660–890 nm

with a slit width of 2.0 mm.

3.13.5 Reaction between APNO or SR-APNO and nitric oxide

APNO were dissolved in ethanolic 20 mM potassium phosphate buffer (pH = 7.4, 50% v/v) and treated with MAHMA-NONOate (prepared in degassed 10 mM aq. KOH) at room temperature or with NO (*g*) until a color change was observed. SR-APNO were dissolved in ethanolic 20 mM potassium phosphate buffer (pH = 7.4, 50% v/v) and treated with MAHMA-NONOate (prepared in degassed 10 mM aq. KOH) at room temperature or were treated methanolic NO (~10 mM, ~60 equiv) in anhydrous methanol for less than 5 minutes at room temperature before the solution was purged under high vacuum and then concentrated under vacuum. CyAPNO was dissolved in 50 mM HEPES (pH 7.4, 0.1% CrEL v/v) and treated with MAHMA-NONOate (prepared in degassed 10 mM aq. KOH).

3.13.6 Selectivity studies

Unless otherwise noted, APNO or SR-APNO were pre-incubated at 37 °C in an ethanolic 20 mM potassium phosphate buffer (pH = 7.4, 50% v/v) for at least 15 min. CyAPNO was pre-incubated at 37 °C in an 50 mM HEPES buffer (pH = 7.4) containing CrEL (0.1% v/v) for at least 15 min. The initial absorbance and/or fluorescence was measured follow by the addition of 100 equiv (APNO, CyAPNO) or 200 equiv (SR-APNO) of various reactive metals, oxygen, nitrogen, and carbonyl species. After addition, the reaction was sealed and incubate at 37 °C (APNO for 1 h, CyAPNO for 0.5 h) or room temperature (SR-APNO for 1 h). Final measurements were recorded, and the relative turn-on was determined by the sum of intensity over the total range of emission. Fe(II) selectivity studies were performed in ethanolic 20 mM HEPES buffer (pH 7.4, 50% v/v) to prevent oxidation. All metal solutions were prepared from their chloride salt in water with the exception of Fe(II) which was prepared from $FeSO_4 \cdot (H_2O)_7$. Aqueous formaldehyde

solutions were depolymerized by heating to solution to 100 °C for greater than 15 min before use. Aqueous dehydroascorbic acid solutions were prepared by heating at 60 °C for greater than 15 min before use. Aqueous perchlorate, nitrite, and nitrate solutions were prepared for their corresponding sodium salts. Superoxide anion was added as a solution of potassium superoxide in DMSO. Nitroxyl was generated *in situ* from a solution of Angeli's salt in degassed 10 mM potassium hydroxide solution. NO was generated *in situ* from a solution of MAHMA-NONOate in degassed 10 mM potassium hydroxide. Hydroxyl radical was generated via Fenton chemistry between Mohr's salt (solution in degassed 1 M aqueous hydrochloric acid) and hydrogen peroxide. Fe(II), nitroxyl, and hydroxyl radical selectivity assays were performed under nitrogen to prevent oxidation. Peroxynitrite was synthesized according to a literature report.[135] All other analytes were prepared by dilution from commercially available sources.

3.13.7 PA imaging in tissue-mimicking phantoms

Tissue phantoms were prepared by mixing agarose (4 g) in a solution of 2% reduced fat milk (2 mL) and deionized H_2O (78 mL). The mixture was heated in a microwave oven until a viscous gel was produced (30 seconds), the gel was then mixed and reheated for an additional 15 30 s to ensure homogeneity. The gel was transferred to a custom Teflon mold made to fit within the Endra bowl system with hypodermic steel tubing inserted to prepare channels for placing FEP tubes (0.08" diameter) containing the samples. After cooling the gel for a minimum of 1 hour at 4 °C, the phantom was removed from the mold. Sample solutions (200 μL) were pipetted into FEP tubing (0.08-inch diameter) and sealed by folding over the ends and securing with a short length of 0.12-inch diameter FEP tubing. APNO (10 μM) or SR-APNO (25 μM for theoretical maximum ratiometric comparisons; 10 μM for PA spectra) was dissolved in an ethanolic 20 mM potassium phosphate buffer (pH 7.4, 50% v/v). t-APNO-5 and t-SR-APNO were generated by reacting

APNO-5 or SR-APNO with NO (500 equiv NO from MAHMA-NONOate) for greater than 1 h at room temperature (complete conversion was confirmed by UV–vis). Images were acquired using Step and Shoot mode with 120 angles and 10 pulses per angle (APNO) or continuous mode with 6 second rotation time (SR-APNO). PA spectra were measured in the same solvent at 10 nm intervals, and signal was integrated over the total range of signal. Mean signals are reported as the average of the two samples and the experiment was performed in experimental triplicate. Fresh samples were prepared for each tAPNO-5 wavelength to limit photo-induced cleavage of the *N*-nitrosated product.

3.13.8 Photostability studies

APNO or SR-APNO and the corresponding *N*-nitrosated product (20 μM for APNO manuscript or 25 μM for SR-APNO manuscript) photostability were measured at their PA maximum in potassium phosphate saline with CrEL (0.1% v/v, APNO manuscript) or ethanolic 20 mM potassium phosphate buffer (pH 7.4, 50% v/v, SR-APNO manuscript) using the OPO laser used in the Nexus 128+ PA tomographer. Samples were irradiated discontinuously, and measurements were acquired in Step and Shoot mode (APNO manuscript, 120 angles and 10 pulses per angle) or continuous mode with a 6 s rotation time (SR-APNO manuscript). The mean signal was acquired, the average PAI was obtained for the two tubes, and relative signals were calculated according to the initial PA signal. Data is reported as the mean ± standard deviation (n = 3). CyAPNO and tCyAPNO stability was assessed under ambient conditions. Dye (5 μM) was incubated at 37 °C in diluted plasma, diluted serum, or 50 mM HEPES buffer (pH 7.4) containing 0.1% CrEL and the absorbance (500 – 900 nm) was monitored at 1, 2, 4, 6, and 18 h and compared to the initial spectra (pre-incubated for 15 min in the dark for proper solubilization).

3.13.9 Mechanistic insights about deamination- and N-nitrosation-based NO sensing

All experiments performed under anoxic conditions were performed in an anaerobic chamber (Coy) equilibrated with a nitrogen-hydrogen (5%) mixture maintained at less than 1 ppm molecular oxygen. Solutions were degassed (3×) using freeze-pump-thaw technique before transferring into the chamber. Solids and solutions were pre-equilibrated overnight before use. Assays were performed with the following ratios with a final buffer concentration of 50 mM HEPES pH 7.4: 500 eq of analyte, DNIC is 1:1:4 Fe:NO:RSH (1μM dye, 500 μM NO or 250 μM MAHMA NONOate, 500 μM iron sulfate heptahydrate, 2000 μM RSH). DNIC were prepared by incubating the iron source with the thiol for at least 5 min prior to the addition of dye and allowed to incubate at room temperature for 1 hour. Samples were then exposed to air and allowed to proceed for at room temperature for an additional hour. Normoxic samples were run in parallel for comparison.

3.13.10 Computational details

Structures were built using Avagadro[136] and were optimized using the universal force field[137] until it converged. Further geometry optimizations were performed sequentially using density functional theory using Guassian 3, 9, or 16. First, the structure was optimized using B3LYP[138,139] with the 6-31(d) basis set in the gas phase followed by B3LYP with the 6-31(d) basis set in implicit methanol solvent. All resulting structures were identified as a ground state by calculating the stretching frequencies. Dihedral angles were measured, using Chimera visualization software,[132] as the positive angle between the plane defined by all of the heavy atoms within the aza-BODIPY core and the plane defined by all heavy atoms in the ring of interest. Dihedral angles were reported as an average if the structure was symmetrical. UV-Vis spectra were calculated from the solvent optimized structure using time-dependent self-consistent frequencies

density functional theory using the CAM-B3LYP functional[140] and 6-31(d) basis set for only singlet excitations in an implicit methanol solvent.

3.13.11 Cell culture

4T1 murine mammary carcinoma cells and 264.7 RAW macrophage cells were acquired from ATCC and Prof. Elvira de Mejia (Food Science and Human Nutrition, UIUC), respectively. Cells were cultured in phenol red free RPMI 1640 medium or Dulbecco's modified eagle medium (DMEM, Corning) supplemented with 10% fetal bovine serum (FBS, Sigma Aldrich), and 1% penicillin/streptomycin (Corning). Cells were incubated at 37 °C with 5% CO_2. Cells were passaged using manual scraping (264.7 RAW macrophage cells) or trypsin (0.25% trypsin with 0.1% EDTA in HBSS without calcium, magnesium, and sodium bicarbonate, Corning, 4T1 murine mammary carcinoma cells) at least every 3 days. Cells were incubated at 37 °C with 5% CO_2 unless specified otherwise. Experiments were performed in 4-well chambered cover glasses (Lab-Tek, Thermo Scientific), 6-well plates (Nunclon Delta Surface, Thermo Scientific), or 96-well plates (Nunclon Delta Surface Flat Bottom, Thermo Scientific).

3.13.12 Trypan blue cytotoxicity assay

6-well plates were seeded with 300,000 cells per well (3 mL of 100,000 cells/mL) and incubated at 37 °C with 5% CO_2 for 48 h (~60% confluent). Media was removed and fresh DMEM with 10% FBS (3 mL) was applied followed by addition of 7.5 μL vehicle control (DMSO) or APNO-5 for a final concentration of 1 or 5 μM. After 3, 6, and 24 h, cells were suspended by scraping, pelleted via centrifugation at 1000 × g for 5 min and the supernatant was discarded. The cell pellet was re-suspended in PBS (300 μL) and mixed 1:1 with trypan blue (0.4% w/v stock in PBS). The mixture was allowed to incubate for 1-3 min at room temperature and then unstained

(viable) and stained (nonviable) cells were counted using a hemocytometer. Viability was calculated as the percent viable cells for the experimental condition relative to the vehicle control.

3.13.13 MTT cytotoxicity assay

A 96-well plate was seeded with 20,000 cells per well (200 μL of 100,000 cells/mL) and incubated at 37 °C with 5% CO_2 for 24 h (~60–70% confluent). Media was removed and fresh serum-free RMPI 1640 containing vehicle control (DMSO), APNO, or SR-APNO (0.5% DMSO or 1.25% DMSO v/v for APNO and SR-APNO, respectively). At various times, the media was removed and replaced with 200 μL 20:1 mixture of FBS-free RMPA 1640 and (3- (4,5-dimethylthiazol-2-yl)-2,5-diphenyl-tetrazolium bromide (MTT, 5 mg/mL stock in PBS). The cells were incubated for 4 h under the same conditions and then the medium was removed and replaced with DMSO (100 μL/well). The absorbance of each well was recorded at 555 nm on a microplate reader. Viability was calculated by the absorbance relative to the vehicle control.

3.13.14 PA imaging of exogenous nitric oxide in 4T1 murine breast cancer cells

A T75 flask of 4T1 murine mammary carcinoma cells was seeded and allowed to grow to confluency (~90%) over 36 h. The cells were trypsinized, suspended in a 15 μM solution of SR-APNO-3 (RMPI 1640 serum-free media with 0.75% DMSO final concentration) and 2×10^6 cells were distributed into each 1.6 mL Eppendorf tube. The cells were stained for 1 h at 37 °C with agitation. After staining, the cells were collected via centrifugation (6,000 rpm, 5 min, 4 °C), washed with PBS (1 mL, same protocol as collection) to remove free dye, and then resuspended in PBS (450 μL). Samples were treated with control (50 μL 10 mM KOH), 1 mM DEA-NONOate (50 μL 10 mM DEA-NONOate in 10 mM KOH), or 5 mM DEA-NONOate (50 μL 50 mM DEA-NONOate in 10 mM KOH) and were allowed to incubate with rocking for 2 h at room temperature. The cells were pelleted via centrifugation (6,000 rpm, 5 min, 4 °C) and imaged directly in the 1.6

mL Eppendorf tube. Images were acquired at the appropriate wavelengths (SR-APNO-3: 790 nm; t-SR-APNO-3: 690 nm) using continuous mode with a 6 s rotation time. Quantification of each cell pellet is reported as the average of the mean signals over the entire area of interest (12.1 mm, slices 130 – 256).

3.13.15 Epifluorescence imaging of exogenous nitric oxide in 4T1 breast cancer cells

6 well plates were seeded with 150,000 4T1 murine mammary carcinoma cells (3 mL of 50,000 cell/mL) in RPMI 1640 media containing 10% FBS and allowed to incubate at 37 °C with 5% CO_2 for 24 h. The media was removed, and the cells were stained with CyAPNO (5 μM) in serum-free RPMI 1640 media for 90 min under the same conditions. After staining was complete, the solution was removed, and the cells were washed with PBS (1.0 mL) and incubated with DEA-NONOate (0.1 or 1 mM) in PBS for 1 h at 37 ºC. Each well was imaged (n = 3) were imaged using the Cy7 filter cube (EVOS fluorescence microscope) and analyzed using ImageJ (NIH).[131] The average fluorescence was measured as the mean of five randomly selected cells and the error is reported between biological replicates (n = 3).

3.13.16 Epifluorescence imaging of nitric oxide under AneroPack® Hypoxic Conditions

24 well plates were seeded with 25,000 4T1 murine mammary carcinoma cells (0.5 mL of 50,000 cell/mL) in RPMI 1640 media containing 10% FBS and allowed to incubate at 37 °C with 5% CO_2 for 24 h. The media was removed, and the cells were stained with CyAPNO (5 μM) in serum-free RPMI 1640 media for 90 min under the same conditions. After staining was complete, the solution was removed, and the cells were washed with PBS (0.5 – 1.0 mL) and incubated in serum-free RPMI media for 6 h at 37 ºC in a sealed container either with or without an AneroPack® (Mitsubishi Gas Company). When performing inhibition studies, the aforementioned solutions was prepared with L-N^G-nitroarginine (L-NNA, 10 μM, non-selective NOS inhibitor). Each well was

imaged (n = 3) were imaged using the Cy7 filter cube (EVOS fluorescence microscope) and analyzed using ImageJ (NIH).[131] The average fluorescence was measured as the mean of five randomly selected cells and the error is reported between biological replicates (n = 3).

3.13.17 Live-subject statement

All animal experiments were performed with the approval of the Institutional Animal Care and Use Committee of the University of Illinois at Urbana–Champaign, following the principles outlined by the American Physiological Society on research animal use.

3.13.18 Saline preparation and in vivo injection formulation

Sterile saline was prepared by dissolving sodium chloride (90 mg) in Milli-Q water (10 mL) and filtering the resulting solution through a Millex-GS 0.22 μm sterile filter. For all *in vivo* injections, a 3.4 mM solution of APNO-5 in DMF was prepared and diluted into sterile saline for a final concentration of 17 μM (0.5% DMF).

3.13.19 PA imaging in a subcutaneous LPS-induced murine inflammation model

All animal experiments were performed with the approval of the Institutional Animal Care and Use Committee of the University of Illinois at Urbana-Champaign, following the principles outlined by the American Physiological Society on research animal use. Six to eight week-old BALB/c mice were obtained from Jackson Laboratory. Lipopolysaccharide was dissolved in sterile saline at a concentration of 1 mg/mL. Hair was removed from the flanks using depilatory cream, and then mice were challenged subcutaneously with either 4 mg/kg of LPS or an equi-volumetric amount of saline in the flank. After 3.5 hours, mice were anaesthetized using isoflurane, and background PA signals were acquired at 680 nm and 770 nm. After an additional 0.5 hours, a 17 μM solution of APNO-5 in sterile saline containing 0.5% DMF was subcutaneously injected into the same flank at 68 μg/kg (80 μL for 20 g mouse). PA signals were monitored every hour for

5 hours in triplicate at 680 nm and 770 nm. Average PA intensities were acquired over the total volume of interest (1 cm^3) and the triplicates were averaged. PA spectra were acquired after 5 h with excitations every 10 nm under the same conditions as previously described, either with or without the administration of APNO.

3.13.20 PA imaging in an intramuscular LPS-induced inflammation in BALB/c mice

Six to eight-week-old BALB/c mice were obtained from Jackson Laboratory and intramuscularly administered lipopolysaccharide in a saline solution (4 mg/kg). After 4 h, APNO-5 or SR-APNO-3 (50 μM, 25 μL) was administered intramuscularly in a sterile saline solution (0.9% NaCl in sterile water) containing 15% DMF (v/v). Inhibition assays were performed by preparing the aforementioned dye solution in sterile saline containing 35 mM L-NMMA for co-administration. Images were acquired in technical replicates ($n = 2$) at the appropriate wavelengths using continuous mode with a 6 s rotation time. Quantification of each image is reported as the average of the mean signals of the technical replicates over the entire area of interest (12.1 mm, slices 130–256). For more clear representation, images corresponding to the probe and *N*-nitrosated products were colored independently and then overlaid using Horos software.

3.13.21 PA imaging of 4T1 murine breast cancer-derived nitric oxide in BALB/c mice with SR-APNO-3

Six to eight-week-old BALB/c mice were obtained from Jackson Laboratory and 4T1 subcutaneous tumors (5×10^4 cells, 50 μL of 1×10^6 cells/mL in 1:1 serum-free RPMI 1640 media and Matrigel) were implanted and allowed to grow for 26 days for a final volume of ~300–400 mm^3. Tumor volumes were measured using a caliper method[141] and the body weight was monitored over the course of the experiment. SR-APNO-3 (50 μM, 25 μL) was administered intratumorally or subcutaneously in a sterile saline solution (0.9% NaCl in sterile water) containing

15% DMF (v/v). Inhibition assays were performed by preparing the aforementioned dye solution in sterile saline containing 35 mM L-NMMA for co-administration. Images were acquired in technical replicates (n = 2) using continuous mode with a 6 s rotation time. Quantification of each image is reported as the average of the mean signals of the technical replicates over the entire area of interest (12.1 mm, slices 130–256). Reported samples sizes correspond to the number of biological replicates (animals). For more clear representation, images corresponding to the probe and *N*-nitrosated products were colored independently and then overlaid using Horos software.

3.13.22 In vivo imaging system (IVIS) imaging of 4T1 murine breast cancer-derived nitric oxide in BALB/c mice with CyAPNO

Five to seven-week-old BALB/c mice were obtained from Jackson Laboratory and 4T1 subcutaneous tumors (1×10^5 cells, 100 μL of 1×10^6 cells/mL in serum-free RPMI 1640 media) were implanted and allowed to grow for 18 days for a final volume of ~100 mm^3. Tumor volumes were measured using a caliper method[141] and the body weight was monitored over the course of the experiment. CyAPNO (10 μM, 100 μL) or the vehicle control were administered retro-orbitally in a sterile saline solution (0.9% NaCl in sterile water) containing 10% DMSO (v/v). Images were acquired with excitation and emission filters corresponding to CyAPNO (675/760 nm) and tCyAPNO (745/840 nm). The fluorescence was monitored in the flank and the tumor and the ratio was monitored over time (up to 8.5 days for clearance). Reported samples sizes correspond to the number of biological replicates (animals).

3.14 References

(1) Dedon, P. C.; Tannenbaum, S. R. Reactive Nitrogen Species in the Chemical Biology of Inflammation. *Arch. Biochem. Biophys.* **2004**, *423* (1), 12–22.

(2) Winterbourn, C. C. Reconciling the Chemistry and Biology of Reactive Oxygen Species. *Nat. Chem. Biol.* **2008**, *4* (5), 278–286.

(3) Giles, G. I.; Jacob, C. Reactive Sulfur Species: An Emerging Concept in Oxidative Stress. *Biol. Chem.* **2002**, *383* (3–4), 375–388.

(4) Mustafa, A. K.; Gadalla, M. M.; Snyder, S. H. Signaling by Gasotransmitters. *Sci. Signal.* **2009**, *2* (68), re2.

(5) Arnold, W. P.; Mittal, C. K.; Katsuki, S.; Murad, F. Nitric Oxide Activates Guanylate Cyclase and Increases Guanosine 3':5'-Cyclic Monophosphate Levels in Various Tissue Preparations. *Proc. Natl. Acad. Sci. U. S. A.* **1977**, *74* (8), 3203–3207.

(6) Furchgott, R.; Zawadski, J. V. The Obligatory Role of Endothelial Cells in the Relaxation of Atrial Smooth Muscle. *Nature* **1980**, *288*, 373–376.

(7) Ignarro, L. J.; Byrns, R. E.; Buga, G. M.; Wood, K. S. Endothelium-Derived Relaxing Factor from Pulmonary Artery and Vein Possesses Pharmacologic and Chemical Properties Identical to Those of Nitric Oxide Radical. *Circ. Res.* **1987**, *61* (6), 866–879.

(8) Palmer, R. M. J.; Ferrige, A. G.; Moncada, S. Nitric Oxide Release Accounts for the Biological Activity of Endothelium-Derived Relaxing Factor. *Nature* **1987**, *327* (11), 524–526.

(9) Wink, D. A.; Hines, H. B.; Cheng, R. Y. S.; Switzer, C. H.; Flores-Santana, W.; Vitek, M. P.; Ridnour, L. A.; Colton, C. A. Nitric Oxide and Redox Mechanisms in the Immune Response. *J. Leukoc. Biol.* **2011**, *89* (6), 873–891.

(10) Snyder, S. Nitric Oxide: First in a New Class of Neurotransmitters. *Science.* **1992**, *257* (5069), 494–496.

(11) Zhou, L.; Zhu, D.-Y. Neuronal Nitric Oxide Synthase: Structure, Subcellular Localization, Regulation, and Clinical Implications. *Nitric oxide* **2009**, *20* (4), 223–230.

(12) Vincent, S. R. Nitric Oxide Neurons and Neurotransmission. *Prog. Neurobiol.* **2010**, *90* (2), 246–255.

(13) Fukumura, D.; Kashiwagi, S.; Jain, R. K. The Role of Nitric Oxide in Tumour Progression. *Nat. Rev. Cancer* **2006**, *6* (7), 521–534.

(14) Vanini, F.; Kashfi, K.; Nath, N. The Dual Role of INOS in Cancer. *Redox Biol.* **2015**, *6*, 334–343.

(15) Heinecke, J. L.; Ridnour, L. A.; Cheng, R. Y. S.; Switzer, C. H.; Lizardo, M. M.; Khanna, C.; Glynn, S. A.; Hussain, S. P.; Young, H. A.; Ambs, S.; et al. Tumor Microenvironment-Based Feed-Forward Regulation of NOS2 in Breast Cancer Progression. *Proc. Natl. Acad. Sci.* **2014**, *111* (17), 6323–6328.

(16) Heinrich, T. A.; Da Silva, R. S.; Miranda, K. M.; Switzer, C. H.; Wink, D. A.; Fukuto, J. M. Biological Nitric Oxide Signalling: Chemistry and Terminology. *Br. J. Pharmacol.* **2013**, *169* (7), 1417–1429.

(17) Ridnour, L. A.; Thomas, D. D.; Switzer, C.; Flores-Santana, W.; Isenberg, J. S.; Ambs, S.; Roberts, D. D.; Wink, D. A. Molecular Mechanisms for Discrete Nitric Oxide Levels in Cancer. *Nitric Oxide - Biol. Chem.* **2008**, *19* (2), 73–76.

(18) Hickok, J. R.; Sahni, S.; Shen, H.; Arvind, A.; Antoniou, C.; Fung, L. W. M.; Thomas, D. D. Dinitrosyliron Complexes Are the Most Abundant Nitric Oxide-Derived Cellular Adduct: Biological Parameters of Assembly and Disappearance. *Free Radic. Biol. Med.* **2011**, *51* (8), 1558–1566.

(19) Hickok, J. R.; Vasudevan, D.; Jablonski, K.; Thomasn, D. D. Oxygen Dependence of Nitric Oxide-Mediated Signaling. *Redox Biol.* **2013**, *1* (1), 203–209.

(20) Thomas, D. D.; Espey, M. G.; Ridnour, L. A.; Hofseth, L. J.; Mancardi, D.; Harris, C. C.; Wink, D. A. Hypoxic Inducible Factor 1α, Extracellular Signal-Regulated Kinase, and P53 Are Regulated by Distinct Threshold

Concentrations of Nitric Oxide. *Proc. Natl. Acad. Sci. U. S. A.* **2004**, *101* (24), 8894–8899.

(21) Thomas, D. D.; Ridnour, L. A.; Isenberg, J. S.; Flores-Santana, W.; Switzer, C. H.; Donzelli, S.; Hussain, P.; Vecoli, C.; Paolocci, N.; Ambs, S.; et al. The Chemical Biology of Nitric Oxide: Implications in Cellular Signaling. *Free Radic. Biol. Med.* **2008**, *45* (1), 18–31.

(22) Floyd, R. A.; Kotake, Y.; Towner, R. A.; Guo, W.-X.; Nakae, D.; Konishi, Y. Nitric Oxide and Cancer Development. *J. Toxicol. Pathol.* **2007**, *20* (2), 77–92.

(23) Thomsen, L.; Miles, D.; Happerfield, L.; Bobrow, L.; Knowles, R.; Moncada, S. Nitric Oxide Synthase Activity in Human Breast Cancer. *Br. J. Cancer* **1995**, *72* (1), 41–44.

(24) Fujimoto, H.; Ando, Y.; Yamashita, T.; Terazaki, H.; Tanaka, Y.; Sasaki, J.; Matsumoto, M.; Suga, M.; Ando, M. Nitric Oxide Synthase Activity in Human Lung Cancer. *Japanese J. Cancer Res.* **1997**, *88* (12), 1190–1198.

(25) Klotz, T.; Bloch, W.; Volberg, C.; Engelmann, U.; Addicks, K. Selective Expression of Inducible Nitric Oxide Synthase in Human Prostate Carcinoma. *Cancer* **1998**, *82* (10), 1897–1903.

(26) Loibl, S.; von Minckwitz, G.; Weber, S.; Sinn, H.-P.; Schini-Kerth, V. B.; Lobysheva, I.; Nepveu, F.; Wolf, G.; Strebhardt, K.; Kaufmann, M. Expression of Endothelial and Inducible Nitric Oxide Synthase in Benign and Malignant Lesions of the Breast and Measurement of Nitric Oxide Using Electron Paramagnetic Resonance Spectroscopy. *Cancer* **2002**, *95* (6), 1191–1198.

(27) Cianchi, F.; Cortesini, C.; Fantappiè, O.; Messerini, L.; Schiavone, N.; Vannacci, A.; Nistri, S.; Sardi, I.; Baroni, G.; Marzocca, C.; et al. Inducible Nitric Oxide Synthase Expression in Human Colorectal Cancer: Correlation with Tumor Angiogenesis. *Am. J. Pathol.* **2003**, *162* (3), 793–801.

(28) Olson, N.; Van Der Vliet, A. Interactions between Nitric Oxide and Hypoxia-Inducible Factor Signaling Pathways in Inflammatory Disease. *Nitric Oxide - Biol. Chem.* **2011**, *25* (2), 125–137.

(29) Feelisch, M. The Chemical Biology of Nitric Oxide - an Outsider's Reflections about Its Role in Osteoarthritis. *Osteoarthr. Cartil.* **2008**, *16* (Supp. 2), S3-13.

(30) Hickok, J. R.; Thomas, D. D. Nitric Oxide and Cancer Therapy: The Emperor Has NO Clothes. *Curr. Pharm. Des.* **2010**, *16* (4), 381–391.

(31) Pereira, J. C. M.; Iretskii, A. V.; Han, R. M.; Ford, P. C. Dinitrosyl Iron Complexes with Cysteine. Kinetics Studies of the Formation and Reactions of DNICs in Aqueous Solution. *J. Am. Chem. Soc.* **2015**, *137* (1), 328–336.

(32) Boese, M.; Keese, M. A.; Becker, K.; Busse, R.; Mülsch, A. Inhibition of Glutathione Reductase by Dinitrosyl-Iron-Dithiolate Complex. *J. Biol. Chem.* **1997**, *272* (35), 21767–21773.

(33) Sahni, S.; Hickok, J. R.; Thomas, D. D. Nitric Oxide Reduces Oxidative Stress in Cancer Cells by Forming Dinitrosyliron Complexes. *Nitric Oxide* **2018**, *76*, 37–44.

(34) Bosworth, C. A.; Toledo, J. C.; Zmijewski, J. W.; Li, Q.; Lancaster, J. R. Dinitrosyliron Complexes and the Mechanism(s) of Cellular Protein Nitrosothiol Formation from Nitric Oxide. *Proc. Natl. Acad. Sci. U. S. A.* **2009**, *106* (12), 4671–4676.

(35) Wolhuter, K.; Whitwell, H. J.; Switzer, C. H.; Burgoyne, J. R.; Timms, J. F.; Eaton, P. Evidence against Stable Protein S-Nitrosylation as a Widespread Mechanism of Post-Translational Regulation. *Mol. Cell* **2018**, *69* (3), 438-450.e5.

(36) Nathan, C.; Xie, Q. Nitric Oxide Synthases: Role, Tolls, and Controls. *Cell* **1994**, *78*, 915–918.

(37) Oess, S.; Icking, A.; Fulton, D.; Govers, R.; Müller-Esterl, W. Subcellular Targeting and Trafficking of Nitric Oxide Synthases. *Biochem. J.* **2006**, *396* (3), 401–409.

(38) Villanueva, C.; Giulivi, C. Subcellular and Cellular Locations of Nitric Oxide Synthase Isoforms as Determinants of Health and Disease. *Free Radic. Biol. Med.* **2010**, *49* (3), 307–316.

(39) Raman, C. S.; Li, H.; Martásek, P.; Král, V.; Masters, B. S. S.; Poulos, T. L. Crystal Structure of Constitutive Endothelial Nitric Oxide Synthase: A Paradigm for Pterin Function Involving a Novel Metal Center. *Cell* **1998**, *95* (7), 939–950.

(40) Marletta, M. A.; Hurshman, A. R.; Rusche, K. M. Catalysis by Nitric Oxide Synthase. *Curr. Opin. Chem. Biol.* **1998**, *2* (5), 656–663.

(41) Abu-Soud, H. M.; Feldman, P. L.; Clark, P.; Stuehr, D. J. Electron Transfer in the Nitric-Oxide Synthases: Characterization of L-Arginine Analogs That Block Heme Iron Reduction. *J. Biol. Chem.* **1994**, *269* (51), 32318–32326.

(42) Zhu, Y.; Silverman, R. B. Revisiting Heme Mechanisms. A Perspective on the Mechanisms of Nitric Oxide Synthase (NOS), Heme Oxygenase (HO), and Cytochrome P450s (CYP450s). *Biochemistry* **2008**, *47* (8), 2231–2243.

(43) Hurshman, A. R.; Krebs, C.; Edmondson, D. E.; Huynh, B. H.; Marletta, M. A. Formation of a Pterin Radical in the Reaction of the Heme Domain of Inducible Nitric Oxide Synthase with Oxygen. *Biochemistry* **1999**, *38* (48), 15689–15696.

(44) Tejero, J.; Stuehr, D. Tetrahydrobiopterin in Nitric Oxide Synthase. *IUBMB Life* **2013**, *65* (4), 358–365.

(45) Hendgen-Cotta, U. B.; Merx, M. W.; Shiva, S.; Schmitz, J.; Becher, S.; Klare, J. P.; Steinhoff, H. J.; Goedecke, A.; Schrader, J.; Gladwin, M. T.; et al. Nitrite Reductase Activity of Myoglobin Regulates Respiration and Cellular Viability in Myocardial Ischemia-Reperfusion Injury. *Proc. Natl. Acad. Sci. U. S. A.* **2008**, *105* (34), 12636.

(46) Gladwin, M. T.; Kim-shapiro, D. B. The Functional Nitrite Reductase Activity of the Heme-Globins. *Blood* **2008**, *112* (7), 2636–2647.

(47) Dungel, P.; Penzenstadler, C.; Ashmwe, M.; Dumitrescu, S.; Stoegerer, T.; Redl, H.; Bahrami, S.; Kozlov, A. V. Impact of Mitochondrial Nitrite Reductase on Hemodynamics and Myocardial Contractility. *Sci. Rep.* **2017**, *7*, 12092.

(48) Zweier, J. L.; Wang, P.; Samouilov, A.; Kuppusamy, P. Enzyme-Independent Formation of Nitric Oxide in Biological Tissues. *Nat. Med.* **1995**, *1* (8), 804–809.

(49) Wang, P. G.; Xian, M.; Tang, X.; Wu, X.; Wen, Z.; Cai, T.; Janczuk, A. J. Nitric Oxide Donors: Chemical Activities and Biological Applications. *Chem. Rev.* **2002**, *102* (4), 1091–1134.

(50) Tsikas, D. Analysis of Nitrite and Nitrate in Biological Fluids by Assays Based on the Griess Reaction: Appraisal of the Griess Reaction in the l-Arginine/Nitric Oxide Area of Research. *J. Chromatogr. B Anal. Technol. Biomed. Life Sci.* **2007**, *851* (1–2), 51–70.

(51) Murphy, M. E.; Noack, E. Nitric Oxide Assay Using Hemoglobin Method. *Methods Enzymol.* **1994**, *233* (C), 240–250.

(52) Komarov, A.; Mattson, D.; Jones, M. M.; Singh, P. K.; Lai, C. S. In Vivo Spin Trapping of Nitric Oxide in

Mice. *Biochem. Biophys. Res. Commun.* **1993**, *195* (3), 1191–1198.

(53) Sharma, R.; Seo, J.-W.; Kwon, S. In Vivo Imaging of Nitric Oxide by Magnetic Resonance Imaging Techniques. *J. Nanomater.* **2014**, *2014*, 523646.

(54) Hong, H.; Sun, J.; Cai, W. Multimodality Imaging of Nitric Oxide and Nitric Oxide Synthases. *Free Radic. Biol. Med.* **2009**, *47* (6), 684–698.

(55) Shim, J. H.; Lee, Y. Amperometric Nitric Oxide Microsensor Based on Nanopore-Platinized Platinum: The Application for Imaging NO Concentrations. *Anal. Chem.* **2009**, *81* (20), 8571–8576.

(56) Jo, A.; Do, H.; Jhon, G. J.; Suh, M.; Lee, Y. Electrochemical Nanosensor for Real-Time Direct Imaging of Nitric Oxide in Living Brain. *Anal. Chem.* **2011**, *83* (21), 8314–8319.

(57) Li, Y.; Hu, K.; Yu, Y.; Rotenberg, S. A.; Amatore, C.; Mirkin, M. V. Direct Electrochemical Measurements of Reactive Oxygen and Nitrogen Species in Non-Transformed and Metastatic Human Breast Cells. *J. Am. Chem. Soc.* **2017**, *139*, 13055–13062.

(58) Griess, P. Bemerkungen Zu Der Abhandlung Der HH. Weselsky Und Benedikt „Ueber Einige Azoverbindungen". *Berichte der Dtsch. Chem. Gesellschaft* **1879**, *12* (1), 426–428.

(59) Feelisch, M.; Noack, E. A. Correlation between Nitric Oxide Formation during Degradation of Organic Nitrates and Activation of Guanylate Cyclase. *Eur. J. Pharmacol.* **1987**, *139* (1), 19–30.

(60) Kojima, H.; Nakatsubo, N.; Kikuchi, K.; Kawahara, S.; Kirino, Y.; Nagoshi, H.; Hirata, Y.; Nagano, T. Detection and Imaging of Nitric Oxide with Novel Fluorescent Indicators: Diaminofluoresceins. *Anal. Chem.* **1998**, *70* (13), 2446–2453.

(61) Mao, Z.; Feng, W.; Li, Z.; Zeng, L.; Lv, W.; Liu, Z. NIR in, Far-Red out: Developing a Two-Photon Fluorescent Probe for Tracking Nitric Oxide in Deep Tissue. *Chem. Sci.* **2016**, *7* (8), 5230–5235.

(62) Eroglu, E.; Gottschalk, B.; Charoensin, S.; Blass, S.; Bischof, H.; Rost, R.; Madreiter-Sokolowski, C. T.; Pelzmann, B.; Bernhart, E.; Sattler, W.; et al. Development of Novel FP-Based Probes for Live-Cell Imaging of Nitric Oxide Dynamics. *Nat. Commun.* **2016**, *7*, 10623.

(63) Li, H.; Wan, A. Fluorescent Probes for Real-Time Measurement of Nitric Oxide in Living Cells. *Analyst* **2015**, *140* (21), 7129–7141.

(64) Nagano, T.; Yoshimura, T. Bioimaging of Nitric Oxide. *Chem. Rev.* **2002**, *102* (4), 1235–1269.

(65) Kashiwagi, S.; Tsukada, K.; Xu, L.; Miyazaki, J.; Kozin, S. V; Tyrrell, J. A.; Sessa, W. C.; Gerweck, L. E.; Jain, R. K.; Fukumura, D. Perivascular Nitric Oxide Gradients Normalize Tumor Vasculature. *Nat. Med.* **2008**, *14* (3), 255–257.

(66) Li, H.; Zhang, D.; Gao, M.; Huang, L.; Tang, L.; Li, Z.; Chen, X.; Zhang, X. Highly Specific C–C Bond Cleavage Induced FRET Fluorescence for in Vivo Biological Nitric Oxide Imaging. *Chem. Sci.* **2017**, *8*, 2199–2203.

(67) Huo, Y.; Miao, J.; Han, L.; Li, Y.; Li, Z.; Shi, Y.; Guo, W. Selective and Sensitive Visualization of Endogenous Nitric Oxide in Living Cells and Animals by a Si-Rhodamine Deoxylactam-Based near-Infrared Fluorescent Probe. *Chem. Sci.* **2017**, *8*, 6857–6864.

(68) Sasaki, E.; Kojima, H.; Nishimatsu, H.; Urano, Y.; Kikuchi, K.; Hirata, Y.; Nagano, T. Highly Sensitive Near-Infrared Fluorescent Probes for Nitric Oxide and Their Application to Isolated Organs. *J. Am. Chem. Soc.* **2005**, *127* (11), 3684–3685.

(69) Dong, X.; Heo, C. H.; Chen, S.; Kim, H. M.; Liu, Z. Quinoline-Based Two-Photon Fluorescent Probe for Nitric Oxide in Live Cells and Tissues. *Anal. Chem.* **2014**, *86* (1), 308–311.

(70) Mao, Z.; Jiang, H.; Li, Z.; Zhong, C.; Zhang, W.; Liu, Z. An N-Nitrosation Reactivity-Based Two-Photon Fluorescent Probe for Specific in Situ Detection of Nitric Oxide. *Chem. Sci.* **2017**, *8*, 4533.

(71) Mao, Z.; Jiang, H.; Song, X.; Hu, W.; Liu, Z. Development of a Silicon-Rhodamine Based Near-Infrared Emissive Two-Photon Fluorescent Probe for Nitric Oxide. *Anal. Chem.* **2017**, *89*, 9620–9624.

(72) Jiang, Y.; Upputuri, P. K.; Xie, C.; Lyu, Y.; Zhang, L.; Xiong, Q.; Pramanik, M.; Pu, K. Broadband Absorbing Semiconducting Polymer Nanoparticles for Photoacoustic Imaging in Second Near-Infrared Window. *Nano Lett.* **2017**, *17* (8), 4964–4969.

(73) Kelm, M. Nitric Oxide Metabolism and Breakdown. *Biochim. Biophys. Acta - Bioenerg.* **1999**, *1411* (2–3), 273–289.

(74) Zhuang, Y.; Xu, Q.; Huang, F.; Gao, P.; Zhao, Z.; Lou, X.; Xia, F. Ratiometric Fluorescent Bioprobe for Highly Reproducible Detection of Telomerase in Bloody Urines of Bladder Cancer Patients. *ACS Sens.* **2016**, *1* (5), 572–578.

(75) Reinhardt, C. J.; Chan, J. Development of Photoacoustic Probes for in Vivo Molecular Imaging. *Biochemistry* **2018**, *57* (2), 194–199.

(76) Shiue, T. W.; Chen, Y. H.; Wu, C. M.; Singh, G.; Chen, H. Y.; Hung, C. H.; Liaw, W. F.; Wang, Y. M. Nitric Oxide Turn-on Fluorescent Probe Based on Deamination of Aromatic Primary Monoamines. *Inorg. Chem.* **2012**, *51* (9), 5400–5408.

(77) Beltrán, A.; Burguete, M. I.; Abánades, D. R.; Pérez-Sala, D.; Luis, S. V; Galindo, F. Turn-on Fluorescent Probes for Nitric Oxide Sensing Based on the Ortho-Hydroxyamino Structure Showing No Interference with Dehydroascorbic Acid. *Chem. Commun.* **2014**, *50* (27), 3579–3581.

(78) Miao, J.; Huo, Y.; Lv, X.; Li, Z.; Cao, H.; Shi, H.; Shi, Y.; Guo, W. Fast-Response and Highly Selective Fluorescent Probes for Biological Signaling Molecule NO Based on N-Nitrosation of Electron-Rich Aromatic Secondary Amines. *Biomaterials* **2016**, *78*, 11–19.

(79) Grossi, M.; Palma, A.; McDonnell, S. O.; Hall, M. J.; Rai, D. K.; Muldoon, J.; Oshea, D. F. Mechanistic Insight into the Formation of Tetraarylazadipyrromethenes. *J. Org. Chem.* **2012**, *77* (20), 9304–9312.

(80) Chen, Z.; Liu, Y.; Wagner, W.; Stepanenko, V.; Ren, X.; Ogi, S.; Würthner, F. Near-IR Absorbing J-Aggregate of an Amphiphilic BF2-Azadipyrromethene Dye by Kinetic Cooperative Self-Assembly. *Angew. Chemie - Int. Ed.* **2017**, *56* (21), 5729–5733.

(81) Tetko, I. V.; Gasteiger, J.; Todeschini, R.; Mauri, A.; Livingstone, D.; Ertl, P.; Palyulin, V. A.; Radchenko, E. V.; Zefirov, N. S.; Makarenko, A. S.; et al. Virtual Computational Chemistry Laboratory - Design and Description. *J. Comput. Aided. Mol. Des.* **2005**, *19* (6), 453–463.

(82) Zhou, E. Y.; Knox, H. J.; Reinhardt, C. J.; Partipilo, G.; Nilges, M. J.; Chan, J. Near-Infrared Photoactivatable Nitric Oxide Donors with Integrated Photoacoustic Monitoring. *J. Am. Chem. Soc.* **2018**, *140* (37), 11686–11697.

(83) Copeland, S.; Warren, H. S.; Lowry, S. F.; Calvano, S. E.; Remick, D. Acute Inflammatory Response to Endotoxin in Mice and Humans Acute Inflammatory Response to Endotoxin in Mice and Humans. *Clin. Diagn. Lab. Immunol.* **2005**, *12* (1), 60–67.

(84) Zhang, X.; Kim, W. S.; Hatcher, N.; Potgieter, K.; Moroz, L. L.; Gillette, R.; Sweedler, J. V. Interfering with

Nitric Oxide Measurements. 4,5-Diaminofluorescein Reacts with Dehydroascorbic Acid and Ascorbic Acid. *J. Biol. Chem.* **2002**, *277* (50), 48472–48478.

(85) Urano, Y.; Kamiya, M.; Kanda, K.; Ueno, T.; Hirose, K.; Nagano, T. Evolution of Fluorescein as a Platform for Finely Tunable Fluorescence Probes. *J. Am. Chem. Soc.* **2005**, *127* (13), 4888–4894.

(86) Knox, H. J.; Kim, T. W.; Zhu, Z.; Chan, J. Photophysical Tuning of N -Oxide-Based Probes Enables Ratiometric Photoacoustic Imaging of Tumor Hypoxia. *ACS Chem. Biol.* **2018**, *13*, 1838–1843.

(87) Zhou, E. Y.; Knox, H. J.; Liu, C.; Zhao, W.; Chan, J. A Conformationally Restricted Aza-BODIPY Platform for Stimulus- Responsive Probes with Enhanced Photoacoustic Properties. *J. Am. Chem. Soc.* **2019**, *141*, 17601–17609.

(88) Knox, H. J.; Hedhli, J.; Kim, T. W.; Khalili, K.; Dobrucki, L. W.; Chan, J. A Bioreducible N-Oxide-Based Probe for Photoacoustic Imaging of Hypoxia. *Nat. Commun.* **2017**, *8*, 1794.

(89) Li, H.; Zhang, P.; Smaga, L. P.; Hoffman, R. A.; Chan, J. Photoacoustic Probes for Ratiometric Imaging of Copper(II). *J. Am. Chem. Soc.* **2015**, *137* (50), 15628–15631.

(90) Zhang, X.; Yu, H.; Xiao, Y. Replacing Phenyl Ring with Thiophene: An Approach to Longer Wavelength Aza-Dipyrromethene Boron Difluoride (Aza-BODIPY) Dyes. *J. Org. Chem.* **2012**, *77* (1), 669–673.

(91) Bellier, Q.; Dalier, F.; Jeanneau, E.; Maury, O.; Andraud, C. Thiophene-Substituted Aza-Bodipy as a Strategic Synthon for the Design of near-Infrared Dyes. *New J. Chem.* **2012**, *36* (3), 768.

(92) Liu, S.; Shi, Z.; Xu, W.; Yang, H.; Xi, N.; Liu, X.; Zhao, Q.; Huang, W. A Class of Wavelength-Tunable near-Infrared Aza-BODIPY Dyes and Their Application for Sensing Mercury Ion. *Dye. Pigment.* **2014**, *103*, 145–153.

(93) Jiang, X. D.; Zhao, J.; Li, Q.; Sun, C. L.; Guan, J.; Sun, G. T.; Xiao, L. J. Synthesis of NIR Fluorescent Thienyl-Containing Aza-BODIPY and Its Application for Detection of Hg2+: Electron Transfer by Bonding with Hg2+. *Dye. Pigment.* **2016**, *125*, 136–141.

(94) Zhao, W.; Carreira, E. M. Conformationally Restricted Aza-Bodipy: A Highly Fluorescent, Stable, near-Infrared-Absorbing Dye. *Angew. Chemie - Int. Ed.* **2005**, *44* (11), 1677–1679.

(95) Zhao, W.; Carreira, E. M. Conformationally Restricted Aza-BODIPY: Highly Fluorescent, Stable near-Infrared Absorbing Dyes. *Chem. - A Eur. J.* **2006**, *12* (27), 7254–7263.

(96) Namiki, S.; Arai, T.; Fujimori, K. High-Performance Caged Nitric Oxide: A New Molecular Design, Synthesis, and Photochemical Reaction. *J. Am. Chem. Soc.* **1997**, *119* (16), 3840–3841.

(97) Ieda, N.; Hotta, Y.; Miyata, N.; Kimura, K.; Nakagawa, H. Photomanipulation of Vasodilation with a Blue-Light-Controllable Nitric Oxide Releaser. *J. Am. Chem. Soc.* **2014**, *136* (19), 7085–7091.

(98) Víteček, J.; Lojek, A.; Valacchi, G.; Kubala, L. Arginine-Based Inhibitors of Nitric Oxide Synthase: Therapeutic Potential and Challenges. *Mediators Inflamm.* **2012**, *2012*, 318087.

(99) Mantovani, A.; Marchesi, F.; Malesci, A.; Laghi, L.; Allavena, P. Tumour-Associated Macrophages as Treatment Targets in Oncology. *Nat. Rev. Clin. Oncol.* **2017**, *14* (7), 399–416.

(100) Wu, Y.; Sun, L.; Zeng, F.; Wu, S. A Conjugated-Polymer-Based Ratiometric Nanoprobe for Evaluating in-Vivo Hepatotoxicity Induced by Herbal Medicine via MSOT Imaging. *Photoacoustics* **2019**, *13* (October 2018), 6–17.

(101) Teng, L.; Song, G.; Liu, Y.; Han, X.; Li, Z.; Wang, Y.; Huan, S.; Zhang, X.-B.; Tan, W. Nitric Oxide-Activated "Dual-Key–One-Lock" Nanoprobe for in Vivo Molecular Imaging and High-Specificity Cancer Therapy. *J. Am. Chem. Soc.* **2019**, *141* (34), 13572–13581.

(102) Knox, H. J.; Chan, J. Acoustogenic Probes: A New Frontier in Photoacoustic Imaging. *Acc. Chem. Res.* **2018**, *51* (11), 2897–2905.

(103) Sun, W.; Guo, S.; Hu, C.; Fan, J.; Peng, X. Recent Development of Chemosensors Based on Cyanine Platforms. *Chem. Rev.* **2016**, *116* (14), 7768–7817.

(104) Gorka, A. P.; Nani, R. R.; Schnermann, M. J. Cyanine Polyene Reactivity: Scope and Biomedical Applications. *Org. Biomol. Chem.* **2015**, *13* (28), 7584–7598.

(105) Zhang, C.; Liu, T.; Su, Y.; Luo, S.; Zhu, Y.; Tan, X.; Fan, S.; Zhang, L.; Zhou, Y.; Cheng, T.; et al. A Near-Infrared Fluorescent Heptamethine Indocyanine Dye with Preferential Tumor Accumulation for in Vivo Imaging. *Biomaterials* **2010**, *31* (25), 6612–6617.

(106) Tan, X.; Luo, S.; Wang, D.; Su, Y.; Cheng, T.; Shi, C. A NIR Heptamethine Dye with Intrinsic Cancer Targeting, Imaging and Photosensitizing Properties. *Biomaterials* **2012**, *33* (7), 2230–2239.

(107) Mishra, A.; Behera, R. K.; Behera, P. K.; Mishra, B. K.; Behera, G. B. Cyanines during the 1990s: A Review. *Chem. Rev.* **2000**, *100* (6), 1973–2011.

(108) Mishra, A.; Jiang, Y.; Roberts, S.; Ntziachristos, V.; Westmeyer, G. G. Near-Infrared Photoacoustic Imaging Probe Responsive to Calcium. *Anal. Chem.* **2016**, *88* (22), 10785–10789.

(109) Zhang, H. K.; Chen, Y.; Kang, J.; Lisok, A.; Minn, I.; Pomper, M. G.; Boctor, E. M. Prostate-Specific Membrane Antigen-Targeted Photoacoustic Imaging of Prostate Cancer in Vivo. *J. Biophotonics* **2018**, *11* (9), 1–6.

(110) Li, X.; Tang, Y.; Li, J.; Hu, X.; Yin, C.; Yang, Z.; Wang, Q.; Wu, Z.; Lu, X.; Wang, W.; et al. A Small-Molecule Probe for Ratiometric Photoacoustic Imaging of Hydrogen Sulfide in Living Mice. *Chem. Commun.* **2019**, *55* (42), 5934–5937.

(111) Yin, L.; Sun, H.; Zhang, H.; He, L.; Qiu, L.; Lin, J.; Xia, H.; Zhang, Y.; Ji, S.; Shi, H.; et al. Quantitatively Visualizing Tumor-Related Protease Activity in Vivo Using a Ratiometric Photoacoustic Probe. *J. Am. Chem. Soc.* **2019**, *141* (7), 3265–3273.

(112) Weber, J.; Bollepalli, L.; Belenguer, A. M.; Antonio, M. Di; De Mitri, N.; Joseph, J.; Balasubramanian, S.; Hunter, C. A.; Bohndiek, S. E. An Activatable Cancer-Targeted Hydrogen Peroxide Probe for Photoacoustic and Fluorescence Imaging. *Cancer Res.* **2019**, *79* (20), 5407–5417.

(113) Toutchkine, A.; Nguyen, D. V.; Hahn, K. M. Merocyanine Dyes with Improved Photostability. *Org. Lett.* **2007**, *9* (15), 2775–2777.

(114) Samanta, A.; Vendrell, M.; Das, R.; Chang, Y. T. Development of Photostable Near-Infrared Cyanine Dyes. *Chem. Commun.* **2010**, *46* (39), 7406–7408.

(115) Lou, Z.; Li, P.; Song, P.; Han, K. Ratiometric Fluorescence Imaging of Cellular Hypochlorous Acid Based on Heptamethine Cyanine Dyes. *Analyst* **2013**, *138* (21), 6291.

(116) Schwechheimer, C.; Rönicke, F.; Schepers, U.; Wagenknecht, H. A. A New Structure-Activity Relationship for Cyanine Dyes to Improve Photostability and Fluorescence Properties for Live Cell Imaging. *Chem. Sci.* **2018**, *9* (31), 6557–6563.

(117) Liu, Y.; Fan, H.; Wen, Y.; Jia, T.; Su, Q.; Li, F. ICT-Based near Infrared Fluorescent Switch-on Probe for Nitric Oxide Bioimaging in Vivo. *Dye. Pigment.* **2019**, *166*, 211–216.

(118) Renikuntla, B. R.; Rose, H. C.; Eldo, J.; Waggoner, A. S.; Armitage, B. A. Improved Photostability and Fluorescence Properties through Polyfluorination of a Cyanine Dye. *Org. Lett.* **2004**, *6* (6), 909–912.

(119) Shank, N. I.; Zanotti, K. J.; Lanni, F.; Berget, P. B.; Armitage, B. A. Enhanced Photostability of Genetically Encodable Fluoromodules Based on Fluorogenic Cyanine Dyes and a Promiscuous Protein Partner. *J. Am. Chem. Soc.* **2009**, *131* (36), 12960–12969.

(120) Grover, T. A.; Ramseyer, J. A.; Piette, L. H. Photolysis of Nitrosamines and Nitrosamides at Neutral PH: A Spin-Trap Study. *Free Radic. Biol. Med.* **1987**, *3* (1), 27–32.

(121) Pan, F.; Wu, B.; Shi, Z. J. Cu-Catalyzed Intramolecular Amidation of Unactivated C(Sp3)-H Bonds to Synthesize N-Substituted Indolines. *Chem. - A Eur. J.* **2016**, *22* (19), 6487–6490.

(122) Sattler, A.; Haufe, G. High Regioselectivity in the Alternative Cleavage of Terminal Epoxides with Different Sources of Nucleophilic Fluoride. *J. Fluor. Chem.* **1994**, *69* (2), 185–190.

(123) Juennemann, J.; Lundt, I.; Thiem, J. Reaction of Epoxyaldonolactones with HF-Amine Complexes. *Acta Chemica Scandinavica*. 1994, pp 265–268.

(124) Ho, T. L.; Wong, C. M. Titanium Trichloride Reactions: Dehalogenation. *Synth. Commun.* **1973**, *3* (3), 237–239.

(125) Weber, J.; Beard, P. C.; Bohndiek, S. E. Contrast Agents for Molecular Photoacoustic Imaging. *Nat. Methods* **2016**, *13* (8), 639–650.

(126) Jiang, Y.; Pu, K. Advanced Photoacoustic Imaging Applications of Near-Infrared Absorbing Organic Nanoparticles. *Small* **2017**, *13* (30), 1–19.

(127) Rong, G.; Corrie, S. R.; Clark, H. A. In Vivo Biosensing: Progress and Perspectives. *ACS Sensors* **2017**, *2* (3), 327–338.

(128) Fu, Q.; Zhu, R.; Song, J.; Yang, H.; Chen, X. Photoacoustic Imaging: Contrast Agents and Their Biomedical Applications. *Adv. Mater.* **2018**, *31*, 1805875.

(129) Zeng, L.; Ma, G.; Lin, J.; Huang, P. Photoacoustic Probes for Molecular Detection: Recent Advances and Perspectives. *Small* **2018**, *14* (30), 1–18.

(130) Patil, K. R.; Mahajan, U. B.; Unger, B. S.; Goyal, S. N.; Belemkar, S.; Surana, S. J.; Ojha, S.; Patil, C. R. Animal Models of Inflammation for Screening of Anti-Inflammatory Drugs: Implications for the Discovery and Development of Phytopharmaceuticals. *Int. J. Mol. Sci.* **2019**, *20* (18), 4367.

(131) Schneider, C. A.; Rasband, W. S.; Eliceiri, K. W. NIH Image to ImageJ: 25 Years of Image Analysis. *Nat. Methods* **2012**, *9* (7), 671–675.

(132) Pettersen, E. F.; Goddard, T. D.; Huang, C. C.; Couch, G. S.; Greenblatt, D. M.; Meng, E. C.; Ferrin, T. E. UCSF Chimera - A Visualization System for Exploratory Research and Analysis. *J. Comput. Chem.* **2004**, *25* (13), 1605–1612.

(133) Suryaraman, M. G.; Viswanathan, A. Preparation of Nitric Oxide: Some Laboratory Methods. *J. Chem. Educ.* **1949**, *26* (11), 594.

(134) Würth, C.; Grabolle, M.; Pauli, J.; Spieles, M.; Resch-Genger, U. Relative and Absolute Determination of

Fluorescence Quantum Yields of Transparent Samples. *Nat. Protoc.* **2013**, *8* (8), 1535–1550.

(135) Uppu, R. M. Synthesis of Peroxynitrite Using Isoamyl Nitrite and Hydrogen Peroxide in a Homogeneous Solvent System. *Anal. Biochem.* **2006**, *354* (2), 165–168.

(136) Hanwell, M. D.; Curtis, D. E.; Lonie, D. C.; Vandermeersch, T.; Zurek, E.; Hutchison, G. R. Avogadro: An Advanced Semantic Chemical Editor, Visualization, and Analysis Platform. *J .Cheminform.* **2012**, *4* (1), 17.

(137) Rappé, A. K.; Casewit, C. J.; Colwell, K. S.; Goddard, W. A.; Skiff, W. M. UFF, a Full Periodic Table Force Field for Molecular Mechanics and Molecular Dynamics Simulations. *J. Am. Chem. Soc.* **1992**, *114* (25), 10024–10035.

(138) Becke, A. D. A New Mixing of Hartree-Fock and Local Density-Functional Theories. *J. Chem. Phys.* **1993**, *98* (2), 1372–1377.

(139) Stephens, P. J.; Devlin, F. J.; Chabalowski, C. F.; Frisch, M. J. Ab Initio Calculation of Vibrational Absorption and Circular Dichroism Spectra Using Density Functional Force Fields. *J. Phys. Chem.* **1994**, *98* (45), 11623–11627.

(140) Yanai, T.; Tew, D. P.; Handy, N. C. A New Hybrid Exchange-Correlation Functional Using the Coulomb-Attenuating Method (CAM-B3LYP). *Chem. Phys. Lett.* **2004**, *393* (1–3), 51–57.

(141) Faustino-Rocha, A.; Oliveira, P. A.; Pinho-Oliveira, J.; Teixeira-Guedes, C.; Soares-Maia, R.; Da Costa, R. G.; Colaço, B.; Pires, M. J.; Colaço, J.; Ferreira, R.; et al. Estimation of Rat Mammary Tumor Volume Using Caliper and Ultrasonography Measurements. *Lab Anim. (NY).* **2013**, *42* (6), 217–224.

(142) Reinhardt, C. J.; Zhou, E. Y.; Jorgensen, M. D.; Partipilo, G.; Chan, J. A Ratiometric Acoustogenic Probe for In Vivo Imaging of Endogenous Nitric Oxide. *J. Am. Chem. Soc.* **2018**, *140*, 1011–1018.

(143) Reinhardt, C. J.; Xu, R.; Chan, J. Nitric Oxide Imaging in Cancer Enabled by Steric Relaxation of a Photoacoustic Probe Platform. *Chem. Sci.* **2020**, *11*, 1587–1592.

APPENDIX A: CHAPTER 2 SUPPLMENTAL FIGURES AND TABLES[4]

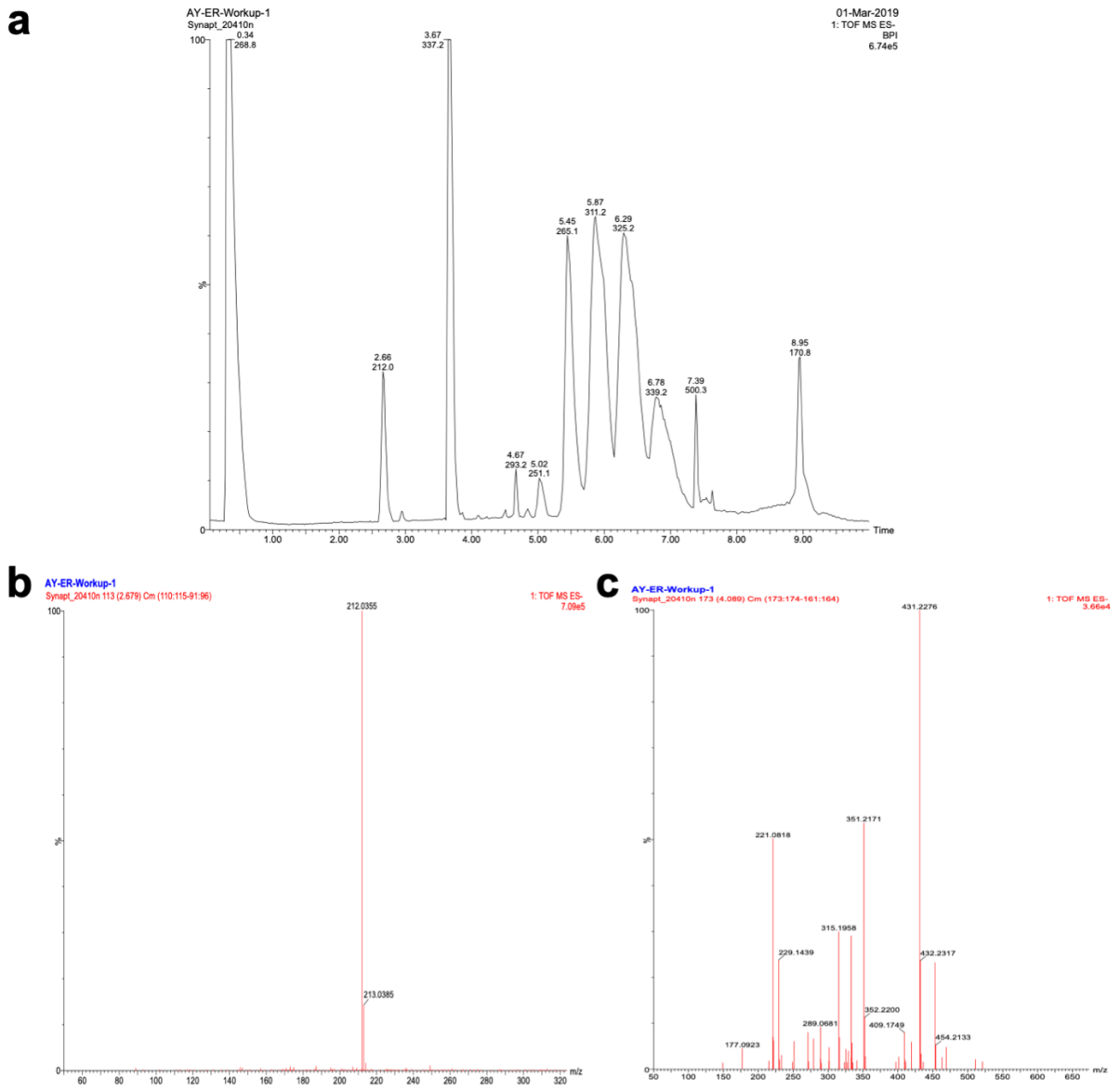

Figure A.1: (a) LC-HRMS analysis of the crude reaction between CoxFluor (10 μM), COX-2 (250 nM), and hemin (1 μM) in 100 mM Tris-HCl buffer (pH 8.0). The products were extracted with EtOAc after incubation at room temperature for 4 h and the organic layer was concentrated under vacuum. Products were separated on a CORTECS™ UPLC C18 column (1.6 μm, 2.1 by 50 mm) with a linear gradient using a combination of solvent A (95% water, 5% acetonitrile, 0.1% TFA) and solvent B (95% acetonitrile, 5% water, 0.1% TFA) at a flow rate of 0.5 mL/minute. Gradient protocol in minutes: 0–0.5 (100% A); 0.5–6 (20% A); 6–8 (100% B); 8–8.1 (80% A); and 8.1–10 (80% A). High resolution spectra for (b) resorufin (HRMS [M - H]$^-$ calc'd mass for $C_{12}H_6NO_3$ = 212.0348, found = 212.0355) and (c) PGH_2 (HRMS [M - H]$^-$ calc'd mass for $C_{20}H_{31}O_5$ = 351.2172, found = 351.2171) were observed.

[4]Portions of this appendix are reprinted or adapted with permissions from the following publication: Yadav, A. K.; Reinhardt, C. J.; Arango, A. S.; Huff, H. C.; Dong, L.; Malkowski, M. G.; Das, A.; Tajkhorshid, E.; Chan, J. An Activity-Based Sensing Approach for the Detection of Cyclooxygenase-2 in Live Cells. *Angew. Chemie Int. Ed.* **2020**, *59*, 3307–3314.[36] Copyright © 2020 John Wiley and Sons, Inc.

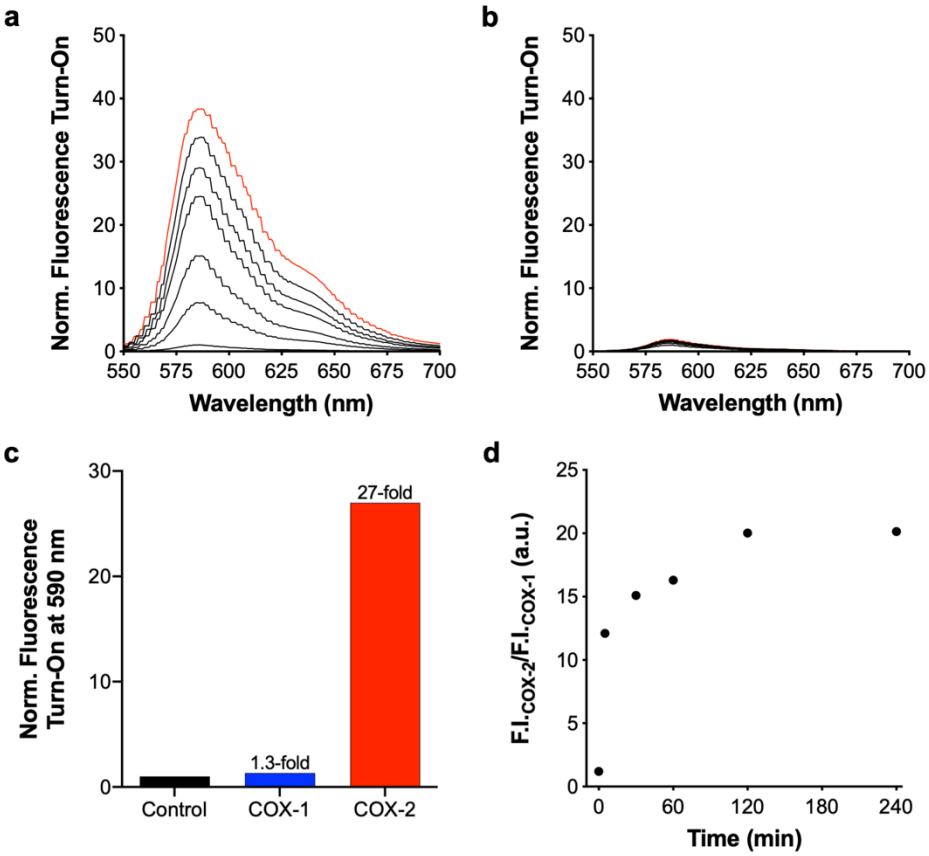

Figure A.2: Representative time-course of CoxFluor fluorescence spectra after treatment with (a) COX-2 or (b) COX-1 over 4 h (red line indicates final time point, normalized to initial timepoint). (c) Comparison of final fluorescence intensity at 590 nm for CoxFluor treated with COX-2 (red) or COX-1 (blue) relative to a buffer control (black). (d) Relative selectivity for COX-2 over COX-1 as a function of time. Reactions were performed at room temperature using the fluorimeter assay protocol (submicroquartz cuvettes) with 10 mM CoxFluor and 250 nM enzyme (COX-1 specific activity is 1.3-fold greater than COX-2 at this concentration) in 100 mM Tris-HCl (pH 8.0).

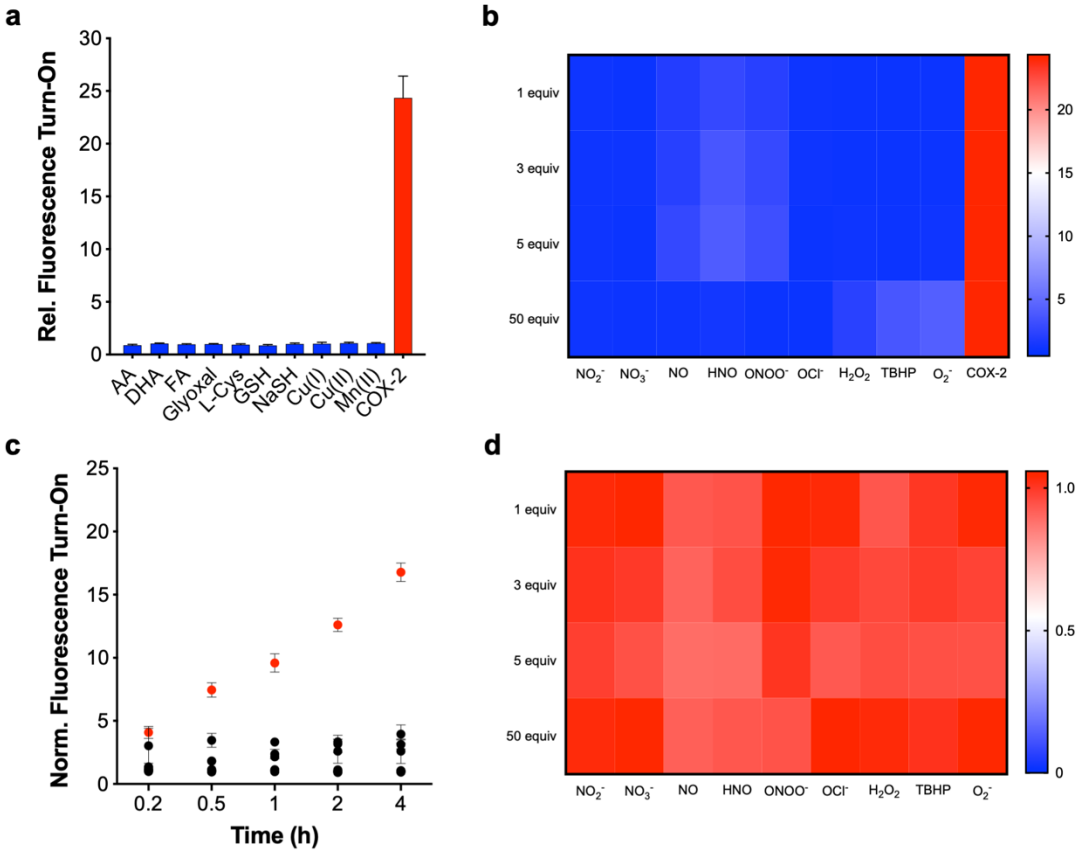

Figure A.3: (a) CoxFluor response to reactive carbonyl (AA: ascorbic acid; DHA: dehydroascorbic acid; FA: formaldehyde; glyoxal), reactive thiols (L-cysteine; GSH: reduced glutathione; NaSH), and metal species (500 μM, 50 equiv). (b) Heat map of the mean fluorescence enhancement of CoxFluor following treatment with 1, 3, 5, or 50 equivalents of RNS or ROS. (c) Representative time course of the relative turn on for COX-2 (250 nM, red) compared to a range of ROS and RNS (5 equivalents). The same results were observed for all other analyte concentrations. (d) Stability of resorufin in the presence of 1, 3, 5, and 50 equiv of ROS and RNS. Fluorescence enhancements were measured for CoxFluor or resorufin (10 μM) using the plate reader assay. Endpoint assays were performed at 4 h and the fluorescence enhancement was calculated relative to a buffer control (100 mM Tris-HCl, pH 8.0) at the corresponding time point. Values are reported as the mean ± standard deviation (n = 3).

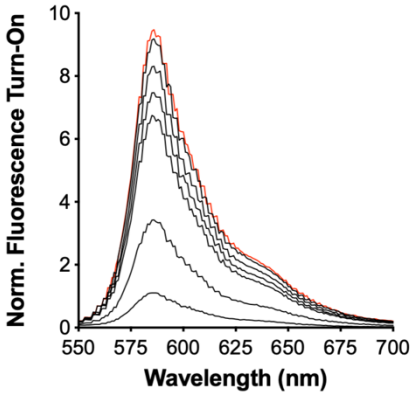

Figure A.4: Relative fluorescence for CoxFluor (10 μM) incubated with COX-2 (250 nM), GSH (1 mM) and hemin (1 μM) over the course of 4 h at room temperature in 100 mM Tris HCl buffer (pH 8.0). Assay was performed according to the fluorimeter assay.

Table A.1: Calculated root-mean-standard-deviation (RMSD, in Å) for the selected structure of COX-1 (PDB ID: 5U6X) compared to a panel of other structures in the protein databank.

PDB	***Alpha Carbons***	***Backbone***	***Heavy***
1PRH[1]	0.15	0.16	0.32
1PTH[2]	0.13	0.15	0.28
1PGE[3]	0.13	0.15	0.28
1PGF[3]	0.13	0.15	0.28
1PGG[3]	0.13	0.14	0.28
1CQE[1]	0.18	0.18	0.34
1EBV[4]	0.17	0.19	0.37
1DIY[5]	0.17	0.19	0.33
1EQG[6]	0.16	0.17	0.33
1EQH[6]	0.16	0.17	0.32
1HT5[6]	0.20	0.22	0.38
1HT8[6]	0.19	0.20	0.36
1FE2[7]	0.17	0.19	0.33
1IGX[8]	0.18	0.20	0.32
1IGZ[8]	0.16	0.18	0.32
1Q4G[9]	0.20	0.21	0.42
1U67[10]	0.18	0.19	0.32
2AYL[11]	0.19	0.19	0.41
2OYE[12]	0.18	0.19	0.32
2OYU[12]	0.16	0.18	0.34
3KK6[13]	0.19	0.22	0.31
3N8V[14]	0.18	0.20	0.36
3N8W[14]	0.18	0.19	0.37
3N8X[14]	0.23	0.24	0.44
3N8Y[14]	0.22	0.23	0.40
3N8Z[14]	0.21	0.2	0.42
4O1Z[15]	0.18	0.19	0.39
5WBE[16]	0.09	0.10	0.19

Table A.2: Calculated RMSD (Å) for the selected structure of COX-2 (PDB ID: 5KIR) compared to a panel of other structures in the protein databank.

PDB	***Alpha Carbons***	***Back Bone***	***Heavy***
1DDX[17]	0.15	0.17	0.28
1PXX[18]	0.17	0.18	0.30
3KRK[19]	0.21	0.21	0.44
3LN0[20]	0.12	0.14	0.28
3LN1[20]	0.14	0.15	0.27
3MQE[20]	0.32	0.34	0.50
3NT1[21]	0.20	0.20	0.43
3NTB[21]	0.18	0.19	0.46
3NTG[20]	0.19	0.20	0.39
3OLT[22]	0.24	0.25	0.41
3OLU[22]	0.23	0.24	0.42
3Q7D[23]	0.22	0.25	0.47
3RR3[23]	0.12	0.14	0.24
3TZI[24]	0.23	0.23	0.47
4FM5[25]	0.15	0.20	0.36
4M10[15]	0.18	0.19	0.39
4M11[15]	0.19	0.21	0.49
4OTJ[26]	0.17	0.18	0.38
4OTY[27]	0.23	0.24	0.43
4PH9[28]	0.20	0.20	0.43
4RRW[29]	0.15	0.15	0.28
4RRX[29]	0.20	0.20	0.38
4RRY[29]	0.19	0.21	0.41
4RRZ[29]	0.15	0.15	0.28
4RS0[29]	0.23	0.23	0.42
4RUT[30]	0.18	0.19	0.40
4Z0L[31]	0.18	0.18	0.33
5F19[32]	0.22	0.22	0.43
5F1A[32]	0.20	0.20	0.43
5FDQ[32]	0.20	0.21	0.44
5IKQ[33]	0.18	0.19	0.42
5IKR[33]	0.20	0.20	0.42
5IKT[33]	0.15	0.16	0.36
5IKV[33]	0.15	0.16	0.38
5W58[34]	0.23	0.23	0.41
6BL3[35]	0.13	0.14	0.27
6BL4[35]	0.15	0.16	0.31

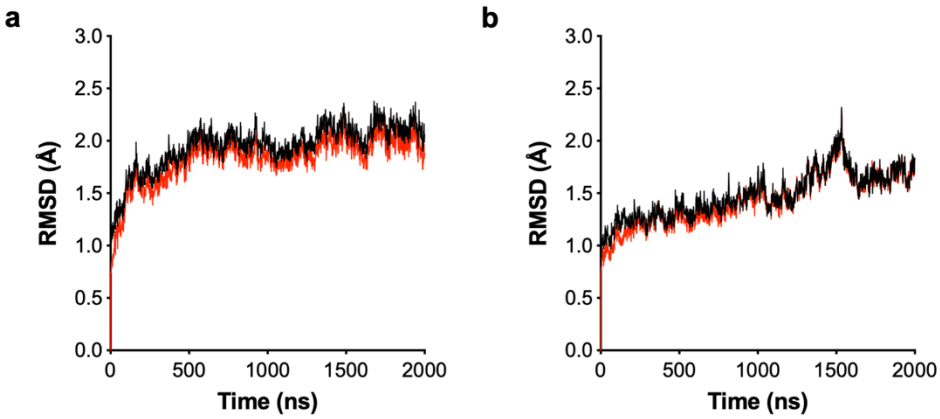

Figure A.5: RMSD of simulated (a) COX-1 and (b) COX-2 versus the initial crystal structure (PDB 5U6X or 5KIR) as a function of simulation time. Monomer A and B are plotted as black and red lines, respectively.

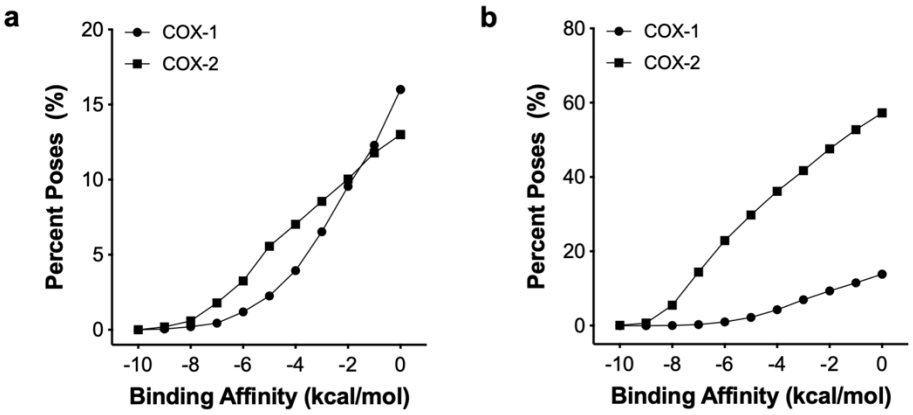

Figure A.6: Percent of the total docked poses of CoxFluor bound within the (a) cyclooxygenase and (b) peroxidase active sites of COX-2 at a particular Vina AutoDock docking score binding affinity.

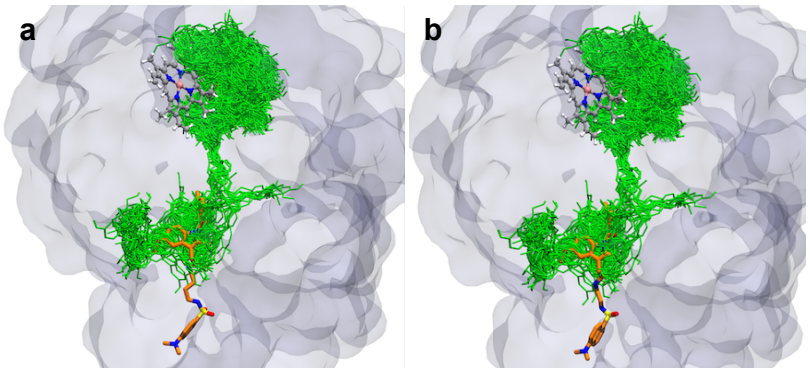

Figure A.7: Comparison between CoxFluor (green, -7 kcal/mol docking score cutoff) bound to COX-2 and dansyl-conjugated indomethacin either (a) without (PDB 6BL3) or (b) with a *n*-butyl-diamine linker (PDB 6BL4).[35]

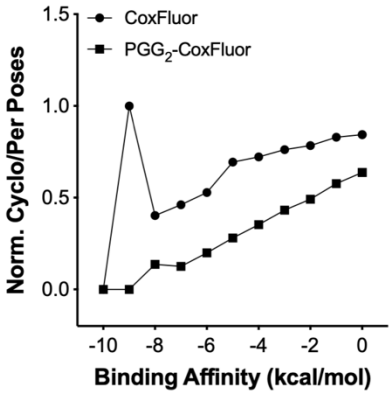

Figure A.8: Normalized ratio of cyclooxygenase to peroxidase binding modes for CoxFluor and PGG_2-CoxFluor intermediate.

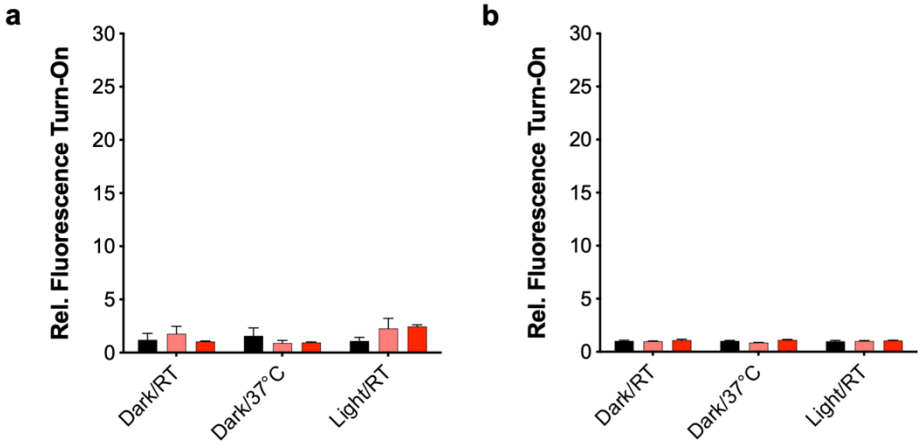

Figure A.9: Stability of (a) CoxFluor and (b) resorufin in Tris-HCl (100 mM, pH 8.0, black) and serum-free DMEM (light red), DMEM with 10% FBS (red) after 8 h at room temperature with or without exposure to ambient light. Values are reported as the mean ± standard deviation (n = 3).

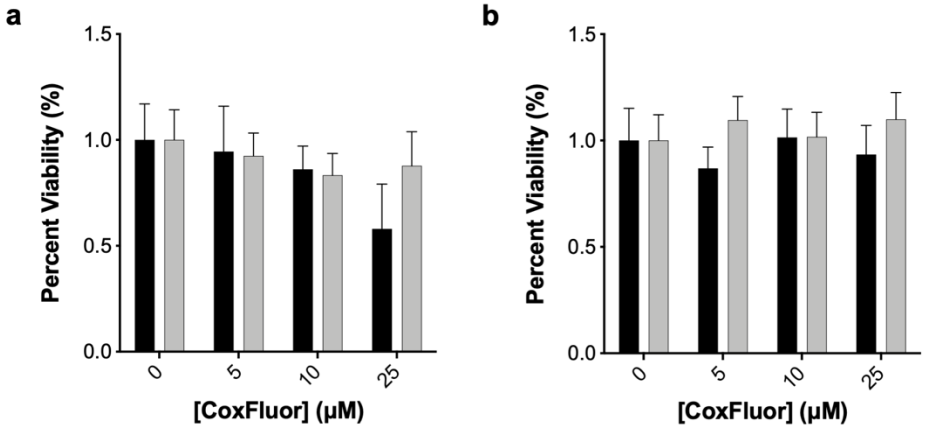

Figure A.10: Cell viability for CoxFluor in (a) HEK 293T cells and (b) RAW 264.7 macrophage cells after 6 h incubation as measured by the trypan blue exclusion assay (black) and MTT assay (grey). Values are reported as the mean ± standard deviation (n = 3).

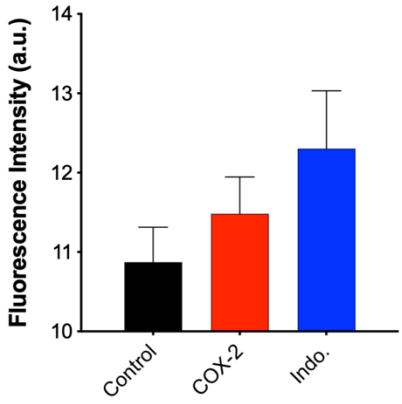

Figure A.11: Quantified confocal imaging of COX-2 activity after 3 h incubation in either non-transfected (control) or transfected HEK 293T cells. Indomethacin inhibition (Indo., 10 µM) was performed in transfected cells. Values are reported as the mean ± standard deviation (n = 3).

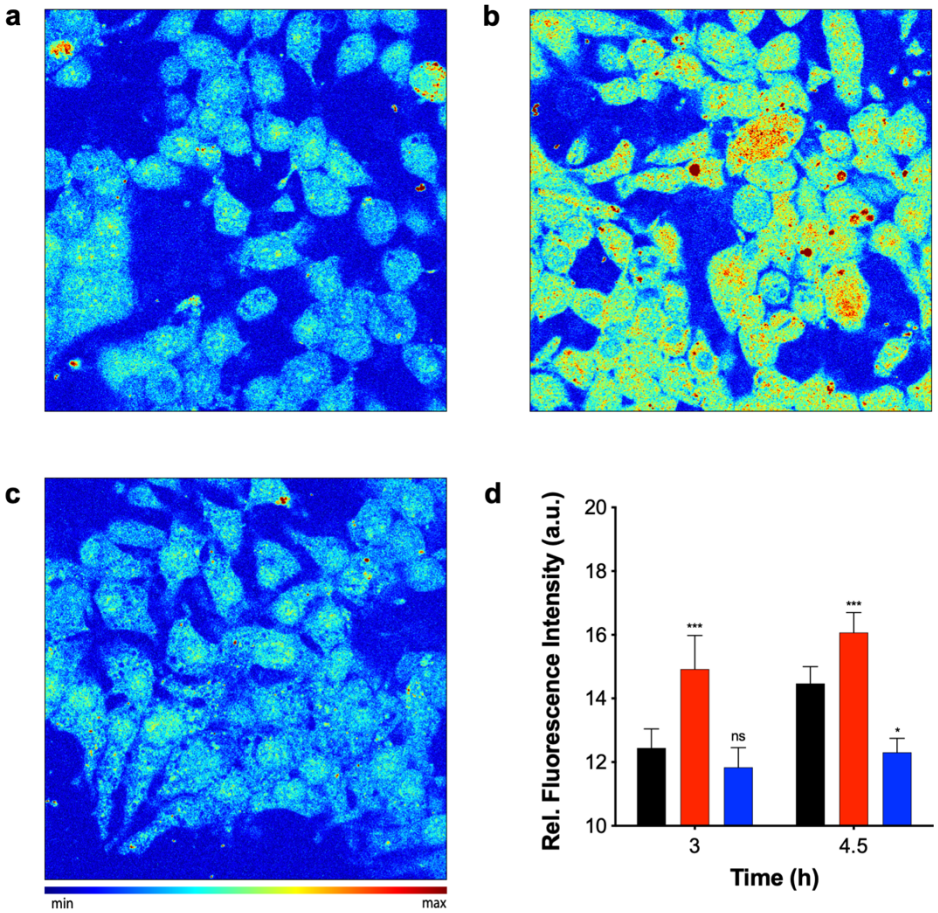

Figure A.12: Confocal imaging of COX-2 activity in (a) control, (b) transfected, and (c) indomethacin-treated transfected HEK 293T cells after 3 or 4.5 h incubation with CoxFluor (10 µM) at 37 ºC (pre-treated with 1 mM NEM for 0.5 h prior to staining). (d) Quantification of images. Values are reported as the mean ± standard deviation (n = 3). Statistical analysis was performed using two-way ANOVA ($\alpha = 0.05$). Fluorescence intensities were compared to the control at each time point using Sidak's multiple comparison test ($\alpha = 0.05$). *, $p < 0.05$; ***, $p < 0.001$. Scale bar (white) represents 10 µm.

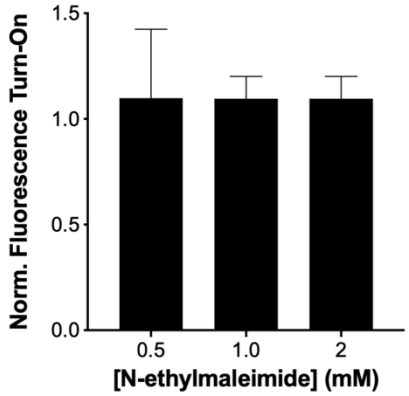

Figure A.13: Normalized fluorescence response for CoxFluor (10 μM) after incubation with COX-2 (250 nM) at varying concentrations of *N*-ethylmaleimide. Samples were incubated at room temperature for 4 h and normalized to the fluorescence with 0 mM *N*-ethylmaleimide. Assay was performed according to the plate reader assay. Values are reported as the mean ± standard deviation (n = 3).

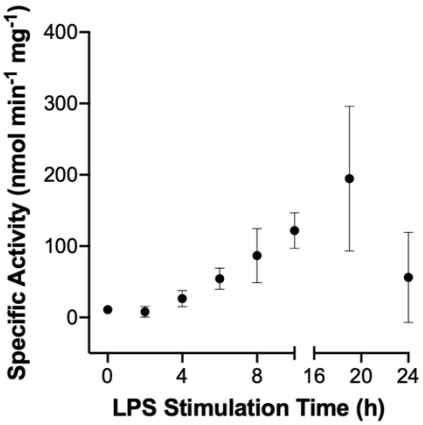

Figure A.14: RAW 264.7 macrophage cell lysate COX-2 activity as a function of LPS stimulation time. Enzymatic activity was measured at room temperature with CoxFluor (10 μM) in 89 mM Tris-HCl buffer (pH 8.0) containing 10% CelLytic M and 1 mM N-ethylmaleimide. Initial rates were measured within the linear region (typically the first 30 seconds) and protein concentration was measured using the BCA assay. Values are reported as the mean ± standard deviation (n = 3).

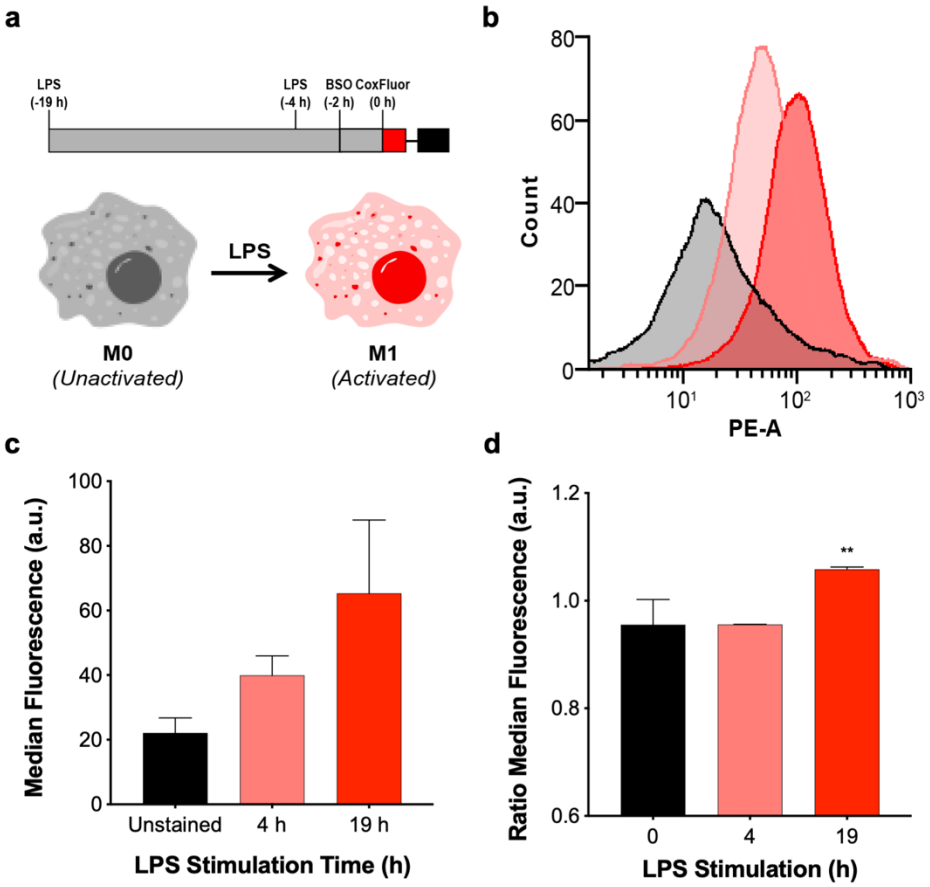

Figure A.15: (a) A schematic representation of the protocol for measuring time-dependent changes in LPS-activated RAW 264.7 macrophage COX-2 activity with flow cytometry. (b) Representative histogram and (c) quantified median fluorescence for unstained (black), and CoxFluor stained cells after 4 (salmon) and 19 h (red) LPS activation. (d) Quantified ratio of median fluorescence between cells stained with CoxFluor to cells stained with CoxFluor in the presence of indomethacin (20 μM). All staining was performed with 10 μM CoxFluor, 200 μM BSO was added 2 h prior to staining, and values are reported as the mean ± standard deviation (n = 3). Statistical analysis was performed using a two-way ANOVA ($\alpha = 0.05$) with Tukey's multiple t test ($\alpha = 0.05$) for comparison of 19 h LPS-stimulation to both 0 and 4 h. **, $p < 0.01$.

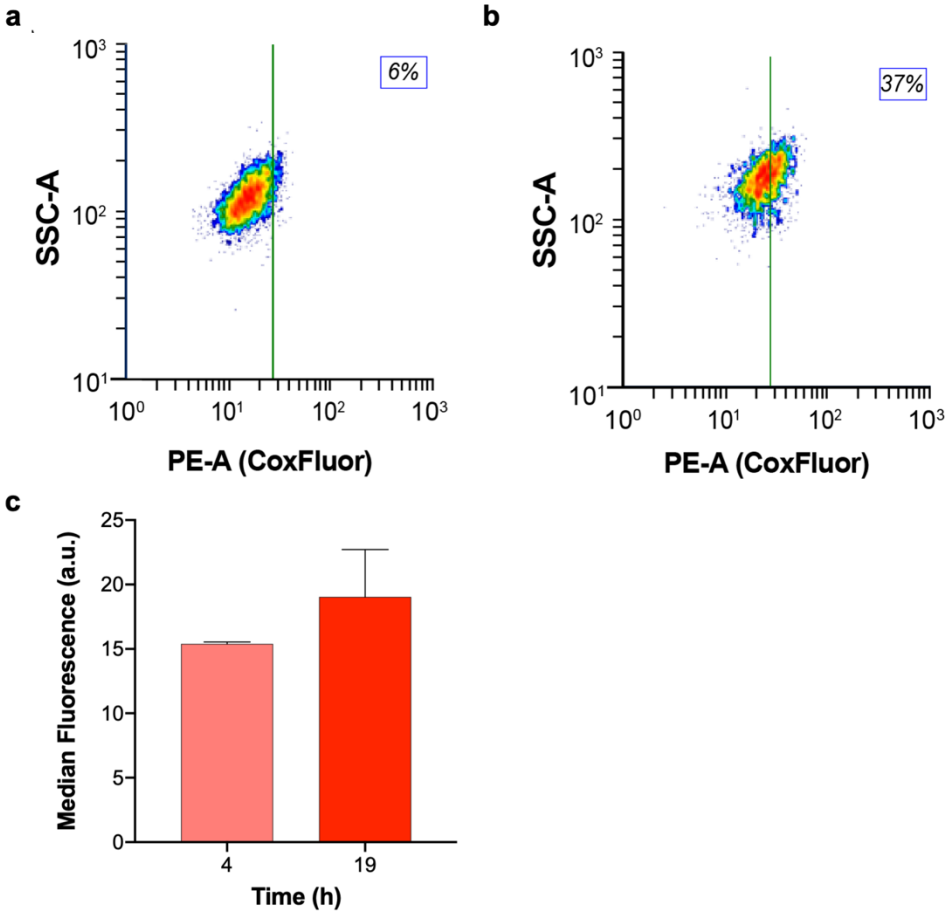

Figure A.16: Representative density plot for LPS-activated RAW 264.7 macrophage cells with flow cytometry without BSO with (a) 4 h or (b) 19 h LPS-stimulation. (c) Quantified median fluorescence for CoxFluor (10 μM) stained cells after 4 (salmon) and 19 h (red) LPS activation. Percentages indicate the percent COX-2 positive cells, as defined by the green line. Values are reported as the mean ± standard deviation (n = 3).

A.1 References

(1) Picot, D.; Loll, P. J.; Garavito, R. M. The X-Ray Crystal Structure of the Membrane Protein Prostaglandin H2 Synthase-1. *Nature* **1994**, *367* (6460), 243–249.

(2) Loll, P. J.; Picot, D.; Garavito, R. M. The Structural Basis of Aspirin Activity Inferred from the Crystal Structure of Inactivated Prostaglandin H2 Synthase. *Nat. Struct. Mol. Biol.* **1995**, *2* (8), 637–643.

(3) Loll, P. J.; Picot, D.; Ekabo, O.; Garavito, R. M. Synthesis and Use of Iodinated Nonsteroidal Antiinflammatory Drug Analogs as Crystallographic Probes of the Prostaglandin H2 Synthase Cyclooxygenase Active Site. *Biochemistry* **1996**, *35* (23), 7330–7340.

(4) Loll, P. J.; Sharkey, C. T.; O'Connor, S. J.; Dooley, C. M.; O'Brien, E.; Devocelle, M.; Nolan, K. B.; Selinsky, B. S.; Fitzgerald, D. J. O-Acetylsalicylhydroxamic Acid, a Novel Acetylating Inhibitor of Prostaglandin H 2 Synthase: Structural and Functional Characterization of Enzyme-Inhibitor Interactions. *Mol. Pharmacol.* **2001**, *60* (6), 1407–1413.

(5) Malkowski, M. G.; Ginell, S. L.; Smith, W. L.; Garavito, R. M. The Productive Conformation of Arachidonic Acid Bound to Prostaglandin Synthase. *Science* **2000**, *289* (5486), 1933–1937.

(6) Selinsky, B. S.; Gupta, K.; Sharkey, C. T.; Loll, P. J. Structural Analysis of NSAID Binding by Prostaglandin H 2 Synthase: Time-Dependent and Time-Independent Inhibitors Elicit Identical Enzyme Conformations †. *Biochemistry* **2001**, *40* (17), 5172–5180.

(7) Thuresson, E. D.; Malkowski, M. G.; Lakkides, K. M.; Rieke, C. J.; Mulichak, A. M.; Ginell, S. L.; Garavito, R. M.; Smith, W. L. Mutational and X-Ray Crystallographic Analysis of the Interaction of Dihomo-γ-Linolenic Acid with Prostaglandin Endoperoxide H Synthases. *J. Biol. Chem.* **2001**, *276* (13), 10358–10365.

(8) Malkowski, M. G.; Thuresson, E. D.; Lakkides, K. M.; Rieke, C. J.; Micielli, R.; Smith, W. L.; Garavito, R. M. Structure of Eicosapentaenoic and Linoleic Acids in the Cyclooxygenase Site of Prostaglandin Endoperoxide H Synthase-1. *J. Biol. Chem.* **2001**, *276* (40), 37547–37555.

(9) Gupta, K.; Selinsky, B. S.; Kaub, C. J.; Katz, A. K.; Loll, P. J. The 2.0 Å Resolution Crystal Structure of Prostaglandin H 2 Synthase-1: Structural Insights into an Unusual Peroxidase. *J. Mol. Biol.* **2004**, *335* (2), 503–518.

(10) Harman, C. A.; Rieke, C. J.; Garavito, R. M.; Smith, W. L. Crystal Structure of Arachidonic Acid Bound to a Mutant of Prostaglandin Endoperoxide H Synthase-1 That Forms Predominantly 11-Hydroperoxyeicosatetraenoic Acid. *J. Biol. Chem.* **2004**, *279* (41), 42929–42935.

(11) Gupta, K.; Selinsky, B. S.; Loll, P. J. 2.0 Å Structure of Prostaglandin H2 Synthase-1 Reconstituted with a Manganese Porphyrin Cofactor. *Acta Crystallogr. Sect. D Biol. Crystallogr.* **2006**, *62* (2), 151–156.

(12) Harman, C. A.; Turman, M. V.; Kozak, K. R.; Marnett, L. J.; Smith, W. L.; Garavito, R. M. Structural Basis of Enantioselective Inhibition of Cyclooxygenase-1 by S-α-Substituted Indomethacin Ethanolamides. *J. Biol. Chem.* **2007**, *282* (38), 28096–28105.

(13) Rimon, G.; Sidhu, R. S.; Lauver, D. A.; Lee, J. Y.; Sharma, N. P.; Yuan, C.; Frieler, R. A.; Trievel, R. C.; Lucchesi, B. R.; Smith, W. L. Coxibs Interfere with the Action of Aspirin by Binding Tightly to One Monomer of Cyclooxygenase-1. *Proc. Natl. Acad. Sci.* **2010**, *107* (1), 28–33.

(14) Sidhu, R. S.; Lee, J. Y.; Yuan, C.; Smith, W. L. Comparison of Cyclooxygenase-1 Crystal Structures: Cross-Talk between Monomers Comprising Cyclooxygenase-1 Homodimers. *Biochemistry* **2010**, *49* (33), 7069–7079.

(15) Xu, S.; Hermanson, D. J.; Banerjee, S.; Ghebreselasie, K.; Clayton, G. M.; Garavito, R. M.; Marnett, L. J. Oxicams Bind in a Novel Mode to the Cyclooxygenase Active Site via a Two-Water-Mediated H-Bonding Network. *J. Biol. Chem.* **2014**, *289* (10), 6799–6808.

(16) Cingolani, G.; Panella, A.; Perrone, M. G.; Vitale, P.; Di Mauro, G.; Fortuna, C. G.; Armen, R. S.; Ferorelli, S.; Smith, W. L.; Scilimati, A. Structural Basis for Selective Inhibition of Cyclooxygenase-1 (COX-1) by Diarylisoxazoles Mofezolac and 3-(5-Chlorofuran-2-Yl)-5-Methyl-4-Phenylisoxazole (P6). *Eur. J. Med. Chem.* **2017**, *138*, 661–668.

(17) Kiefer, J. R.; Pawlitz, J. L.; Moreland, K. T.; Stegeman, R. A.; Hood, W. F.; Marnett, L. J.; Gierse, J. K.; Stevens, A. M.; Goodwin, D. C.; Rowlinson, S. W.; et al. Structural Insights into the Stereochemistry of the Cyclooxygenase Reaction. *Nature* **2002**, *405* (6782), 97–101.

(18) Rowlinson, S. W.; Kiefer, J. R.; Prusakiewicz, J. J.; Pawlitz, J. L.; Kozak, K. R.; Kalgutkar, A. S.; Stallings, W. C.; Kurumbail, R. G.; Marnett, L. J. A Novel Mechanism of Cyclooxygenase-2 Inhibition Involving Interactions with Ser-530 and Tyr-385. *J. Biol. Chem.* **2003**, *278* (46), 45763–45769.

(19) Vecchio, A. J.; Simmons, D. M.; Malkowski, M. G. Structural Basis of Fatty Acid Substrate Binding to Cyclooxygenase-2. *J. Biol. Chem.* **2010**, *285* (29), 22152–22163.

(20) Wang, J. L.; Limburg, D.; Graneto, M. J.; Springer, J.; Hamper, J. R. B.; Liao, S.; Pawlitz, J. L.; Kurumbail, R. G.; Maziasz, T.; Talley, J. J.; et al. The Novel Benzopyran Class of Selective Cyclooxygenase-2 Inhibitors. Part 2: The Second Clinical Candidate Having a Shorter and Favorable Human Half-Life. *Bioorganic Med. Chem. Lett.* **2010**, *20* (23), 7159–7163.

(21) Duggan, K. C.; Walters, M. J.; Musee, J.; Harp, J. M.; Kiefer, J. R.; Oates, J. A.; Marnett, L. J. Molecular Basis for Cyclooxygenase Inhibition by the Non-Steroidal Anti-Inflammatory Drug Naproxen. *J. Biol. Chem.* **2010**, *285* (45), 34950–34959.

(22) Vecchio, A. J.; Malkowski, M. G. The Structural Basis of Endocannabinoid Oxygenation by Cyclooxygenase-2. *J. Biol. Chem.* **2011**, *286* (23), 20736–20745.

(23) Duggan, K. C.; Hermanson, D. J.; Musee, J.; Prusakiewicz, J. J.; Schneib, J. L.; Carter, B. D.; Banerjee, S.; Oates, J. A.; Marnett, L. J. (R)-Profens Are Substrate-Selective Inhibitors of Endocannabinoid Oxygenation by COX-2. *Nat. Chem. Bio.* **2011**, *7* (11), 803–809.

(24) Vecchio, A. J.; Orlando, B. J.; Nandagiri, R.; Malkowski, M. G. Investigating Substrate Promiscuity in Cyclooxygenase-2: The Role of Arg-120 and Residues Lining the Hydrophobic Groove. *J. Biol. Chem.* **2012**, *287* (29), 24619–24630.

(25) Windsor, M. A.; Hermanson, D. J.; Kingsley, P. J.; Xu, S.; Crews, B. C.; Ho, W.; Keenan, C. M.; Banerjee, S.; Sharkey, K. A.; Marnett, L. J. Substrate-Selective Inhibition of Cyclooxygenase-2: Development and Evaluation of Achiral Profen Probes. *ACS Med. Chem. Lett.* **2012**, *3* (9), 759–763.

(26) Uddin, M. J.; Crews, B. C.; Xu, S.; Ghebreselasie, K.; Daniel, C. K.; Kingsley, P. J.; Banerjee, S.; Marnett, L. J. Antitumor Activity of Cytotoxic Cyclooxygenase-2 Inhibitors. *ACS Chem. Biol.* **2016**, *11* (11), 3052–3060.

(27) Windsor, M. A.; Valk, P. L.; Xu, S.; Banerjee, S.; Marnett, L. J. Exploring the Molecular Determinants of Substrate-Selective Inhibition of Cyclooxygenase-2 by Lumiracoxib. *Bioorganic Med. Chem. Lett.* **2013**, *23* (21), 5860–5864.

(28) Orlando, B. J.; Lucido, M. J.; Malkowski, M. G. The Structure of Ibuprofen Bound to Cyclooxygenase-2. *J. Struct. Biol.* **2015**, *189* (1), 62–66.

(29) Blobaum, A. L.; Xu, S.; Rowlinson, S. W.; Duggan, K. C.; Banerjee, S.; Kudalkar, S. N.; Birmingham, W. R.; Ghebreselasie, K.; Marnett, L. J. Action at a Distance: Mutations of Peripheral Residues Transform Rapid Reversible Inhibitors to Slow, Tight Binders of Cyclooxygenase-2. *J. Biol. Chem.* **2015**, *290* (20), 12793–12803.

(30) Kudalkar, S. N.; Nikas, S. P.; Kingsley, P. J.; Xu, S.; Galligan, J. J.; Rouzer, C. A.; Banerjee, S.; Ji, L.; Eno, M. R.; Makriyannis, A.; et al. 13-Methylarachidonic Acid Is a Positive Allosteric Modulator of Endocannabinoid Oxygenation by Cyclooxygenase. *J. Biol. Chem.* **2015**, *290* (12), 7897–7909.

(31) Neumann, W.; Xu, S.; Sárosi, M. B.; Scholz, M. S.; Crews, B. C.; Ghebreselasie, K.; Banerjee, S.; Marnett, L. J.; Hey-Hawkins, E. Nido-Dicarbaborate Induces Potent and Selective Inhibition of Cyclooxygenase-2. *ChemMedChem* **2016**, *11* (2), 175–178.

(32) Lucido, M. J.; Orlando, B. J.; Vecchio, A. J.; Malkowski, M. G. Crystal Structure of Aspirin-Acetylated Human Cyclooxygenase-2: Insight into the Formation of Products with Reversed Stereochemistry. *Biochemistry* **2016**, *55* (8), 1226–1238.

(33) Orlando, B. J.; Malkowski, M. G. Substrate-Selective Inhibition of Cyclooxygeanse-2 by Fenamic Acid

Derivatives Is Dependent on Peroxide Tone. *J. Biol. Chem.* **2016**, *291* (29), 15069–15081.

(34) Goodman, M. C.; Xu, S.; Rouzer, C. A.; Banerjee, S.; Ghebreselasie, K.; Migliore, M.; Piomelli, D.; Marnett, L. J. Dual Cyclooxygenase-Fatty Acid Amide Hydrolase Inhibitor Exploits Novel Binding Interactions in the Cyclooxygenase Active Site. *J. Biol. Chem.* **2018**, *293* (9), 3028–3038.

(35) Xu, S.; Uddin, M. J. J.; Banerjee, S.; Marnett, L. J. L. J.; Jashim Uddin, M.; Banerjee, S.; Duggan, K.; Musee, J.; Kiefer, J. R.; Ghebreselasie, K.; et al. Conjugated Indomethacin Fluorescent Inhibitors Utilize Membrane Binding Domain of Cyclooxygenase-2 to Accommodate Tethered Moiety. *J. Biol. Chem.* **2019**, *294* (22), 8690–8689.

(36) Yadav, A. K.; Reinhardt, C. J.; Arango, A. S.; Huff, H. C.; Dong, L.; Malkowski, M. G.; Das, A.; Tajkhorshid, E.; Chan, J. An Activity-Based Sensing Approach for the Detection of Cyclooxygenase-2 in Live Cells. *Angew. Chemie Int. Ed.* **2020**, *59*, 3307–3314.

APPENDIX B: MOLECULAR DYNAMICS AND ENSEMBLE DOCKING

B.1 Introduction

This appendix outlines the general procedures for performing molecular dynamic simulations and ensemble docking with NAMD/VMD[1,2] and AutoDock Vina.[3] The information in this section, as well as the scripts, were compiled with the help of Mr. Andres S. Arango (Tajkhorshid Laboratory, University of Illinois at Urbana-Champaign).

B.2 Molecular dynamics

The following discussion is with regards to performing molecular dynamics experiments in NAMD and VMD.[1,2] Information about PSFGEN can be found in the tutorials (provided online from University of Illinois at Urbana-Champaign). If no molecular dynamics are required for the analysis, proceed directly to Appendix B.3 for discussions regarding docking.

Load VMD and access QwikMD through extensions and simulation. Set up the dynamics experiment using either easy run (e.g., solvent, temperature, salt concentration, simulation time, equilibration times, etc.) or advanced run (e.g., steered MD, fitting into Cryo-EM densities, or quantum molecular dynamics for reactions). Load the PDB file through the browser. This will rename and prepare residues using NAMD conventions. If the structure contains problems, it will indicate them as flashing objects. These must be fixed before simulation. Typically, these are crystallographic molecules (e.g., sugars, cofactors, heme, etc.). To check this list, use structure manipulation to identify. This will list topologies and parameters that must be removed or modified (e.g., chiral centers, *cis*-peptide bonds, sequence gaps, torsion angle outliers, or torsion angle marginals). Delete all that are not required for the simulation (delete and apply). To add

parameters, select the molecule of interest and upload using TopoParam. If there is a reason that something needs to be altered (e.g., binding a ligand to the heme) it is necessary to create a psf file using psfgen. This defines connectivity, which is absent from pdb files, and requires tcl scripting that calls psfgen and all necessary CHARMM topology files[4] (found on QwikMD or on CHARMM website), loads the original pdb and psf files, and then patch the desired structure to be at the specific location.

If scripting, use:

```
package require psfgen
topology ../../par/filename
        mol new simulation.re.pdb
        readpsf Simulation.ref.psf

coordinate Simulation.ref.pdb

patch atomtype PROB:location
guesscoord
        writepsf ref.removed.psf
        writepdb ref.removed.pdb
exit
```

The topology files and the term for the desired atom time atom type modification can be found in the parameter folders (made by user or from VMD). Search the files for the desired structure (e.g., using grep command). Be careful about the class of compounds that classifies the atom type (e.g., prot for proteins, lipid for lipids, etc.). Then open the file to determine the acronym for the atom type. It is imperative to check that it is correct after patching and after simulation (e.g., atoms should not overlap). One common problem is that several atoms will have coordinates at the origin (search for 0, 0, 0), which will cause NAMD to crash.

After complete, ignore any structure alerts that are not relevant. Prepare the location for the files to be saved using the prepare tool. QwikMD will prepare the structure according to the

specifications as a config file (used in runs of NAMD and outputs visualized in VMD). Equilibrations and relaxation provide the protein with the ability to solvate and readjust amino acid side chains prior to releasing the backbone. This prevents undesirable deviation from the initial structure. A general method (gradual release) for this is outlined in Chapter 2 for simulating COX-1 and COX-2 (see section 2.19.12 for additional information). A simpler alternative is to set an initial equilibration without the backbone and then proceeding directly to the simulation. Start equilibration simulation to begin. This can be performed directly in VMD/QwikMD or uploaded to a cluster (these submission commands are cluster-dependent).

The simulation will output the simulation trajectory as separate files. You can look at the RMSD changes of the peptide backbone over time to confirm that any removed constituents (e.g., oligosaccharides) are non-essential during the time frame of the simulation. If this converges, one can assume that the protein structure was not significantly altered during the simulation (microsecond versus nanosecond for conformational changes and simulation).

Note that it is possible to simulate the ligand within a static or dynamic protein. This should typically be performed after identifying the ideal ligand and it requires ligand parameterization. If the ligand is not currently in a database, it is necessary to generate parameters. In VMD, one can use the forcefield toolkit with Gaussian. This can be found under extensions, modeling, and then forcefield toolkit (FFTK). Alternatively, cgenff (CHARMM General Force Field) can be used online (cgenf.umaryland.edu) from a mol2 or pdb file. This creates parameters based off data from current databases and will indicate how reliable the generated forcefield is. Often cgenff is used as a starting point, and can be refined further with FFTK when needed. Always begin with FFTK. After the molecular dynamics are complete, continue to section B.2 for ensemble docking.

B.3 Static and ensemble docking

The following discussion is regards to performing molecular docking in AutoDock Vina.[3] Protein modifications do not require PSFGEN patching if molecular dynamics are not being performed. Draw the modification using another program (e.g., Avogadro, Chimera),[5,6] minimize with an appropriate forcefield, and save as a pdb file. This can be used directly for molecular docking experiments. Analysis is performed by docking the ligand of interest into each simulation trajectory pdb file. This can also be used for rigid docking (without molecular dynamic), although this would not enable docking into transient or cryptic pockets. This can be scripted or performed manually in AutoDockTools.

Docking requires the following: simulation trajectory or protein structure, the ligand structure (pdbqt format), and the grid box for docking. Load the structures of the protein and ligand and alter any flexible residues using the embedded tools. For example, it is possible to enable or prevent bonds from rotating during docking (e.g., maintaining planarity in aromatic compounds). Initially, the simulation data will be a pdb file and it must be converted to a pdbqt file for docking. This can be achieved by loading into AutoDockTools, which initiates the conversion. To save it in the pdbqt format via Output, use the file and save as functions. Alternatively, this can be scripted. This file contains the coordinates for the atoms and the ligand name (typically included as UNK). If the docking experiments are to be scripted, it is necessary to change the name (either manually or with scripting).

Next, it is necessary to define the area for docking (the grid box). If simulations were performed, it is recommended to overlay the first and last pose to ensure proper orientation of the grid box for visualization (all poses should be aligned prior to loading in AutoDock tools). Grid box is prepared in Grid using the Grid Box tool. This allows the user to define the cartesian

coordinates for the box and the spacing in angstroms. Grid spacing of 1 angstrom is typically used as a starting point (decreasing will increase the computational cost with 1 being around the atomistic resolution). Exhaustiveness is defined as the maximum number of poses into each pdb file (typically 40). If you have a large docking box, use a small exhaustiveness (inversely related).

After setting up the AutoDock experiment, a conf file will be generated for each pose and will contain the files for the ligand and receptor, the grid box information, exhaustiveness, number of modes, energy range and outputs for the pdbqt and log files. This can then be run and analyzed directly in the software, with the user option of how many CPUs to allocate. These can be submitted using a script (high-throughput) or directly performed in AutoDockTools (low-throughput).

<u>If scripting, use:</u>

for i in (1..*totalnumber*)
echo "Currently performing docking dock.$(i).conf"
sourceforvina --config *configurationfilename*$(i).conf –cpu *cpunumber*
done

<u>To use it without a script, only use the following when in the Vina location of the computer:</u>

sourceforvina --config *configurationfilename*$(*number*).conf –cpu *cpunumber*

If you use the GUI for AutoDockTools, it is possible to output a configuration file after setting up the docking parameters, which can then be applied to all of the poses. After running the docking experiment, the data will be exported as log and pdbqt files. Analysis of the log file provides the affinity score (kcal/mol) and the distance RMSD from best pose (lower bound and upper bound). Structural data will be saved as pdbqt files for analysis in VMD. Note that several

issues can arise when opening this file type in VMD. It is recommended to convert to the pdb format prior to visualization. This can be generated by deleting the last two columns of the atom coordinate (corresponding to the qt). Load the protein frames onto the ligand structure using VMD. Assess the protein-ligand interactions by merging the pdb structures and visualizing in VMD. Important considerations include the frequency of docking at the particular site and the calculated affinity (docking score). Clustering provides a visual for the docking locations based on docking score (typically use RMSD-based clustering with the VMD command "measure cluster" although other clustering methods are possible).

To determine the percent poses with a certain binding energy, search the ligand.pdb files and sum the number of Remark Vina Results with that number or less kcal/mol (note that 0 and -0 are different and must be accounted for in the analysis). To assess the binding pocket, define the interaction between the ligand the protein as specific cutoff and then quantify the number of possess at each site; this can be done by measuring the distance from the center of mass of the desired receptor region to the center of mass of the docked ligand. When performing static docking, you can run the experiment several times or have a high exhaustiveness to increase sampling (will not show transient pockets).

B.4 References

(1) Phillips, J. C.; Braun, R.; Wang, W.; Gumbart, J.; Tajkhorshid, E.; Villa, E.; Chipot, C.; Skeel, R. D.; Kalé, L.; Schulten, K. Scalable Molecular Dynamics with NAMD. *J. Comput. Chem.* **2005**, *26* (16), 1781–1802.

(2) Humphrey Dalke Schulten, W. A. K. Visual Molecular Dyanmics. *J. Mol. Graph.* **1996**, *14* (1), 33–38.

(3) Trott, O.; Olson, A. J. AutoDock Vina: Improving the Speed and Accuracy of Docking with a New Scoring Function, Efficient Optimization, and Multithreading. *J. Comput. Chem.* **2010**, *31* (2), 455–461.

(4) Huang, J.; Rauscher, S.; Nawrocki, G.; Ran, T.; Feig, M.; De Groot, B. L.; Grubmüller, H.; MacKerell, A. D. CHARMM36m: An Improved Force Field for Folded and Intrinsically Disordered Proteins. *Nat. Methods* **2017**, *14* (1), 71–73.

(5) Hanwell, M. D.; Curtis, D. E.; Lonie, D. C.; Vandermeersch, T.; Zurek, E.; Hutchison, G. R. Avogadro: An Advanced Semantic Chemical Editor, Visualization, and Analysis Platform. *J .Cheminform.* **2012**, *4* (1), 17.

(6) Pettersen, E. F.; Goddard, T. D.; Huang, C. C.; Couch, G. S.; Greenblatt, D. M.; Meng, E. C.; Ferrin, T. E. UCSF Chimera - A Visualization System for Exploratory Research and Analysis. *J. Comput. Chem.* **2004**, *25* (13), 1605–1612.

APPENDIX C: CHAPTER 3 SUPPLMENTAL FIGURES, TABLES, AND DETAILED SYNTHETIC PROCEDURES[5]

Table C.1: Photophysical characterization of APNO in chloroform. Fluorescent quantum yield measured relative to an indocyanine green standard.

APNO	λ_{max} (nm)	ε ($M^{-1}cm^{-1}$)	Φ
1	720	4.70×10^4	0.02
2	735	8.70×10^4	0.0071
3	684	3.50×10^4	0.0024
4	755	6.80×10^4	0.0008
5	755	3.43×10^4	0.0003

[5]Portions of this chapter are reprinted or adapted with permissions from the following publications: (1) Reinhardt, C. J.; Zhou, E. Y.; Jorgensen, M. D.; Partipilo, G.; Chan, J. A Ratiometric Acoustogenic Probe for In Vivo Imaging of Endogenous Nitric Oxide. *J. Am. Chem. Soc.* **2018**, *140*, 1011–1018.[11] Copyright © 2018 American Chemical Society. (2) Reinhardt, C. J.; Xu, R.; Chan, J. Nitric Oxide Imaging in Cancer Enabled by Steric Relaxation of a Photoacoustic Probe Platform. *Chem. Sci.* **2020**, *11*, 1587–1592.[12] Copyright © 2020 Royal Society of Chemistry.

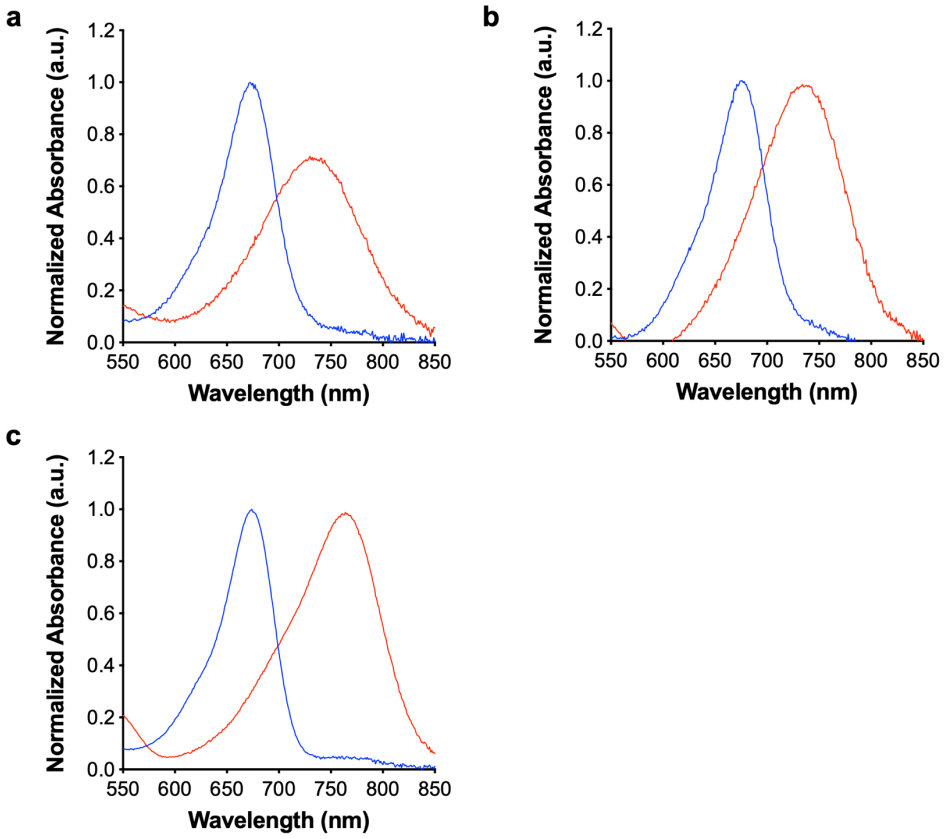

Figure C.1: UV-vis absorbance profiles for (a) APNO-1, (b) APNO-2, (c) APNO-4 (2 μM) in ethanolic 20 mM potassium phosphate buffer (pH 7.4, 50 % v/v).

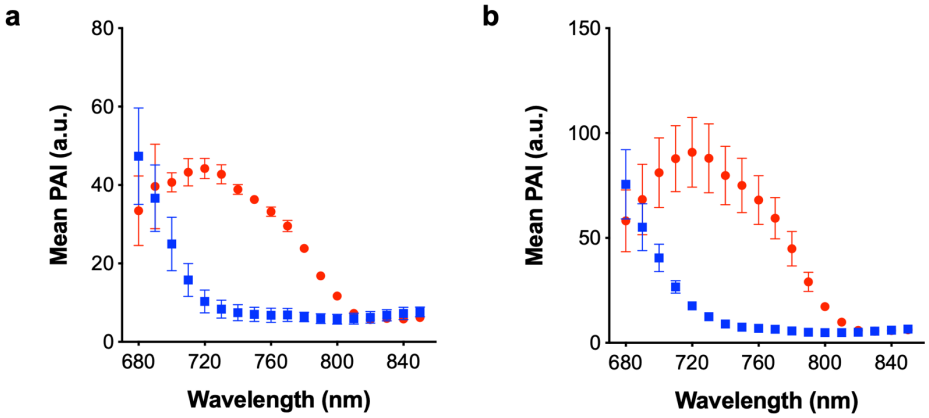

Figure C.2: PA spectra (a) APNO-1, (b) APNO-2 and their corresponding products (10 μM) in ethanolic 20 mM potassium phosphate buffer (pH 7.4, 50 % v/v). Data represented as mean ± standard deviation (n = 3).

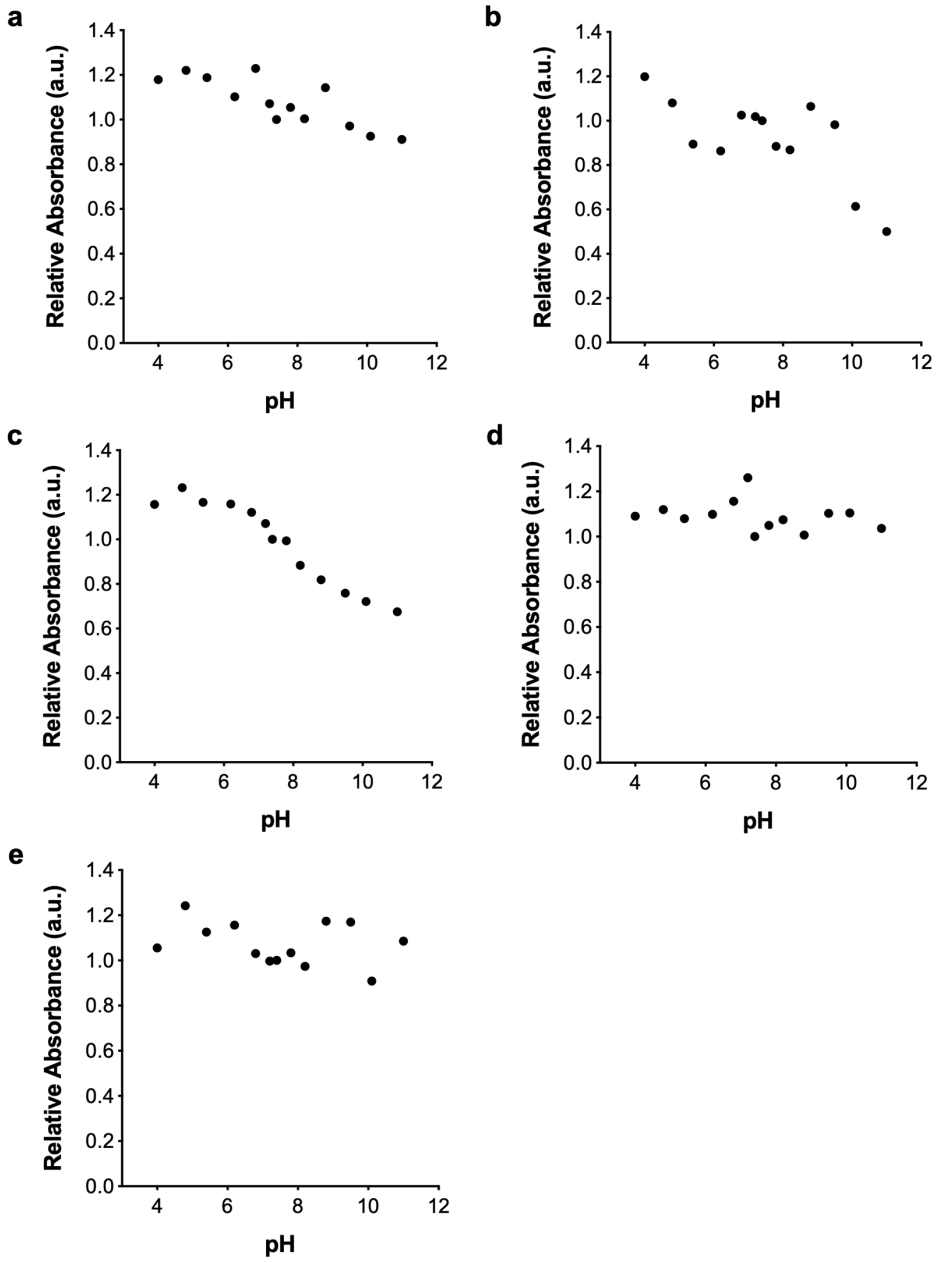

Figure C.3: APNO (2 μM) pH profile in ethanolic 20 mM Britton-Robinson buffer (50 % v/v).[1,2]

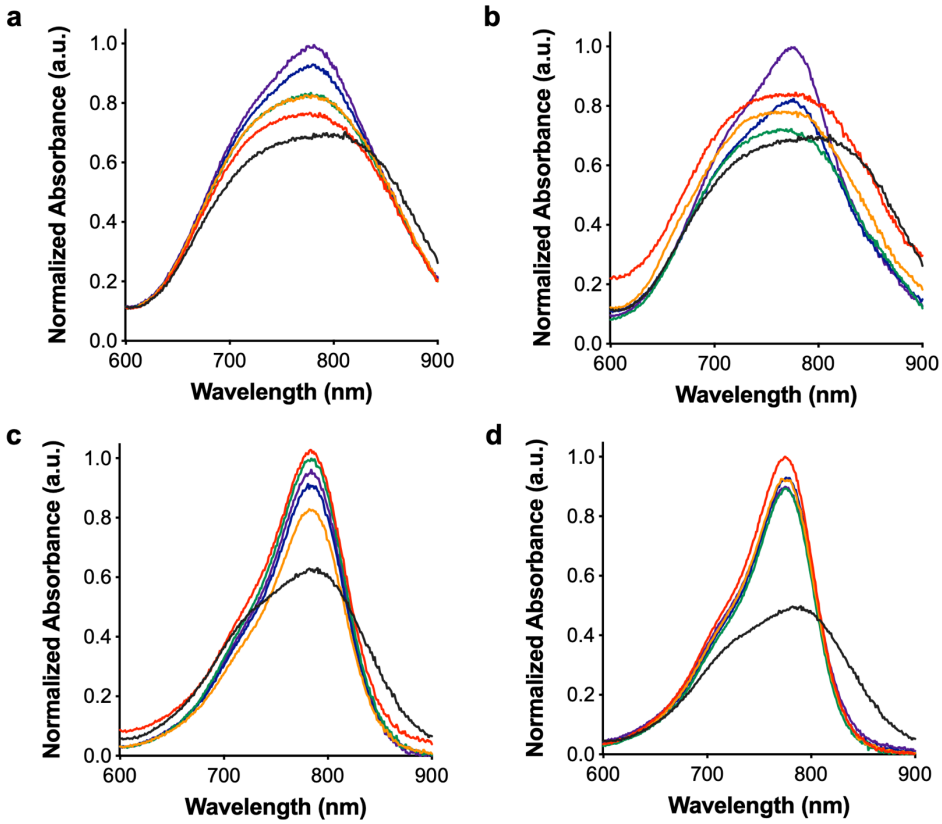

Figure C.4: Effect of surfactant concentration on (a-b) APNO-4 and (c-d) APNO-5 aggregation/nanoparticle formation. UV-vis spectra were recorded of dye solutions (2 µM) in variable (a, c) Cremophor EL (CrEL) and (b, d) sodium dodecyl sulfate (SDS) solutions of phosphate buffer saline solution (pH 7.4).

Table C.2: Tabulation of calculated partition coefficients (clogP) for APNO and tAPNO. Structures were draw in Avagadro[3] and ChemDraw (version 15.0) for ALOGPS[4] and ChemDraw predictions (Chemical Properties Tool), respectively.

APNO	ALOGPS	ChemDraw	tAPNO	ALOGPS	ChemDraw
1	4.88	7	1	6.68	8.32
2	5.05	7.53	2	7.38	8.38
3	5.07	7.53	3	5.41	8.34
4	7.6	8.66	4	7.26	8.66
5	3.8	3.95	5	3.77	3.96

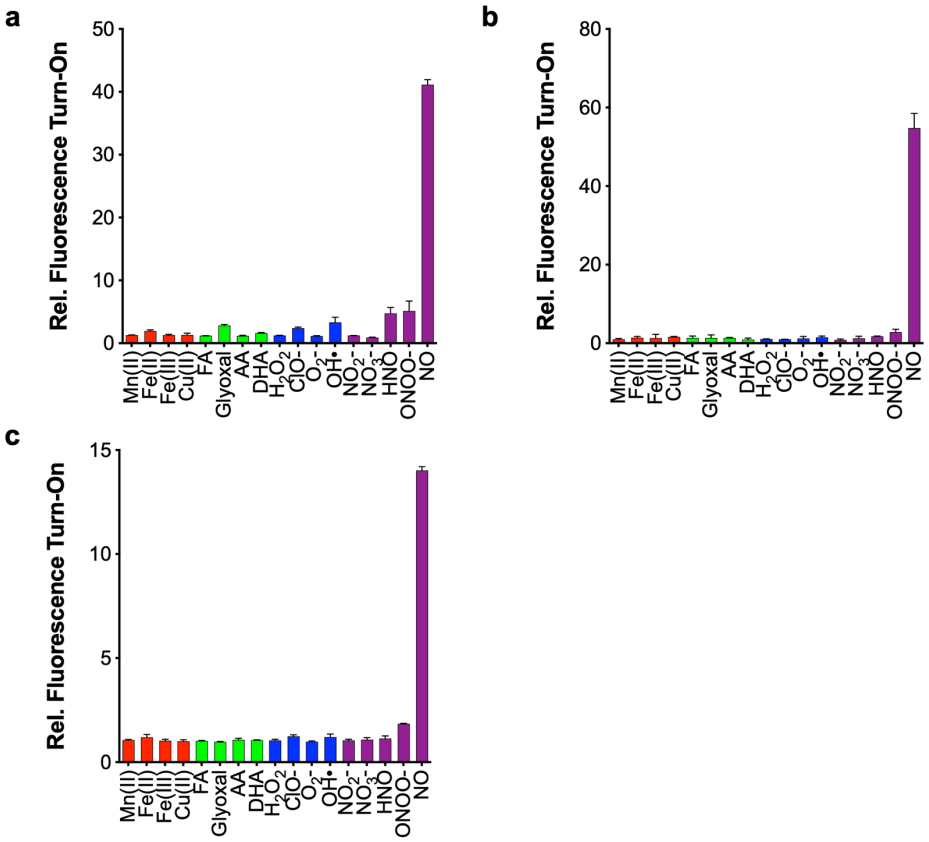

Figure C.5: Selectivity studies for (a) APNO-1, (b) ANPO-2, and (c) APNO-3. 2 μM dye was treated with excess (100 equiv) reactive metal (red), carbonyl (green), oxygen (blue), or nitrogen (purple) species in ethanolic 20 mM potassium phosphate buffer (pH 7.4, 50% v/v). Fluorescence turn-on was determined after 1 h incubation 37 °C. Data represented as mean ± standard deviation (n = 3).

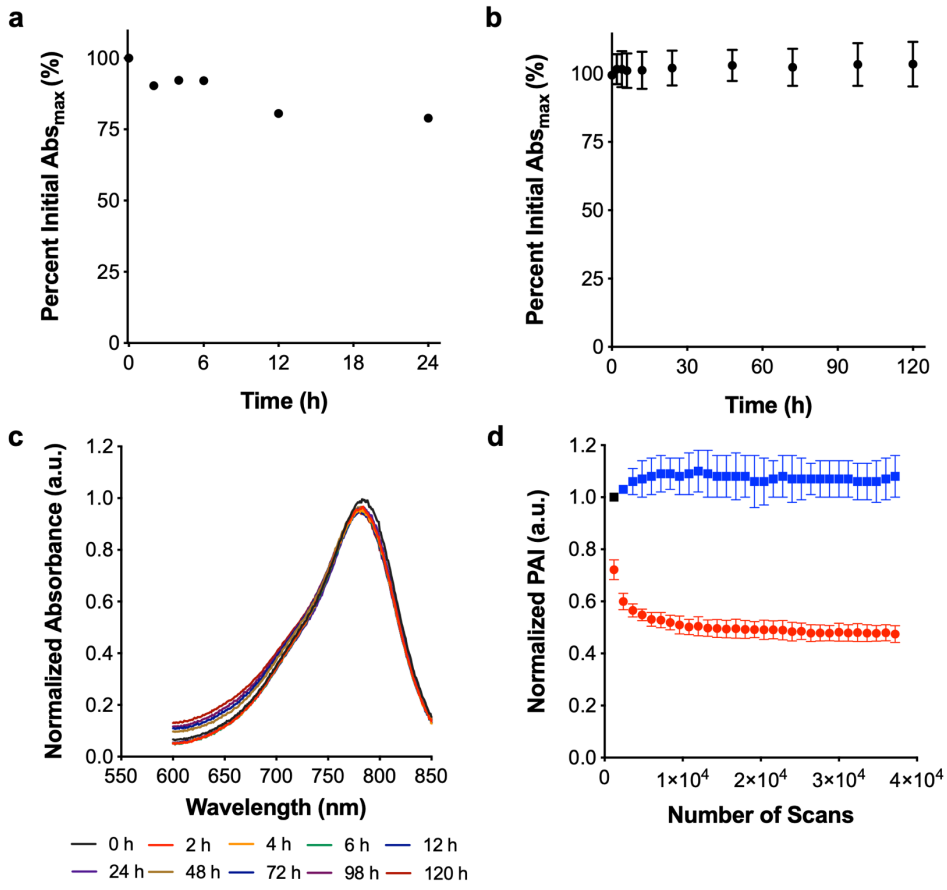

Figure C.6: (a) Stability of APNO-5 (2 mM) in DMSO stock under ambient light and at room temperature. Measurements were acquired by preparing 2 µM solutions of the sample in ethanolic 20 mM potassium phosphate buffer (pH 7.4, 50 % v/v). (b) Stability of of APNO-5 (2 µM) in 0.1 % CrEL phosphate buffer saline (pH 7.4, v/v) at 37 °C as measured by the maximal absorbance. (c) UV-vis spectra of APNO-5 (2 µM) in 0.1 % CrEL phosphate buffer saline (pH 7.4, v/v) at 37 °C. (d) Photostability of APNO-5 (red) and tAPNO-5 (blue) in 0.1 % CrEL phosphate buffer saline (pH 7.4, v/v). Data represented as mean ± standard deviation (n = 3).

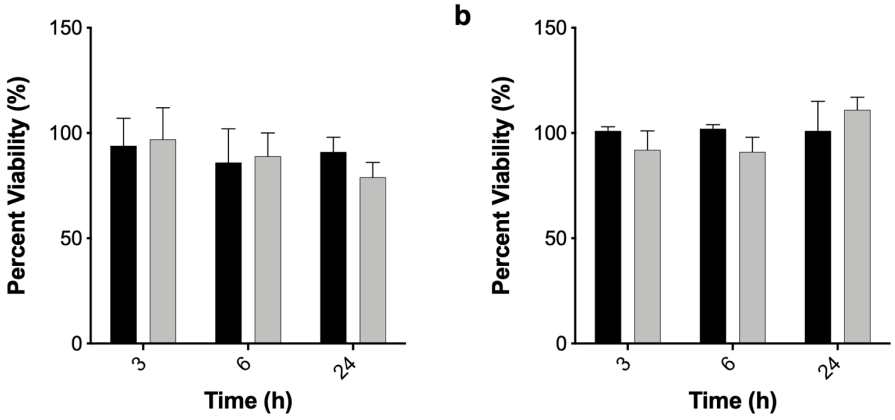

Figure C.7: APNO-5 (1 µM, black; 5 µM, red) biocompatibility according to (a) trypan blue dye exclusion assay and (b) MTT cell viability assay in RAW 264.7 macrophage cells. Data represented as mean ± standard deviation (n = 3).

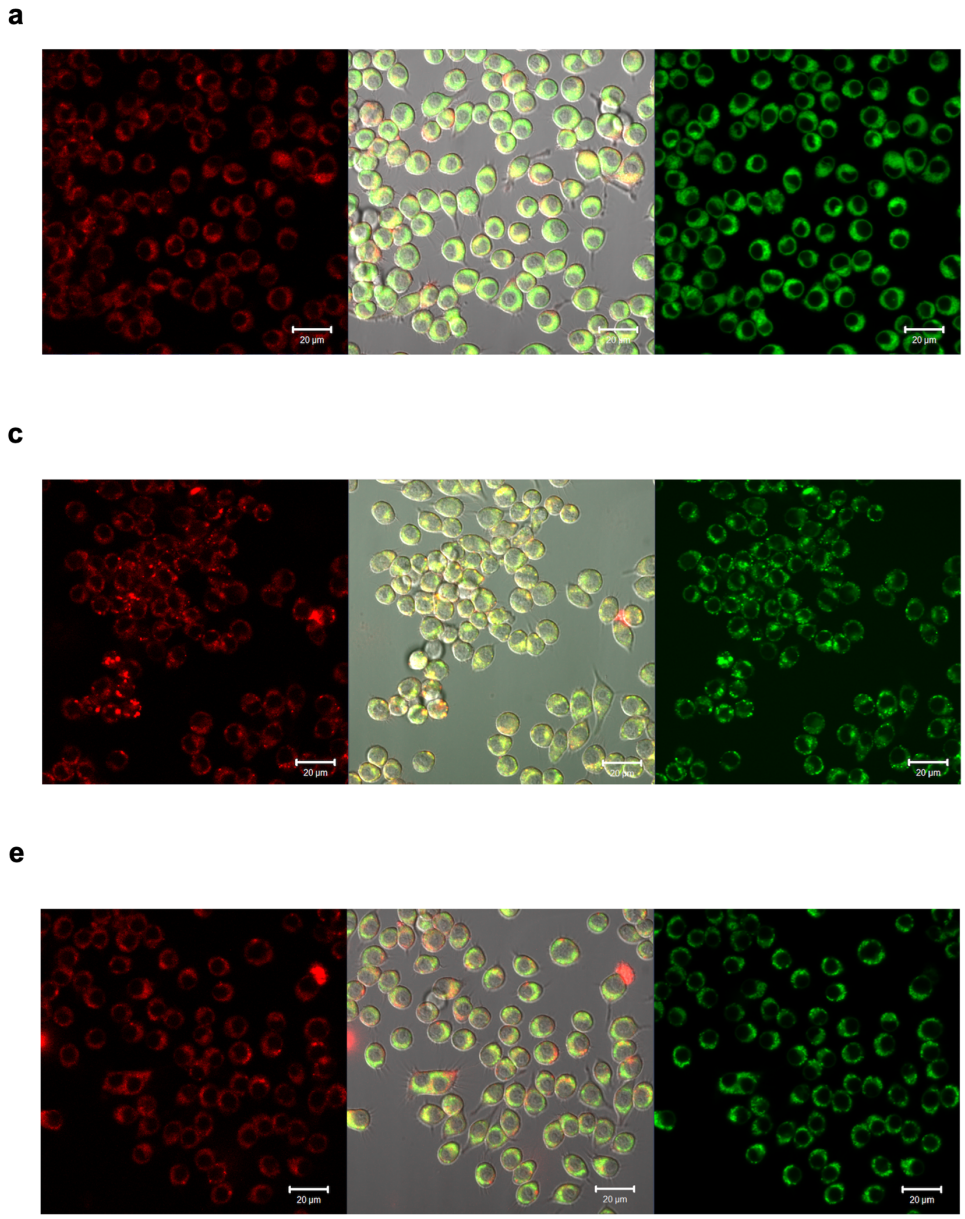

Figure C.8: Colocalization studies of APNO-5 with (a) ER-Tracker™ Green, (b) LysoTracker® Green DND-26, and (c) MitoTracker® Green FM in RAW 264.7 macrophage cells. Pearson coefficients were calculated for as 0.6, 0.8, and 0.7, respectively.

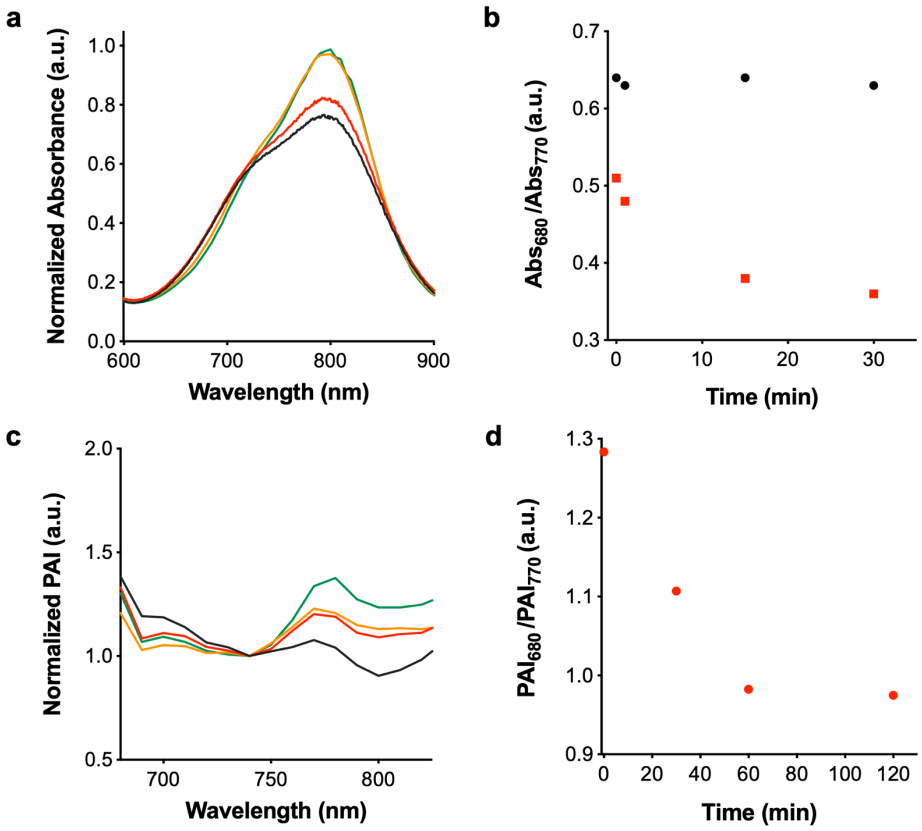

Figure C.9: (a) Time dependent UV-vis absorbance profile of APNO-5 (50 µM) in saline with rat liver microsomes (10 µL). (b) Ratio of absorbance at 680 nm and 770 nm for APNO-5 (50 µM) either in the presence or absence of rat liver microsomes (10 µL) as a function of time. (c) Time dependent, normalized PA spectrum of APNO-5 (68 µg/kg) following s.c. injection into the flank of a mouse. (d) Ratio of PAI_{680}/PAI_{770} for APNO-5 (68 µg/kg) following s.c. injection into the flank of the mouse. Note that all *in vitro* experiments were incubated at 37 °C throughout the experiment and the mouse was allowed to wake up in between *in vivo* time points. Time points are 0 (black), 30 (red), 60 (orange), and 120 (green) min for a/c.

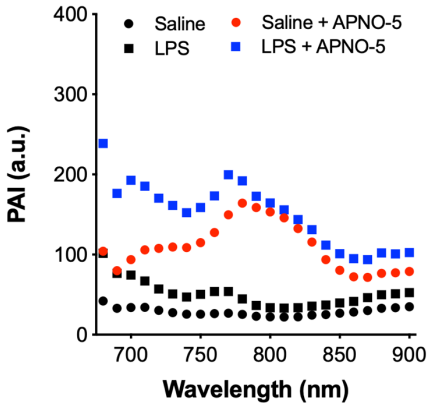

Figure C.10: *In vivo* PA spectra of mice treated with LPS (4 mg/kg) or saline (equal volume) both in the presence and absence of APNO-5 (68 µg/kg). Contrast-free images were acquired 9 h after the administration of LPS or saline. APNO-5 spectra were acquired 5 h after the administration of dye (9 h after the administration of LPS or saline). Note that background signals were comparable for all of the mice before treatment.

a

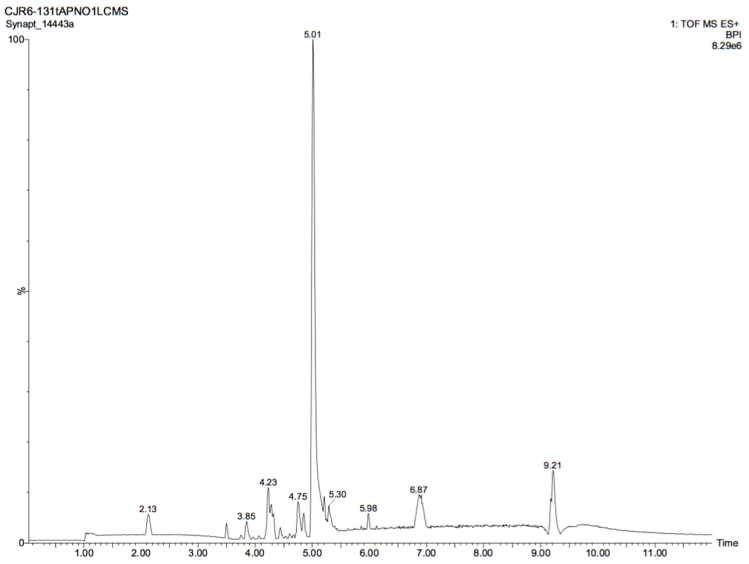

b

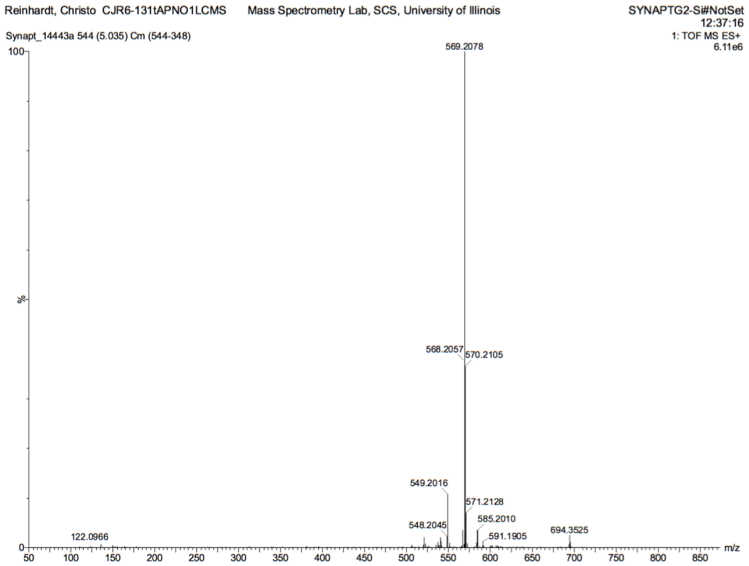

Figure C.11: (a) Chromatograph and (b) HR-MS of tAPNO-1 ESI-LC/MS analysis. tAPNO-1 was prepared by treating APNO-1 (20 μM) in ethanolic water (50 % v/v) with NO (*g*). Products were separated on a CORTECS^{TM} UPLC C18 column (1.6 μm, 2.1 by 50 mm) with a linear gradient using a combination of solvent A (95% water, 5% acetonitrile, 0.1% TFA) and solvent B (95% acetonitrile, 5% water, 0.1% TFA) at a flow rate of 0.4 mL/minute. Linear gradient protocol in minutes: 0–1 (80% A); 1—8 (100% B); 8–8.1 (80% A); and 8.1–12 (80% A). Identified tAPNO-1 (calc'd [M]+H 569.2073, found 569.2078 Da).

a

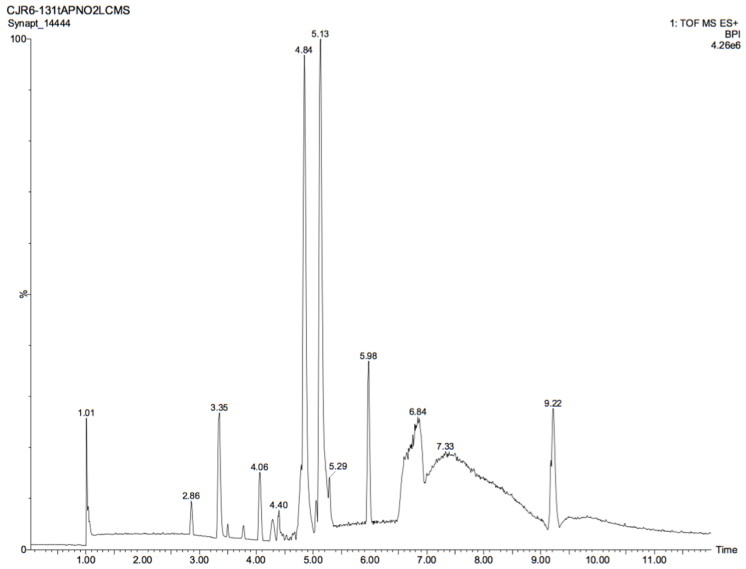

b

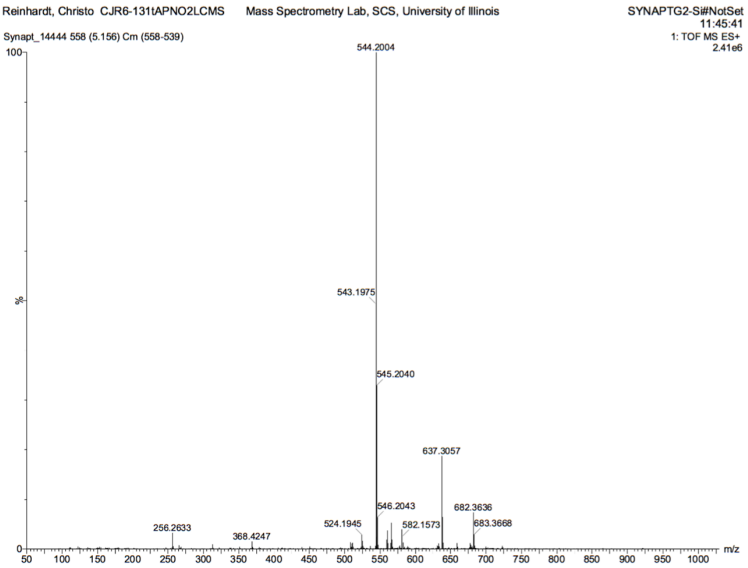

Figure C.12: (a) Chromatograph and (b) HR-MS of tAPNO-2 ESI-LC/MS analysis. tAPNO-2 was prepared by treating APNO-2 (20 μM) in ethanolic water (50 % v/v) with NO (*g*). Products were separated on a CORTECS^{TM} UPLC C18 column (1.6 μm, 2.1 by 50 mm) with a linear gradient using a combination of solvent A (95% water, 5% acetonitrile, 0.1% TFA) and solvent B (95% acetonitrile, 5% water, 0.1% TFA) at a flow rate of 0.4 mL/minute. Linear gradient protocol in minutes: 0–1 (80% A); 1—8 (100% B); 8–8.1 (80% A); and 8.1–12 (80% A). Identified tAPNO-2 (calc'd [M]+H 544.2008, found 544.2014 Da).

a

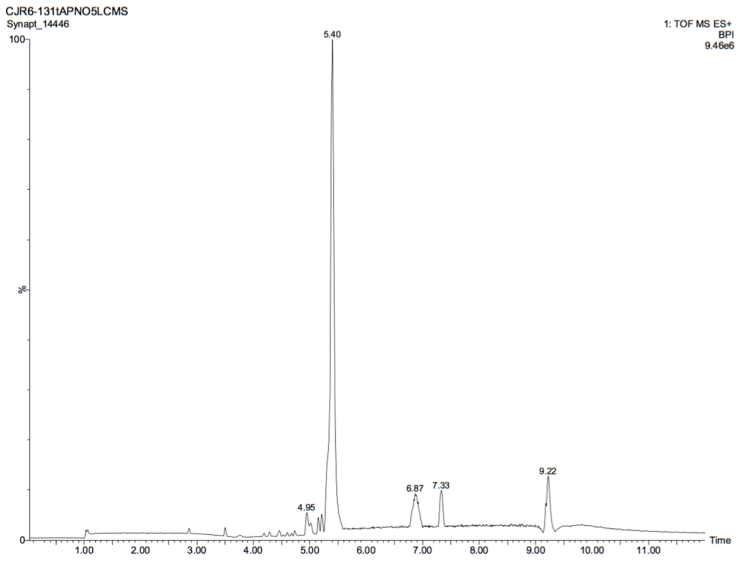

b

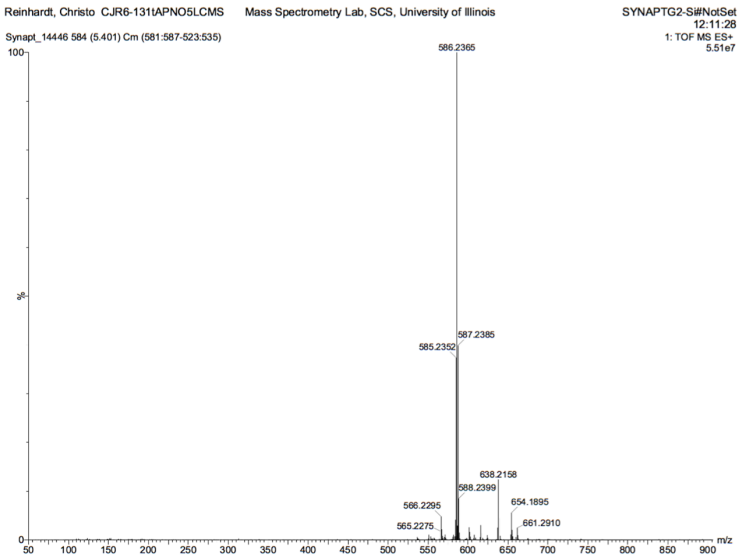

Figure C.13: (a) Chromatograph and (b) HR-MS of tAPNO-4 ESI-LC/MS analysis. tAPNO-4 was prepared by treating APNO-4 (20 μM) in ethanolic water (50 % v/v) with NO (*g*). Products were separated on a CORTECS^{TM} UPLC C18 column (1.6 μm, 2.1 by 50 mm) with a linear gradient using a combination of solvent A (95% water, 5% acetonitrile, 0.1% TFA) and solvent B (95% acetonitrile, 5% water, 0.1% TFA) at a flow rate of 0.4 mL/minute. Linear gradient protocol in minutes: 0–1 (80% A); 1—8 (100% B); 8–8.1 (80% A); and 8.1–12 (80% A). Identified tAPNO-4 (calc'd [M]+H 616.2332, found 616.2338 Da).

a

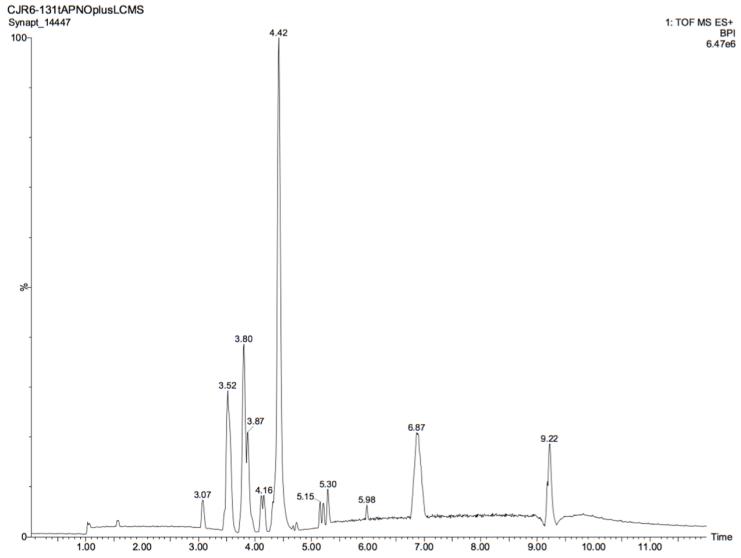

b

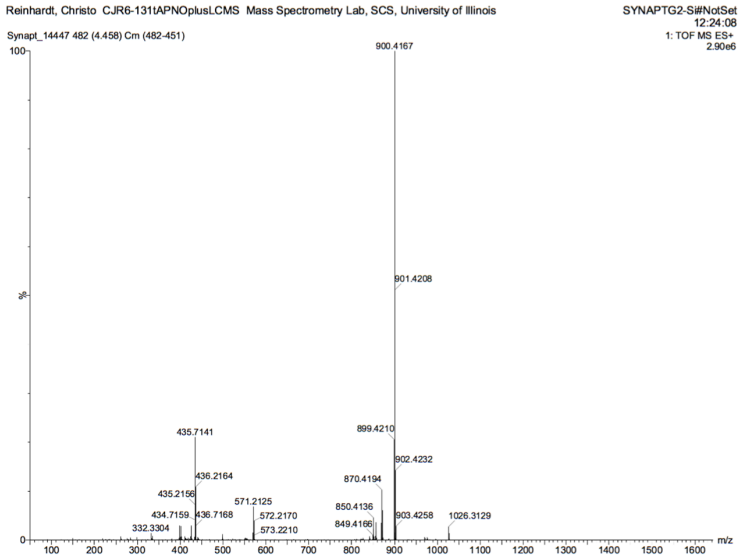

Figure C.14: (a) Chromatograph and (b) HR-MS of tAPNO-5 ESI-LC/MS analysis. tAPNO-5 was prepared by treating APNO-5 (20 μM) in ethanolic water (50 % v/v) with NO (*g*). Products were separated on a CORTECS^{TM} UPLC C18 column (1.6 μm, 2.1 by 50 mm) with a linear gradient using a combination of solvent A (95% water, 5% acetonitrile, 0.1% TFA) and solvent B (95% acetonitrile, 5% water, 0.1% TFA) at a flow rate of 0.4 mL/minute. Linear gradient protocol in minutes: 0–1 (80% A); 1—8 (100% B); 8–8.1 (80% A); and 8.1–12 (80% A). Identified tAPNO-5 (calc'd $[M]^+$ 900.4180, found 900.4167 Da).

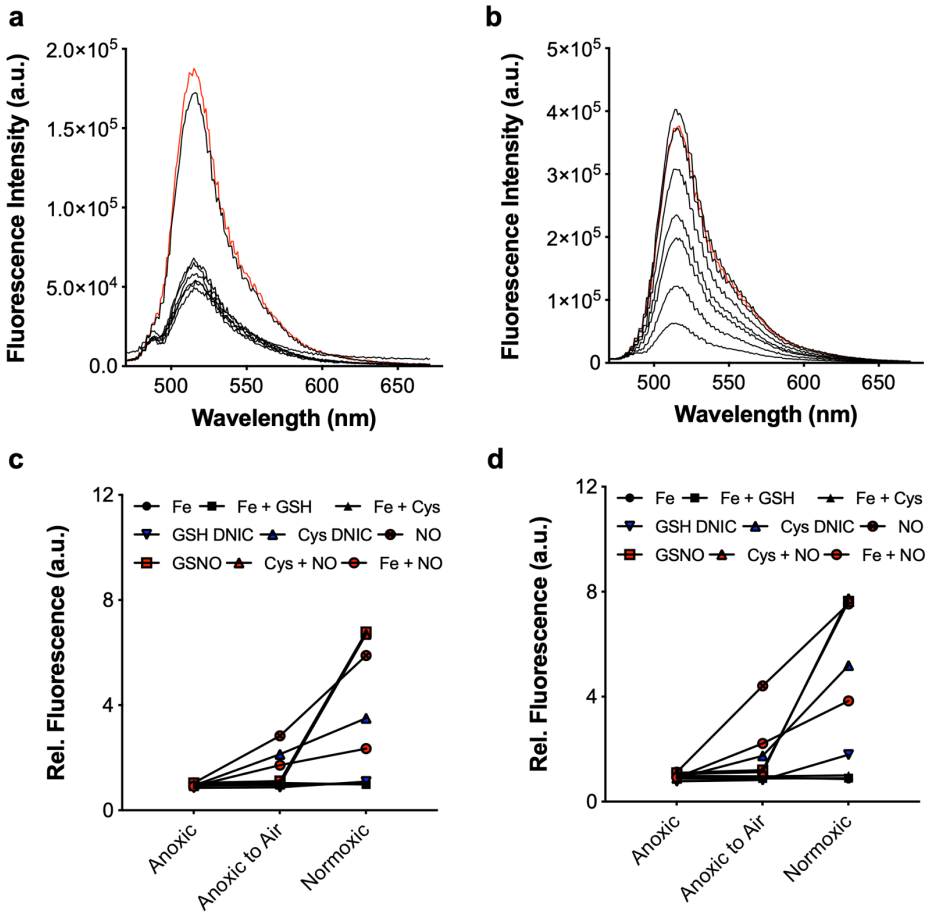

Figure C.15: Reactions between (a) TG-2 and (b) TG3 with DNIC under anoxic (black), anoxic then air (blue), or normoxic (red) conditions. Dye (1 μM) was added to mixtures (500 μM, 1:1:4, Fe:NO:RSH pre-incubated open for 5 min) in 50 mM HEPES (pH 7.4) and the solution was incubated at room temperature for 1 h. Fluorescence is normalized to a dye control.

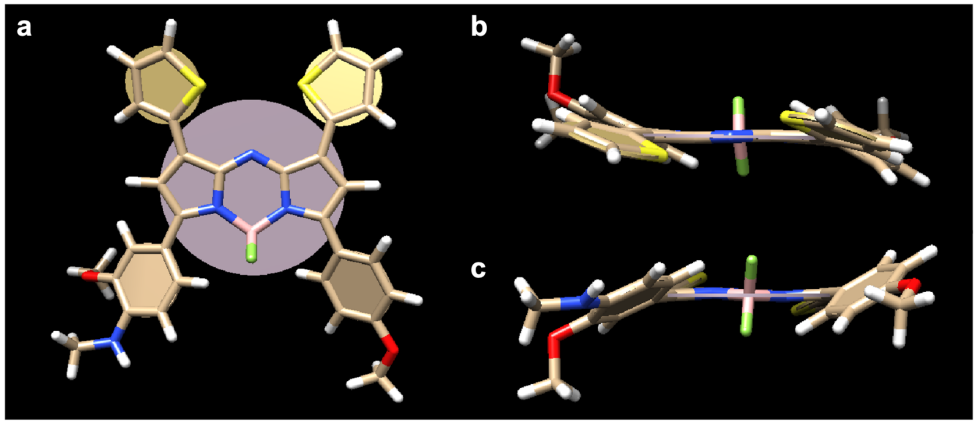

d

	θ_{top}	θ_{bottom}	Wavelength (nm)	f
Ph/Ph:Ph/Ph	27.8	32.6	618	0.93
Ph/Ph:$Thio_{Br}$/$Thio_{Br}$	27.5	21.9	650	0.98
Ph/Ph:Thio/Thio	27.4	21.8	637	0.88
Thio/Thio:Thio/Thio	14.0	21.7	667	0.84
APNO-5	29.1	31.3	654	0.98
SR-APNO-1	20.5	30.9	663	0.99
SR-APNO-2	21.0	30.4	657	0.94
SR-APNO-3	19.2	30.7	669	0.95
tAPNO-5	29.1	34.0	599	0.94
t-SR-APNO-1	20.9	33.6	620	0.88
t-SR-APNO-2	18.1	34.6	620	0.89
t-SR-APNO-3	18.5	35.0	630	0.85

e

	azaBODIPY		SR-APNO		t-SR-APNO	
Functional	Top	Bottom	Top	Bottom	Top	Bottom
UFF	0.67	0.90	0.60	0.26	0.9	0.96
$B3LYP_{gas}$	0.59	0.66	0.69	0.82	0.9	0.39
$B3LYP_{MeOH}$	0.60	0.66	0.64	0.15	0.89	0.30

Figure C.16: (a-c) Representative structure and definition of planes for the aza-BODIPY and SR-aza-BODIPY platforms. Planes corresponding to the phenyl (Ph), thiophene (Thio), and aza-BODIPY core are defined by all heavy atoms in the plane. Dihedral angle is calculated between each ring and the core and reported as the average of the absolute values. (d) Tabulated average dihedral angles from reported X-ray crystallographic data (names defined as top-left/top-right: bottom-left/bottom-right: Ph/Ph:Ph/Ph, Ph/Ph:Thio-Br/Thio-Br, Ph/Ph:Thio/Thio, and Thio/Thio:Thio/Thio),[5,6] APNO-5, and SR-APNO series after geometry optimization using B3LYP in implicit methanol with the corresponding time-dependent DFT calculation of absorption maxima with CAM B3LYP in implicit methanol. (e) Linear regressions for measured calculated absorbance maximum versus dihedral angle. Note that poor correlation between the bottom dihedral angles and calculated absorption maxima was because this was not sampled with the structures.

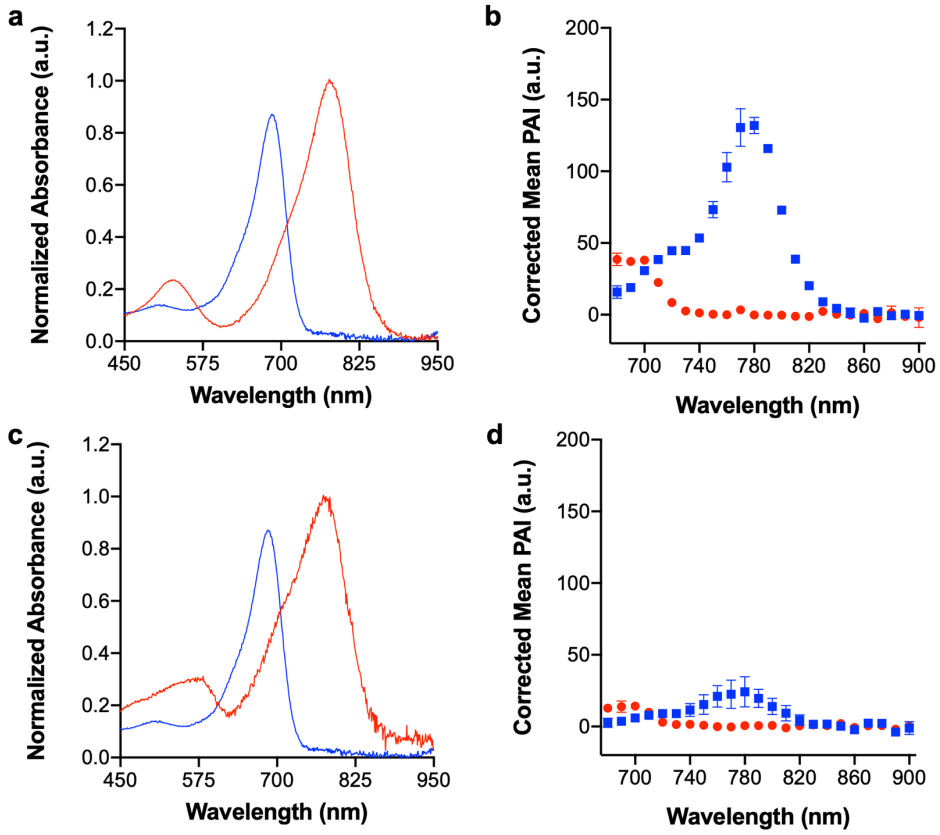

Figure C.17: UV-Vis (2 µM) and PA spectra (10 µM) for (a-b) SR-APNO-1 and (c-d) SR-APNO-2 in ethanolic 20 mM potassium phosphate buffer (pH 7.4, 50% v/v). The probe and *N*-nitrosated products are depicted as red and blue, respectively. Data is reported as the mean ± standard deviation ($n = 3$).

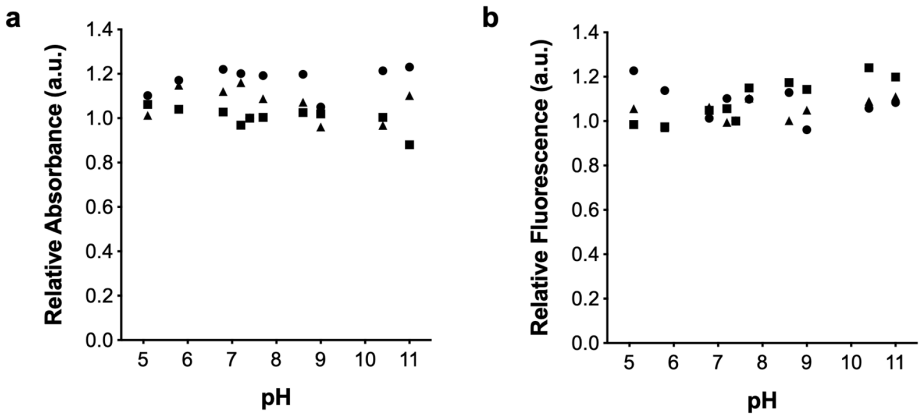

Figure C.18: The effect of pH on SR-APNO (2.5 µM) (a) absorbance (350–950 nm) and (b) fluorescence (excitation at 650 nm, emission collected from 660-950 nm) properties in ethanolic 20 mM Britton-Robinson buffer (50% v/v).[1,7] Relative absorbance and fluorescence are calculated relative to the absorption maxima and sum fluorescence intensity at pH 7.4. SR-APNO-1, SR-APNO-2, and SR-APNO-3 are depicted as triangles, squares, and circles, respectively. No changes were observed in either the absorption or emission spectra.

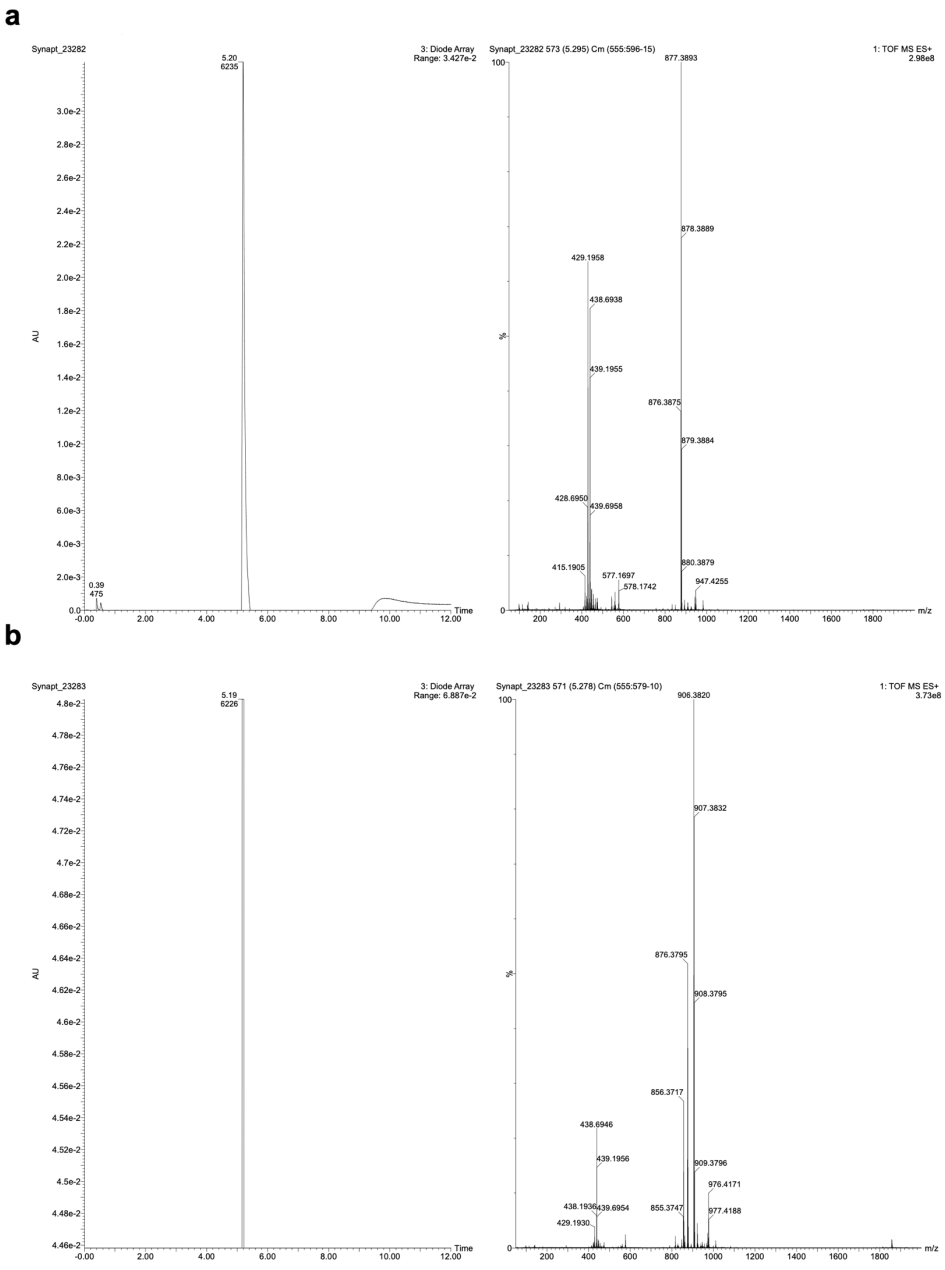

Figure C.19: LC-HRMS analysis of the crude reaction (a) before and (b) after SR-APNO-1 (167 μM), and methanolic NO (~10 mM, ~60 equiv) in anhydrous methanol. The reaction was initiated with the addition of saturated methanolic nitric oxide and then allowed to react at room temperature for less than 5 minutes. The solution was purged under high vacuum and then concentrated under vacuum before analysis. Products were separated on a CORTECS™ UPLC C18 column (1.6 μm, 2.1 by 50 mm) with a linear gradient using a combination of solvent A (95% water, 5% acetonitrile, 0.1% TFA) and solvent B (95% acetonitrile, 5% water, 0.1% TFA) at a flow rate of 0.4 mL/minute. Linear gradient protocol in minutes: 0–1 (80% A); 1–4 (40% A); 4–8 (100% B); 8–8.1 (80% A); and 8.1–12 (80% A). LC was monitored using a PDA detector between 350 and 500 nm (left). Identified SR-APNO-1 (calc'd $[M]^+$ 877.3837, found 877.3893 Da), and t-SR-APNO-1 (calc'd $[M]^+$ 906.3744, found 906.3820 Da). *N*-nitrosated product was corroborated using ESI-HRMS t-SR-APNO-1 (calc'd $[M]^+$ 906.3744, found 906.3757 Da).

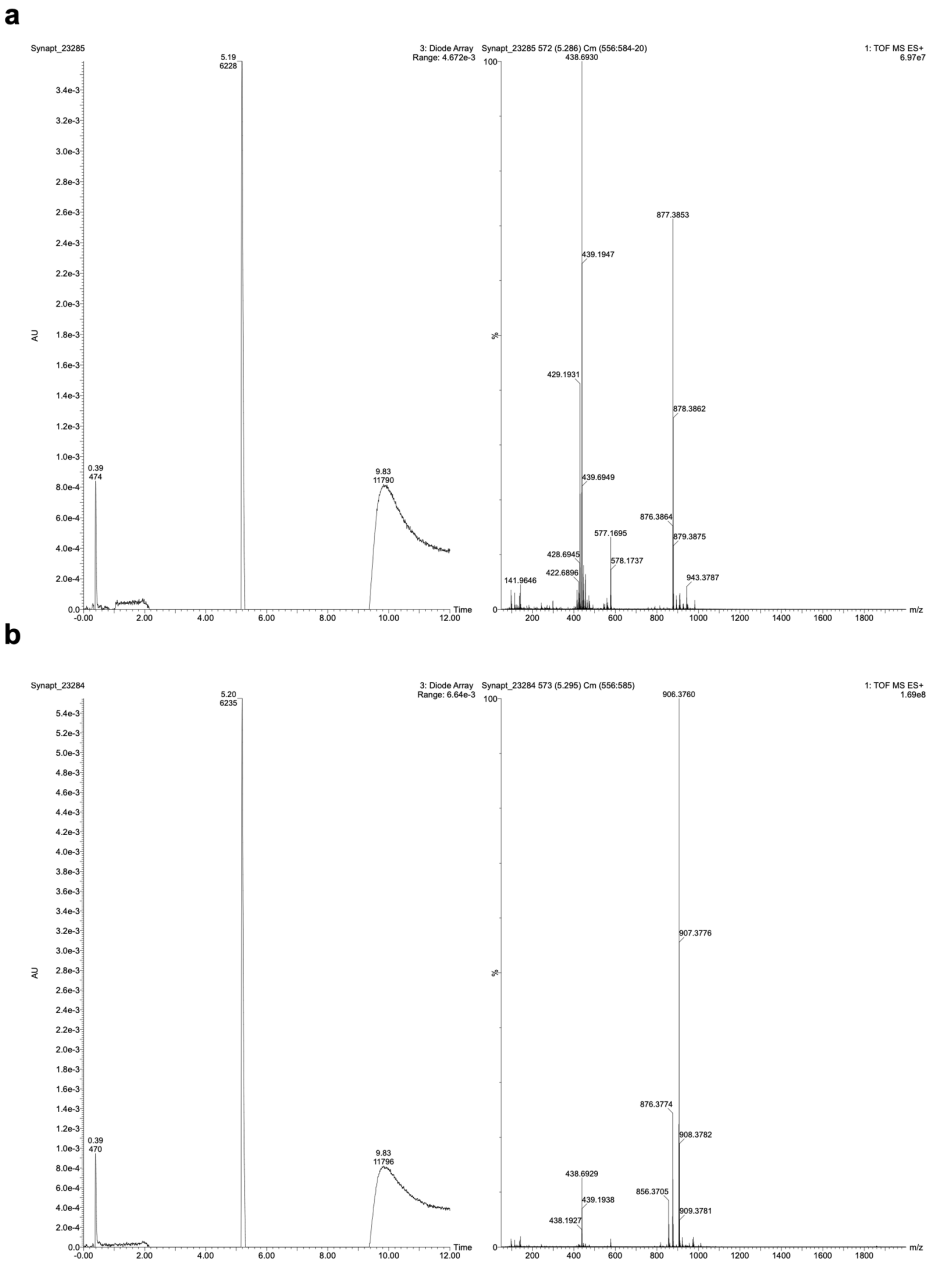

Figure C.20: LC-HRMS analysis of the crude reaction (a) before and (b) after SR-APNO-2 (167 μM), and methanolic NO (~10 mM, ~60 equiv) in anhydrous methanol. The reaction was initiated with the addition of saturated methanolic nitric oxide and then allowed to react at room temperature for less than 5 minutes. The solution was purged under high vacuum and then concentrated under vacuum before analysis. Products were separated on a CORTECS^{TM} UPLC C18 column (1.6 μm, 2.1 by 50 mm) with a linear gradient using a combination of solvent A (95% water, 5% acetonitrile, 0.1% TFA) and solvent B (95% acetonitrile, 5% water, 0.1% TFA) at a flow rate of 0.4 mL/minute. Linear gradient protocol in minutes: 0–1 (80% A); 1–4 (40% A); 4–8 (100% B); 8–8.1 (80% A); and 8.1–12 (80% A). LC was monitored using a PDA detector between 350 and 500 nm (left). Identified SR-APNO-2 (calc'd $[M]^+$ 877.3845, found 877.3853), t-SR-APNO-2 calc'd $[M]^+$ 906.3744, found 906.3760 Da). *N*-nitrosated product was corroborated using ESI-HRMS t-SR-APNO-2 (calc'd $[M]^+$ 906.3744, found 906.3762 Da).

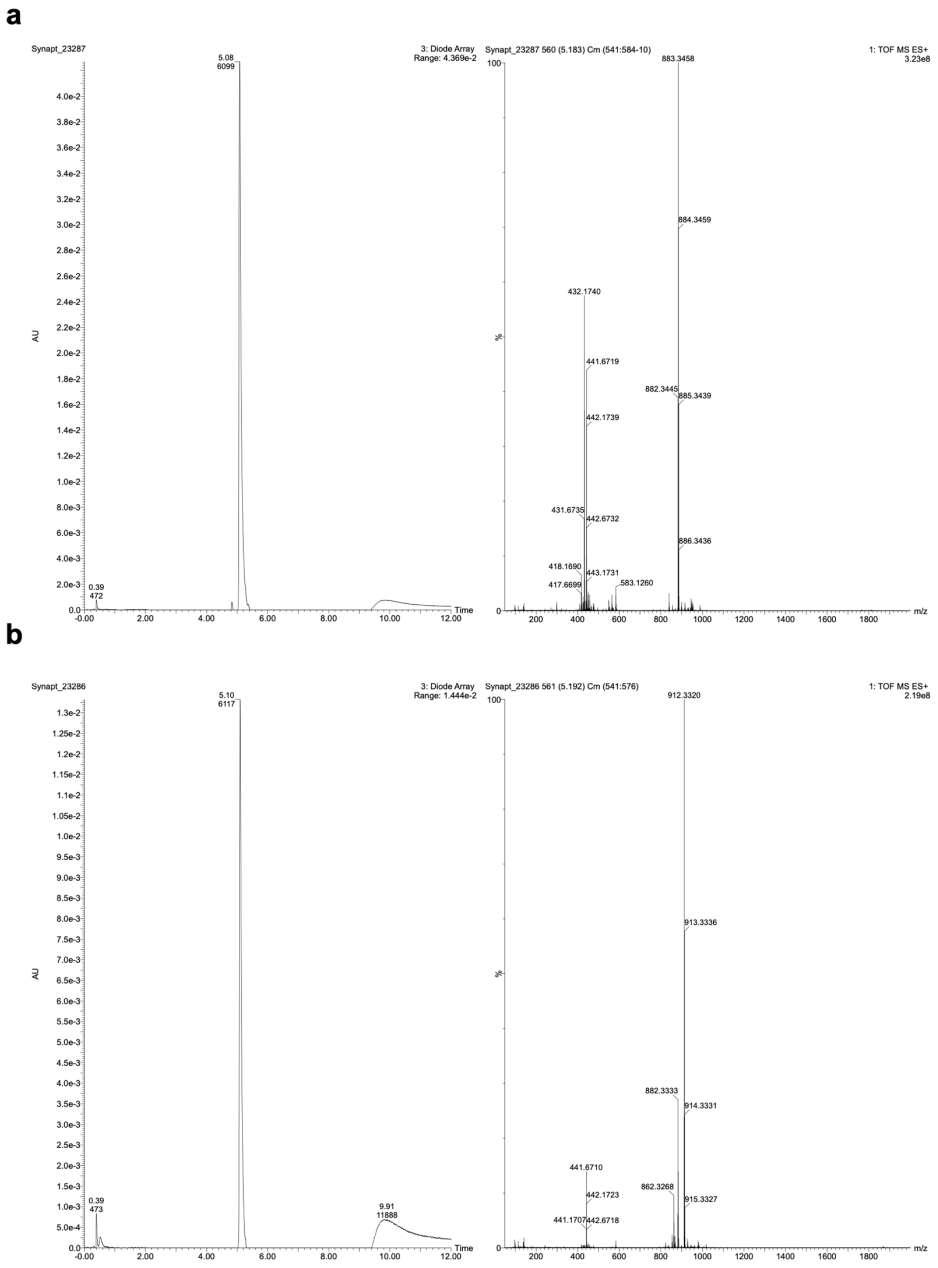

Figure C.21: LC-HRMS analysis of the crude reaction (a) before and (b) after SR-APNO-3 (167 μM), and methanolic NO (~10 mM, ~60 equiv) in anhydrous methanol. The reaction was initiated with the addition of saturated methanolic nitric oxide and then allowed to react at room temperature for less than 5 minutes. The solution was purged under high vacuum and then concentrated under vacuum before analysis. Products were separated on a CORTECS^{TM} UPLC C18 column (1.6 μm, 2.1 by 50 mm) with a linear gradient using a combination of solvent A (95% water, 5% acetonitrile, 0.1% TFA) and solvent B (95% acetonitrile, 5% water, 0.1% TFA) at a flow rate of 0.4 mL/minute. Linear gradient protocol in minutes: 0–1 (80% A); 1–4 (40% A); 4–8 (100% B); 8–8.1 (80% A); and 8.1–12 (80% A). LC was monitored using a PDA detector between 350 and 500 nm (left). Identified SR-APNO-3 (calc'd $[M]^+$ 883.3047, found 883.3458 Da), t-SR-APNO-3 (calc'd $[M]^+$ 912.3308, found 912.3320 Da). *N*-nitrosated product was corroborated using ESI-HRMS t-SR-APNO-3 (calc'd $[M]^+$ 912.3308, 912.3321 found Da).

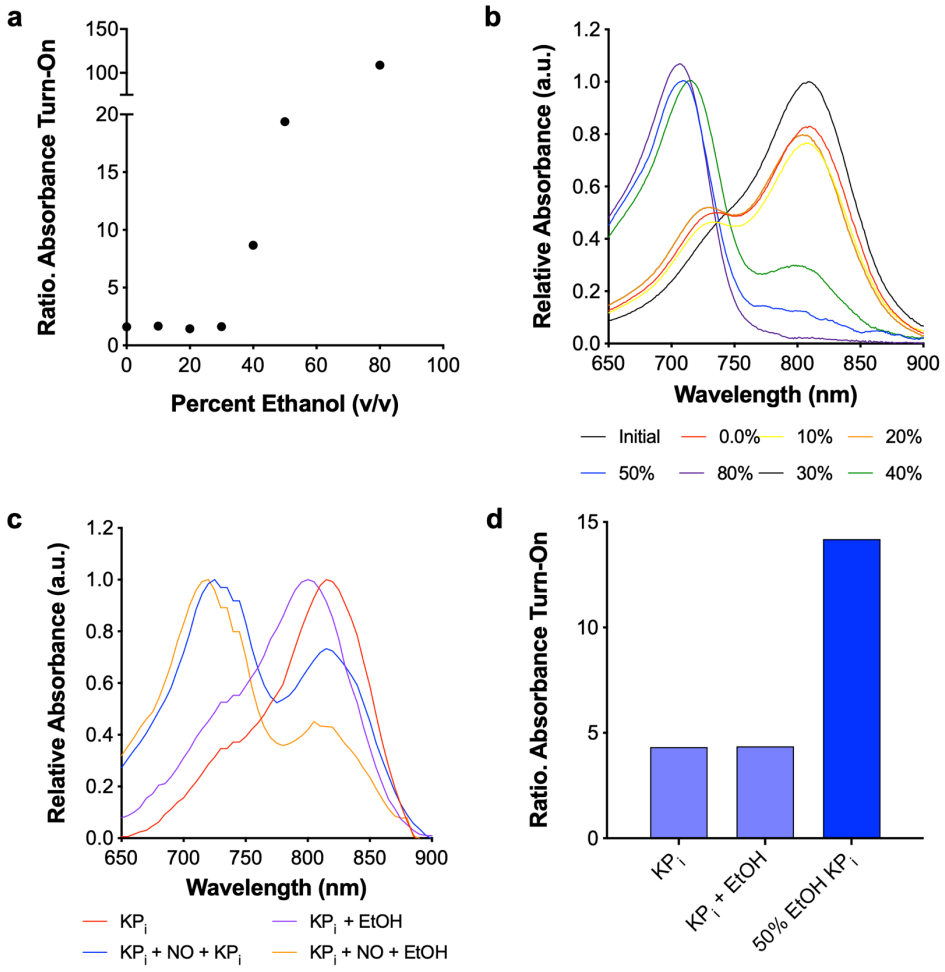

Figure C.22: Effect of ethanol content in 20 mM potassium phosphate buffer (pH 7.4, 0.1% CrEL v/v) on the (a) ratiometric absorbance response and (b) UV-vis spectra. Reactions were performed with SR-APNO-3 (4 μM) and DEA-NONOate (1.33 mM, 2 mM NO) at room temperature for 20 min (approximately 1.25 half-lives). (c) UV-vis spectra and (d) ratiometric absorbance responses for dilution experiments to investigate the source of ethanol effects. Reactions were performed with SR-APNO-3 (4 μM) and DEA-NONOate (1.33 mM in 10 mM KOH, 2 mM NO) or control (equal volume 10 mM KOH) in 20 mM potassium phosphate buffer (pH 7.4, 0.1% CrEL v/v) at room temperature for 1 h and then diluted in additional buffer (KP_i) or ethanol (EtOH).

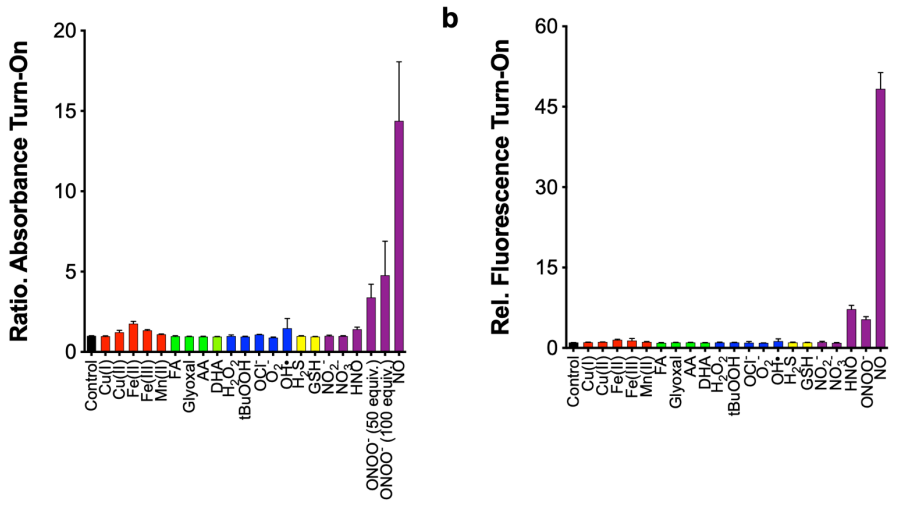

Figure C.23: (a) Fluorescence and (b) UV-vis analysis of SR-APNO-3's (4 μM) selectivity against a panel of reactive metals (red), carbonyl (green), oxygen (blue), thiol (yellow) and nitrogen (purple) species (800 μM, 200 equiv unless noted otherwise) in ethanolic 20 mM potassium phosphate buffer (pH 7.4, 50% v/v) or ethanolic 20 mM HEPES buffer (pH 7.4, 50% v/v, Fe(II) only). Minor fluorescence enhancement (less than 15% of NO response) was observed after treatment with HNO. This, along with the lack of change in UV-vis, is consistent with the small quantities of NO that are released from Angeli's salt (the nitroxyl donor).[8] Note that the slight response from peroxynitrite is only observed in the UV-vis due to dye decomposition after treatment with minor reactivity from residual isoamyl nitrite. Data is reported as the mean ± standard deviation (n = 3).

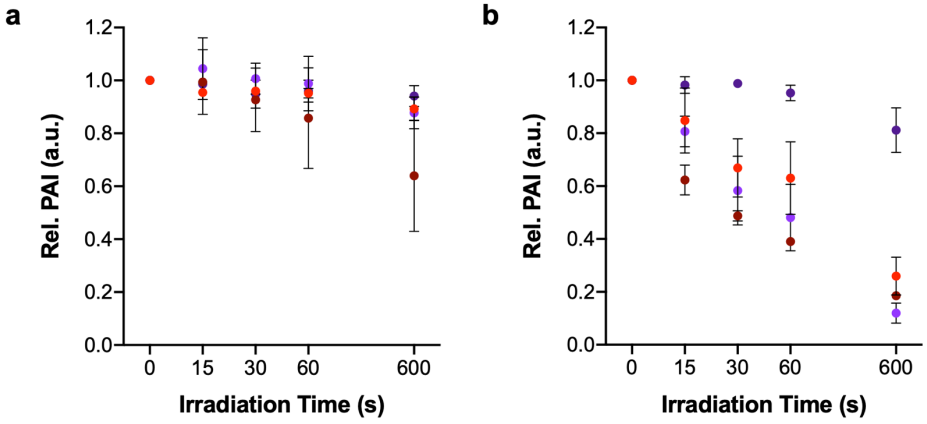

Figure C.24: APNO or SR-APNO and corresponding *N*-nitrosated product (25 μM) photostability at their PA maximum in ethanolic 20 mM potassium phosphate buffer (pH 7.4, 50% v/v) using the OPO laser used in the Nexus 128+ PA tomographer. Samples were irradiated discontinuously, and measurements were acquired in continuous mode with a 6 s rotation time. APNO-5, SR-APNO-1, SR-APNO-2, and SR-APNO-3 are depicted as red, cayenne, light purple, and purple, respectively. Data is reported as the mean ± standard deviation (n = 3).

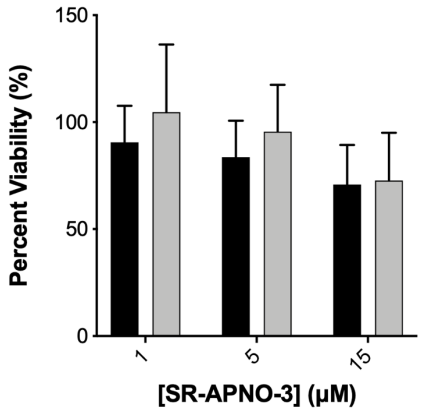

Figure C.25: MTT toxicity assay for SR-APNO-3 in 4T1 mouse mammary carcinoma cells (black, 24 h) and RAW 264.7 macrophages (grey, 8 h). Data is reported as the mean ± standard deviation (n = 4).

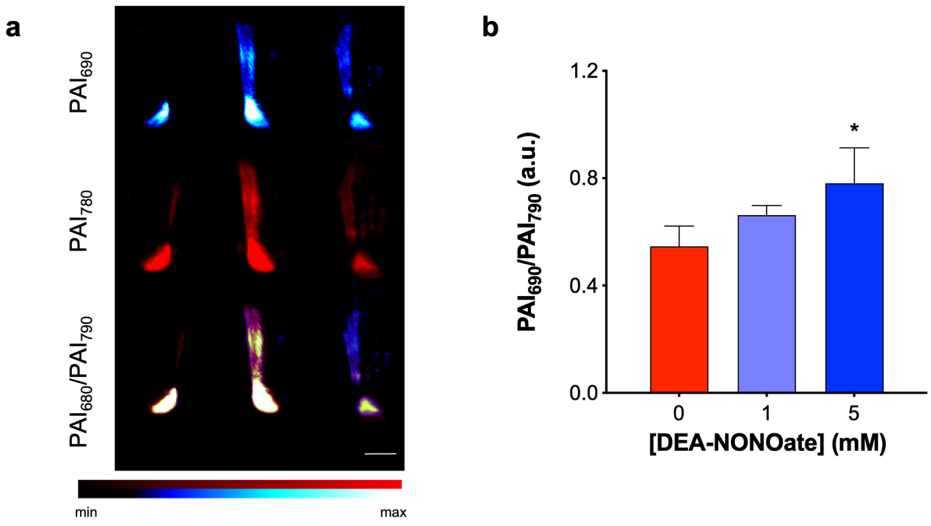

Figure C.26: (a) PA imaging of 4T1 murine breast cancer cells stained with SR-APNO-3 (15 μM) for 1 h, washed with PBS, and then treated with DEA-NONOate for 2 h (1 or 5 mM). Representatives images corresponding to the *N*-nitroso product (blue, 690 nm, top), SR-APNO-3 (red, 790 nm, middle), and the image fusion (blue/red, 690/790 nm, bottom). (b) Quantified ratiometric PA response for the cell pellets. Statistical analysis was performed using a one-way ANOVA and Tukey's multiple comparisons (α = 0.05). *, $p < 0.05$. Data is reported as the mean ± standard deviation (n = 3). Scale bar represents 4.0 mm.

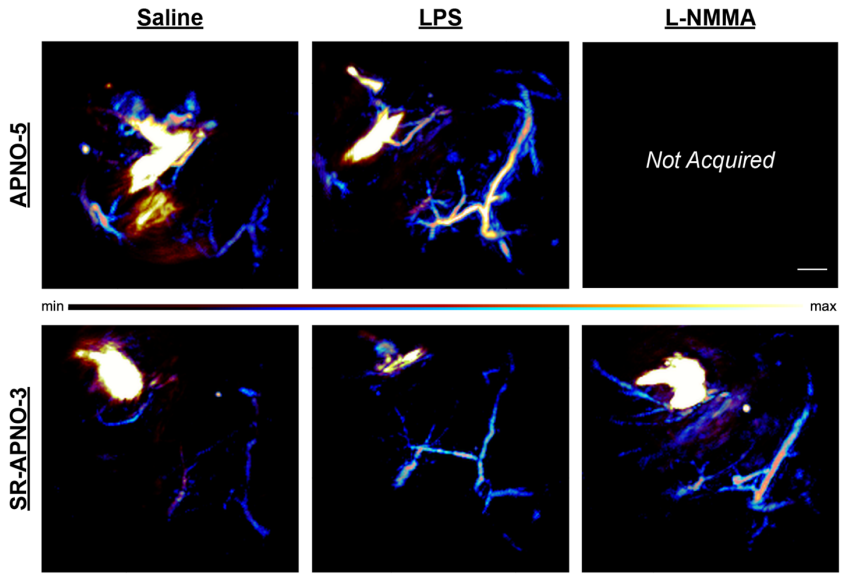

Figure C.27: PA imaging of LPS-induced inflammation (4 mg/kg, i.m.) in BALB/c mice with APNO-5 (top) and SR-APNO-3 (bottom). After a 4 h induction period, APNO-5 or SR-APNO-3 (50 μM, 25 μL, i.m., final concentration of 15% DMF v/v) was administered. Inhibition was performed using L-NMMA (35 mM). Representatives images correspond to saline- (left), LPS- (middle) and LPS and L-NMMA-treated mice. The *N*-nitroso product (blue, 690 nm) and SR-APNO-3 (red, 790 nm), are shown in a merged image (blue/red, 690/790 nm). Scale bar represents 2.0 mm.

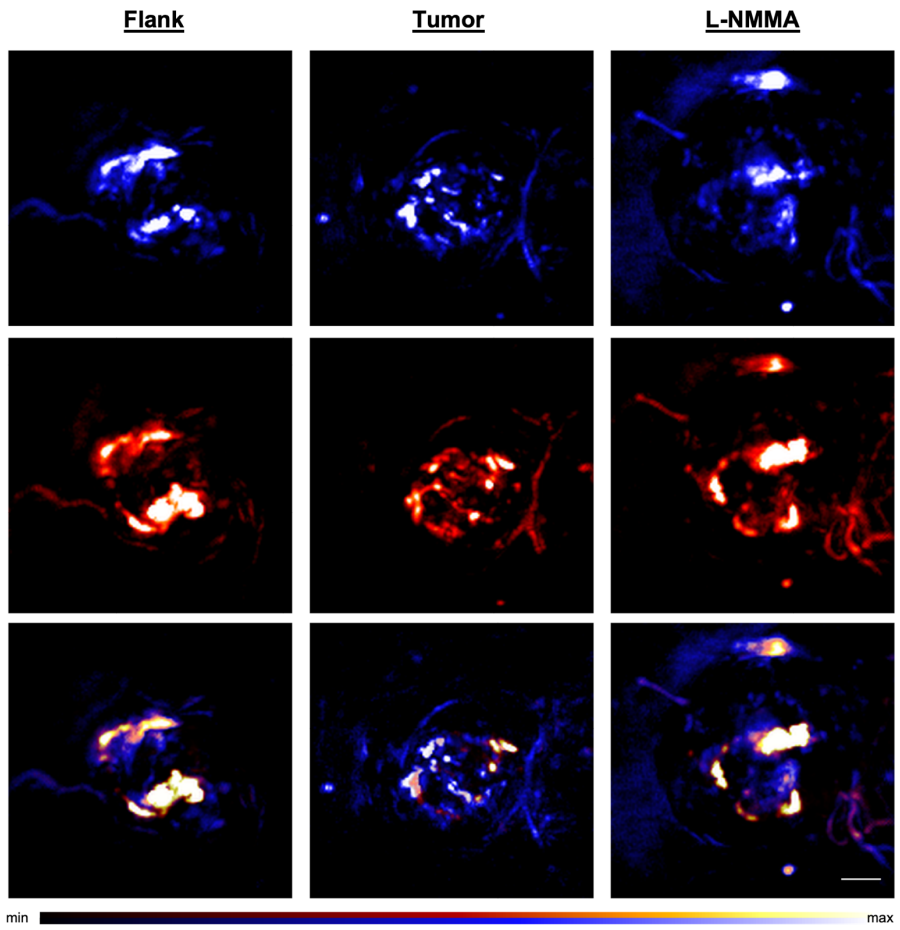

Figure C.28: PA imaging of cancer-derived NO in a 4T1 heterotopic allograft model of breast cancer. SR-APNO-3 (50 μM, 25 μL, final concentration of 15% DMF v/v) was administered either subcutaneously or intratumorally. Inhibition was performed using L-NMMA (35 mM). Representatives images correspond to the *N*-nitroso product (blue, 690 nm, top), SR-APNO-3 (red, 790 nm, middle), and merged images (blue/red, 690/790 nm, bottom). Scale bar represents 2.0 mm.

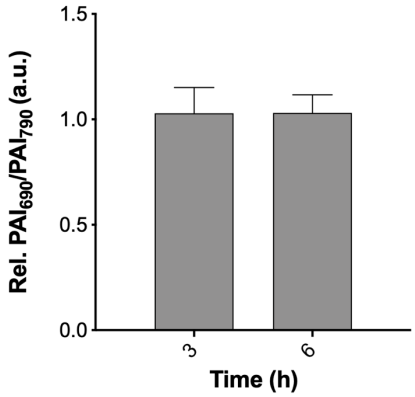

Figure C.29: PA imaging of 4T1 tumors following intratumoral treatment with 35 mM L-NMMA in sterile saline with 15% DMF. No change in signal was observed in the absence of SR-APNO-3. Data is reported as the mean ± standard deviation ($n = 3$).

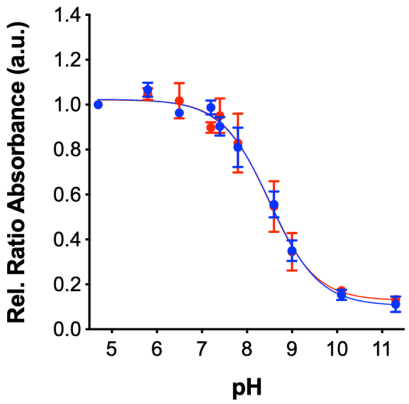

Figure C.30: CyAPNO and tCyAPNO (5 µM) pH profile in 40 mM Britton-Robinson buffer[1,2] containing 0.1% CrEL (v/v). Samples were allowed to solubilize for 2 h prior to acquiring spectra. CyAPNO and tCyAPNO are plotted as blue and red, respectively. Data is reported as the mean ± standard deviation (n = 3). pK_a = 8.5 for both compounds.

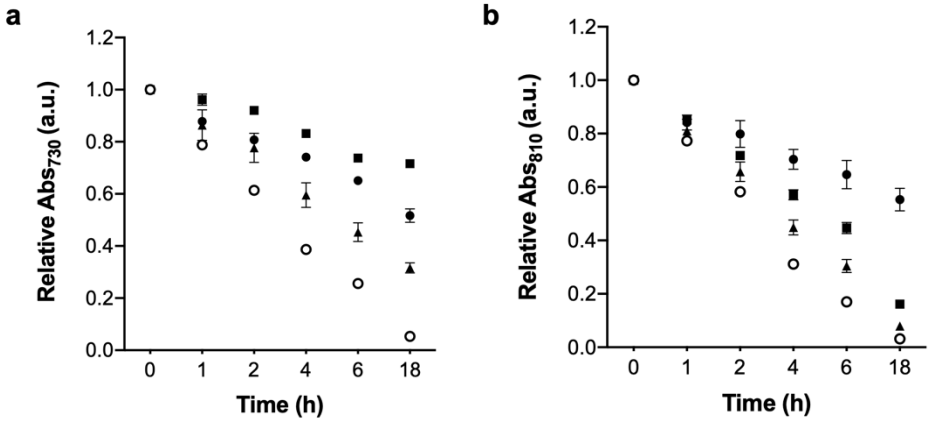

Figure C.31: (a) CyAPNO and (b) tCyAPNO (5 µM) stability under ambient conditions. Stability was assessed in DMSO (square), diluted human plasma (40% v/v, circle), diluted human serum (40% v/v, triangle), and 50 mM HEPES buffer (pH = 7.4) containing 0.1% CrEL (v/v, open circle). Data is reported as the mean ± standard deviation (n = 3).

C.1 Detailed synthetic procedures

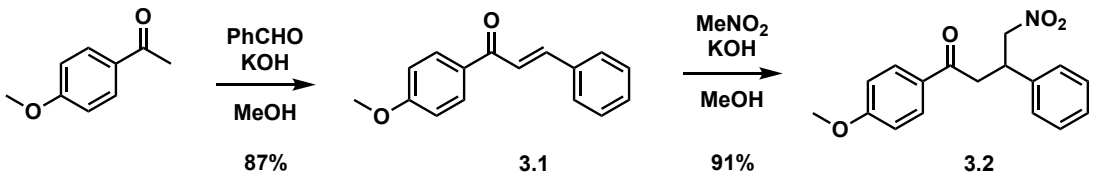

Scheme C.1: Synthesis of compound **3.2**.

[(E)-1-(4-methoxyphenyl)-3-phenylprop-2-en-1-one] (3.1): To a solution of 4'methoxyacetophenone (10 g, 66.9 mmol, 1 equiv) and benzaldehyde (6.83 mL, 61.9 mmol, 0.9 equiv), in EtOH (130 mL) at 0 °C was added a 10 M solution of aq. KOH (20.7 mL, 207 mmol, 3.1 equiv). The reaction was allowed to warm to room temperature and stir for 1.5 h. The resulting white precipitate was collected via filtration to afford the product (13.9 g, 58.33 mmol, 87% yield). R_f = 0.42 (3:14 v/v EtOAc/Hexanes). ^{1}H NMR (500 MHz, $CDCl_3$) δ 8.07 – 8.02 (m, 2H), 7.81 (d, *J* = 15.7 Hz, 1H), 7.67 – 7.62 (m, 2H), 7.55 (d, *J* = 15.6 Hz, 1H), 7.41 (tdd, *J* = 4.8, 3.5, 1.4 Hz, 3H), 7.01 – 6.96 (m, 2H), 3.89 (s, 3H). ^{13}C NMR (125 MHz, $CDCl_3$) δ 188.83, 163.56, 144.08, 135.23, 131.24, 130.95, 130.45, 129.05, 128.49, 122.03, 113.98, 55.63.

[1-(4-methoxyphenyl)-4-nitro-3-phenylbutan-1-one] (3.2): To a suspension of **3.1** (4.8 g, 20.1 mmol, 1 equiv) and nitromethane (13.6 mL, 254 mmol, 13 equiv) in EtOH (35 mL) was added a 10 M solution of aq. KOH (0.34 mL, 3.4 mmol, 0.2 equiv) and the was stirred at room temperature for 3 h. The reaction was monitored via TLC. When complete, the reaction was quenched with sat. NH_4Cl and extracted with EtOAc (3×). The combined organic fractions were dried over Na_2SO_4. The compound was concentrated to afford a white solid (5.48 g, 18.3 mmol, 91% yield), which was used without further purification. Note that the compound decomposes on silica. R_f = 0.37 (1:3 v/v EtOAc/Hexanes). ^{1}H NMR (500 MHz, $CDCl_3$) 7.96 – 7.89 (m, 2H), 7.40 – 7.33 (m, 2H), 7.33 – 7.26 (m, 3H), 6.99 – 6.91 (m, 2H), 4.86 (dd, *J* = 12.5, 6.4 Hz, 1H), 4.71 (dd, *J* = 12.5, 8.1 Hz, 1H), 4.24 (tt, *J* = 7.9, 6.4 Hz, 1H), 3.89 (s, 3H), 3.44 (dd, *J* = 17.4, 6.3 Hz, 1H), 3.39 (dd, *J* = 17.4, 7.7 Hz, 1H). ^{13}C NMR (125 MHz, $CDCl_3$) δ 195.43, 163.97, 139.42, 130.49, 129.61, 129.18, 127.95, 127.59, 114.02, 79.76, 55.66, 41.31, 39.58.

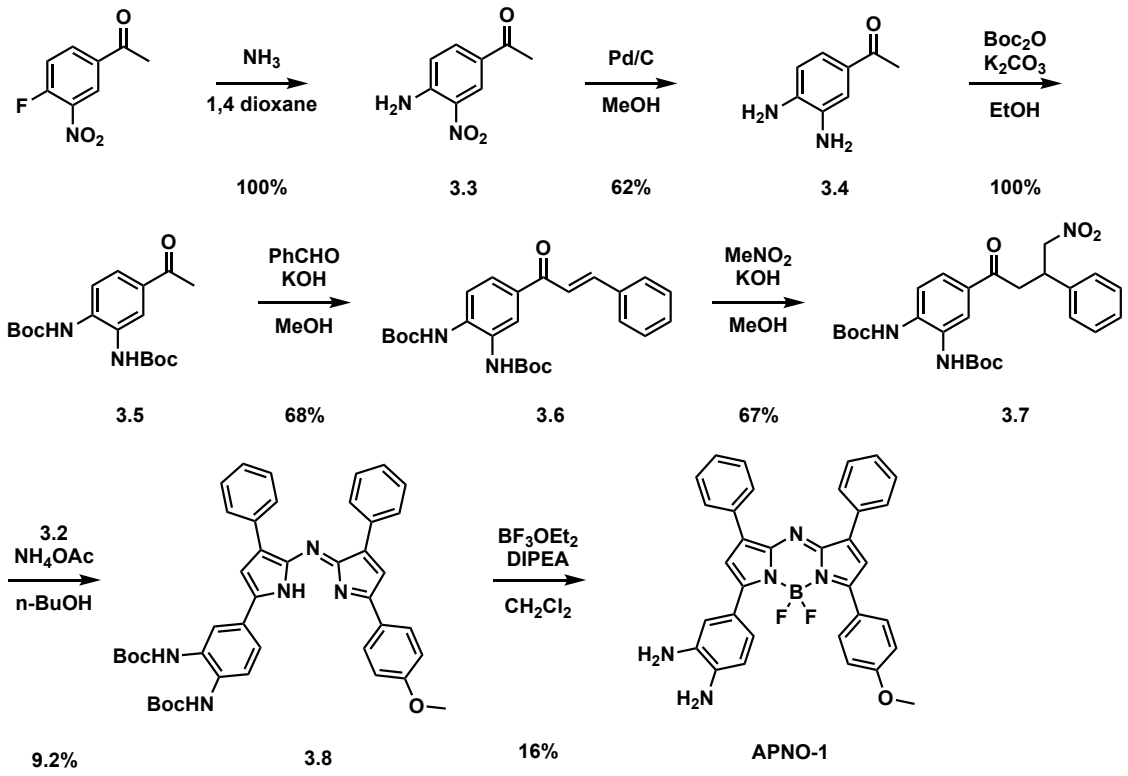

Scheme C.2: Synthesis of **APNO-1**.

4'-Amino-3'-nitroacetophenone (3.3): A solution of 4'-fluoro-3'-nitroacetophenone (11.5 g, 63.0 mmol, 1.0 equiv) and 7 M solution of ammonia in methanol (90.0 mL, 15.0 equiv) in 1,4-dioxane (85.0 mL) was stirred under nitrogen in a sealed pressure flask at 100 °C for 2 h. Reaction progress was monitored by TLC. When judged to be complete, the reaction was cooled to room temperature and sparged with nitrogen to remove excess ammonia. The solution was concentrated to afford a solid, suspended in sat. $NaHCO_3$, and extracted with EtOAc (3×). The combined organic fractions were dried over Na_2SO_4, filtered, and concentrated to afford an orange solid (11.4 g, 63.0 mmol, 100 % yield), which was used without purification. R_f = 0.17 (1:3 v/v EtOAc/Hexanes). ^{1}H NMR (500 MHz, $CDCl_3$) δ 8.74 (d, J = 2.1 Hz, 1H), 8.00 (dd, J = 8.8, 2.0 Hz, 1H), 6.86 (d, J = 8.8 Hz, 1H), 6.67 – 6.39 (bs, 2H), 2.57 (s, 3H). ^{13}C NMR (125 MHz, $CDCl_3$) δ 195.11, 147.73, 134.65, 128.47, 126.84, 119.00, 26.15.

3',4'-Diaminoacetophenone (3.4): A suspension of **3.3** (2.5 g, 13.6 mmol, 1 equiv) and 10 wt. % Pd/C (0.25 g, 10 % w/w) in MeOH (70.0 mL) was stirred under a H_2 (g) atmosphere maintained using a balloon at room temperature for 12 h. When the reaction was judged to be complete by TLC, it was filtered through a pad of Celite and washed with MeOH. The filtrate was concentrated and purified via silica gel column chromatography (1:9 v/v MeOH/CH_2Cl_2 with 0.1 % TEA) to afford the product as a brown solid (1.26 g, 8.4 mmol, 62% yield). R_f = 0.45 (3:97 v/v MeOH/CH_2Cl_2 with 0.1 % TEA). ^{1}H NMR (500 MHz, MeOD) δ 7.36 – 7.31 (m, 2H), 6.68 – 6.61 (m, 1H), 2.46 (s, 3H). ^{13}C NMR (125 MHz, MeOD) δ 199.74, 143.70, 134.25, 128.36, 123.75, 117.30, 114.66, 25.97.

Di-*tert*-butyl (4-acetyl-1,2-phenylene)dicarbamate (3.5): A suspension of **3.4** (1.4 g, 9 mmol, 1 equiv), K_2CO_3 (7.8 g, 36.0 mmol, 4 equiv), and di-*tert*-butyl-dicarbonate (3.8 g, 27.0 mmol, 3 equiv) in EtOH (9 mL) was stirred at 45 °C for 18 h. When judged to be complete by TLC the reaction was quenched with sat. $NaHCO_3$ and extracted with EtOAc (3×). The combined organic fractions were concentrated and purified via silica gel column chromatography (2:3 v/v EtOAc/Hexanes) to afford a white hygroscopic foam (3.2 g, 9.0 mmol, 100% yield). R_f = 0.20 (3:17 v/v EtOAc/Hexanes). ^{1}H NMR (500 MHz, $CDCl_3$) δ 7.92 (s, 1H), 7.83 (d, *J* = 8.6 Hz, 1H), 7.73 (dd, *J* = 8.5, 2.0 Hz, 1H), 7.20 (bs, 1H), 6.67 (bs, 1H), 2.55 (s, 3H), 1.513 (s, 9H), 1.509 (s, 9H). ^{13}C NMR (125 MHz, $CDCl_3$) δ 196.90, 154.21, 152.99, 136.57, 132.97, 128.04, 126.67, 125.59, 121.84, 81.63, 28.36, 28.34, 26.59.

Di-*tert*-butyl (4-cinnamoyl-1,2-phenylene) dicarbamate (3.6). A solution of **3.5** (2.7 g, 7.6 mmol, 1 equiv) and benzaldehyde (0.78 mL, 7.6 mmol, 1 equiv) in EtOH (25.0 mL) was cooled to 0 °C in an ice bath and treated with a 10 M aq. solution of KOH (2.3 mL, 22.8 mmol, 3 equiv). The reaction was allowed to stand in the refrigerator at 4 °C for 20 h. The reaction was

quenched with sat. NH_4Cl and extracted with EtOAc (3×). The combined organic fractions were dried over Na_2SO_4, concentrated, and purified via silica gel column chromatography (3:17 v/v EtOAc/Hexanes) to afford an off-white solid (2.3 g, 5.3 mmol, 68% yield). R_f = 0.55 (3:7 v/v EtOAc/Hexanes). ^{1}H NMR (500 MHz, $CDCl_3$) δ 7.95 (s, 1H), 7.93 – 7.86 (m, 1H), 7.82 (dd, *J* = 8.5, 2.1 Hz, 1H), 7.78 (d, *J* = 15.7 Hz, 1H), 7.66 – 7.59 (m, 2H), 7.48 (d, *J* = 15.7 Hz, 1H), 7.40 (dd, *J* = 4.9, 1.9 Hz, 3H), 7.33 (bs, 1H), 6.78 (bs, 1H), 1.524 (s, 9H), 1.520 (s, 9H). ^{13}C NMR δ 188.87, 154.30, 153.00, 144.81, 134.99, 133.79, 130.60, 129.03, 128.61, 126.89, 126.02, 125.99, 125.93, 121.75, 81.62, 81.39, 77.36, 28.36, 28.34.

Di-*tert*-butyl (4-(4-nitro-3-phenylbutanoyl)-1,2-phenylene)dicarbamate (3.7). A solution of **3.6** (2.2 g, 5.0 mmol, 1 equiv) and nitromethane (0.6 g, 10.1 mmol, 2 equiv) in EtOH (10.0 mL) was cooled to 0 °C in an ice bath and treated with a 10 M aq. solution of KOH (0.1 mL, 1.0 mmol, 0.2 equiv). The reaction was stirred at 40 °C for 20 h, diluted with brine, and extracted with EtOAc (3×). The combined organic fractions were dried over Na_2SO_4, concentrated, and purified via silica gel column chromatography (1:3 v/v EtOAc/Hexanes) to afford an off-white solid (1.7 g, 3.4 mmol, 67% yield). R_f = 0.38 (1:3 v/v EtOAc/Hexanes). ^{1}H NMR (500 MHz, $CDCl_3$) δ 7.86 (s, 1H), 7.84 – 7.79 (m, 1H), 7.66 (dd, *J* = 8.4, 2.1 Hz, 1H), 7.40 – 7.22 (m, 6H), 6.72 (s, 1H), 4.84 (dd, *J* = 12.6, 6.4 Hz, 1H), 4.70 (dd, *J* = 12.6, 8.3 Hz, 1H), 4.22 (quint, *J* = 7.0 Hz, 1H), 3.39 (qd, *J* = 17.6, 7.0 Hz, 2H), 1.55 (s, 9H), 1.54 (s, 9H).^{13}C NMR (125 MHz, $CDCl_3$) δ 195.46, 154.17, 152.92, 139.28, 137.02, 132.02, 129.12, 128.32, 128.12, 127.91, 127.59, 126.23, 125.39, 125.27, 121.81, 81.71, 81.58, 79.62, 41.44, 39.40, 28.33, 28.31.

***tert*-Butyl (Z)-(2-((tert-butoxycarbonyl)amino)-4-(5-((5-(4-methoxyphenyl)-3-phenyl-2H-pyrrol-2-ylidene)amino)-4-phenyl-1H-pyrrol-2-yl)phenyl)carbamate (3.8):** A solution of **3.7** (0.4 g, 0.8 mmol, 1 equiv) and **3.2** (0.5 g, 1.6 mmol, 2 equiv) in *n*-butanol (16.0 mL) was heated

to 90 °C to ensure all reactants were dissolved. NH_4OAc (1.0 g, 12.3 mmol, 15 equiv) was added and the reaction was stirred at 90 °C for 8 h. The reaction was concentrated under reduced pressure, suspended in brine, and extracted with CH_2Cl_2 (3×). The combined organic layers were dried over Na_2SO_4, concentrated, and purified via silica gel column chromatography (1:1 v/v CH_2Cl_2/Hexanes to CH_2Cl_2, step gradient). All fractions containing product were pooled and concentrated to afford a dark blue solid (0.05 g, 0.075 mmol, 9.2% yield), which was used without further purification. R_f = 0.57 (3:7 v/v EtOAc/Hexanes).

APNO-1: A solution of **3.8** (0.05 g, 0.75 mmol, 1 equiv) and *N,N*-diisopropylethylamine (0.1 g, 0.8 mmol, 10 equiv) in anhydrous CH_2Cl_2 was cooled to 0 °C in an ice bath and treated dropwise with boron trifluoride diethyl etherate (0.13 mL, 1.15 mmol, 15 equiv). The reaction was stirred at room temperature for 18 h under a nitrogen atmosphere, quenched with H_2O (5.0 mL), and extracted with CH_2Cl_2 (3×). The combined organic layers were concentrated and purified via silica gel column chromatography (1:99 v/v MeOH/CH_2Cl_2 with 0.1 % TEA) to afford the product as a green solid (6.6 mg, 0.01 mmol, 16% yield). R_f = 0.35 (1:99 v/v MeOH/CH_2Cl_2). ^{1}H NMR (500 MHz, $CDCl_3$) δ 8.10 – 8.02 (m, 7H), 7.65 (d, *J* = 2.1 Hz, 1H), 7.61 (dd, *J* = 8.3, 2.0 Hz, 1H), 7.48 – 7.37 (m, 7H), 7.10 (d, *J* = 1.0 Hz, 1H), 7.03 – 6.99 (m, 2H), 6.98 (s, 1H), 6.76 (d, *J* = 8.3 Hz, 1H), 3.89 (s, 3H). ^{11}B NMR (161 MHz, $CDCl_3$) δ 1.16 (t, *J* = 32.8 Hz). ^{19}F NMR (471 MHz, $CDCl_3$) δ -131.75 (dd, *J* = 64.1, 32.1 Hz). HR-MS (ESI, TOF) calc'd for $[M+H]^+$ 558.2277, found 558.2268.

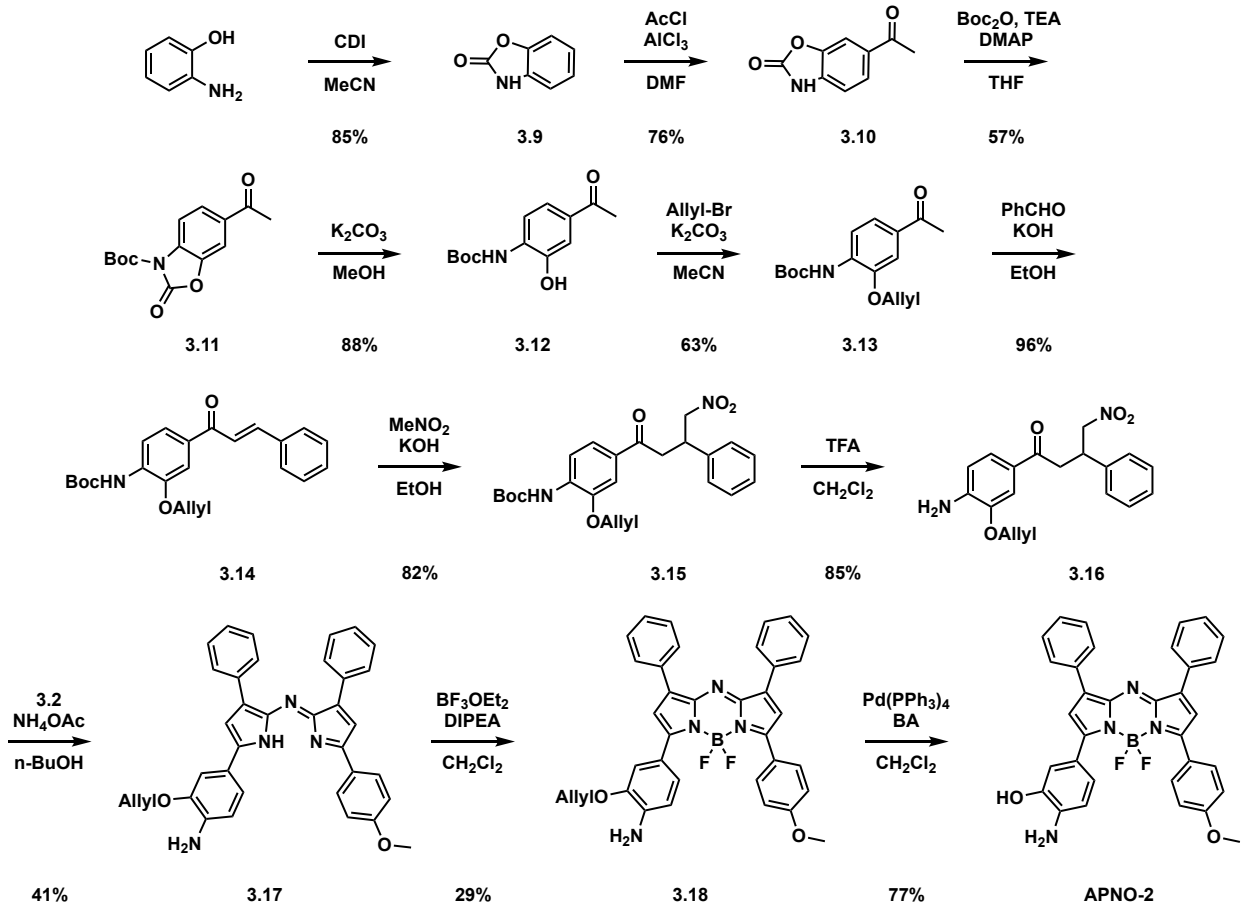

Scheme C.3: Synthesis of **APNO-2**.

Benzo[d]oxazol-2(3H)-one (3.9): A solution of 2-aminophenol (10.0 g, 92.0 mmol, 1 equiv) and di(1H-imidazol-1-yl)methanone (CDI) (37.0 g, 228.0 mmol, 2.5 equiv) in anhydrous MeCN (250.0 mL) was stirred at 70 °C for 4 h. When judged to be complete by TLC, the reaction was concentrated and suspended in EtOAc. Excess CDI was quenched with 2 M aq. HCl and the organic layer was washed sequentially with a 2 M solution of aq. HCl (3×), sat. $NaHCO_3$, and H_2O (2×). The organic fraction was dried over Na_2SO_4 and concentrated to afford an orange solid (10.5 g, 78.0 mmol, 85% yield), which was used without further purification. R_f = 0.39 (3:7 v/v EtOAc/Hexanes). ^{1}H NMR (500 MHz, DMSO-d_6) δ 11.56 (bs, 1H), 7.29 – 7.24 (m, 1H), 7.17 – 7.11 (m, 1H), 7.10 – 7.04 (m, 2H). ^{13}C NMR (125 MHz, DMSO-d_6) δ 154.43, 143.35, 130.40, 123.75, 121.80, 109.76, 109.48.

6-Acetylbenzo[d]oxazol-2(3H)-one (3.10): The product was synthesized according to previously reported protocols.[9] A flame-dried two-neck round bottom flask was charged with aluminum trichloride (156 g, 1.16 mol, 10 equiv). The solid was heated to 45 °C under a nitrogen atmosphere and treated with dropwise addition of anhydrous DMF (26.0 mL). Compound **3.9** (15.7 g, 116.2 mmol, 1 equiv) was added portion-wise to the slurry. Acetyl chloride (50.0 mL, 697.0 mmol, 6 equiv) was added dropwise via addition funnel then heated to 75 °C for 2 h. The reaction was slowly poured into ice and the resultant precipitate was filtered and rinsed with H_2O to afford an orange solid (15.6 g, 88.0 mmol, 76% yield), which was used without further purification. R_f = 0.23 (1:1 v/v EtOAc/Hexanes) ^{1}1H NMR (500 MHz, DMSO-d_6) δ 12.04 (s, 1H), 7.83, (m, 2H), 7.20 – 7.17 (m, 1H), 2.56 (s, 3H). ^{13}C NMR (125 MHz, DMSO-d_6) δ 196.30, 154.41, 143.28, 134.81, 131.21, 125.33, 109.33, 109.03, 26.60.

***tert*-Butyl 6-acetyl-2-oxobenzo[d]oxazole-3(2H)-carboxylate (3.11):** Di-*tert*-butyl-dicarbonate (38.5 g, 175.9 mmol, 2 equiv) was added to a solution of **3.10** (15.6 g, 88.0 mmol, 1 equiv), TEA (8.8 g, 88.0 mmol, 1 equiv) and DMAP (10.7 g, 88.0 mmol, 1 equiv) in THF (250.0 mL). The reaction was stirred at room temperature for 1 h, poured into sat. $NaHCO_3$, and extracted with EtOAc (3×). The combined organic fractions were dried over Na_2SO_4, concentrated under reduced pressure and purified via silica gel column chromatography (1:1 v/v EtOAc/Hexanes) to afford the product as a white solid (13.9 g, 50.1 mmol, 57% yield). R_f = 0.31 (3:17 v/v EtOAc/Hexanes). ^{1}H NMR (400 MHz, $CDCl_3$) δ 7.89 – 7.84 (m, 1H), 7.80 – 7.74 (m, 2H), 2.60 (s, 3H), 1.66 (s, 9H). ^{13}C NMR (100 MHz, $CDCl_3$) δ196.25, 149.20, 147.38, 141.99, 134.26, 131.56, 125.78, 114.48, 109.74, 87.16, 28.13, 26.83.

***tert*-Butyl (4-acetyl-2-hydroxyphenyl)carbamate (3.12):** A suspension of **3.11** (13.9 g, 50.1 mmol, 1 equiv) and K_2CO_3 (6.96 g, 50.4 mmol, 1 equiv) in MeOH (250 mL) was stirred at room

temperature for 9 h under a nitrogen atmosphere. The volatiles were removed under reduced pressure and the resulting residue was dissolved in EtOAc, treated with sat. NH_4Cl, and the product was extracted with EtOAc (3×). The combined organic fractions were dried over Na_2SO_4, concentrated, and purified via silica gel column chromatography (2:3 v/v EtOAc/Hexanes) to afford an orange solid (11.1 g, 44.0 mmol, 88% yield). R_f = 0.35 (3:7 v/v EtOAc/Hexanes). ^{1}H NMR (500 MHz, $CDCl_3$) δ 8.46 (bs, 1H), 7.84 – 7.79 (m, 1H), 7.67 (d, *J* = 2.0 Hz, 1H), 7.48 (dd, *J* = 8.5, 1.9 Hz, 1H), 2.56 (s, 1H), 1.53 (s, 5H). ^{13}C NMR (125 MHz, $CDCl_3$) δ 198.83, 153.35, 145.42, 132.23, 132.03, 122.79, 118.28, 115.42, 81.84, 28.40, 26.55.

***tert*-Butyl (4-acetyl-2-(allyloxy)phenyl)carbamate (3.13):** A suspension of **3.12** (3.6 g, 14.3 mmol, 1 equiv), allyl bromide (3.1 mL, 35.8 mmol, 2.5 equiv) and K_2CO_3 (3.95 g, 28.6 mmol, 2 equiv) in anhydrous MeCN (30.0 mL) was stirred at 45 °C for 3 h. The reaction was quenched with H_2O and extracted with EtOAc (3×). The combined organic fractions were dried over Na_2SO_4, concentrated, and purified via silica gel column chromatography (3:17 v/v EtOAc/Hexanes) to afford the product as a white solid (2.6 g, 9.0 mmol, 63% yield). R_f = 0.39 (3:17 v/v EtOAc/Hexanes). ^{1}H NMR (500 MHz, $CDCl_3$) δ 8.19 (d, *J* = 8.4 Hz, 1H), 7.55 (dd, *J* = 8.4, 1.8 Hz, 1H), 7.49 (d, *J* = 1.8 Hz, 1H), 7.31 (bs, 1H), 6.08 (ddt, *J* = 17.2, 10.7, 5.5 Hz, 1H), 5.42 (dq, *J* = 17.3, 1.5 Hz, 1H), 5.34 (dq, *J* = 10.5, 1.3 Hz, 1H), 4.66 (dt, *J* = 5.5, 1.5 Hz, 2H), 2.55 (s, 3H), 1.54 (s, 9H). ^{13}C NMR (125 MHz, $CDCl_3$) δ 197.04, 152.41, 146.24, 133.32, 132.58, 131.35, 123.52, 118.75, 116.72, 109.99, 81.26, 69.75, 28.43, 26.40.

***tert*-Butyl (2-(allyloxy)-4-cinnamoylphenyl)(methyl)carbamate (3.14):** A 10 M aq. solution of KOH (0.44 mL, 4.4 mmol, 1.2 equiv) was added dropwise to a solution of **3.13** (1.1 g, 3.65 mmol, 1 equiv) and benzaldehyde (0.41 mL, 4.0 mmol, 1.1 equiv) in EtOH (8.0 mL). After stirring at room temperature for 12 h, the reaction was quenched with sat. NH_4Cl and extracted

with EtOAc (3×). The organic layers were dried over Na_2SO_4, concentrated, and purified via silica gel column chromatography (3:17 v/v EtOAc/Hexanes) to afford the product as a yellow solid (1.3 g, 3.43 mmol, 96% yield). R_f = 0.41 (1:9 v/v EtOAc/Hex). ^{1}H NMR (500 MHz, $CDCl_3$) δ 8.24 (d, *J* = 8.5 Hz, 1H), 7.79 (d, *J* = 15.6 Hz, 1H), 7.67 (dd, *J* = 8.5, 1.9 Hz, 1H), 7.65 – 7.61 (m, 2H), 7.59 (d, *J* = 1.8 Hz, 1H), 7.55 (d, *J* = 15.6 Hz, 1H), 7.43 – 7.38 (m, 3H), 7.36 (s, 1H), 6.09 (ddt, *J* = 17.3, 10.7, 5.5 Hz, 1H), 5.43 (dq, *J* = 17.2, 1.6 Hz, 1H), 5.34 (dq, *J* = 10.5, 1.3 Hz, 1H), 4.68 (dt, *J* = 5.6, 1.5 Hz, 2H), 1.54 (s, 9H). ^{13}C NMR (125 MHz, $CDCl_3$) δ 188.58, 152.30, 146.39, 144.06, 135.08, 133.17, 132.53, 132.09, 130.40, 128.95, 128.45, 123.11, 121.68, 118.70, 116.59, 110.67, 81.15, 69.68, 28.35.

***tert*-Butyl (2-(allyloxy)-4-(4-nitro-3-phenylbutanoyl)phenyl)carbamate (3.15):** A solution of **3.14** (1.8 g, 4.63 mmol, 1 equiv) and nitromethane (0.5 mL, 9.26 mmol, 2 equiv) in EtOH (15 mL) was treated with a 10 M aq. solution of KOH (0.09 mL, 0.9 mmol, 0.2 equiv). The reaction was stirred at room temperature for 14 h and then quenched with sat. NH_4Cl. The reaction mixture was extracted with EtOAc (3×). The combined organic fractions were dried over Na_2SO_4, concentrated, and purified via silica gel column chromatography (3:17 v/v EtOAc/Hexanes) to afford the product as a yellow foam (1.4 g, 3.18 mmol, 82% yield). R_f = 0.25 (1:9 v/v EtOAc/Hexanes). ^{1}H NMR (500 MHz, $CDCl_3$) δ 8.18 (d, *J* = 8.5 Hz, 1H), 7.51 (dd, *J* = 8.5, 1.9 Hz, 1H), 7.44 (d, *J* = 1.9 Hz, 1H), 7.37 – 7.27 (m, 6H), 6.07 (ddt, *J* = 17.3, 10.7, 5.5 Hz, 1H), 5.41 (dq, *J* = 17.2, 1.5 Hz, 1H), 5.34 (dq, *J* = 10.5, 1.2 Hz, 1H), 4.83 (dd, *J* = 12.5, 6.5 Hz, 1H), 4.70 – 4.65 (m, 1H), 4.64 (dt, *J* = 5.5, 1.5 Hz, 2H), 4.21 (ddd, *J* = 14.4, 7.9, 6.5 Hz, 1H), 3.43 (dd, *J* = 17.4, 6.4 Hz, 1H), 3.35 (dd, *J* = 17.4, 7.6 Hz, 1H), 1.54 (s, 9H). ^{13}C NMR (125 MHz, $CDCl_3$) δ 195.60, 152.34, 146.33, 139.38, 133.80, 132.45, 130.44, 129.19, 127.96, 127.59, 122.90, 118.86, 116.72, 110.03, 81.42, 79.76, 69.78, 41.28, 39.68, 28.43.

1-(3-(Allyloxy)-4-aminophenyl)-4-nitro-3-phenylbutan-1-one (3.16): A solution of **3.15** (2.4 g, 6.4 mmol, 1 equiv) in CH_2Cl_2 (24.0 mL) was cooled to 0 °C in an ice bath and treated with dropwise addition of TFA (6.0 mL). After stirring at room temperature for 2 h, the reaction was cooled to 0 °C in an ice bath and quenched by dropwise addition of sat. $NaHCO_3$. The reaction was extracted with CH_2Cl_2 (3×). The combined organic layers were dried over Na_2SO_4 and concentrated to afford the product as a yellow oil (1.9 g, 5.58 mmol, 85% yield), which was used without further purification. R_f = 0.25 (3:17 v/v EtOAc/Hexanes). ^{1}H NMR (500 MHz, $CDCl_3$) δ 7.45 – 7.38 (m, 2H), 7.36 – 7.29 (m, 2H), 7.31 – 7.25 (m, 3H), 6.64 (d, *J* = 8.0 Hz, 1H), 6.06 (ddt, *J* = 17.2, 10.6, 5.4 Hz, 1H), 5.41 (dq, *J* = 17.3, 1.6 Hz, 1H), 5.30 (dq, *J* = 10.5, 1.4 Hz, 1H), 4.84 (dd, *J* = 12.5, 6.4 Hz, 1H), 4.67 (dd, *J* = 12.5, 8.4 Hz, 1H), 4.60 (dt, *J* = 5.4, 1.5 Hz, 2H), 4.20 (tt, *J* = 8.2, 6.2 Hz, 1H), 3.36 (dd, *J* = 17.1, 6.2 Hz, 1H), 3.30 (dd, *J* = 17.1, 7.9 Hz, 1H).^{13}C NMR (125 MHz, $CDCl_3$) δ 194.95, 145.49, 142.45, 139.63, 132.97, 129.14, 127.87, 127.59, 126.91, 123.89, 118.20, 112.83, 110.80, 79.84, 69.38, 40.96, 39.85.

(Z)-2-(Allyloxy)-4-(5-((5-(4-methoxyphenyl)-3-phenyl-2H-pyrrol-2-ylidene)amino)-4-phenyl-1H-pyrrol-2-yl)aniline (3.17): A suspension of **3.16** (0.96 g, 2.8 mmol, 1 equiv) and **3.2** (1.7 g, 5.6 mmol, 2 equiv) in *n*-butanol (50 mL) was heated to 110 °C to dissolve all solids. NH_4OAc (3.3 g, 43.5 mmol, 15 equiv) was added in one portion and the reaction was stirred at the same temperature for 4 h. Volatiles were removed under reduced pressure, suspended in brine, and extracted with EtOAc (3×). The combined organic layers were dried over Na_2SO_4, concentrated, and purified via silica gel column chromatography (step gradient from 1:1 v/v CH_2Cl_2/Hexanes with 0.1 % TEA to 4:1 CH_2Cl_2/Hexanes with 0.1 % TEA) to afford the product as a blue solid (0.65 g, 1.18 mmol, 41% yield). R_f = 0.42 (3:7 v/v EtOAc/Hexanes). ^{1}H NMR (500 MHz, DMSO-d_6) δ 8.09 (dd, *J* = 13.1, 7.7 Hz, 4H), 7.82 (d, *J* = 7.9 Hz, 2H), 7.76 (s, 1H),

7.69 – 7.63 (m, 2H), 7.48 – 7.37 (m, 5H), 7.36 – 7.27 (m, 2H), 7.26 (s, 1H), 7.04 (d, *J* = 8.2 Hz, 2H), 6.83 (d, *J* = 8.3 Hz, 1H), 6.20 (ddt, *J* = 16.0, 10.7, 5.4 Hz, 1H), 6.03 (s, 2H), 5.56 (d, *J* = 17.8 Hz, 1H), 5.36 (d, *J* = 10.6 Hz, 1H), 4.78 (d, *J* = 5.3 Hz, 2H), 3.81 (s, 3H). ^{13}C NMR (125 MHz, DMSO-d_6) δ 165.43, 159.82, 156.82, 145.28, 145.07, 143.99, 143.95, 143.45, 141.35, 141.15, 134.14, 133.91, 133.68, 133.55, 133.15, 129.01, 128.72, 128.40, 128.22, 128.16, 127.78, 127.11, 126.52, 124.51, 123.59, 121.07, 119.44, 118.21, 117.09, 114.77, 113.18, 109.53, 109.22, 79.80, 79.17, 68.33, 55.38.

2-(Allyloxy)-4-(5,5-difluoro-7-(4-methoxyphenyl)-1,9-diphenyl-5H-5l4,6l4-dipyrrolo[1,2-c:2',1'-f][1,3,5,2]triazaborinin-3-yl)aniline (3.18): A solution of **3.17** (0.40 g, 0.72 mmol, 1 equiv) and *N,N*-diisopropylethylamine (1.4 g, 10.8 mmol, 15 equiv) in anhydrous CH_2Cl_2 (30.0 mL) was treated with the portion-wise addition of boron trifluoride diethyl etherate (2.6 mL, 21.6 mmol, 30 equiv) at 0 °C. The reaction was stirred at room temperature for 24 h under a nitrogen atmosphere. The reaction progress was monitored via UV-Vis at 724 nm in chloroform indicating formation of the product. Upon completion the reaction was quenched with sat. $NaHCO_3$ and extracted with CH_2Cl_2 (3×). The combined organic layers were dried over Na_2SO_4, concentrated, purified twice by silica gel column chromatography (1:19 v/v MeOH/ CH_2Cl_2 and 4:1 CH_2Cl_2/Hexanes) to afford the product as a red solid (0.12 g, 0.2 mmol, 29% yield). R_f = 0.17 (1:9 v/v MeOH/CH_2Cl_2). ^{1}H NMR (500 MHz, DMSO-d_6) δ 8.25 – 8.19 (m, 2H), 8.14 – 8.11 (m, 2H), 8.10 – 8.07 (m, 2H), 8.02 (d, *J* = 1.9 Hz, 1H), 7.99 (dd, *J* = 8.8, 2.1 Hz, 1H), 7.98 (s, 1H), 7.59 – 7.52 (m, 2H), 7.53 – 7.46 (m, 3H), 7.42 – 7.36 (m, 1H), 7.28 (s, 1H), 7.09 – 7.03 (m, 2H), 6.83 (s, 2H), 6.81 (d, *J* = 8.7 Hz, 1H), 6.91 – 6.73 (m, 3H), 6.18 (ddt, *J* = 17.4, 10.6, 5.3 Hz, 1H), 5.54 (dq, *J* = 17.3, 1.7 Hz, 1H), 5.34 (dd, *J* = 10.5, 1.6 Hz, 1H), 4.70 (dt, *J* = 5.3, 1.5 Hz, 2H), 3.85 (s, 3H). ^{13}C NMR (125 MHz, DMSO-d_6) δ 160.29, 159.76, 149.29, 146.58,

145.81, 144.45, 142.15, 141.57, 135.80, 133.24, 133.17, 133.06, 131.58, 130.57, 130.53, 130.49, 129.58, 129.05, 128.88, 128.58, 128.51, 128.45, 128.19, 128.13, 127.77, 125.30, 124.76, 121.95, 117.90, 116.32, 116.09, 113.90, 113.68, 113.52, 68.85, 55.33. ^{11}B NMR (161 MHz, DMSO-d_6) δ 1.29 (t, J = 30.8 Hz). ^{19}F NMR (471 MHz, DMSO-d_6) δ -130.11 (dd, J = 67.0, 30.8 Hz).

APNO-2: A suspension of **3.18** (0.047 g, 0.078 mmol, 1 equiv), 1,3-dimethylbarbituric acid (1,3-DMBA) (0.015 g, 0.12 mmol, 1.5 equiv), $Pd(PPh_3)_4$ (0.009 g, 0.008 mmol, 0.1 equiv), in anhydrous CH_2Cl_2 (10 mL) was stirred under nitrogen atmosphere at room temperature for 12 h. The reaction was treated with sat. $NaHCO_3$ and extracted with CH_2Cl_2 (3×). The combined organic layers were dried over Na_2SO_4, concentrated, and purified via silica gel column chromatography (1:99 v/v MeOH/CH_2Cl_2) to afford the product as a red solid (0.033 g, 0.060 mmol, 77% yield) R_f = 0.32 (1:99 v/v MeOH/CH_2Cl_2). ^{1}H NMR (500 MHz, DMSO-d_6) δ 9.95 (s, 1H), 8.20 (dt, J = 6.4, 1.4 Hz, 2H), 8.14 – 8.09 (m, 2H), 8.07 – 8.04 (m, 2H), 7.90 – 7.81 (m, 3H), 7.59 – 7.53 (m, 2H), 7.52 – 7.46 (m, 3H), 7.41 – 7.36 (m, 1H), 7.23 (s, 1H), 7.12 – 7.03 (m, 2H), 6.77 (d, J = 8.4 Hz, 1H), 6.69 (s, 2H), 3.87 (s, 3H). ^{13}C NMR (125 MHz, DMSO-d_6) δ 160.14, 148.95, 146.76, 145.83, 143.62, 141.92, 141.47, 135.21, 133.19, 131.58, 130.57, 129.52, 129.02, 128.59, 128.49, 128.40, 127.99, 124.96, 122.32, 116.91, 115.98, 115.73, 113.98, 113.51, 55.35. ^{11}B NMR (161 MHz, DMSO-d_6) δ 1.21 (t, J = 33.7 Hz). ^{19}F NMR (471 MHz, DMSO-d_6) δ -130.00 (dd, J = 66.2, 31.3 Hz). HR-MS (ESI, TOF) calc'd $[M+H]^+$ 559.2117, found 559.2125.

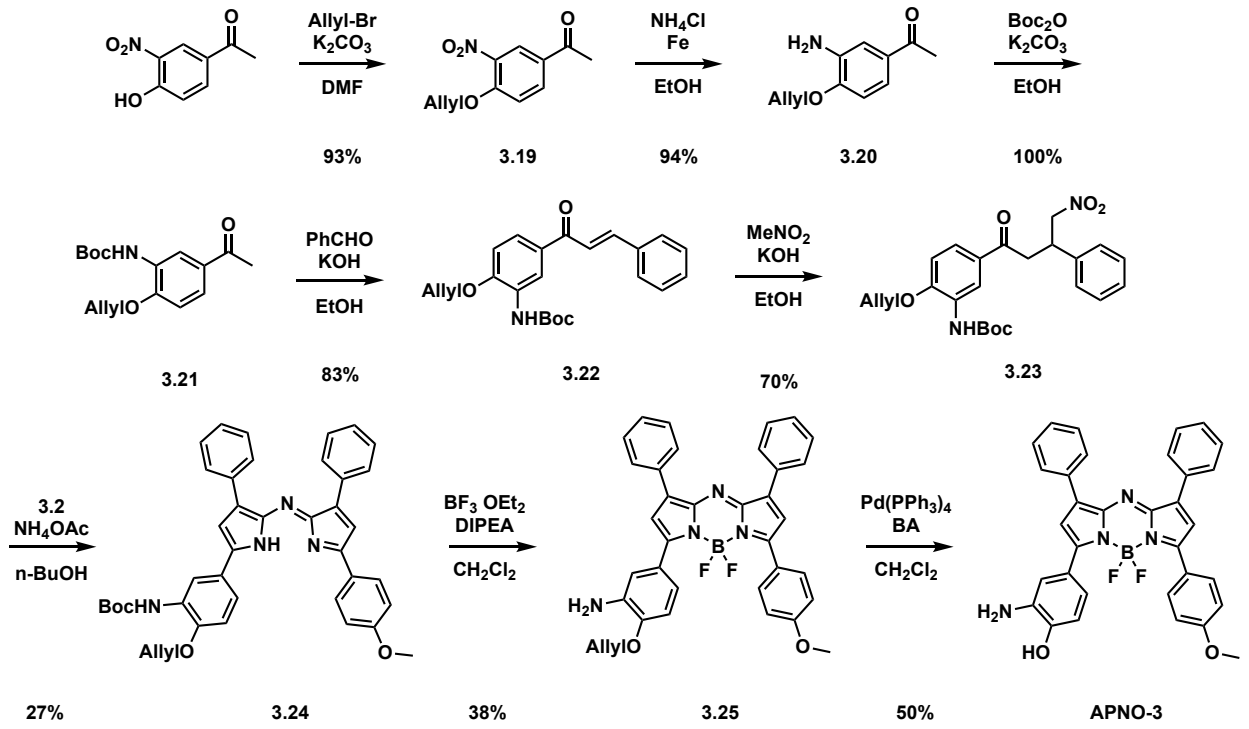

Scheme C.4: Synthesis of **APNO-3**.

1-(4-(Allyloxy)-3-nitrophenyl)ethan-1-one (3.19): A suspension of 1-(4-hydroxy-3-nitrophenyl)ethan-1-one (0.9 g, 5.0 mmol, 1 equiv) and K_2CO_3 (1.0 g, 7.5 mmol, 1.5 equiv) in anhydrous DMF (10 mL) was cooled to 0 °C in an ice bath. Allyl bromide (0.65 mL, 7.5 mmol, 1.5 equiv) was added dropwise and the mixture was stirred at 55 °C for 16 h. Completion was observed via TLC. After cooling to room temperature, the reaction was diluted with brine and extracted with a 2:1 v/v mixture of CH_2Cl_2/isopropanol. The combined organic fractions were dried over Na_2SO_4 and concentrated to afford an oil that crystallized to a yellow solid (1.03 g, 4.66 mmol, 93% yield). The product was used without further purification. R_f = 0.40 (3:7 v/v EtOAc/Hexanes). ^{1}H NMR (500 MHz, $CDCl_3$) δ 8.31 (d, *J* = 2.3 Hz, 1H), 8.04 (dd, *J* = 8.8, 2.2 Hz, 1H), 7.09 (d, *J* = 8.8 Hz, 1H), 5.96 (ddt, *J* = 17.2, 10.3, 4.9 Hz, 1H), 5.43 (dq, *J* = 17.3, 1.6 Hz, 1H), 5.28 (d, *J* = 10.6, 1H), 4.70 (d, *J* = 2.0 Hz, 2H), 2.52 (s, 3H). ^{13}C NMR (125 MHz,

$CDCl_3$) δ 194.77, 154.97, 139.29, 133.86, 130.89, 129.46, 125.89, 118.70, 114.38, 77.41, 77.16, 76.90, 70.15, 26.24.

1-(4-(Allyloxy)-3-aminophenyl)ethan-1-one (3.20): A flask was charged with **3.19** (220 mg, 1.0 mmol, 1.0 equiv), NH_4Cl (54.5 mg, 1.0 mmol, 1.0 equiv), H_2O (2 mL) and EtOH (8 mL). Iron powder (560 mg, 10.0 mmol, 10 equiv) was added to the rapidly stirred reaction mixture which was then heated to 80 °C for 4 h. The mixture was diluted with brine and sequentially extracted with EtOAc and a 2:1 v/v mixture of CH_2Cl_2:isopropanol. The combined organic layers were dried over Na_2SO_4 and concentrated to an oil, which crystallized to a beige solid (179 mg, 0.935 mmol, 94% yield). The product was used without further purification. R_f = 0.40 (1:3 v/v EtOAc/Hexanes). ^{1}H NMR (500 MHz, $CHCl_3$) δ 7.36 – 7.30 (m, 2H), 6.77 (d, *J* = 8.6 Hz, 1H), 6.05 (ddt, *J* = 16.2, 10.5, 5.3 Hz, 1H), 5.40 (d, *J* = 17.3 Hz, 1H), 5.30 (d, *J* = 10.5 Hz, 1H), 4.61 (d, *J* = 5.3 Hz, 2H), 2.50 (s, 3H). ^{13}C NMR (125 MHz, $CDCl_3$) δ 197.43, 150.17, 136.42, 132.73, 130.78, 120.36, 118.17, 114.19, 110.54, 69.22, 26.39.

***tert*-Butyl (5-acetyl-2-(allyloxy)phenyl)carbamate (3.21):** A suspension of **3.20** (179 mg, 0.935 mmol, 1.0 equiv), di-*tert*-butyl-dicarbonate (408 mg, 1.87 mmol, 2.0 equiv), K_2CO_3 (194 mg, 1.4 mmol, 1.5 equiv), and EtOH (2 mL) was stirred at 45 °C for 8 h, diluted with brine and extracted with EtOAc (3×). The organic layers were dried over Na_2SO_4 and concentrated to a thick yellow oil which solidified overnight (272.4 mg, 0.935 mmol, 100% yield). R_f = 0.31 (1:9 v/v EtOAc/Hexanes). ^{1}H NMR (500 MHz, $CDCl_3$) δ 8.72 (s, 1H), 7.64 (dd, *J* = 8.6, 2.1 Hz, 1H), 7.08 (s, 1H), 6.89 (d, *J* = 8.6 Hz, 1H), 6.07 (ddt, *J* = 17.2, 10.8, 5.4 Hz, 1H), 5.41 (dd, *J* = 17.3, 1.4 Hz, 1H), 5.36 (dd, *J* = 10.5, 1.3 Hz, 1H), 4.67 (dd, *J* = 5.3, 1.5 Hz, 2H), 2.58 (d, *J* = 0.7 Hz, 3H), 1.55 (s, 9H). ^{13}C NMR (125 MHz, $CDCl_3$) δ 197.41, 152.73, 150.13, 132.34, 130.83, 128.26, 123.27, 118.92, 118.85, 110.83, 69.78, 28.51, 26.74.

***tert*-Butyl (2-(allyloxy)-5-cinnamoylphenyl)carbamate (3.22):** A solution of **3.21** (217 mg, 0.73 mmol, 1.0 equiv), EtOH (1.6 mL), benzaldehyde (82 µL, 0.8 mmol, 1.1 equiv), and a 10 M aq. solution of KOH (219 µL, 2.19 mmol, 3 equiv) was stirred at room temperature for 3.5 h. Upon consumption of **3.21**, the reaction was concentrated, and the residue was taken up in brine and EtOAc. The aqueous layer was extracted with EtOAc; the organic layers were dried and concentrated to a pale yellow solid (230 mg, 0.60 mmol, 83% yield). Used without further purification. R_f = 0.20 (1:9 v/v EtOAc/Hexanes). ^{1}H NMR (500 MHz, $CDCl_3$) δ 7.81 (d, *J* = 15.6 Hz, 1H), 7.71 (dd, *J* = 8.6, 2.2 Hz, 1H), 7.64 (dd, *J* = 7.3, 2.2 Hz, 2H), 7.56 (d, *J* = 15.6 Hz, 1H), 7.42 – 7.36 (m, 3H), 7.13 (s, 1H), 6.91 (d, *J* = 8.6 Hz, 1H), 6.06 (ddt, *J* = 17.3, 10.6, 5.4 Hz, 1H), 5.40 (d, *J* = 17.4 Hz, 1H), 5.34 (d, *J* = 10.4 1H), 4.65 (dd, *J* = 5.4, 1.6 Hz, 2H), 1.56 (s, 9H). ^{13}C NMR (125 MHz, $CDCl_3$) δ 215.81, 188.97, 152.59, 150.03, 144.02, 143.99, 135.11, 132.22, 132.19, 131.51, 130.29, 128.88, 128.50, 128.26, 123.83, 122.01, 118.77, 118.50, 110.85, 69.65, 28.39.

***tert*-Butyl (2-(allyloxy)-5-(4-nitro-3-phenylbutanoyl)phenyl)carbamate (3.23):** To a round bottom flask was added **3.22** (458 mg, 1.21 mmol, 1.0 equiv), EtOH (2.5 mL), nitromethane (0.2 mL), and a 10 M aq. solution of KOH (0.12 mL, 1.20 mmol, 1.0 equiv). The reaction mixture was stirred 45 °C for 5 h. The reaction mixture was diluted in brine and extracted with EtOAc. The organic layers were dried over Na_2SO_4, concentrated, and purified by silica gel column chromatography (3:17 v/v EtOAc/Hexanes to 1:4 v/v EtOAc/Hexanes) to afford the product as a clear oil (370 mg, 0.84 mmol, 70% yield). R_f = 0.28 (1:9 v/v EtOAc/Hexanes). ^{1}H NMR (500 MHz, CD_2Cl_2) δ 8.72 (s, 1H), 7.60 (d, *J* = 8.55, 1H), 7.33 (m, 4 h), 7.19 (s, 1H), 6.91 (d, *J* = 8.63, 1H), 6.09 (ddt, *J* = 16.53, 10.83, 5.43, 1H), 5.40 (d, *J* = 13.94, 1H), 5.36 (d, *J* = 13.94, 1H), 4.88 (dd, *J* = 12.65, 6.01, 1H), 4.72 (dd, *J* = 12.65, 6.01), 4.68 (d, *J* = 5.42, 2H), 4.23 (p, *J* =

6.82, 1H), 3.41 (m, 2H), 3.36 (ddd, *J* = 17.63, 7.69, 1.59), 1.57 (s, 9H). ^{13}C NMR (125 MHz, CD_2Cl_2) δ 196.00, 152.96, 150.96, 140.25, 132.78, 130.20, 129.37, 128.97, 128.10, 123.66, 119.011, 118.22, 118.02, 111.20, 81.16, 80.20, 70.22, 41.82, 40.01, 28.57.

***tert*-Butyl (Z)-(2-(allyloxy)-5-(5-((5-(4-methoxyphenyl)-3-phenyl-2H-pyrrol-2-ylidene)amino)-4-phenyl-1H-pyrrol-2-yl)phenyl)carbamate (3.24):** A suspension of **3.23** (207 mg, 0.47 mmol, 1.0 equiv) and **3.2** (281 mg, 0.94 mmol, 2.0 equiv) in *n*-butanol (9 mL) was heated to 70 °C until the solids were dissolved. NH_4OAc (543 mg, 7.05 mmol, 15 equiv) was added in one portion and the reaction mixture stirred at 120 °C for 5 h. Then, the reaction was cooled, concentrated via rotary evaporation, and taken up in CH_2Cl_2. The organic layer was washed with brine (5×), dried, concentrated, and purified by silica gel column chromatography (1:1 v/v CH_2Cl_2/Hexanes) to obtain a blue solid with a reddish shine (81.5 mg, 0.125 mmol, 27% yield). R_f = 0.71 (8:2 v/v CH_2Cl_2/Hexanes). ^{1}H NMR (500 MHz, $CDCl_3$) δ 8.05 (ddd, *J* = 8.3, 3.3, 1.3 Hz, 4H), 7.94 (d, *J* = 8.8 Hz, 2H), 7.50 (dd, *J* = 8.5, 2.2 Hz, 1H), 7.41 (td, *J* = 7.6, 2.5 Hz, 4H), 7.34 (ddd, *J* = 7.2, 4.4, 1.7 Hz, 2H), 7.17 (s, 1H), 7.14 (d, *J* = 2.3 Hz, 2H), 7.03 (d, *J* = 8.8 Hz, 2H), 6.92 (d, *J* = 8.5 Hz, 1H), 6.10 (ddt, *J* = 17.3, 10.6, 5.4 Hz, 1H), 5.44 (dq, *J* = 17.2, 1.5 Hz, 1H), 5.37 (dt, *J* = 10.5, 1.4 Hz, 1H), 4.66 (dt, *J* = 5.4, 1.5 Hz, 2H), 3.86 (s, 3H), 1.59 (s, 9H). ^{13}C NMR (125 MHz, $CDCl_3$) δ161.37, 155.69, 153.52, 152.61, 150.22, 148.53, 147.92, 142.65, 141.38, 134.16, 134.08, 132.69, 129.23, 129.21, 129.17, 128.52, 128.28, 128.24, 127.86, 127.73, 125.68, 125.22, 120.95, 118.64, 115.97, 115.02, 114.80, 114.49, 111.67, 80.59, 69.81, 55.57, 28.59.

2-(Allyloxy)-5-(5,5-difluoro-7-(4-methoxyphenyl)-1,9-diphenyl-5H-5l4,6l4-dipyrrolo[1,2-c:2',1'-f][1,3,5,2]triazaborinin-3-yl)aniline (3.25): A solution of **3.24** (48.5 mg, 0.075 mmol, 1.0 equiv) and *N,N*-diisopropylethylamine (0.195 mL, 1.12 mmol, 15 equiv) in anhydrous

CH_2Cl_2 was treated with boron trifluoride diethyl etherate (0.142 mL, 1.12 mmol, 15 equiv). The reaction mixture was stirred under a nitrogen atmosphere at room temperature for 1 h. Upon consumption of **3.24,** as judged by TLC (2:1 v/v CH_2Cl_2/Hexanes), the reaction mixture was diluted in CH_2Cl_2 and washed with sat. $NaHCO_3$. The organic layer was dried over Na_2SO_4, concentrated, and purified by silica gel column chromatography (2:1 v/v CH_2Cl_2/toluene) to afford the product as a blue-green solid (17 mg, 0.028 mmol, 38% yield). R_f = 0.35 (8:2 v/v CH_2Cl_2/Hexanes). ^{1}H NMR (500 MHz, $CDCl_3$) δ 7.98 (ddd, *J* = 8.2, 2.8, 1.3 Hz, 4H), 7.83 (d, *J* = 8.9 Hz, 2H), 7.34 (td, *J* = 7.6, 1.6 Hz, 4H), 7.27 (dd, *J* = 7.3, 1.6 Hz, 2H), 7.24 (tt, *J* = 4.1, 2.0 Hz, 2H), 7.06 (s, 1H), 7.01 (s, 1H), 6.97 (d, *J* = 8.8 Hz, 2H), 6.84 (d, *J* = 8.9 Hz, 1H), 6.05 (ddt, *J* = 17.3, 10.6, 5.3 Hz, 1H), 5.39 (dq, *J* = 17.3, 1.6 Hz, 1H), 5.28 (dq, *J* = 10.5, 1.4 Hz, 1H), 4.60 (dt, *J* = 5.4, 1.5 Hz, 2H), 3.83 (s, 3H). ^{13}C NMR (125 MHz, $CDCl_3$) δ 161.40, 154.90, 154.07, 149.97, 148.92, 148.30, 142.44, 141.81, 137.10, 134.12, 134.09, 133.11, 129.17, 129.15, 128.33, 127.91, 127.87, 125.58, 125.40, 118.15, 117.87, 114.75, 114.65, 114.27, 112.81, 112.09, 69.49, 55.66, 29.86. ^{19}F NMR (471 MHz, $CDCl_3$) δ -131.69 (dd, *J* = 63.7, 31.6 Hz).

APNO-3. To a round bottom flask was added **3.25** (17 mg, 28.0 μmol, 1.0 equiv), 1,3-dimethylbarbituric acid (6.6 mg, 43.0 μmol, 1.5 equiv), and $Pd(PPh_3)_4$ (3.3 mg, 3 μmol, 0.1 equiv) under nitrogen, followed by anhydrous CH_2Cl_2 (3 mL). The reaction mixture was stirred at room temperature for 11 h. Upon consumption of **31** as judged by TLC, the reaction mixture was diluted in CH_2Cl_2 and washed with brine and sat. $NaHCO_3$. The organic layers were dried over Na_2SO_4, concentrated, and purified by silica gel column chromatography (1:99 v/v MeOH/ CH_2Cl_2) to afford the product as a green solid (7.9 mg, 0.014 mmol, 50% yield). R_f = 0.21 (1:1 v/v CH_2Cl_2/Hexanes). ^{1}H NMR (500 MHz, $CDCl_3$) δ 8.12 – 7.99 (m, 6H), 7.53 (s, 1H), 7.49 – 7.36 (m, 7H), 7.05 – 6.95 (m, 4H), 6.77 (d, *J* = 8.1 Hz, 1H), 3.87 (s, 3H). ^{11}B NMR (161 MHz,

$CDCl_3$) 1.05 (t, J = 32.00). ^{19}F NMR (471 MHz, $CDCl_3$) δ -131.49 (dd, J = 63.04, 32). HR-MS (ESI, TOF) calc'd $[M+H]^+$ 559.2117, found 559.2112.

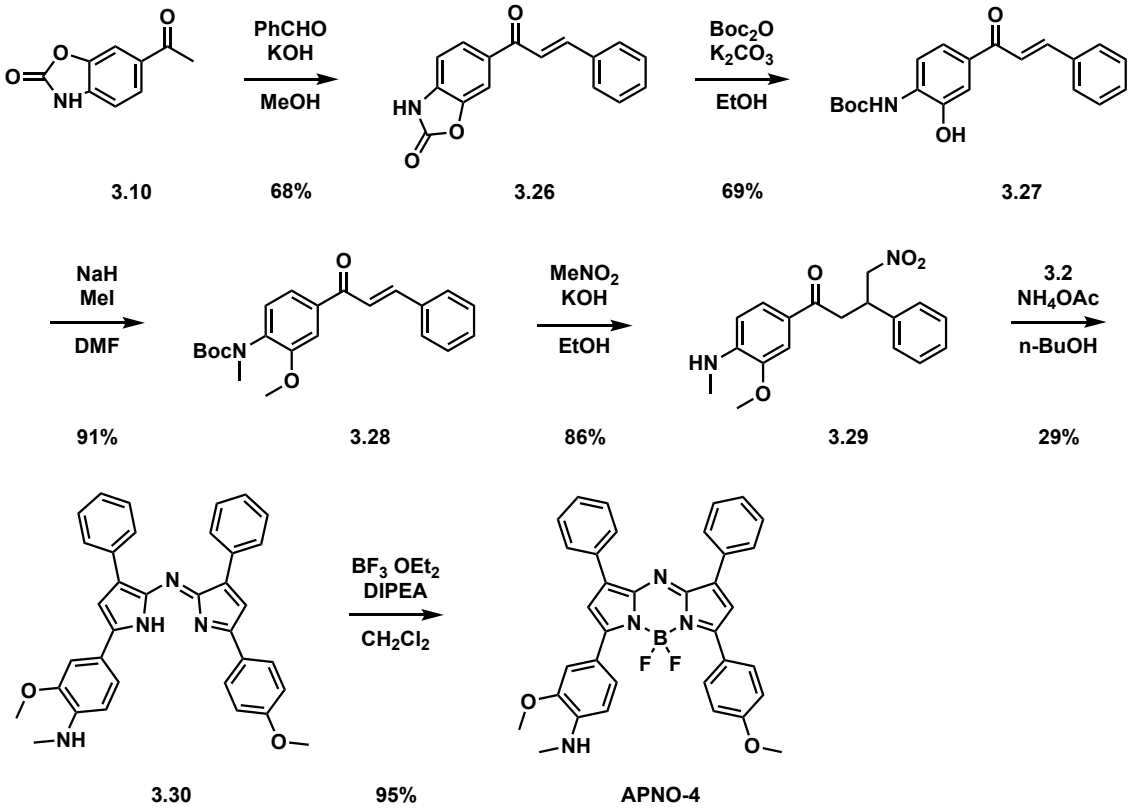

Scheme C.5: Synthesis of **APNO-4**.

6-Cinnamoylbenzo[d]oxazol-2(3H)-one (3.26): A solution of **3.10** (8.0 g, 45.3 mmol, 1 equiv) and benzaldehyde (4.8 g, 45.3 mmol. 1 equiv) in EtOH (100 mL) was treated with dropwise addition of a 10 M solution of aq. KOH (13.6 mL, 136.0 mmol, 3 equiv). The reaction was allowed to stir at room temperature for 4 h. The slurry was concentrated to an orange solid and recrystallized in EtOH to yield the product as a yellow solid (8.3 g, 48.4 mmol, 68% yield). R_f = 0.48 (2:1:7 v/v Acetone/MeOH/Hexanes). ^1H NMR (400 MHz, DMSO-d_6) δ 12.11 (s, 1H), 8.10 (d, J = 1.4 Hz, 1H), 8.06 (dd, J = 8.2, 1.6 Hz, 1H), 7.98 (d, J = 15.6 Hz, 1H), 7.89 (dd, J = 6.7, 2.9 Hz, 2H), 7.73 (d, J = 15.5 Hz, 1H), 7.45 (m, 3H), 7.23 (d, J = 8.1 Hz, 1H). ^{13}C NMR (100 MHz, DMSO-d_6) δ 187.30, 154.49, 143.78, 143.50, 134.98, 134.76, 131.85, 130.58, 128.93,

128.91, 125.78, 125.74, 121.77, 109.60, 109.56, 109.54.

***tert*-Butyl (4-cinnamoyl-2-hydroxyphenyl) carbamate (3.27):** A suspension of **3.26** (0.9 g, 3.4 mmol, 1 equiv), K_2CO_3 (1.4 g, 10 mmol, 3 equiv), and di-*tert*-butyl dicarbonate (1.5 g, 7 mmol, 2 equiv) in MeOH (16 mL) was stirred at 45 °C for 3 h. The reaction was diluted with sat. $NaHCO_3$ and extracted with EtOAc (3×). The combined organic layers were dried over Na_2SO_4, concentrated, and purified via silica gel column chromatography (3:7 v/v EtOAc/Hexanes) to afford the product as a yellow solid (0.8 g, 2.3 mmol, 69% yield). R_f = 0.44 (3:7 v/v EtOAc/Hexanes). ^{1}H NMR (500 MHz, $CDCl_3$) δ 8.51 (bs, 1H), 7.93 – 7.88 (m, 2H), 7.81 (d, *J* = 15.6 Hz, 1H), 7.67 – 7.59 (m, 3H), 7.56 (d, *J* = 15.7 Hz, 1H), 7.43 – 7.39 (m, 3H), 7.30 (s, 1H), 1.55 (s, 9H). ^{13}C NMR (125 MHz, $CDCl_3$) δ189.94, 153.28, 145.71, 145.04, 134.97, 132.88, 132.26, 130.76, 129.09, 128.70, 122.66, 121.71, 118.18, 116.10, 81.77, 28.42.

***tert*-Butyl (4-cinnamoyl-2-methoxyphenyl)(methyl) carbamate (3.28):** A 38 mL pressure flask under nitrogen was charged with **3.27** (0.6 g, 1.8 mmol, 1 equiv), anhydrous DMF (8 mL), MeI (1.2 g, 8.8 mmol, 5 equiv), and NaH (60 % w/w, 2 g, 5.5 mmol, 3 equiv) at 0 °C. The reaction was allowed to warm to room temperature and was stirred for 1 h. The reaction was then heated to 70 °C for 3 h. The reaction was quenched with water and extracted with EtOAc (3×). The organic layers were combined, concentrated, and purified via silica gel column chromatography (3:17 v/v EtOAc/Hexanes) to afford the product as a yellow solid (5.9 g, 1.6 mmol, 91% yield). R_f = 0.24 (1:9 v/v EtOAc/Hexanes). ^{1}H NMR (500 MHz, $CDCl_3$) δ 7.85 (d, J = 15.7 Hz, 1H), 7.70 – 7.63 (m, 4H), 7.58 (d, J = 15.6 Hz, 1H), 7.43 (qd, J = 3.8, 1.7 Hz, 3H), 7.32 (d, J = 8.4 Hz, 1H), 3.94 (s, 3H), 3.21 (s, 3H), 1.45 (s, 9H). ^{13}C NMR (125 MHz, $CDCl_3$) δ 189.15, 155.05, 154.77, 144.64, 137.50, 136.91, 134.71, 130.45, 128.84, 128.36, 128.32, 121.65, 121.20, 111.14, 79.86, 55.50, 36.65, 28.13.

1-(3-Methoxy-4-(methylamino)phenyl)-4-nitro-3-phenylbutan-1-one (3.29): A solution of **3.28** (0.53 g, 1.4 mmol, 1 equiv) and nitromethane (0.87 g, 14 mmol, 10 equiv) in EtOH (3 mL) was treated with a 1 M solution of aq. KOH (0.29 mL, 0.2 equiv). The reaction was stirred at 60 °C for 7 h. The reaction was diluted with brine, extracted with EtOAc (3×), and concentrated. The crude intermediate was dissolved in CH_2Cl_2 (8 mL) and cooled to 0 °C in an ice bath. Trifluoroacetic acid (2 mL) was added dropwise and the reaction was allowed to stir at room temperature for 3 h. The reaction was quenched with sat. $NaHCO_3$ and extracted with CH_2Cl_2 (3×). The combined organic fractions were dried over Na_2SO_4, concentrated, and purified via silica gel column chromatography (3:7 v/v EtOAc/Hexanes) to afford the product as a brown solid (0.40 g, 1.2 mmol, 86% yield). R_f = 0.47 (3:7 v/v EtOAc/Hexanes). ^{1}H NMR (500 MHz, $CDCl_3$) δ 7.45 (dd, *J* = 8.3, 1.9 Hz, 1H), 7.28 (d, *J* = 1.9 Hz, 1H), 7.27 – 7.16 (m, 6H), 6.40 (d, *J* = 8.3 Hz, 1H), 4.82 (s, 1H), 4.78 (dd, *J* = 12.5, 6.3 Hz, 1H), 4.60 (dd, *J* = 12.5, 8.5 Hz, 1H), 4.13 (tt, *J* = 8.3, 6.1 Hz, 1H), 3.79 (s, 3H), 3.30 (dd, *J* = 16.9, 6.2 Hz, 1H), 3.23 (dd, *J* = 16.9, 8.0 Hz, 1H), 2.85 (s, 3H). ^{13}C NMR (125 MHz, $CDCl_3$) δ194.87, 146.29, 144.41, 139.75, 129.11, 127.81, 127.60, 124.86, 124.62, 107.80, 106.78, 79.88, 55.69, 40.82, 40.00, 29.81.

1-(3-Methoxy-4-(methylamino)phenyl)-4-nitro-3-phenylbutan-1-one (3.30): A suspension of **3.29** (0.211 g, 0.641 mmol, 1 equiv) and **3.2** (0.387 g, 1.29 mmol, 2 equiv) in *n*-butanol (15 mL) was heated to 110 °C until all of the solids dissolved. NH_4OAc (0.749 g, 9.71 mmol, 15 equiv) was added to the reaction in one portion. The reaction was stirred at 110 °C for 4 h. After complete, the solution was concentered as an azeotrope with toluene to afford a blue-green solid. The crude residue was diluted with brine and extracted with CH_2Cl_2 (3×). The combined organic fractions were dried over Na_2SO_4 and purified via silica gel column chromatography (13:7 v/v CH_2Cl_2/Hexanes). The fractions containing product were collected, precipitated from

CH_2Cl_2/Hexanes at 0 °C (3×), filtered, and collected. The filtrate was re-purified via silica gel column chromatography (3:7 v/v EtOAc/Hexanes) to afford the product as a dark red solid (0.196 g, 0.184 mmol, 29% yield). R_f = 0.39 (3:7 v/v EtOAc/Hexanes). ^{1}H NMR (500 MHz, DMSO-d_6) δ 12.84 (s, 1H), 8.12 (dd, *J* = 16.9, 7.6 Hz, 4H), 7.89 – 7.78 (m, 4H), 7.68 (d, *J* = 1.8 Hz, 1H), 7.52 – 7.38 (m, 5H), 7.35 – 7.29 (m, 2H), 7.07 (d, *J* = 8.4 Hz, 2H), 6.69 (d, *J* = 8.3 Hz, 1H), 6.41 (q, *J* = 5.1 Hz, 1H), 4.07 (s, 3H), 3.86 (s, 3H), 2.88 (d, *J* = 4.9 Hz, 3H). ^{13}C NMR (125 MHz, DMSO-d_6) δ 165.90, 159.80, 157.31, 146.55, 145.46, 143.80, 140.84, 140.62, 134.20, 133.46, 133.15, 128.72, 128.28, 128.23, 128.10, 127.07, 126.40, 125.04, 123.59, 121.37, 118.81, 117.04, 114.75, 108.86, 108.17, 107.09, 55.40, 55.18, 29.37.

APNO-4. Boron trifluoride diethyl etherate (0.15 mL, 1.2 mmol, 15 equiv) was added to a solution of **3.30** (0.043 g, 0.079 mmol, 1 equiv) and *N,N*-diisopropylethylamine (0.21 mL, 1.2 mmol, 15 equiv) in anhydrous CH_2Cl_2 (3.2 mL). The reaction was stirred at room temperature for 14 h under a nitrogen atmosphere, quenched with sat. $NaHCO_3$, and extracted with CH_2Cl_2 (3×). The combined organic layers were dried over Na_2SO_4, concentrated, and purified by silica gel column chromatography (step gradient, 3:7 v/v EtOAc/Hexanes then 13:7 v/v CH_2Cl_2/Hexanes) to afford the product as a red solid (0.044 g, 0.075 mmol, 95% yield). R_f = 0.22 (1:1 v/v CH_2Cl_2/Hexanes). ^{1}H NMR (500 MHz, DMSO-d_6) δ 8.23 (d, *J* = 8.7 Hz, 2H), 8.15 (d, *J* = 8.8 Hz, 1H), 8.12 (d, *J* = 7.7 Hz, 2H), 8.08 (d, *J* = 8.7 Hz, 2H), 8.04 (s, 1H), 7.98 – 7.95 (m, 1H), 7.55 (t, *J* = 7.5 Hz, 2H), 7.52 – 7.45 (m, 3H), 7.38 (t, *J* = 7.4 Hz, 1H), 7.26 (s, 1H), 7.20 – 7.14 (m, 1H), 7.07 (d, *J* = 8.5 Hz, 2H), 6.74 (d, *J* = 8.8 Hz, 1H), 3.94 (s, 3H), 3.86 (s, 3H), 2.93 (d, *J* = 5.1 Hz, 3H). ^{13}C NMR (125 MHz, DMSO-d_6) δ 160.70, 160.22, 149.36, 147.20, 146.51, 145.87, 142.52, 141.96, 135.88, 133.62, 132.09, 130.97, 130.93, 130.89, 130.03, 129.54, 129.04, 128.97, 128.89, 128.52, 125.32, 122.62, 116.45, 116.41, 114.40, 109.49, 56.07, 55.83, 29.79. ^{11}B

NMR (161 MHz, DMSO-d_6) δ 1.40 (t, J = 34.5 Hz). ^{19}F NMR (471 MHz, DMSO-d_6) δ -130.04 (dd, J = 67.0, 30.6 Hz). HR-MS (ESI, TOF) calc'd for $[M+H]^+$ 587.2430, found 587.2440.

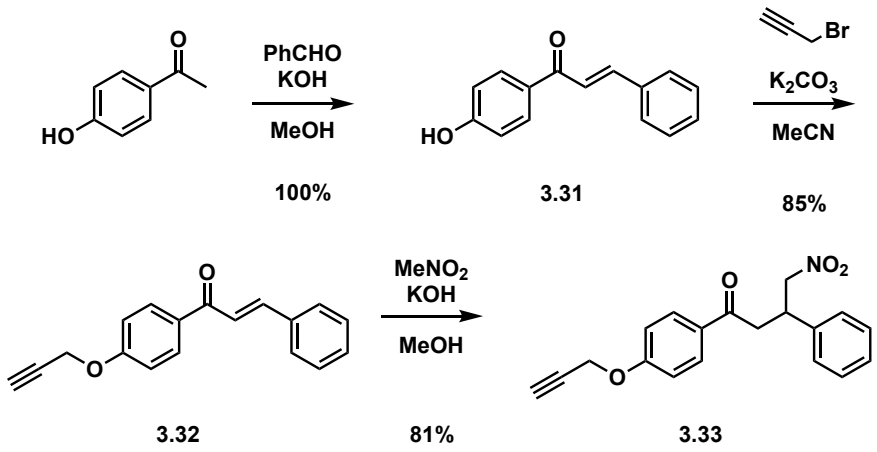

Scheme C.6: Synthesis of compound **3.33**.

(E)-1-(4-Hydroxyphenyl)-3-phenylprop-2-en-1-one (3.31): A solution of 1-(4-hydroxyphenyl)ethan-1-one (10.0 g, 73.8 mmol, 1 equiv) and benzaldehyde (7.8 g, 73.8 mmol, 1 equiv) in EtOH (140 mL) was cooled to 0 °C in an ice bath and treated with dropwise addition of a 10 M aq. solution of KOH (22.1 mL, 221 mmol, 3 equiv). The reaction was stirred at room temperature for 24 h. The reaction was quenched with conc. HCl to a pH of approximately 1. The mixture was stirred at 0 °C for 30 min then filtered to afford the product as a light yellow solid (18.7g, 73.8 mmol, 100% yield). R_f = 0.39 (3:7 v/v EtOAc/Hexanes). ^{1}H NMR (500 MHz, DMSO-d_6) δ 10.54 (s, 1H), 8.07 (d, J = 8.4 Hz, 2H), 7.92 (d, J = 15.6 Hz, 1H), 7.88 – 7.84 (m, 2H), 7.68 (d, J = 15.6 Hz, 1H), 7.48 – 7.38 (m, 3H), 6.92 (d, J = 8.4 Hz, 2H). ^{13}C NMR (125 MHz, DMSO-d_6) δ 187.12, 162.31, 142.70, 134.89, 131.18, 130.32, 129.03, 128.89, 128.72, 122.12, 115.42.

(E)-3-Phenyl-1-(4-(prop-2-yn-1-yloxy)phenyl)prop-2-en-1-one (3.32): A flame-dried round bottom flask was charged with **3.31** (3.1 g, 13.7 mmol, 1 equiv), K_2CO_3 (2.4 g, 17.1 mmol, 1.25 equiv), and DMF (30 mL) under nitrogen. Propargyl bromide (3.2 mL, 17.2 mmol, 1.25 equiv)

was added and the reaction was stirred at room temperature for 24 h. The reaction was quenched in sat. $NaHCO_3$, extracted with EtOAc, and washed with sat. $NaHCO_3$ (3×). The combined organic layers were collected, dried over Na_2SO_4, concentrated, and purified via silica gel column chromatography (gradient from 1:9 v/v EtOAc/Hexanes to 1:3 v/v EtOAc/Hexanes) to afford the product as a white solid (3.0 g, 11.7 mmol, 85% yield). R_f = 0.24 (1:9 v/v EtOAc/Hexanes). ^{1}H NMR (500 MHz, $CDCl_3$) δ 8.10 – 8.01 (m, 2H), 7.81 (d, *J* = 15.7 Hz, 1H), 7.67 – 7.61 (m, 2H), 7.54 (d, *J* = 15.7 Hz, 1H), 7.46 – 7.39 (m, 3H), 7.13 – 7.04 (m, 2H), 4.78 (d, *J* = 2.4 Hz, 2H), 2.57 (t, *J* = 2.4 Hz, 1H). ^{13}C NMR (125 MHz, $CDCl_3$) δ 188.84, 161.32, 144.31, 135.15, 131.98, 130.85, 130.52, 129.06, 128.50, 121.94, 114.85, 77.93, 77.91, 76.34, 76.28, 56.00.

4-Nitro-3-phenyl-1-(4-(prop-2-yn-1-yloxy)phenyl)butan-1-one (3.33): A mixture of **3.32** (1.18 g, 4.5 mmol, 1 equiv) and nitromethane (3.6 mL, 66.8 mmol, 15 equiv) in EtOH (9.0 mL) was dropwise treated with 10 M aq. solution of KOH (0.090 mL, 0.2 equiv). The resulting mixture was stirred at room temperature for 24 h. After complete, the reaction was quenched with sat. $NaHCO_3$ and extracted with EtOAc (3×). The organic fraction was washed with sat. $NaHCO_3$ (3×), concentrated, and purified via silica gel column chromatography (1:3 v/v EtOAc/Hexanes) to afford an off-white solid (1.18 g, 3.63 mmol, 81% yield). R_f = 0.39 (3:7 v/v EtOAc/Hexanes). ^{1}H NMR (500 MHz, $CDCl_3$) δ 7.97 – 7.91 (m, 2H), 7.39 – 7.33 (m, 2H), 7.32 – 7.27 (m, 3H), 7.06 – 7.00 (m, 2H), 4.86 (dd, *J* = 12.5, 6.5 Hz, 1H), 4.78 (d, *J* = 2.4 Hz, 2H), 4.71 (dd, *J* = 12.5, 8.1 Hz, 1H), 4.24 (tt, *J* = 7.9, 6.4 Hz, 1H), 3.45 (dd, *J* = 17.5, 6.4 Hz, 1H), 3.39 (dd, *J* = 17.5, 7.6 Hz, 1H), 2.58 (t, *J* = 2.4 Hz, 1H). ^{13}C NMR (125 MHz, $CDCl_3$) δ 195.41, 161.73, 139.35, 130.40, 130.31, 129.18, 127.96, 127.57, 114.89, 79.73, 77.74, 76.41, 56.01, 41.34, 39.52.

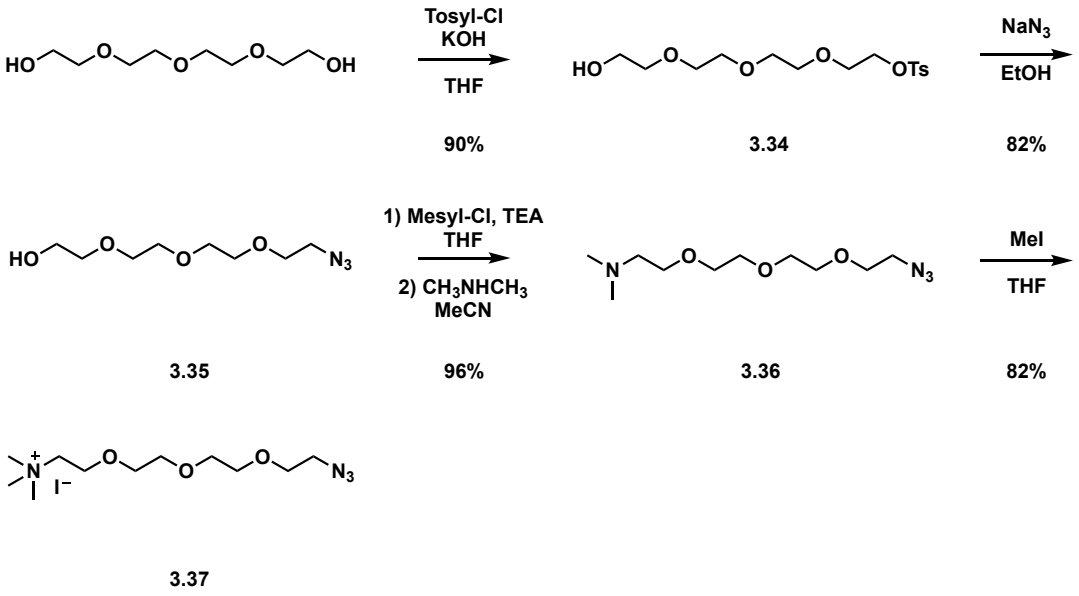

Scheme C.7: Synthesis of compound **3.37**.

[2-(2-(2-(2-hydroxyethoxy)ethoxy)ethoxy)ethyl 4-methylbenzenesulfonate] (3.34): The product was synthesized according to previously reported protocols.[7] Briefly, tetraethyleneglycol (8.67 g, 44.6 mmol, 8.4 equiv) was dissolved in THF (2.1 mL) followed by the addition of a 4 M aq. solution of sodium hydroxide (2.13 mL, 8.52 mmol, 1.6 equiv). The reaction was cooled to 0 °C and tosyl chloride (1.01 g, 5.31 mmol, 1 equiv) in THF (6 mL) was added dropwise. The reaction was allowed to stir for 3 h at the same temperature. The product was extracted with CH_2Cl_2 (3×) from cold water. The combined organic fractions were washed with water (2×) and dried over Na_2SO_4. The organic fractions were concentrated to afford a clear oil (1.66 g, 4.76 mmol, 90% yield), which was used without further purification. R_f = 0.25 (3:97 v/v MeOH/CH_2Cl_2).

[2-(2-(2-(2-azidoethoxy)ethoxy)ethoxy)ethan-1-ol] (3.35). The product was synthesized according to previously reported protocols.[7] Briefly, a solution of **3.34** (3.96 g, 11.38 mmol, 1 equiv) and sodium azide (1.85g, 28.5 mmol, 2.5 equiv) in EtOH (45 mL) was refluxed at 80 °C under a nitrogen atmosphere for 14 h. The reaction was cooled to room temperature, diluted with

water, and volatiles were removed. The product was extracted with EtOAc (3×) from the water. The organic fractions were dried over Na_2SO_4 and concentrated to afford a yellow oil (2.05 g, 9.36 mmol, 82% yield), which was used without further purification. R_f (1:9 v/v MeOH/$CHCl_3$) 0.70. ^{1}H NMR (500 MHz, $CDCl_3$) δ 3.73 (dd, *J* = 5.3, 3.7 Hz, 2H), 3.67 (d, *J* = 1.5 Hz, 10H), 3.63 – 3.59 (m, 2H), 3.40 (t, *J* = 5.1 Hz, 2H). ^{13}C NMR (125 MHz, $CDCl_3$) δ 72.63, 70.81, 70.78, 70.70, 70.44, 70.16, 61.87, 50.80.

[2-(2-(2-(2-azidoethoxy)ethoxy)ethoxy)-N,N-dimethylethan-1-amine] (3.36). A solution of **3.35** (0.75 g, 3.42 mmol, 1 equiv), and triethylamine (1.4 mL, 10.3 mmol, 3 equiv) in anhydrous THF (17.1 mL) was cooled to 0 °C in an ice bath. Methanesulfonyl chloride (Mesyl-Cl, 0.54 mL, 2 equiv) was added dropwise under a nitrogen atmosphere and stirred at 0 °C for 1 h. 40 % w/w aq. dimethylamine (4.3 mL, 34.2 mmol, 10 equiv) was added dropwise and stirred for an additional 24 h at room temperature. The product was purified by silica gel column chromatography (1:4 v/v MeOH/$CHCl_3$) to afford a brown oil (0.807 g, 3.28 mmol, 96% yield). R_f (1:4 v/v MeOH/$CHCl_3$) 0.52. ^{1}H NMR (500 MHz, DMSO-d_6) δ 3.61 – 3.59 (m, 2H), 3.58 – 3.45 (m, 10H), 3.39 (dd, *J* = 5.6, 4.4 Hz, 2H), 2.41 – 2.37 (m, 2H), 2.15 (s, 6H). ^{13}C NMR (125 MHz, DMSO-d_6) δ 69.81, 69.80, 69.70, 69.64, 69.62, 69.25, 68.60, 58.29, 49.99, 45.53.

[2-(2-(2-(2-azidoethoxy)ethoxy)ethoxy)-N,N,N-trimethylethan-1-aminium iodide] (3.37) - A pressure vial was charged with **3.36** (0.51 g, 2 mmol, 1 equiv), anhydrous acetonitrile (4 mL), and MeI (0.64 mL, 10.2 mmol, 5 equiv) under nitrogen. The reaction was heated to 60 °C for 72 h. When complete according to TLC, the product was loaded onto celite and purified by silica gel chromatography (1:4 v/v MeOH/$CHCl_3$) to afford a pale yellow solid (0.81 g, 1.7 mmol, 82% yield). R_f (1:4 v/v MeOH/$CHCl_3$) 0.40. ^{1}H NMR (500 MHz, CD_3CN) δ 3.88 (m, 2H), 3.65 – 3.57 (m, 10H), 3.54 – 3.51 (m, 2H), 3.37 (t, J = 4.9 Hz, 2H), 3.15 (s, 9H). ^{13}C NMR (125 MHz,

CD_3CN) δ 71.08, 71.05, 70.96, 70.78, 70.42, 66.50, 66.48, 66.45, 65.41, 55.01, 54.97, 54.94, 51.44.

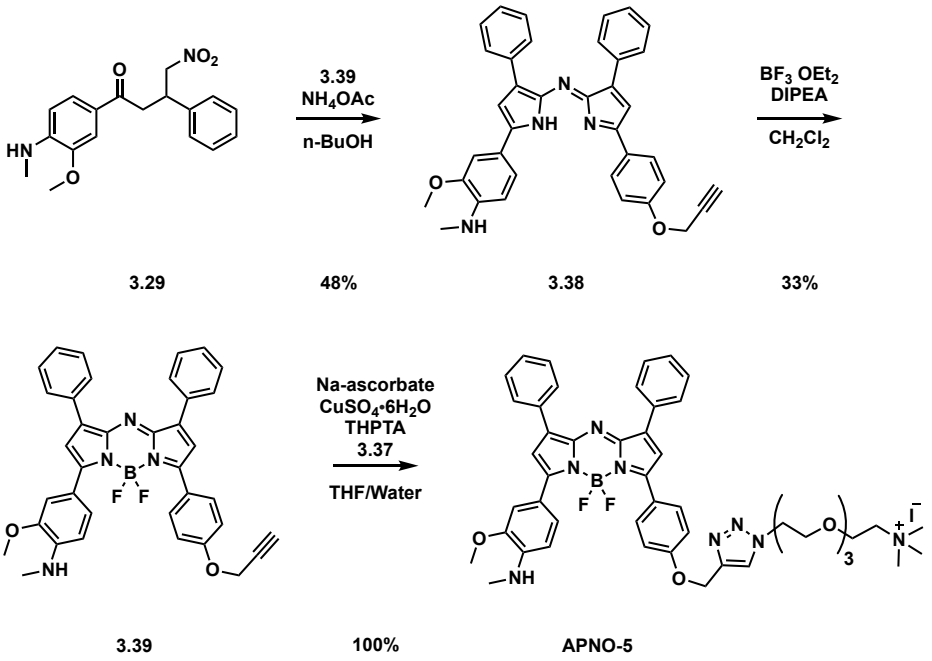

Scheme C.8: Synthesis of **APNO-5.**

(Z)-2-Methoxy-N-methyl-4-(4-phenyl-5-((3-phenyl-5-(4-(prop-2-yn-1-yloxy)phenyl)-2H-pyrrol-2-ylidene)amino)-1H-pyrrol-2-yl)aniline (3.38): A suspension of **3.29** (0.40 g, 1.2 mmol, 1 equiv) and **3.33** (0.80 g, 2.5 mmol, 2 equiv) in *n*-butanol (25 mL) was heated to 110 °C to dissolve all solids. NH_4OAc (1.4 g, 19 mmol, 15 equiv) was added in one portion and the reaction stirred at the same temperature for 5 h. The reaction was azeotroped with PhMe and dried to a blue-green solid. The product was extracted from brine with CH_2Cl_2 (3×). The combined organic fractions were dried over Na_2SO_4 and purified twice via silica gel column chromatography (3:7 v/v EtOAc/Hexanes then 4:1 CH_2Cl_2/Hexanes) to afford the product as a dark green solid (340 mg, 0.60 mmol, 48% yield). R_f = 0.50 (3:7 v/v EtOAc/Hexanes). ^{1}H NMR (500 MHz, $CDCl_3$) δ 8.07 – 8.03 (m, 4H), 7.67 – 7.63 (m, 2H), 7.52 – 7.48 (m, 2H), 7.43 – 7.33 (m, 5H), 7.32 – 7.27 (m, 1H), 7.24 (s, 1H), 6.91 (d, *J* = 2.0 Hz, 1H), 6.89 (s, 1H), 6.54 (d, *J* = 8.1

Hz, 1H), 4.66 (d, *J* = 2.5 Hz, 2H), 3.93 (s, 3H), 2.90 (s, 3H), 2.56 (t, *J* = 2.4 Hz, 1H). ^{13}C NMR (125 MHz, $CDCl_3$) 165.10, 157.81, 157.16, 146.83, 146.36, 142.93, 142.52, 141.97, 135.43, 134.75, 133.79, 129.30, 128.78, 128.26, 128.22, 128.12, 128.12, 127.09, 126.44, 125.66, 124.00, 120.73, 119.45, 115.39, 108.94, 108.27, 106.90, 78.46, 75.98, 55.98, 55.30, 29.91.

4-(5,5-Difluoro-1,9-diphenyl-7-(4-(prop-2-yn-1-yloxy)phenyl)-5H-5l4,6l4-dipyrrolo[1,2-c:2',1'-f][1,3,5,2]triazaborinin-3-yl)-2-methoxy-*N*-methylaniline (3.39): A solution of **7** (0.077 g, 0.14 mmol, 1 equiv) and *N*,*N*-diisopropylethylamine (0.36 mL, 2.1 mmol, 15 equiv) in anhydrous CH_2Cl_2 (5.5 mL) was cooled to 0 °C in an ice bath and treated portion-wise with boron trifluoride diethyl etherate (0.18 mL × 3, 4.3 mmol, 45 equiv) over 24 h. After each addition, the reaction was allowed to warm to room temperature. When complete, the reaction was diluted with sat. $NaHCO_3$ and extracted with CH_2Cl_2 (3×). The combined organic fractions were dried over Na_2SO_4, concentrated, and purified via silica gel column chromatography (3:7 v/v EtOAc/Hexanes) to afford the product as a dark purple solid (0.027 g, 0.045 mmol, 33% yield). R_f = 0.29 (3:7 v/v EtOAc/Hexanes). ^{1}H NMR (500 MHz, $CDCl_3$) δ 8.11 - 8.03 (m, 7H), 7.96 (s, 1H), 7.78 (dd, *J* = 8.6, 2.0 Hz, 1H), 7.49 – 7.39 (m, 6H), 7.36 (t, *J* = 7.3 Hz, 1H), 7.07 – 7.02 (m, 2H), 6.93 (s, 1H), 6.64 – 6.57 (m, 1H), 4.76 (d, *J* = 2.4 Hz, 2H), 3.94 (s, 3H), 2.97 (s, 3H), 2.57 (q, *J* = 2.6 Hz, 1H). ^{13}C NMR (125 MHz, $CDCl_3$) δ 160.63, 158.78, 152.53, 147.06, 146.35, 143.84, 143.69, 143.52, 139.05, 133.54, 132.43, 131.07, 129.58, 129.44, 129.39, 129.08, 128.81, 128.77, 128.61, 128.55, 128.39, 127.42, 126.40, 120.09, 118.38, 116.69, 115.27, 114.76, 110.96, 108.45, 78.45, 75.96, 55.97, 55.78, 29.85. ^{11}B NMR (161 MHz, $CDCl_3$) δ 1.34 (t, *J* = 32.8 Hz). ^{19}F NMR (471 MHz, $CDCl_3$) δ -131.51 (dd, *J* = 66.0, 32.9 Hz).

APNO-5: Compound **3.39** (0.046 g, 0.076 mmol, 1 equiv), tris(3-hydroxypropyltriazolylmethyl)amine (0.007 g, 0.015, 0.2 equiv), **3.37** (0.099 g, 0.25 mmol, 3.5

equiv), and copper sulfate pentahydrate (0.095g, 0.38 mmol, 5 equiv), were dissolved in degassed THF (3.8 mL), then sodium ascorbate (0.023 g, 0.11 mmol, 1.5 equiv) in degassed water (0.8 mL) was added under nitrogen. The reaction was allowed to stir at room temperature for 3 h. When the reaction was complete, the product was extracted with 3:7 v/v MeOH/CH_2Cl_2 (3×) from sat. aq. NaI. The combined organic layers were dried over Na_2SO_4 and concentrated under reduced pressure. The crude residue was purified via preparatory TLC (1:9 v/v H_2O/MeCN). The product was recovered in 1:9 v/v MeOH/CH_2Cl_2 with sonication, filtered, and dried to afford the product as a red solid (0.077 g, 0.076 mmol, 100% yield). R_f = 0.55 (1:9 v/v H_2O/MeCN). ^{1}H NMR (500 MHz, DMSO-d_6) δ 8.26 (s, 1H), 8.25 – 8.22 (m, 2H), 8.16 (dd, J = 8.8, 2.0 Hz, 1H), 8.14 – 8.11 (m, 2H), 8.09 (d, J = 9.0 Hz, 2H), 8.06 (s, 1H), 7.99 – 7.96 (m, 1H), 7.56 (dd, J = 8.2, 6.6 Hz, 2H), 7.49 (td, J = 7.5, 5.7 Hz, 3H), 7.41 – 7.35 (m, 1H), 7.27 (s, 1H), 7.23 – 7.16 (m, 3H), 6.75 (d, J = 8.9 Hz, 1H), 5.27 (s, 2H), 4.57 (t, J = 5.2 Hz, 2H), 3.95 (s, 3H), 3.84 (t, J = 5.2 Hz, 2H), 3.82 – 3.77 (m, 2H), 3.58 – 3.51 (m, 5H), 3.50 – 3.48 (m, 5H), 3.06 (s, 9H), 2.94 (d, J = 5.2 Hz, 3H). ^{13}C NMR (125 MHz, DMSO-d_6) δ 159.42, 149.00, 147.30, 146.52, 145.96, 142.83, 142.61, 141.90, 135.72, 133.62, 132.04, 130.88, 130.19, 130.08, 129.55, 129.06, 128.99, 128.87, 128.53, 125.67, 125.49, 116.42, 116.35, 115.10, 109.53, 70.24, 70.04, 70.00, 69.88, 69.80, 69.14, 64.89, 64.49, 61.71, 56.10, 53.60, 53.57, 53.54, 49.93, 29.81. ^{11}B NMR (161 MHz, DMSO-d_6) δ 1.33 (t, J = 34.5 Hz). ^{19}F NMR (471 MHz, DMSO-d_6) δ -129.98 (dd, J = 67.0, 29.9 Hz). HR-MS (ESI, TOF) calc'd $[M]^+$ 902.4258, found 902.4345.

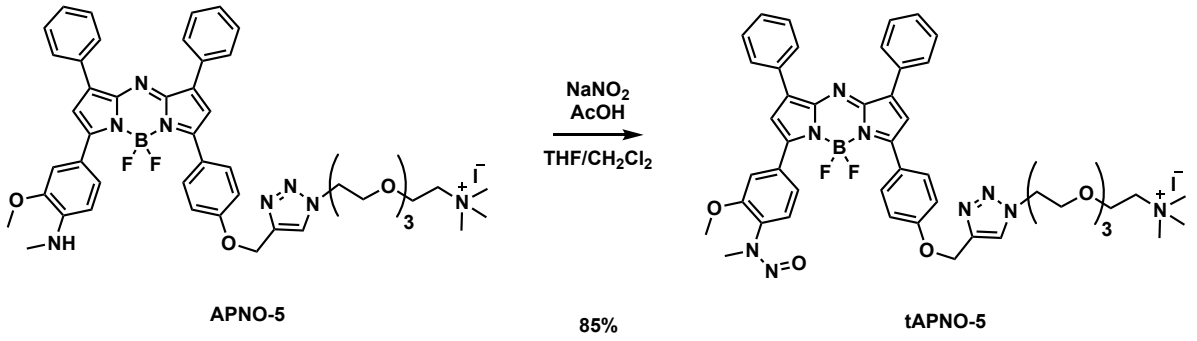

Scheme C.9: Synthesis of **tAPNO-5**.

tAPNO-5. To a solution of APNO-5 (15.6 mg, 15.6 μmol, 1 equiv) in THF (3.2 mL), acetic acid (0.4 mL), and CH_2Cl_2 (0.8 mL) at 0 °C was added sodium nitrite (5.6 mg, 81.5 μmol, 5.2 equiv) and the reaction was allowed to stir at the same temperature for 30 minutes. The reaction was warmed to room temperature, additional acetic acid (0.4 mL) and sodium nitrite (2.6 mg, 37.8 μmol, 2.4 equiv) were added and allowed to stir for 2.5 h. The reaction was diluted in CH_2Cl_2 and washed with sat. $NaHCO_3$. The organic layer was dried over Na_2SO_4 and concentrated to a green solid. The product was purified via alumina column chromatography (1:19 v/v MeOH/CH_2Cl_2) to afford a green solid (22.6 mg, 13.2 μmol, 85% yield). ^{1}H NMR (500 MHz, DMSO-d_6) δ 8.33 (d, J = 8.8 Hz, 2H), 8.27 (s, 1H), 8.22 (d, J = 7.5 Hz, 2H), 8.17 (d, J = 7.8 Hz, 2H), 7.93 (s, 1H), 7.87 (s, 1H), 7.83 (d, J = 8.3 Hz, 1H), 7.64 – 7.46 (m, 8H), 7.31 (d, J = 8.9 Hz, 2H), 5.33 (s, 2H), 4.56 (t, J = 5.2 Hz, 2H), 3.98 (s, 3H), 3.83 (t, J = 5.2 Hz, 2H), 3.80 (m, 2H), 3.53 (m, 4H), 3.50 – 3.46 (m, 6H), 3.36 (s, 3H), 3.07 (s, 9H). ^{19}F NMR (470 MHz, DMSO-d_6) δ -

130.14 (dd, J = 64.2, 31.4 Hz). HR-MS (ESI, TOF) calc'd for $[M]^+$ 900.8153, found 900.4191.

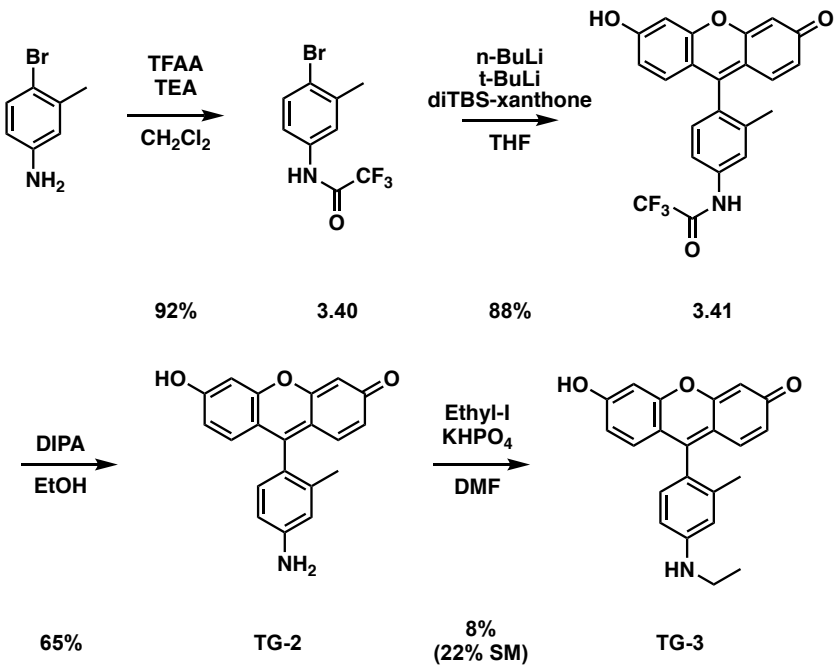

Scheme C.10: Synthesis of **TG-2** and **TG-3.**

N-(4-bromo-3-methylphenyl)-2,2,2-trifluoroacetamide (3.40): To a solution of 4-bromo-3-methylaniline (0.209 g, 1.12 mmol, 1 equiv) and TEA (0.31 mL, 2.27 mmol, 2 equiv) in anhydrous THF (6 mL) was added trifluoroacetic anhydride (dropwise, 0.19 mL, 2.83 mmol, 1.2 equiv) at room temperature. The reaction was allowed to stir at the same temperature for 0.5 h. The reaction was diluted with EtOAc, quenched with water, and the organic layer was washed with water (3×) and then brine (1×). The organic layer was dried over Na_2SO_4 and concentrated to a solid and used without purification (0.292 g, 1.04 mmol, 92 % yield).

2,2,2-trifluoro-N-(4-(6-hydroxy-3-oxo-3H-xanthen-9-yl)-3-methylphenyl)acetamide (3.41): A solution of **3.40** (0.659 g, 2.34 mmol, 1.5 equiv) in anhydrous THF (4 mL) was treated dropwise with *n*-BuLi (2.5 M in hexanes, 0.94 mL, 0.15 g, 2.30 mmol, 1.5 equiv) at -78 °C and the reaction was allowed to proceed at the same temperature for 20 min before the addition of *t*-BuLi (1.7 M in pentanes, 2.1 mL, 0.23 g, 3.6 mmol, 2.3 equiv). After an additional 15 min. 3,6-

bis((tert-butyldimethylsilyl)oxy)-9H-xanthen-9-one[10] (0.713 g, 1.56 mmol, 1 equiv) in anhydrous THF (4 mL) was added and the reaction was allowed to stir at the same temperature for 1 h before allowing it to warm to room temperature for an additional 2.5 h. The reaction was quenched by the addition of 2 M aq. HCl and heated at 50 °C for 14 h. The reaction was diluted with brine and extracted with 40% isopropanol/CH_2Cl_2 (3×). The organic layer was dried over Na_2SO_4, concentrated, and purified via silica gel chromatography (7.5% MeOH/CH_2Cl_2) to afford an orange solid (0.570 g, 1.38 mmol, 88 % yield). ^{1}H NMR (500 MHz, CD3OD) δ 7.73 (s, 1H), 7.67 (dd, *J* = 8.2, 2.2 Hz, 1H), 7.53 (s, 1H), 7.16 (d, *J* = 8.5 Hz, 2H), 7.02 (d, *J* = 9.2 Hz, 2H), 6.71 – 6.63 (m, 6H), 2.03 (s, 3H).

TG-2: A solution of **3.41** (0.122 mg, 296 μmol, 1 equiv) in EtOH (0.75 mL) was treated with dipropylamine (0.3 mL, 0.22 g, 2.2 mmol, 7.4 equiv) and the reaction was heated to 80 °C for 24 h. The reaction was cooled to room temperature, dissolved in MeOH, and loaded onto celite. Purification via silica chromatography (7.5% MeOH/CH_2Cl_2) afforded the product as an orange solid (60.7 mg, 191 μmol, 65% yield). ^{1}H NMR (500 MHz, CD_3OD) δ 7.20 (d, *J* = 9.0 Hz, 2H), 6.92 (d, *J* = 8.1 Hz, 1H), 6.77 (d, *J* = 2.2 Hz, 1H), 6.74 – 6.67 (m, 6H), 1.93 (s, 3H).

TG-3: To a solution of **TG-2** (60.7 mg, 191 μmol, 1 equiv) and K_2HPO_4 (70.4 mg, 404 μmol, 2.1 equiv) in anhydrous DMF (1 mL) was added ethyl iodide (19 μL, 37 mg, 240 μmol, 1.2 equiv) and the reaction was heated to 70 °C for 18 h. The reaction was cooled to room temperature, quenched in brine, and extracted with 10% MeOH/CH_2Cl_2 (3×). The organic layer was concentrated and purified via silica chromatography (7.5% Me MeOH/CH_2Cl_2) to afford an orange solid (5.5 mg, 16 μmol, 8.3%) with starting material recollected (13.5 mg, 42.5 μmol, 22%). ^{1}H NMR (500 MHz, MeOD) δ 7.24 – 7.18 (m, 2H), 6.92 (d, *J* = 8.2 Hz, 1H), 6.70 (d, *J* = 8.3 Hz, 4H), 6.67 – 6.60 (m, 2H), 3.18 (q, *J* = 7.1 Hz, 2H), 1.92 (s, 3H), 1.26 (t, *J* = 7.1 Hz, 3H).

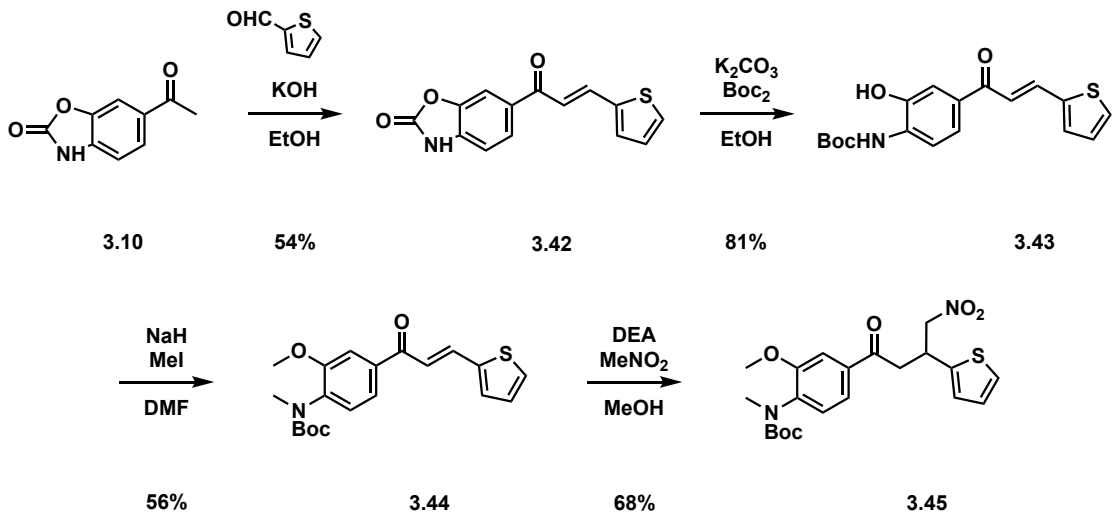

Scheme C.11: Synthesis of compound **3.45.**

(E)-6-(3-(thiophen-2-yl)acryloyl)benzo[d]oxazol-2(3H)-one (3.42): A solution of **3.10** (3.49 g, 19.7 mmol, 1.0 equiv) and 2-thiophenecarboxaldehyde (2.03 mL, 21.7 mmol, 1.1 equiv) in EtOH (100.0 mL) was treated with dropwise addition of aq. KOH (10 M, 5.92 mL, 59.2 mmol, 3.0 equiv). The reaction was allowed to stir at room temperature for 12 h. After completion, the mixture was concentrated and purified via silica gel column chromatography (1% $MeOH/CH_2Cl_2$) to afford the product as a yellow solid (2.88 g, 10.6 mmol, 54% yield). $R_f = 0.09$ (25% Acetone/Hexanes). ^1H NMR (500 MHz, DMSO-d_6) δ 12.06 (s, 1H), 8.01 (d, J = 1.5 Hz, 1H), 7.99 (dd, J = 8.1, 1.7 Hz, 1H), 7.90 (d, J = 15.2 Hz, 1H), 7.78 (d, J = 4.9 Hz, 1H), 7.69 – 7.68 (m, 1H), 7.60 (d, J = 15.2 Hz, 1H), 7.22 (d, J = 8.1 Hz, 1H), 7.19 (dd, J = 5.0, 3.6 Hz, 1H). ^{13}C NMR (125 MHz, DMSO-d_6) δ 187.30, 154.89, 143.94, 140.23, 136.90, 135.35, 133.12, 132.24, 130.87, 129.14, 126.05, 120.59, 109.97, 109.80. HRMS (ESI, TOF) calc'd for $[M+H]^+$ 272.0381, found 272.0387.

***tert*-butyl (E)-(2-hydroxy-4-(3-(thiophen-2-yl)acryloyl)phenyl)carbamate (3.43).** A solution of **3.42** (2.63 g, 9.69 mmol, 1.0 equiv), K_2CO_3 (4.01 g, 29.0 mmol, 3.0 equiv), di-*tert*-butyl dicarbonate (8.50 g, 38.9 mmol, 4.0 equiv) in MeOH (50.0 mL) was heated to 45 ˚C for 7 h. The

reaction was quenched with sat. ammonium chloride and then the product extracted with EtOAc (3×). The organic layers were combined, dried over anhydrous Na_2SO_4, concentrated, and purified via silica gel column chromatography (30% EtOAc/Hexanes with 0.1% AcOH) to afford the product as a yellow solid (2.69 g, 7.80 mmol, 81% yield). R_f = 0.28 (30% EtOAc/Hexanes). ^{1}H NMR (500 MHz, $CDCl_3$) δ 8.34 (s, 1H), 7.94 (d, *J* = 15.2 Hz, 1H), 7.85 (d, *J* = 1.9 Hz, 1H), 7.81 (d, *J* = 8.4 Hz, 1H), 7.59 (dd, *J* = 8.4, 1.8 Hz, 1H), 7.43 (d, *J* = 5.1 Hz, 1H), 7.21 (s, 1H), 7.12 – 7.07 (m, 1H), 1.55 (s, 9H). ^{13}C NMR (125 MHz, $CDCl_3$) δ 189.02, 153.29, 145.69, 140.43, 137.21, 133.04, 132.14, 131.80, 128.99, 128.36, 122.31, 120.40, 118.43, 116.35, 81.79, 28.28. HRMS (ESI, TOF) calc'd for $[M+H]^+$ 346.1113, found 346.1119.

***tert*-butyl (E)-(2-methoxy-4-(3-(thiophen-2-yl)acryloyl)phenyl)(methyl)carbamate (3.44):** A pressure flask was charged with **3.43** (2.63 g, 7.62 mmol, 1.0 equiv), anhydrous DMF (38.0 mL), MeI (2.43 mL, 38.2 mmol, 5.0 equiv), and NaH (60 wt %, 9.18 mg, 23.0 mmol, 3.0 equiv) at 0 ˚C. The reaction was allowed to warm to room temperature and stirred for 1 h before heating to 70 ˚C for 12 h. The reaction cooled to room temperature and then was diluted in brine. The product was extracted with EtOAc (3×), the organic layers were combined, dried over anhydrous Na_2SO_4, concentrated and purified via silica gel column chromatography (25% EtOAc/Hexanes) to afford the product as a yellow solid (1.60 g, 4.30 mmol, 56% yield). R_f = 0.13 (10% EtOAc/Hexanes). ^{1}H NMR (500 MHz, $CDCl_3$) δ 7.94 (d, *J* = 15.3 Hz, 1H), 7.58 – 7.54 (m, 2H), 7.43 – 7.39 (m, 1H), 7.36 (d, *J* = 3.6 Hz, 1H), 7.31 (d, *J* = 15.3 Hz, 1H), 7.28 – 7.24 (m, 1H), 7.08 (dd, *J* = 5.1, 3.6 Hz, 1H), 3.91 (s, 3H), 3.15 (s, 3H), 1.39 (s, 9H). ^{13}C NMR (125 MHz, $CDCl_3$) δ 188.96, 155.29, 155.05, 140.46, 137.67, 137.34, 137.14, 132.20, 128.98, 128.49, 121.25, 120.66, 111.29, 80.15, 55.78, 36.87, 28.35. HRMS (ESI, TOF) calc'd for $[M+H]^+$ 374.1426, found 374.1432.

***tert*-butyl (2-methoxy-4-(4-nitro-3-(thiophen-2-yl)butanoyl)phenyl)(methyl)carbamate (3.45):** A solution of **3.42** (1.00 g, 2.68 mmol, 1.0 equiv), nitromethane (0.72 mL, 13.0 mmol, 5.0 equiv), and diethylamine (0.83 mL, 8.10 mmol, 3.0 equiv) in MeOH (30.0 mL) was heated to 65 ˚C for 14 h. The reaction was concentrated and purified via silica gel column chromatography (30% EtOAc/Hexanes) to afford the product as a yellow solid (0.62 g, 2.68 mmol, 53% yield). R_f = 0.34 (30% EtOAc/Hexanes). ^{1}H NMR (500 MHz, $CDCl_3$) δ 7.46 (d, *J* = 7.4 Hz, 2H), 7.19 (d, *J* = 8.0 Hz, 1H), 7.13 (d, *J* = 5.1 Hz, 1H), 6.91 (d, *J* = 3.4 Hz, 1H), 6.86 (t, *J* = 4.4 Hz, 1H), 4.78 (dd, *J* = 12.7, 6.3 Hz, 1H), 4.66 (dd, *J* = 12.8, 7.8 Hz, 1H), 4.49 (p, *J* = 6.9 Hz, 1H), 3.82 (s, 3H), 3.45 (qd, *J* = 17.7, 6.7 Hz, 2H), 3.09 (s, 3H), 1.34 (s, 9H). ^{13}C NMR (125 MHz, $CDCl_3$) δ 195.63, 155.05, 154.67, 141.87, 137.66, 135.57, 128.56, 127.06, 125.45, 124.61, 120.95, 110.56, 80.02, 79.80, 55.55, 42.23, 36.64, 34.77, 28.15. HRMS (ESI, TOF) calc'd for $[M+H]^+$ 435.1590, found 435.1601.

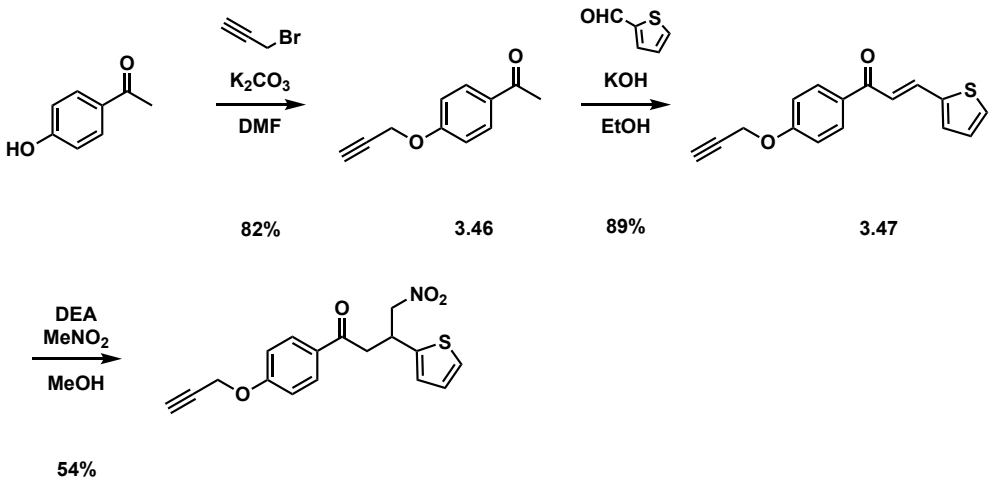

Scheme C.12: Synthesis of compound **3.48**.

1-(4-(prop-2-yn-1-yloxy)phenyl)ethan-1-one (3.46): A suspension of 1-(4-hydroxyphenyl)ethan-1-one (575 mg, 4.23 mmol, 1.0 equiv), K_2CO_3 (759 mg, 5.49 mmol, 1.3 equiv) in anhydrous DMF (10.0 mL) was treated with 3-bromoprop-1-yne (0.52 mL, 5.49 mmol, 1.3 equiv) and heated to 65 ˚C for 1 h. The reaction was added with water and filtered by

vacuum to afford the product as a pale yellow solid (603 mg, 4.23 mmol, 82% yield). R_f = 0.24 (10% EtOAc/Hexanes). ^{1}H NMR (500 MHz, $CDCl_3$) δ 7.86 (d, *J* = 9.0 Hz, 2H), 6.64 (d, *J* = 9.1 Hz, 2H), 3.04 (s, 6H), 2.50 (s, 3H). ^{13}C NMR (125 MHz, $CDCl_3$) δ 196.36, 153.39, 130.51, 125.36, 110.60, 40.02, 25.98. HRMS (ESI, TOF) calc'd for $[M+H]^+$ 175.0759, found 175.0764.

(*E*)-1-(4-(prop-2-yn-1-yloxy)phenyl)-3-(thiophen-2-yl)prop-2-en-1-one (3.47): A solution of **3.46** (1.69 g, 9.72 mmol, 1.0 equiv) and thiophene-2-carbaldehyde (1.0 mL, 11.0 mmol, 1.2 equiv) in EtOH (50.0 mL) was treated dropwise with an aq. solution of KOH (10 M, 2.90 mL, 29.2 mmol, 3.0 equiv). The reaction was allowed to stir at room temperature for 1 h before the resulting yellow precipitate was collected via filtration to afford the product as a yellow solid (2.32 g, 9.72 mmol, 89% yield). R_f = 0.26 (10% EtOAc/Hexanes). ^{1}H NMR (500 MHz, $CDCl_3$) δ 8.03 (d, *J* = 8.6 Hz, 2H), 7.93 (d, *J* = 15.3 Hz, 1H), 7.40 (d, *J* = 5.0 Hz, 1H), 7.36 – 7.30 (m, 2H), 7.10 – 7.04 (m, 3H), 4.77 (d, *J* = 2.4 Hz, 2H), 2.56 (t, *J* = 2.4 Hz, 1H). 13C NMR (125 MHz, $CDCl_3$) δ 188.10, 161.22, 140.54, 136.62, 131.85, 131.78, 130.64, 128.55, 128.33, 120.59, 114.74, 77.82, 76.18, 55.89. HRMS (ESI, TOF) calc'd for $[M+H]^+$ 269.0636, found 269.0623.

4-nitro-1-(4-(prop-2-yn-1-yloxy)phenyl)-3-(thiophen-2-yl)butan-1-one (3.48): A solution of **3.47** (3.41 g, 12.7 mmol, 1.0 equiv), nitromethane (3.44 mL, 63.6 mmol, 5.0 equiv), and diethylamine (4.0 mL, 38.17 mmol, 3.0 equiv) in MeOH (130.0 mL) was heated to 65 ˚C for 14 h. The reaction was concentrated and purified via silica gel column chromatography (20% EtOAc/Hexanes) to afford the product as a yellow solid (2.30 g, 6.98 mmol, 54% yield). R_f = 0.27 (20% EtOAc/Hexanes). ^{1}H NMR (500 MHz, $CDCl_3$) δ 7.95 – 7.92 (m, 2H), 7.21 (dt, *J* = 5.0, 1.2 Hz, 1H), 7.04 – 7.01 (m, 2H), 6.97 – 6.93 (m, 2H), 4.87 – 4.82 (m, 1H), 4.76 (dd, *J* = 2.4, 1.0 Hz, 2H), 4.70 (ddd, *J* = 12.6, 7.6, 1.0 Hz, 1H), 3.52 – 3.40 (m, 2H), 2.55 (t, *J* = 2.4 Hz, 1H), 2.17 (s, 1H), 1.54 (s, 1H). ^{13}C NMR (125 MHz, $CDCl_3$) δ 206.89, 194.85, 161.71, 142.01,

130.31, 130.06, 127.12, 125.53, 124.66, 114.81, 79.92, 76.28, 55.89, 41.97, 34.86, 30.91. HRMS (ESI, TOF) calc'd for $[M+H]^+$ 330.0800, found 330.0790.

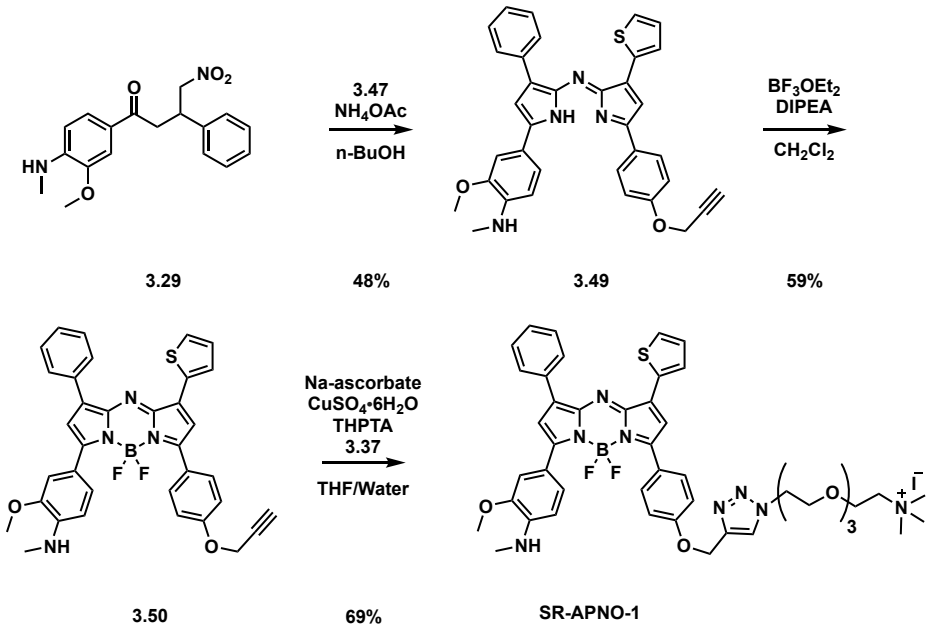

Scheme C.13: Synthesis of **SR-APNO-1**.

***tert*-butyl (*Z*)-(2-methoxy-4-(4-phenyl-5-((5-(4-(prop-2-yn-1-yloxy)phenyl)-3-(thiophen-2-yl)-2*H*-pyrrol-2-ylidene)amino)-1*H*-pyrrol-2-yl)phenyl)(methyl)carbamate (3.49):** A suspension of **3.29** (267.7 mg, 815.2 μmol, 1.0 equiv), and **3.48** (805.5 mg, 2.45 mmol, 3.0 equiv) in *n*-butanol (16.0 mL) was heated to 110 ˚C to dissolve all solids. NH_4OAc (942.6 mg, 12.23 mmol, 15 equiv) was added in a single portion and the reaction was stirred at the same temperature for 5 h. Volatiles were removed under reduced pressure, the residue was suspended in brine, and the product was extracted with CH_2Cl_2 (3×). The combined organic layers were dried over anhydrous Na_2SO_4, concentrated, and purified via silica gel column chromatography (90% CH_2Cl_2/Hexanes) to afford the product as blue solid (219.8 mg, 0.82 mmol, 48% yield). R_f = 0.32 (50% CH_2Cl_2/Hexanes) ^1H NMR (500 MHz, $CDCl_3$) δ 8.12 – 8.09 (m, 2H), 7.77 – 7.73 (m, 2H), 7.65 (dd, *J* = 3.6, 1.2 Hz, 1H), 7.58 (dd, J = 8.2, 1.8 Hz, 1H), 7.55 (d, *J* = 1.8 Hz, 1H),

7.47 (dd, *J* = 8.2, 7.0 Hz, 2H), 7.41 – 7.36 (m, 1H), 7.33 (dd, *J* = 5.0, 1.1 Hz, 1H), 7.08 (dd, *J* = 5.1, 3.6 Hz, 1H), 7.02 – 6.98 (m, 2H), 6.88 (s, 1H), 6.64 (d, *J* = 8.3 Hz, 1H), 4.93 – 4.85 (m, 1H), 4.75 (d, *J* = 2.4 Hz, 2H), 4.03 (s, 3H), 3.01 – 2.95 (m, 3H), 2.58 (t, *J* = 2.3 Hz, 1H). ^{13}C NMR (125 MHz, $CDCl_3$) δ 163.62, 158.13, 156.09, 146.95, 146.30, 144.15, 143.13, 142.90, 136.97, 133.80, 131.23, 129.68, 128.31, 128.24, 127.40, 126.81, 126.35, 125.87, 125.77, 123.86, 120.70, 119.05, 115.50, 108.47, 108.21, 106.97, 78.37, 76.08, 56.08, 55.47, 30.02, 29.85. HRMS (ESI, TOF) calc'd for $[M+H]^+$ 569.1987, found 569.1994.

4-(5,5-difluoro-1-phenyl-7-(4-(prop-2-yn-1-yloxy)phenyl)-9-(thiophen-2-yl)-5H-5λ4,6λ4-dipyrrolo[1,2-c:2',1'-f][1,3,5,2]triazaborinin-3-yl)-2-methoxy-N-methylaniline (3.50): A solution of **3.49** (97.2 mg, 0.17 mmol, 1.0 equiv) and *N,N*-diisopropylethylamine (0.45 mL, 2.56 mmol, 15.0 equiv) in anhydrous CH_2Cl_2 (8.5 mL) was treated with boron trifluoride diethyl etherate (0.33 mL, 2.56 mmol, 15.0 equiv). The reaction was allowed to stir at room temperature for 3 h under a nitrogen atmosphere. After completion, the reaction was quenched with minimal sat. aq. $NaHCO_3$ and diluted in brine. The product was extracted with CH_2Cl_2 (3×), the combined organic layers were dried over anhydrous Na_2SO_4, concentrated, and purified via silica gel column chromatography (80% CH_2Cl_2/Hexanes) to afford the product as a purple solid (62.3 mg, 0.10 mmol, 59% yield). R_f = 0.31 (50% CH_2Cl_2/Hexanes) ^{1}H NMR (500 MHz, $CDCl_3$) δ 8.15 – 8.12 (m, 2H), 8.05 – 8.02 (m, 2H), 7.96 (d, *J* = 1.9 Hz, 1H), 7.78 (dd, *J* = 8.5, 2.0 Hz, 1H), 7.69 (dd, *J* = 3.7, 1.1 Hz, 1H), 7.53 – 7.49 (m, 2H), 7.47 – 7.43 (m, 2H), 7.25 (s, 1H), 7.12 (dd, *J* = 5.1, 3.7 Hz, 1H), 7.04 (d, *J* = 9.0 Hz, 2H), 6.83 (s, 1H), 6.63 (d, *J* = 8.6 Hz, 1H), 4.76 (d, *J* = 2.4 Hz, 2H), 3.94 (s, 3H), 2.99 (d, *J* = 5.3 Hz, 3H), 2.56 (t, *J* = 2.4 Hz, 1H). ^{13}C NMR (125 MHz, $CDCl_3$) δ 160.44, 158.84, 152.94, 146.38, 143.81, 143.14, 135.83, 132.45, 131.03, 129.77, 129.41, 128.66, 128.60, 128.38, 127.77, 127.48, 127.38, 126.23, 125.49, 120.29, 118.54, 115.64,

114.76, 114.46, 110.94, 108.47, 78.43, 75.96, 55.98, 55.80, 31.74, 29.81, 22.81, 14.27. ^{19}F NMR (471 MHz, $CDCl_3$) δ -131.18 (dd, *J* = 65.4, 32.5 Hz). ^{11}B NMR (161 MHz, $CDCl_3$) δ 1.28 (t, *J* = 32.7 Hz). HRMS (ESI, TOF) calc'd for $[M+H]^+$ 616.1916, found 616.1988.

SR-APNO-1: A solution of **3.50** (18.2 mg, 28.8 μmol, 1.0 equiv), 3,3',3''-((nitrilotris(methylene))tris(1H-1,2,3-triazole-4,1-diyl))tris(propan-1-ol) (4.50 mg, 10.4 μmol, 0.4 equiv), **3.37** (38.3 mg, 98.5 μmol, 3.4 equiv), and copper(II) sulfate pentahydrate (36.0 mg, 144.1 μmol, 5.0 equiv), in anhydrous THF (6.0 mL) was treated with dropwise sodium ascorbate (8.6 mg, 43.2 μmol, 1.5 equiv) in water (0.7 mL, degassed) at room temperature for 3 h under nitrogen atmosphere. The volatiles were removed by reduced pressure and the residual was diluted in 50% MeOH/CH_2Cl_2 and washed with sat. aq. sodium iodide (2×). The combined organic layers were dried over anhydrous Na_2SO_4, concentrated, and purified via silica gel column chromatography (10% MeOH/$CHCl_3$) to afford the product as a purple solid (20.3 mg, 19.9 μmol, 69% yield). R_f = 0.22 (10% MeOH/$CHCl_3$). ^{1}H NMR (500 MHz, CD_2Cl_2) δ 8.18 – 8.13 (m, 2H), 8.08 – 8.02 (m, 1H), 7.91 (s, 1H), 7.83 (dd, *J* = 8.6, 2.0 Hz, 1H), 7.71 (dd, *J* = 3.7, 1.2 Hz, 1H), 7.54 (dd, *J* = 8.2, 6.7 Hz, 2H), 7.50 – 7.45 (m, 2H), 7.32 (s, 1H), 7.17 – 7.10 (m, 3H), 6.90 (s, 1H), 6.68 (s, 0H), 5.29 (s, 2H), 4.62 – 4.52 (m, 2H), 3.96 (s, 3H), 3.90 (q, *J* = 4.9, 4.4 Hz, 2H), 3.75 (dq, *J* = 7.5, 2.7 Hz, 2H), 3.64 – 3.50 (m, 7H), 3.42 – 3.35 (m, 2H), 3.04 (s, 8H), 3.00 (d, *J* = 4.8 Hz, 3H). ^{13}C NMR (125 MHz, CD_2Cl_2) δ 160.25, 159.50, 146.85, 146.23, 144.14, 143.60, 135.30, 133.31, 132.02, 130.88, 129.57, 129.50, 128.84, 128.62, 127.71, 127.61, 127.49, 125.65, 124.45, 120.52, 117.92, 114.73, 114.08, 110.65, 108.37, 70.49, 70.39, 70.22, 70.11, 69.30, 66.23, 64.87, 61.80, 55.86, 55.04, 55.01, 54.98, 50.55, 29.69. ^{19}F NMR (471 MHz, CD_2Cl_2) δ -130.30 (dd, *J* = 65.4, 32.3 Hz). ^{11}B NMR (161 MHz, CD_2Cl_2) δ 1.27 (t, *J* = 32.9 Hz). HRMS (ESI, TOF) calc'd for $[M]^+$ 877.3837, found 877.3842.

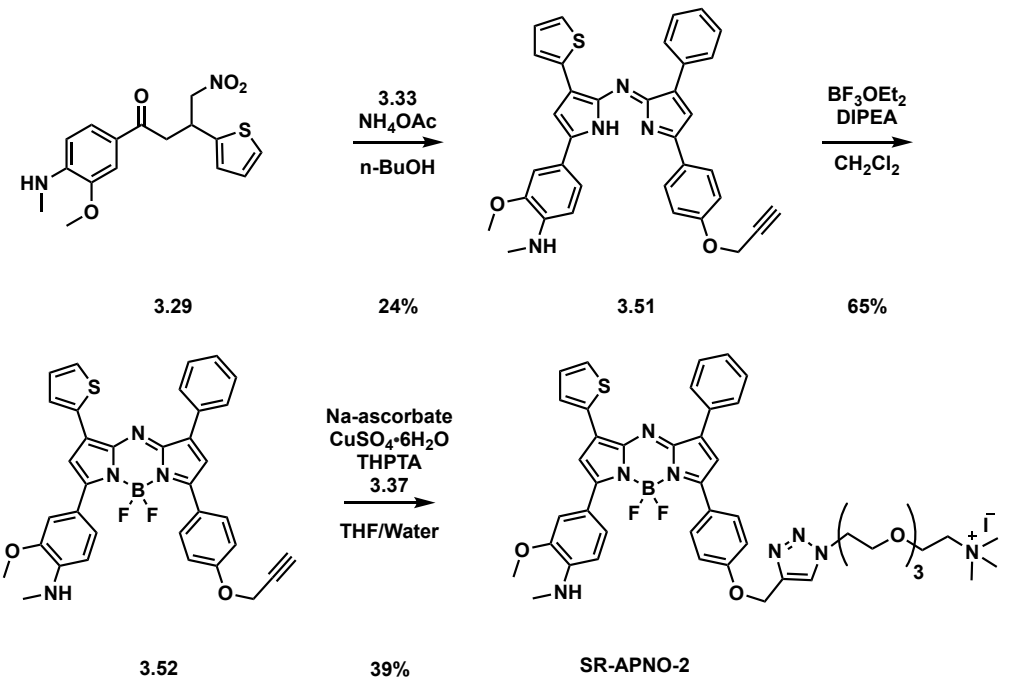

Scheme C.14: Synthesis of **SR-APNO-2**.

***tert*-butyl (*Z*)-(2-methoxy-4-(5-((3-phenyl-5-(4-(prop-2-yn-1-yloxy)phenyl)-2*H*-pyrrol-2-ylidene)amino)-4-(thiophen-2-yl)-1*H*-pyrrol-2-yl)phenyl)(methyl)carbamate (3.51):** A suspension of **3.33** (415.5 mg, 956.2 μmol, 1.0 equiv), and **3.45** (947.6 mg, 2.93 mmol, 3.1 equiv) in *n*-butanol (19.0 mL) was heated to 110 ˚C to dissolve all solids. NH_4OAc (1.106 g, 14.34 mmol, 15 equiv) was added in a single portion and reaction was stirred at the same temperature for 6 h. Volatiles were removed under reduced pressure, the residue was suspended in brine, and the product was extracted with CH_2Cl_2 (3×). The combined organic layers were dried over anhydrous Na_2SO_4, concentrated, and purified via silica gel column chromatography (90% CH_2Cl_2/Hexanes) to afford the product as a blue solid (131.2 mg, 0.96 mmol, 24% yield). R_f = 0.48 (100% CH_2Cl_2) ^{1}H NMR (500 MHz, $CDCl_3$) δ 8.08 – 8.05 (m, 2H), 7.94 – 7.91 (m, 2H), 7.73 – 7.71 (m, 1H), 7.47 (dd, *J* = 8.4, 6.9 Hz, 2H), 7.44 (d, *J* = 7.5 Hz, 2H), 7.41 – 7.37 (m, 2H), 7.15 (s, 1H), 7.10 (dd, *J* = 5.1, 3.7 Hz, 1H), 7.09 – 7.03 (m, 2H), 4.79 (d, *J* = 2.4 Hz, 2H), 4.01 (s, 3H), 3.20 (s, 3H), 2.60 – 2.58 (m, 1H), 1.43 (s, 9H). ^{13}C NMR (125 MHz, $CDCl_3$) δ

159.46, 158.78, 155.30, 155.24, 144.06, 136.07, 135.74, 133.57, 131.55, 129.52, 128.32, 128.28, 128.20, 127.50, 127.33, 126.98, 125.84, 119.20, 115.83, 115.49, 111.77, 108.61, 80.01, 77.98, 76.17, 55.97, 55.42, 47.43, 29.72, 28.34, 14.14. HRMS (ESI, TOF) calc'd for $[M+H]^+$ 668.2457, found 669.2540.

4-(5,5-difluoro-9-phenyl-7-(4-(prop-2-yn-1-yloxy)phenyl)-1-(thiophen-2-yl)-5H-5λ4,6λ4-dipyrrolo[1,2-c:2',1'-f][1,3,5,2]triazaborinin-3-yl)-2-methoxy-N-methylaniline (3.52): A solution of **3.51** (183.6 mg, 0.32 mmol, 1.0 equiv) and *N,N*-diisopropylethylamine (0.84 mL, 4.84 mmol, 15 equiv) in anhydrous CH_2Cl_2 (16.0 mL) was treated with boron trifluoride diethyl etherate (0.62 mL, 4.84 mmol, 15 equiv). The reaction was stirred at room temperature for 6 h under a nitrogen atmosphere and then was quenched with minimal sat. aq. $NaHCO_3$. The solution was then diluted with brine and the product was extracted with CH_2Cl_2 (3×). The combined organic layers were dried over anhydrous Na_2SO_4, concentrated, and purified via silica gel column chromatography (80% CH_2Cl_2/Hexanes) to afford the product as a purple solid (128.7 mg, 0.32 mmol, 65% yield). R_f = 0.36 (50% CH_2Cl_2/Hexanes) ^{1}H NMR (500 MHz, $CDCl_3$) δ 8.11 – 8.08 (m, 2H), 8.07 – 8.04 (m, 2H), 7.93 (s, 1H), 7.83 (dd, *J* = 3.7, 1.1 Hz, 1H), 7.75 (dd, *J* = 8.5, 2.0 Hz, 1H), 7.52 (dd, *J* = 5.0, 1.1 Hz, 1H), 7.48 (t, *J* = 7.7 Hz, 2H), 7.39 (td, *J* = 7.1, 1.3 Hz, 1H), 7.17 – 7.12 (m, 2H), 7.06 – 7.02 (m, 2H), 6.92 (s, 1H), 6.61 (d, *J* = 8.5 Hz, 1H), 5.10 (s, 1H), 4.76 (d, *J* = 2.4 Hz, 2H), 3.93 (s, 3H), 2.97 (s, 3H), 2.56 (t, *J* = 2.4 Hz, 1H). ^{13}C NMR (125 MHz, $CDCl_3$) δ 160.88, 158.67, 152.43, 146.39, 146.20, 143.66, 143.25, 139.16, 138.02, 134.41, 133.42, 130.97, 129.91, 129.34, 128.89, 128.46, 128.29, 127.82, 127.08, 126.32, 118.22, 116.99, 116.86, 114.62, 110.71, 108.30, 78.31, 75.83, 55.84, 55.66, 31.61, 29.66, 22.67, 14.14. ^{19}F NMR (471 MHz, $CDCl_3$) δ -131.08 (dd, *J* = 65.3, 32.4 Hz). ^{11}B NMR (161 MHz, $CDCl_3$) δ 1.29 (t, *J* = 32.7 Hz). HRMS (ESI, TOF) calc'd for $[M+H]^+$ 569.1987, found 569.1994.

SR-APNO-2: A solution of **3.52** (28.2 mg, 44.7 μmol, 1.0 equiv), 3,3',3''-((nitrilotris(methylene))tris(1H-1,2,3-triazole-4,1-diyl))tris(propan-1-ol) (5.60 mg, 12.9 μmol, 0.3 equiv), **3.37** (57.2 mg, 147 μmol, 3.3 equiv), and copper(II) sulfate pentahydrate (55.7 mg, 223 μmol, 5.0 equiv), in anhydrous THF (8.9 mL) was treated with dropwise sodium ascorbate (46.2 mg, 233.0 μmol, 5.2 equiv) in water (1.1 mL, degassed) at room temperature under nitrogen atmosphere. The reaction was allowed to stir at the same temperature for 2 h before heating to 65 ˚C for an additional 4 h. The volatiles were removed by reduced pressure, the reaction was diluted in 50% MeOH/DCM, and the organic layer was washed with sat. aq. sodium iodide (2×). The combined organic layers were dried over anhydrous Na_2SO_4, concentrated, and purified via silica gel column chromatography (10% MeOH/$CHCl_3$) to afford the product as a purple solid (17.6 mg, 17.3 μmol, 39% yield). R_f = 0.25 (10% MeOH/$CHCl_3$). ^{1}H NMR (500 MHz, CD_2Cl_2) δ 8.14 – 8.10 (m, 2H), 8.07 (d, J = 8.4 Hz, 2H), 7.94 (bs, 1H), 7.89 (d, J = 1.9 Hz, 1H), 7.86 (dd, *J* = 3.8, 1.1 Hz, 1H), 7.81 (dd, *J* = 8.5, 2.0 Hz, 1H), 7.60 (dd, *J* = 5.0, 1.1 Hz, 1H), 7.51 (t, *J* = 7.6 Hz, 2H), 7.44 – 7.39 (m, 1H), 7.23 (s, 1H), 7.19 (dd, *J* = 5.1, 3.7 Hz, 1H), 7.14 (d, *J* = 8.5 Hz, 2H), 6.98 (s, 1H), 6.67 (d, *J* = 8.5 Hz, 1H), 4.57 (t, *J* = 4.9 Hz, 2H), 3.97 (s, 3H), 3.91 (t, *J* = 4.9 Hz, 2H), 3.74 (dt, *J* = 6.8, 3.0 Hz, 2H), 3.62 – 3.58 (m, 2H), 3.54 (m, 6H), 3.39 – 3.35 (m, 2H), 3.05 (s, 9H), 3.01 (s, 3H). 13C NMR (126 MHz, CD_2Cl_2) δ 160.87, 159.46, 151.66, 146.37, 146.21, 144.09, 142.95, 138.84, 133.98, 133.18, 130.98, 130.52, 129.23, 129.13, 128.56, 128.46, 127.92, 127.32, 125.88, 117.77, 117.19, 116.67, 114.72, 110.56, 108.31, 70.56, 70.36, 70.30, 70.17, 69.19, 66.20, 64.86, 61.84, 55.85, 55.00, 54.97, 54.95, 50.62, 31.93, 29.68, 22.69, 13.87. ^{19}F NMR (471 MHz, CD_2Cl_2) δ -130.31 (dd, *J* = 60.0, 27.5 Hz). ^{11}B NMR (161 MHz, CD_2Cl_2) δ 1.27 (t, *J* = 32.8 Hz). HRMS (ESI, TOF) calc'd for $[M]^+$ 877.3845, found 877.3844.

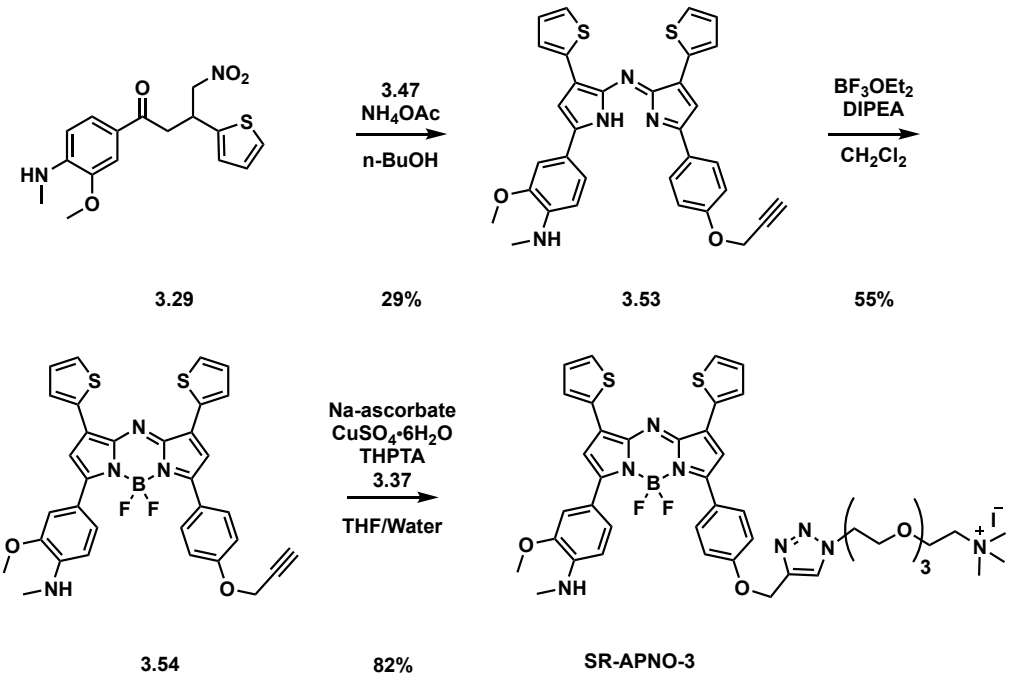

Scheme C.15: Synthesis of **SR-APNO-3**.

***tert*-butyl (Z)-(2-methoxy-4-(5-((5-(4-(prop-2-yn-1-yloxy)phenyl)-3-(thiophen-2-yl)-2H-pyrrol-2-ylidene)amino)-4-(thiophen-2-yl)-1H-pyrrol-2-yl)phenyl)(methyl)carbamate (3.53):** A suspension of **3.45** (0.24 g, 0.55 mmol, 1.0 equiv), and **3.48** (0.49 g, 1.50 mmol, 2.7 equiv) in *n*-butanol (11.0 mL) was heated to 110 ˚C to dissolve all solids. NH_4OAc (0.84 g, 11.0 mmol, 20 equiv) was added in a single portion and reaction was stirred at the same temperature for 6 h. Volatiles were removed under reduced pressure, the resulting solid was suspended in brine, and the product was extracted with CH_2Cl_2 (3×). The combined organic layers were dried over anhydrous Na_2SO_4, concentrated, and purified via silica gel column chromatography (step gradient: 90% CH_2Cl_2/Hexanes, 100% CH_2Cl_2, then 1% MeOH/CH_2Cl_2) to afford the product as a blue solid (0.11 g, 0.55 mmol, 29% yield). R_f = 0.63 (100 % CH_2Cl_2) ^{1}H NMR (500 MHz, DMSO-d_6) δ 12.77 (s, 1H), 8.17 – 8.12 (m, 2H), 7.97 (d, *J* = 3.6 Hz, 1H), 7.90 – 7.86 (m, 1H), 7.76 (d, *J* = 5.0 Hz, 1H), 7.72 (d, *J* = 5.0 Hz, 1H), 7.64 (d, *J* = 1.8 Hz, 1H), 7.62 – 7.57 (m, 2H), 7.52 (s, 1H), 7.40 (d, *J* = 8.1 Hz, 1H), 7.24 (ddd, *J* = 6.8, 5.0, 3.6 Hz, 2H), 7.17 (d, *J* = 8.8 Hz,

2H), 4.97 (d, *J* = 2.4 Hz, 2H), 4.06 (s, 3H), 3.69 (t, *J* = 2.3 Hz, 1H), 3.11 (s, 3H), 1.37 (s, 9H). ^{13}C NMR (125 MHz, DMSO-d_6) δ 159.77, 159.49, 154.86, 154.07, 151.63, 149.52, 145.08, 138.12, 135.19, 134.78, 133.70, 133.64, 130.32, 129.07, 128.98, 128.27, 128.24, 127.95, 127.82, 127.41, 126.89, 124.69, 118.87, 115.67, 115.56, 112.14, 108.82, 79.12, 78.80, 78.76, 55.78, 55.49, 55.45, 27.90.HRMS (ESI, TOF) calc'd for $[M+H]^+$ 675.2100, found 675.2103.

4-(5,5-difluoro-7-(4-(prop-2-yn-1-yloxy)phenyl)-1,9-di(thiophen-2-yl)-5*H*-5λ^4,6λ^4-dipyrrolo[1,2-*c*:2',1'-*f*][1,3,5,2]triazaborinin-3-yl)-2-methoxy-*N*-methylaniline (3.54): A solution of **3.53** (0.24 g, 0.35 mmol, 1.0 equiv) and *N,N*-diisopropylethylamine (0.92 mL, 5.20 mmol, 15 equiv) in anhydrous CH_2Cl_2 (15.0 mL) was treated with boron trifluoride diethyl etherate (0.67 mL, 5.20 mmol, 15 equiv). The reaction was stirred at room temperature for 3 h under a nitrogen atmosphere. The reaction was quenched with minimal sat. aq. $NaHCO_3$ and then extracted with CH_2Cl_2 (3×) from brine. The combined organic layers were dried over anhydrous Na_2SO_4, concentrated, and purified via silica gel column chromatography (step gradient: 20% CH_2Cl_2/Hexanes to 60% CH_2Cl_2/Hexanes, 10% steps) to afford the product as a purple solid (0.12 g, 0.19 mmol, 55% yield). R_f = 0.25 (50% CH_2Cl_2/Hexanes) ^{1}H NMR (500 MHz, CD_2Cl_2) δ 8.04 (d, *J* = 2.1 Hz, 1H), 8.02 (d, J = 3.0 Hz, 2H), 7.91 (d, *J* = 1.9 Hz, 1H), 7.85 – 7.79 (m, 2H), 7.60 (dd, *J* = 5.0, 1.2 Hz, 1H), 7.51 (dd, *J* = 5.1, 1.1 Hz, 1H), 7.25 – 7.21 (m, 2H), 7.19 (dd, *J* = 5.1, 3.6 Hz, 1H), 7.08 – 7.03 (m, 2H), 6.88 (s, 1H), 6.66 (d, *J* = 8.6 Hz, 1H), 5.27 (q, *J* = 5.5 Hz, 1H), 4.79 (d, *J* = 2.4 Hz, 2H), 3.94 (s, 3H), 2.99 (d, *J* = 5.0 Hz, 3H), 2.63 (t, *J* = 2.3 Hz, 1H). ^{13}C NMR (125 MHz, CD_2Cl_2) δ 161.22, 159.27, 152.39, 146.97, 146.83, 144.74, 142.99, 138.35, 136.15, 134.81, 133.42, 131.40, 131.36, 130.38, 130.09, 128.82, 128.70, 128.45, 128.30, 128.05, 126.61, 118.36, 115.14, 111.23, 108.83, 78.85, 76.14, 56.43, 56.24, 30.26, 30.07. ^{19}F NMR (471 MHz, CD_2Cl_2) δ -130.74 (dd, *J* = 65.4, 32.6 Hz). ^{11}B NMR (161

MHz, CD_2Cl_2) δ 1.22 (t, *J* = 32.7 Hz). HRMS (ESI, TOF) calc'd for $[M+H]^+$ 623.1558, found 623.1568.

SR-APNO-3: A solution of **3.55** (23.8 mg, 38.0 μmol, 1.0 equiv), 3,3',3''-((nitrilotris(methylene))tris(1H-1,2,3-triazole-4,1-diyl))tris(propan-1-ol) (3.15 mg, 7.25 μmol, 0.2 equiv), **3.37** (44.0 mg, 114 μmol, 2.97 equiv), copper(II) sulfate pentahydrate (96.1 mg, 385 μmol, 10 equiv), and anhydrous THF (1.9 mL) was treated dropwise with a solution of sodium ascorbate (15.8 mg, 79.8 μmol, 2.1 equiv) in water (382 μL, degassed). The reaction was then heated to 65 ˚C for 3 h under nitrogen atmosphere. The volatiles were removed under reduced pressure, the residue was diluted in 50% MeOH/CH_2Cl_2, and the organic layer was washed with sat. aq. sodium iodide (2×). The organic layer was collected, dried over anhydrous Na_2SO_4, concentrated, and purified via silica gel column chromatography (5 % MeOH/$CHCl_3$) to afford the product as a purple solid (31.8 mg, 31.5 μmol, 82% yield). R_f = 0.09 (5% MeOH/$CHCl_3$). ^{1}H NMR (500 MHz, DMSO-d_6) δ 8.33 (s, 1H), 8.26 (s, 1H), 8.15 (d, *J* = 3.7 Hz, 1H), 8.13 – 8.08 (m, 1H), 8.05 (d, *J* = 8.5 Hz, 2H), 7.98 – 7.87 (m, 4H), 7.74 (d, *J* = 5.0 Hz, 1H), 7.34 – 7.29 (m, 1H), 7.25 – 7.22 (m, 1H), 7.22 – 7.15 (m, 4H), 6.74 (d, *J* = 8.9 Hz, 1H), 5.26 (s, 2H), 4.57 (t, *J* = 5.2 Hz, 2H), 3.94 (s, 3H), 3.84 (t, *J* = 5.3 Hz, 2H), 3.82 – 3.77 (m, 2H), 3.57 – 3.46 (m, 12H), 3.32 (s, 3H), 3.08 (s, 9H), 2.93 (d, *J* = 5.1 Hz, 3H). ^{13}C NMR (125 MHz, DMSO-d_6) δ 159.89, 158.99, 148.74, 146.10, 146.02, 145.41, 142.34, 140.59, 136.89, 134.90, 133.06, 131.53, 130.40, 130.16, 130.01, 129.52, 128.95, 128.21, 127.99, 127.55, 125.03, 119.35, 116.01, 114.60, 114.12, 110.84, 109.01, 79.20, 69.56, 69.52, 69.40, 69.32, 68.67, 64.39, 64.02, 61.23, 55.62, 53.07, 53.04, 49.45, 29.33, 18.55. ^{19}F NMR (471 MHz, DMSO-d_6) δ -129.11 (dd, *J* = 66.4, 29.7 Hz). ^{11}B NMR (161 MHz, DMSO-d_6) δ 1.26 (t, *J* = 33.1 Hz). HRMS (ESI, TOF) calc'd for $[M]^+$ 883.3047, found 883.3395.

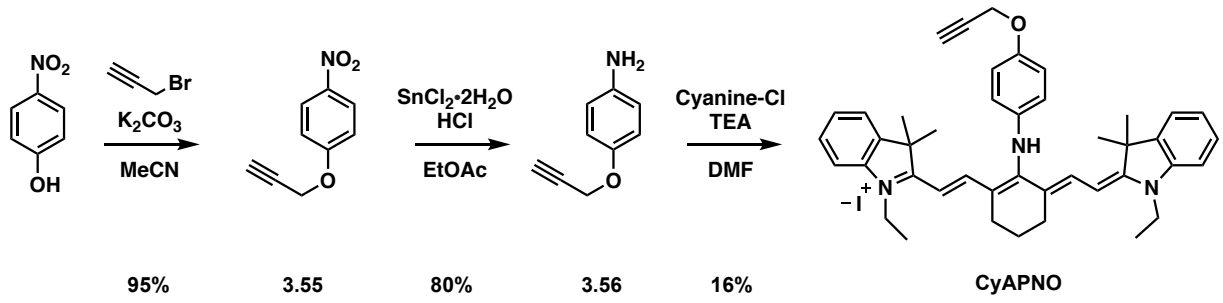

Scheme C.16: Synthesis of **CyAPNO**.

1-nitro-4-(prop-2-yn-1-yloxy)benzene (3.55): A solution of 4-nitrophenol (1.00g, 7.20 mmol, 1 equiv) in anhydrous acetonitrile (10 mL) was treated with potassium carbonate (1.09 g, 7.92 mmol, 1.1 equiv) and propargyl bromide (0.96 mL, 1.29 g, 8.65 mmol, 1.2 equiv). The reaction was allowed to proceed at 80 °C for 19 h before cooling to room temperature and diluting with EtOAc. The solution was washed with sat. aq. sodium bicarbonate (2×) and then brine (1×). The organic layer was dried over anhydrous Na_2SO_4 and concentrated under reduced pressure to afford the product as a white solid (1.22 g, 6.91 mmol, 95% yield). ^{1}H NMR (500 MHz, $CDCl_3$) δ 8.26 – 8.20 (m, 2H), 7.09 – 7.03 (m, 2H), 4.80 (d, J = 2.4 Hz, 2H), 2.58 (t, J = 2.4 Hz, 1H). ^{13}C NMR (125 MHz, $CDCl_3$) δ 162.48, 142.34, 126.00, 115.14, 56.45. HRMS (EI-TOF) for [M+] calc'd 177.04260, found 177.04267.

4-(prop-2-yn-1-yloxy)aniline (3.56): To a mixture of **3.55** (0.199 g, 1.13 mmol, 1 equiv) and stannous chloride dihydrate (1.91 g, 8.47 mmol, 7.5 equiv) were added EtOAc (2.3 mL) and then conc. aq. HCl (11.7 M, 0.96 mL, 0.41 g, 11 mmol, 10 equiv). The reaction was heated to 80 °C for 12 h before cooling to room temperature. The reaction was quenched with sat. aq. sodium bicarbonate and then extracted with CH_2Cl_2 (3×). The organic layer was dried over anhydrous Na_2SO_4 and concentrated under reduced pressure. The product was purified via silica chromatography (75% EtOAc/Hexanes) to afford the product as a yellow-brown oil (0.132 g, 0.896 mmol, 80% yield). ^{1}H NMR (500 MHz, $CDCl_3$) δ 6.86 – 6.79 (m, 2H), 6.68 – 6.61 (m,

2H), 4.61 (d, J = 2.4 Hz, 2H), 3.49 (bs, 1H), 2.49 (t, J = 2.4 Hz, 1H). ^{13}C NMR (125 MHz, $CDCl_3$) δ 150.87, 141.06, 116.57, 116.38, 79.27, 75.26, 56.90. HRMS (ESI-TOF) for [M+H] calc'd 148.0762, found 148.0755.

CyAPNO: Cy7-Cl[1] (509 mg, 0.80 mmol, 1 equiv) and **3.56** (147 mg, 1.0 mmol, 1.3 equiv) were dissolved in anhydrous DMF (15 mL) and then treated with TEA (0.12 mL, 89 mg, 0.88 mmol, 1.1 equiv). The reaction was heated at 55 °C for 3 h before cooling to room temperature and diluting with excess brine. The product was extracted with CH_2Cl_2 (3×). The organic layer was dried over anhydrous Na_2SO_4 and concentrated under reduced pressure. The product was purified via silica chromatography (7.5% MeOH/CH_2Cl_2). Pure fractions were pooled, concentrated and re-dissolved in CH_2Cl_2. The organic layer was washed once with sat. aq. potassium iodide, 1M aq. HCl, dried over minimal Na_2SO_4, and concentrated to afford the product as a blue solid (95.2 mg, 0.127 mmol, 16% yield). ^{1}H NMR (400 MHz, $CDCl_3$) δ 8.07 (d, J = 14.2 Hz, 2H), 7.49 – 7.37 (m, 2H), 7.30 – 7.16 (m, 6H), 7.07 (t, J = 7.5 Hz, 2H), 6.93 – 6.87 (m, 4H), 5.74 (dd, J = 13.7, 3.6 Hz, 2H), 4.57 (d, J = 2.4 Hz, 1H), 3.95 (q, J = 7.3 Hz, 4H), 2.54 (t, J = 6.4 Hz, 5H), 2.45 (t, J = 2.4 Hz, 1H), 1.91 (q, J = 6.5 Hz, 2H), 1.40 (s, 12H), 1.34 (t, J = 7.2 Hz, 6H). HRMS (ESI-TOF) for [M+] calc'd 622.3797, found 622.3798.

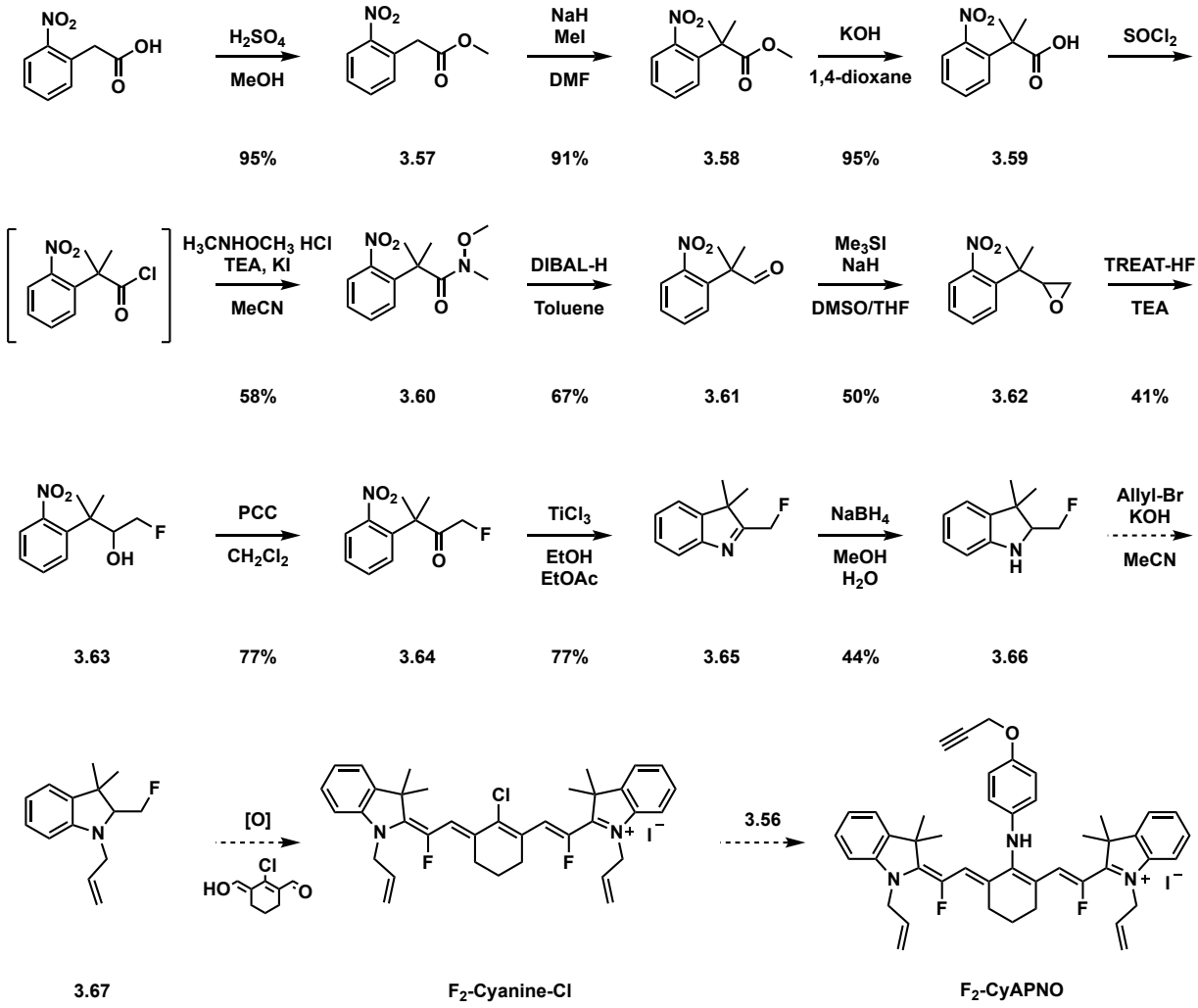

Scheme C.17: Synthesis of **F_2-Cyanine-Cl**.

Methyl 2-(2-nitrophenyl)acetate (3.57). The compound was prepared according to a modified procedure by Sulikowski and coworkers.[2] A solution of 2-nitrophenylacetic acid (32.3 g, 178 mmol, 1.0 equiv) in anhydrous MeOH (180 mL), was treated with concentrated sulfuric acid (18.4 M, 1.94 mL, 35.7 mmol, 0.2 equiv) and refluxed for 5 h. The reaction was then cooled to room temperature, concentrated under reduced pressure and diluted in EtOAc. The organic layer was washed with sat. aq. sodium bicarbonate (2×) and brine (1×), and then dried over anhydrous Na_2SO_4. The solution was concentrated under reduced pressure to afford the product as a light-

yellow oil (32.9 g, 169 mmol, 95%), which was used without further purification. Spectroscopic analyses were consistent with previous reports.

Methyl 2-methyl-2-(2-nitrophenyl)propanoate (3.58). The compound was prepared according to a modified procedure by Glorius and coworkers.[3] To solution of **3.57** (32.9 g, 169 mmol, 1.0 equiv) and MeI (26.4 mL, 422 mmol, 2.5 equiv) in anhydrous DMF (300 mL) was added NaH (60 wt. %, 20.2 g, 506 mmol, 3.0 equiv) portion-wise at 0 °C. After the evolution of gas subsided, additional MeI (26.4 mL, 422 mmol, 2.5 equiv) was added at the same temperature and then the reaction was allowed to warm to room temperature and continue stirring for 13 h. The reaction was quenched by adding it to ice and then the mixture was diluted in EtOAc. The mixture was further diluted with brine and the product was extracted with EtOAc (3×). The organic layers were combined, dried over anhydrous Na_2SO_4, concentrated under reduced pressure, and the product was purified via silica chromatography (20% EtOAc/hexanes) to afford the product as yellow oil (34.1 g, 153 mmol, 91%). Spectroscopic analyses were consistent with previous reports.

2-methyl-2-(2-nitrophenyl)propanoic acid (3.59). To a 250 mL pressure flask were added **3.58** (17.1 g, 76.6 mmol, 1.0 equiv), 1,4-dioxane (3.83 mL) and aq. potassium hydroxide (10 M, 38.3 mL, 38. mmol, 5.0 equiv). The vessel was sealed and then heated to 130 °C for 3 h. When the reaction was complete according to TLC, it was cooled to room temperature over the course of 1 h and then acidified with aq. HCl (2 M, 250 mL, 6.5 equiv) to a pH of ~1. The product was collected via filtration as an light red solid (16.2 g, 72.5 mmol, 95%). Note that the product can be further purified by recrystallization in hexanes with a minimal amount of EtOAc to afford an off-white solid, although it is not necessary for subsequent reactions. ^{1}H NMR (500 MHz, $CDCl_3$) δ 11.42 (s, 1H), 7.94 (d, J = 8.1 Hz, 1H), 7.60 (d, J = 4.3 Hz, 2H), 7.44 – 7.37 (m, 1H),

1.68 (s, 6H). ^{13}C NMR (125 MHz, $CDCl_3$) δ 181.98, 148.37, 138.78, 133.54, 128.22, 128.03, 125.80, 46.43, 27.18.

***N*-methoxy-*N*,2-dimethyl-2-(2-nitrophenyl)propanamide (3.60).** A solution of **3.59** (29.3 g, 140 mmol, 1.0 equiv) in thionyl chloride (100 mL) was refluxed at 80 °C overnight under a nitrogen atmosphere. The reaction mixture was concentrated under reduced pressure and cooled to 0 °C before potassium iodide (7.4 g, 45 mmol, 0.3 equiv), *N,O*-dimethylhydroxylamine hydrochloride (28.9 g, 296 mmol, 2.1 equiv) and acetonitrile (200 mL) were added. Dropwise addition of TEA (97 mL, 700 mmol, 5 equiv) in acetonitrile (170 mL) initiated the reaction at the same temperature. The reaction was allowed to warm to room temperature and proceed for 3 h. The reaction was quenched with minimal water and concentrated under reduced pressure. The reaction was acidified with aq. HCl (1M) to a pH of less than 3 and then extracted with CH_2Cl_2 (3×). The organic layer was dried over anhydrous Na_2SO_4 and concentrated under reduced pressure. The product was purified via silica chromatography (50% EtOAc/hexanes) to afford an orange-red oil (20.3 g, 80.5 mmol, 58%). ^{1}H NMR (500 MHz, $CDCl_3$) δ 7.76 – 7.67 (m, 1H), 7.57 – 7.48 (m, 2H), 7.34 (m, 1H), 3.10 (s, 3H), 2.90 (s, 3H), 1.57 (s, 6H).

2-methyl-2-(2-nitrophenyl)propanal (3.61). To a solution of **3.60** (10.1 g, 40.0 mmol, 1.0 equiv) in toluene (130 mL) at -78 °C was added DIBAL-H (1M in heptane, 140 mL, 140mmol, 3.5 equiv) over 30 min. After addition, the reaction was allowed to stir at the same temperature for 3 h. The reaction was quenched by slow addition of methanol (32 mL) and then it was diluted with EtOAc. The mixture was treated with sat. aq. Rochelle's salt and allowed to stir until all the solids dissolved. The organic layer was washed with sat. aq. Rochelle's salt (2×) and brine (1×). The solution was dried over anhydrous Na_2SO_4 and then the product was purified via silica chromatography (20% EtOAc/hexanes) to afford an orange-red oil (5.2 g, 40.0 mmol, 67%). ^{1}H

NMR (400 MHz, $CDCl_3$) δ 9.61 (s, 1H), 7.93 (dd, *J* = 8.1, 1.5 Hz, 1H), 7.64 (ddd, *J* = 7.9, 7.2, 1.5 Hz, 1H), 7.57 (dd, *J* = 8.0, 1.5 Hz, 1H), 7.46 (ddd, *J* = 8.1, 7.3, 1.5 Hz, 1H), 1.53 (s, 6H). 13C NMR (101 MHz, CDCl3) δ 200.67, 137.74, 133.64, 129.35, 128.45, 125.88, 49.64, 24.37.

2-(2-(2-nitrophenyl)propan-2-yl)oxirane (3.62). To a mixture of NaH (60 wt. %, 3.4 g, 84.9 mmol, 2 equiv), and trimethylsulfonium iodide (17.3 g, 84.9 mmol, 2 equiv) in anhydrous THF (70 mL) at 0 °C, was added **3.61** (8.2 g, 42.4 mmol, 1 equiv) in anhydrous DMSO (70 mL) and anhydrous THF (36 mL) dropwise. After addition, the reaction was allowed to warm to room temperature and stir for 5 h. The reaction solution was then cooled to at 0 °C and quenched with aq. HCl (2M, 35 mL). The resulting solution was diluted in 1:1 EtOAc/diethyl ether and washed with brine (3×). The organic layer was dried over Na_2SO_4 and concentrated under reduced pressure. The product was purified via silica chromatography (20% EtOAc/hexanes) to afford a yellow-brown oil (4.4 g, 21.2 mmol, 50%). ^{1}H NMR (400 MHz, $CDCl_3$) δ 7.65 (dd, *J* = 7.8, 1.0 Hz, 1H), 7.49 (ddd, *J* = 8.1, 6.2, 2.7 Hz, 1H), 7.39 – 7.33 (m, 2H), 3.12 (dd, *J* = 3.9, 2.8 Hz, 1H), 2.82 (t, *J* = 4.3 Hz, 1H), 2.74 (dd, *J* = 4.5, 2.8 Hz, 1H), 1.41 (s, 3H), 1.27 (s, 3H).

1-fluoro-3-methyl-3-(2-nitrophenyl)butan-2-ol (3.63). A Teflon vial was charged with **3.62** (2.4 g, 11.5 mmol, 1 equiv), triethylamine trihydrofluoride (TREAT-HF, 9.26 mL, 57.4 mmol, 5 equiv) and TEA (16 mL, 114.9 mmol, 10 equiv) and sealed in a high pressure bomb and the reaction was heated to 115 °C for 72 h. The reaction was cooled to room temperature before it was diluted by EtOAc and quenched with sat. aq. calcium chloride. The organic layer was washed with sat. aq. calcium chloride (2×), and then brine (1×). The organic layer was dried over anhydrous Na_2SO_4, concentrated under reduced pressure, and purified via silica chromatography (20% EtOAc/hexanes) to afford an oil (1.1 g, 4.7 mmol, 41%). ^{1}H NMR (400 MHz, $CDCl_3$) δ 7.60 (d, *J* = 8.1 Hz, 1H), 7.49 (ddd, *J* = 8.3, 5.3, 3.5 Hz, 1H), 7.41 – 7.32 (m, 2H), 4.56 – 4.47

(m, 1H), 4.44 – 4.26 (m, 2H), 1.42 (d, *J* = 7.3 Hz, 6H). ^{19}F NMR (376 MHz, $CDCl_3$) δ -230.14 – -230.91 (m).

1-fluoro-3-methyl-3-(2-nitrophenyl)butan-2-one (3.64). 3.63 (1.1 g, 4.7 mmol, 1 equiv) in DCM (10 mL) was added dropwise to a mixture of PCC (1.2 g, 5.7 mmol, 1.2 equiv) and celite (200% w/w relative to PCC) in CH_2Cl_2 (20 mL). The reaction was then allowed to stir for 16 h at room temperature. The reaction was filtered through a bed of celite and washed with EtOAc (3×). The filtrate was purified via silica chromatography (10% EtOAc/hexanes) to afford the product as a solid (0.81 g, 3.6 mmol, 77%). ^{1}H NMR (400 MHz, $CDCl_3$) δ 7.58 (dd, *J* = 7.9, 1.4 Hz, 1H), 7.47 (dd, *J* = 8.0, 1.7 Hz, 1H), 7.38 (td, *J* = 7.6, 1.4 Hz, 1H), 7.22 – 7.14 (m, 1H), 4.94 (d, J = 47.2 Hz, 2H), 1.60 (s, 6H). ^{19}F NMR (376 MHz, $CDCl_3$) δ -228.97 (t, *J* = 47.2 Hz).

2-(fluoromethyl)-3,3-dimethyl-3*H*-indole (3.65). To a solution of **3.64** (98.7 mg, 438 μmol, 1.0 equiv) in EtOAc (4.38 mL) and EtOH (4.38 mL) was added titanium(III) chloride (2.79 mL, 2.63 mmol, 6 equiv), dropwise, at -20 °C. The reaction was allowed to proceed at 4 °C for 16 h without stirring. The reaction was then allowed to warm to room temperature before it was quenched with brine containing 10% sat. bicarbonate. The product was extracted with chloroform (3×). The organic layer was dried over anhydrous Na_2SO_4 and purified via silica chromatography (20% EtOAc/hexanes) to afford an oil (59.9 mg, 338 μmol, 77%). ^{1}H NMR (500 MHz, $CDCl_3$) δ 7.68 – 7.58 (m, 1H), 7.36 – 7.27 (m, 3H), 5.47 (d, *J* = 46.7 Hz, 2H), 1.44 (s, 6H). ^{19}F NMR (470 MHz, $CDCl_3$) δ -229.01 (t, *J* = 46.8 Hz). HRMS (ESI-TOF) for [M+] calc'd 178.1032, found 178.1032.

2-(fluoromethyl)-3,3-dimethylindoline (3.66). To a solution of **3.65** (69.9 mg, 394 μmol, 1.0 equiv) in MeOH (20 mL) and water (10 mL), was added sodium borohydride (17.9 mg, 473 μmol, 1.2 equiv), portion-wise, at 0 °C. The reaction was allowed to stir for 4 h at the same

temperature. After completion, the product was extracted with DCM (3×) and the organic layer was dried over anhydrous Na_2SO_4. Concentration under reduced pressure afforded the product as a white solid (30.8 mg, 172 μmol, 44%), which was used without further purification. ^{1}H NMR (400 MHz, $CDCl_3$) δ 7.12 – 6.96 (m, 2H), 6.79 (td, *J* = 7.4, 1.1 Hz, 1H), 6.71 – 6.65 (m, 1H), 4.72 – 4.54 (m, 1H), 4.51 – 4.37 (m, 1H), 3.76 (ddd, *J* = 15.0, 8.8, 4.1 Hz, 1H), 1.41 (s, 3H), 1.15 (s, 3H). ^{19}F NMR (376 MHz, CDCl3) δ -227.38 (td, *J* = 47.3, 15.1 Hz).

C.2 References

(1) Britton, H. T. S.; Robinson, A. R. Universal Buffer Solutions and the Dissociation Constant of Veronal. *J. Chem. Soc.* **1931**, *0*, 1456–1462.

(2) Reynolds III, J. E.; Josowicz, M.; Tyler, P.; Vegh, R. B.; Solntsev, K. M. Spectral and Redox Properties of the GFP Synthetic Chromophores as a Function of PH in Buffered Media. *Chem. Commun.* **2013**, *49* (71), 7788.

(3) Hanwell, M. D.; Curtis, D. E.; Lonie, D. C.; Vandermeersch, T.; Zurek, E.; Hutchison, G. R. Avogadro: An Advanced Semantic Chemical Editor, Visualization, and Analysis Platform. *J .Cheminform.* **2012**, *4* (1), 17.

(4) Tetko, I. V.; Gasteiger, J.; Todeschini, R.; Mauri, A.; Livingstone, D.; Ertl, P.; Palyulin, V. A.; Radchenko, E. V.; Zefirov, N. S.; Makarenko, A. S.; et al. Virtual Computational Chemistry Laboratory - Design and Description. *J. Comput. Aided. Mol. Des.* **2005**, *19* (6), 453–463.

(5) Bellier, Q.; Dalier, F.; Jeanneau, E.; Maury, O.; Andraud, C. Thiophene-Substituted Aza-Bodipy as a Strategic Synthon for the Design of near-Infrared Dyes. *New J. Chem.* **2012**, *36* (3), 768.

(6) Zhang, X.; Yu, H.; Xiao, Y. Replacing Phenyl Ring with Thiophene: An Approach to Longer Wavelength Aza-Dipyrromethene Boron Difluoride (Aza-BODIPY) Dyes. *J. Org. Chem.* **2012**, *77* (1), 669–673.

(7) DeForest, C. A.; Tirrell, D. A. A Photoreversible Protein-Patterning Approach for Guiding Stem Cell Fate in Three-Dimensional Gels. *Nat. Mater.* **2015**, *14* (5), 523–531.

(8) Amatore, C.; Arbault, S.; Ducrocq, C.; Hu, S.; Tapsoba, I. Angeli's Salt (Na2N2O3) Is a Precursor of HNO and NO: A Voltammetric Study of the Reactive Intermediates Released by Angeli's Salt Decomposition. *ChemMedChem* **2007**, *2*, 898–903.

(9) Liacha, M.; Yous, S.; Poupaert, J. H.; Depreux, P.; Aichaoui, H. Friedel-Crafts Acylation of 2(3H)-Benzoxazolone: Investigation of the Role of the Catalyst and Microwave Activation. *Monatsh. Chem.* **1999**, *130*, 1393–1397.

(10) Urano, Y.; Kamiya, M.; Kanda, K.; Ueno, T.; Hirose, K.; Nagano, T. Evolution of Fluorescein as a Platform for Finely Tunable Fluorescence Probes. *J. Am. Chem. Soc.* **2005**, *127* (13), 4888–4894.

(11) Reinhardt, C. J.; Zhou, E. Y.; Jorgensen, M. D.; Partipilo, G.; Chan, J. A Ratiometric Acoustogenic Probe for In Vivo Imaging of Endogenous Nitric Oxide. *J. Am. Chem. Soc.* **2018**, *140*, 1011–1018.

(12) Reinhardt, C. J.; Xu, R.; Chan, J. Nitric Oxide Imaging in Cancer Enabled by Steric Relaxation of a Photoacoustic Probe Platform. *Chem. Sci.* **2020**, *11*, 1587–1592.

APPENDIX D: ELECTRON PARAMAGNETIC RESONANCE SPECTROSCOPY FOR MONITING NITRIC OXIDE RELEASE[6]

D.1 Introduction

tAPNO-5's photodecomposition was hypothesized to occur via photoinduced electron transfer from the electron rich aryl to the *N*-nitroso. This would then result in cleavage of the sessile bond to release APNO-5 (after protonation) and NO. A redshifted chromophore (λ_{max} = 676 nm) was observed after prolonged light irradiation, consistent with this proposal.[1,2]

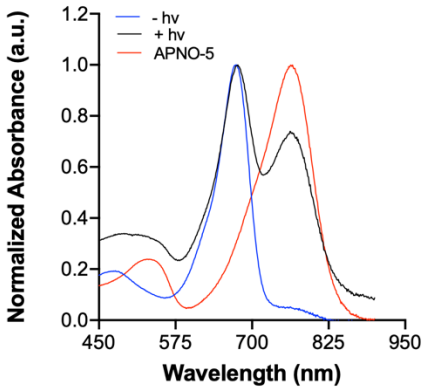

Figure D.1: UV-Vis spectra of tAPNO-5 before and after acquiring a PA spectrum from 680 – 900 nm. Authentic APNO-5 solution for comparison. All dye solutions were 10 μM and were prepared in 20 mM ethanolic potassium phosphate buffer (pH = 7.4, 50% v/v).

This light-induced decomposition was leveraged to develop the first single-photon NIR small-molecule NO donors with an integrated PA readout (photoNOD-1 and photoNOD-2). To decrease the propensity of capturing the release NO, the *o*-methoxy substituent was removed from the trigger. This enabled monitoring of analyte release in deep tissue following light irradiation. The utility was highlighted in a proof-of-concept small-animal model. Subcutaneous 4T1 tumors

[6]Portions of this chapter are reprinted or adapted with permissions from the following publication: (1) Zhou, E. Y.; Knox, H. J.; Reinhardt, C. J.; Partipilo, G.; Nilges, M. J.; Chan, J. Near-Infrared Photoactivatable Nitric Oxide Donors with Integrated Photoacoustic Monitoring. *J. Am. Chem. Soc.* **2018**, *140* (37), 11686–11697.[3] Copyright © 2018 American Chemical Society.

were established on the outer flanks of BALB/c mice. photoNOD-1 was administered systemically, via retroorbital injection, and only one of the tumors was irradiated. Under these conditions, it was possible to selectively induce apoptosis in the irradiated tumor with no affects in the non-irradiated tumor.[3,4]

This section outlines the general procedures for confirming and quantifying nitric oxide release from small molecule donors using the iron-*N*-methyl-D-glucamine dithiocarbamate complex, $Fe(MGD)_2$, as a NO-selective trap for electron paramagnetic resonance (EPR) spectroscopy. This can be used to either evaluate the stability of probes or the release of NO donors. The following protocols correspond to the Varian E-line 12" Century Series X-band CW EPR (VarianXBand) spectrometer.

D.2 Electron paramagnetic resonance for monitoring nitric oxide release

Degas septum-capped vials containing water, an organic cosolvent (typically the donor or probe should be soluble at 2 – 5 mM, DMF will be used for this example), or 10 mM potassium hydroxide for 30 minutes at room temperature with a steady stream of nitrogen gas. It is imperative to exclude oxygen contaminations until completing the irradiation because $Fe(MGD)_2$ is only specific for NO under anoxic conditions. It is important to note that nitrite can also produce detectable amounts of NO under anoxic conditions, so proper conditions are required to prevent false positives.[5,6]

Prepare the probe or donor solution (5 mM) in a septum-capped vial using degassed DMF and seal under nitrogen atmosphere. In a separate vial, transfer solid iron sulfate heptahydrate or MGD, evacuate the container, and then place the sample under nitrogen. Repeat this process three times to minimize contamination by molecular oxygen. Dissolve the solids with the appropriate

amount of degassed water for a final concentration of (8 mM Fe(II) and 40 mM MGD). These stock solutions are used to prepare each sample in sealed, degassed septum-capped vials. Final ratios of 1:4:20 (donor/probe:Fe(II):MGD) are used to maximize complex formation and trapping efficiency. A 50% cosolvent solution was selected to ensure solubility of the constituents while limiting sample heating during EPR measurements. The ratio of the donor to $Fe(MGD)_2$ and cosolvent percentage can be all modified, as necessary.

Irradiate each sample with an appropriate excitation source (e.g., a pre-warmed photoacoustic tomographer, LED light) at the wavelength of interest. Irradiation times can be varied to monitor release kinetics (e.g., 0, 5, and 40 min irradiations). After complete, open the vials and collect the sample using capillary action into a hematocrit. Seal both the top and bottom with wax tube sealant and place the capillary tube in a quartz EPR tube for acquisition.

D.3 Acquiring electron paramagnetic resonance spectra

The following protocol has been adapted, with permission, from Dr. Mark J. Nilges (EPR Research Center, University of Illinois at Urbana-Champaign).

First, sign into ChemFOM to turn on the instrument and begin the setup process. Turn on the water flow to cool the magnetic jackets of the instrument. It is essential to ensure that the water continues to flow throughout the experiment to prevent overheating. Turn on the console power switch, magnet switch (on Field dial, set 10,000 position to 0), amplifier, and set the microwave bridge for the following settings: power 30 dB; reference arm off, and mode to tune. Then turn on the microwave frequency counter, insert the sample, and begin tuning the cavity. Center the klystron mode pattern (on the scope) using the frequency knob. Maximize the cavity resonance dip using the iris, then lower the power to 40 dB. Turn the reference arm to on and adjust the phase

to make the dip symmetrical. After it is satisfactorily symmetrical, turn the reference arm off and turn the klystron mode to operate. Center the needle on the AFC meter with the frequency. Once centered, turn on the reference arm and adjust the phase to maximize the detected current reading. Increase the power to the desired level (provided below for the nitric oxide trapping experiments) while keeping the detected current between 200 and 250 A) with the iris. Verify that the AFC has not shifted (repeat if it has, proceed if it has not). Record the modulation frequency and power for reference. Set the modulation amplitude, gain; sweep width, scan time, and number of scans. The measurement can then be performed.

When changing samples, it is necessary to return the power to 30 dB, turn off the reference arm, and change the mode to tune. Change the sample and then center the klystron pattern on the scope using the frequency knob. Confirm that the cavity resonance dip is maximized (it should if the samples are similar). Change the klystron mode to operate and center the needle on the AFC meter using the frequency. Turn the reference arm on and adjust the phase to maximize the determined current reading. Reperform the power adjustment while maintaining the determined current using the iris and acquire. Note that minor to no changes are required if the samples are similar. To turn off the instrument: turn the power down to 30 dB, turn the reference arm to off, the mode to tune and then standby, and then turn off the microwave frequency counter, amplifier, magnet switch (on field dial), the console power switch, the water, and sign out of the ChemFOM system.

Acquire the EPR spectra of each sample at room temperature using the following parameters: Modulation frequency: 100 kHz; Modulation amplitude: 2.5 G; Gain: 4000; Sweep width: 100 G; Scan time: 0.5 min per scan, 6 scans; Microwave power: 12 dB; Microwave frequency, 9.30 GHz

Generate a calibration curve for quantification using an established NO donor (e.g., MAHMA-NONOate) or saturated aqueous solution. NONOate donors should be prepared in degassed, aqueous potassium hydroxide (10 mM) at a range of concentrations. Prepare the samples in an identical fashion to probe/donor allow the sample to incubate for at least 20 half-lives. Confirm NO-release by the characteristic MGD_2-Fe-NO triplet (g = 2.04) and quantify using the calibration curve (EPR intensity peak height to NO concentration). Representative data is provided in Figure D.2.

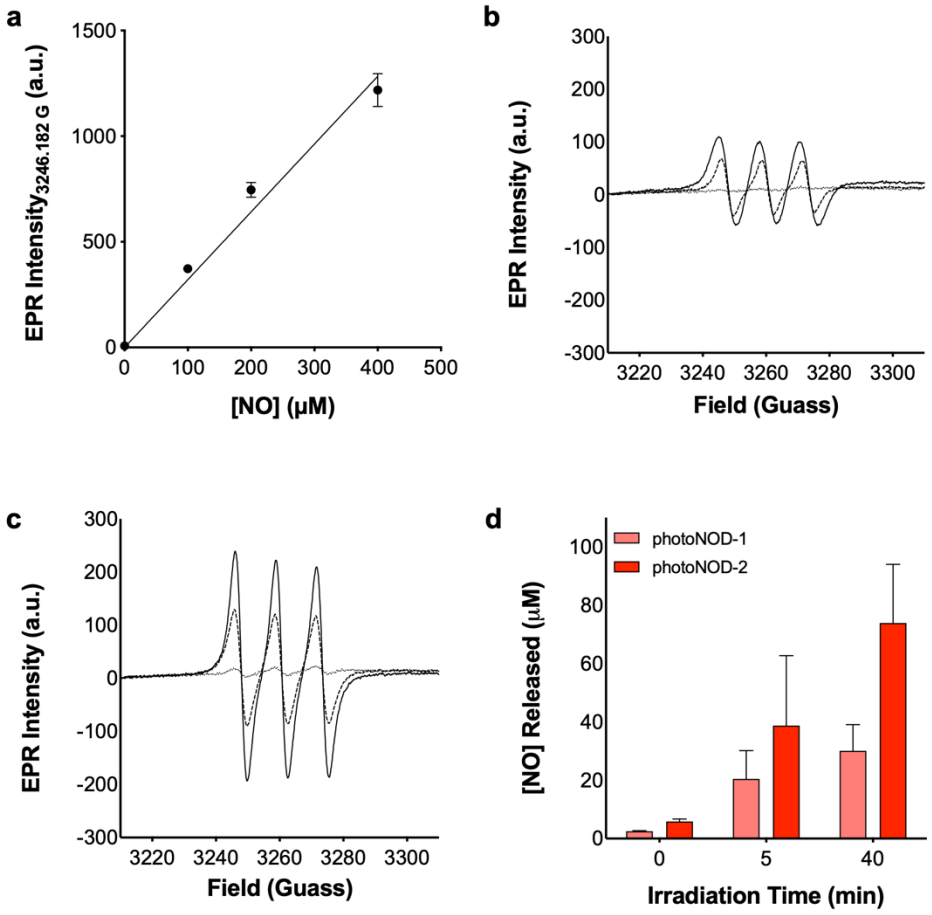

Figure D.2: (a) Calibration curve for NO from MAHMA-NONOate using the $Fe(MGD)_2$ NO-selective spin trap. (b) EPR spectra collected after 0, 5, and 40 min of irradiation of (b) photoNOD-1 (690 nm) or (c) photoNOD-2 (680 nm) (200 μM in water containing 50% DMF v/v) in the presence of $Fe(MGD)_2$. (d) Quantification of NO release. Data presented as mean ± standard deviation (n = 3).

D.4 References

(1) Namiki, S.; Arai, T.; Fujimori, K. High-Performance Caged Nitric Oxide: A New Molecular Design, Synthesis, and Photochemical Reaction. *J. Am. Chem. Soc.* **1997**, *119* (16), 3840–3841.

(2) Ieda, N.; Hotta, Y.; Miyata, N.; Kimura, K.; Nakagawa, H. Photomanipulation of Vasodilation with a Blue-Light-Controllable Nitric Oxide Releaser. *J. Am. Chem. Soc.* **2014**, *136* (19), 7085–7091.

(3) Zhou, E. Y.; Knox, H. J.; Reinhardt, C. J.; Partipilo, G.; Nilges, M. J.; Chan, J. Near-Infrared Photoactivatable Nitric Oxide Donors with Integrated Photoacoustic Monitoring. *J. Am. Chem. Soc.* **2018**, *140* (37), 11686–11697.

(4) Zhou, E. Y.; Knox, H. J.; Reinhardt, C. J.; Partipilo, G.; Chan, J. B. T.-M. in E. Near-Infrared Photoactivatable Nitric Oxide Donors with Photoacoustic Readout. In *Methods in Enzymology*; Academic Press, 2020; 10.1016/bs.mie.2020.05.003.

(5) Tsuchiya, K.; Yoshizumi, M.; Houchi, H.; Mason, R. P. Nitric Oxide-Forming Reaction between the Iron-N-Methyl-D-Glucamine Dithiocarbamate Complex and Nitrite. *J. Biol. Chem.* **2000**, *275* (3), 1551–1556.

(6) Komarov, A. M.; Reif, A.; Schmidt, H. H. H. W. In Vitro Detection of Nitric Oxide and Nitroxyl by Electron Paramagnetic Resonance. *Methods Enzymol.* **2002**, *359* (1985), 18–27.